Design, Construction, and Testing of a Cherenkov Coincidence Detector for Proton Beam Therapy

Master of Science Dissertation

University of Siegen

Department of Physics

Experimental Particle and Astroparticle Physics Group

Kaveh Kooshkjalali

Supervisor: Prof. Dr. Ivor Fleck

April 2023

Design, Construction, and Testing of a Cherenkov Coincidence Detector for Proton Beam Therapy

Master-Arbeit

zur Erlangung des akademischen Grades

Master of Science

(M.Sc.)

Universität Siegen

Department Physik

vorgelegt von

Kaveh Kooshkjalali

April 2023

To Afghan women

deprived of education

Contents

Abstract

Proton beam Therapy is one of the prominent treatments for cancer patients. However, lack of real-time data concerning the location and dose of the beam vis-à-vis the tumor tissue often results in side effects in patients. Such information can be provided by the gamma emitted from the excited tissue following irradiation, prompting the need for a gamma detector capable of resolving photons above 0.5 MeV. A Compton camera is, in theory, an ideal means for detection of photons emitted from the tumor tissue, ergo providing real-time feedback for such treatments. In a Compton camera, high energy photons emitted from the excited nuclei within the tumor tissue enter a radiator material and produce a photon and an electron due to Compton Effect. Conventional modalities rely solely on detection of the Compton photon in order to reconstruct the incident photon. Such methods, however, suffer from Compton photon's depth of interaction and incomplete energy deposition uncertainties.

This work presents an experimental detection system designed to detect Compton Electron's energy and direction. The Compton electron information supplements the Compton photon to reconstruct the incident photon. Electrons from a $^{90}Sr/^{90}Y$ source are used to create Cherenkov photons in a PMMA radiator, in contact with an 8×8 SiPM array with $3 \times 3mm^2$ read-out channels. The SiPM detects Cherenkov photons in coincidence using a 64-channel ASIC. A correlation between electron energy and Cherenkov photon yield at the SiPM detector is achieved by a magnetic system designed to separate electrons based on their energy. The SiPM is maintained at subzero temperatures to minimize noise.

Electron energy has been successfully reconstructed and a Cherenkov cone has been observed in the detector. This work opens the door for implementation of an improved Compton camera, utilizing dual detection of Compton photons and electrons simultaneously for radiation therapy.

1. Introduction

1.1 Motivation

Radiation therapy is one of the primary cancer treatments with more than 50% of cancer patients receiving some form of radiation as a solution **[1]**. It includes emission of photons or charged particles on the cancer tissue in order to either eliminate or shrink the malignant cells. Radiation therapy has been in use for well over a century. Physicians used X-Ray therapy for cancer treatment in the early 20^{th} century **[2]**. With the goal being elimination of the malignant tumor while leaving the healthy tissue intact, Proton Beam Therapy (PBT) is one of the prominent methods used in external beam radiation therapy.

Other types of beams such as carbon ion or photons are also used. However, such methods are not as discriminatory as PBT is when it comes to affecting healthy cells. Secondary cancer emergence due to irradiation of healthy tissues is a common side effect of such treatments **[3]**. What differentiates PBT is the protons' propensity to deposit almost all of their energy at the end of their path in a region known as Bragg Peak **[4]**. As early as 1977, the proton beam is shaped to the geometry of the target to broaden the Bragg peak to match the length of the cancer tissue **[5]**. This method is known as Spread-Out Bragg Peak (SOBP). **Figure 1.1** demonstrates the behavior of different types of radiation.

At the same time, any range-related uncertainties in dose delivery of the proton beam can lead to irradiation of critical, healthy tissues as shown in **Figure 1.1**. The common practice is Image-Guided Radiation Therapy (IGRT), where the cancer area is scanned via CT, MRI, PET, or PET-CT before, during, and after the beam therapy to calibrate the beam to the target. While this method works to some degree, there are always uncertainties involved. A real-time monitoring of the beam while the radiation therapy is ongoing can provide crucial information which would spare the healthy tissue and subsequently decrease the probability of radiation-related secondary cancer in patients. Real-time imaging during PBT requires constant feed of information on the interaction at irradiated tissue. Depositing their energy in the cancer cell, the protons excite the nuclei in the cancer tissue. De-excitation of the nuclei involves emission of gamma rays. Energy and momentum information of the gamma rays reveal the depth and dose delivery of the initial proton beam.

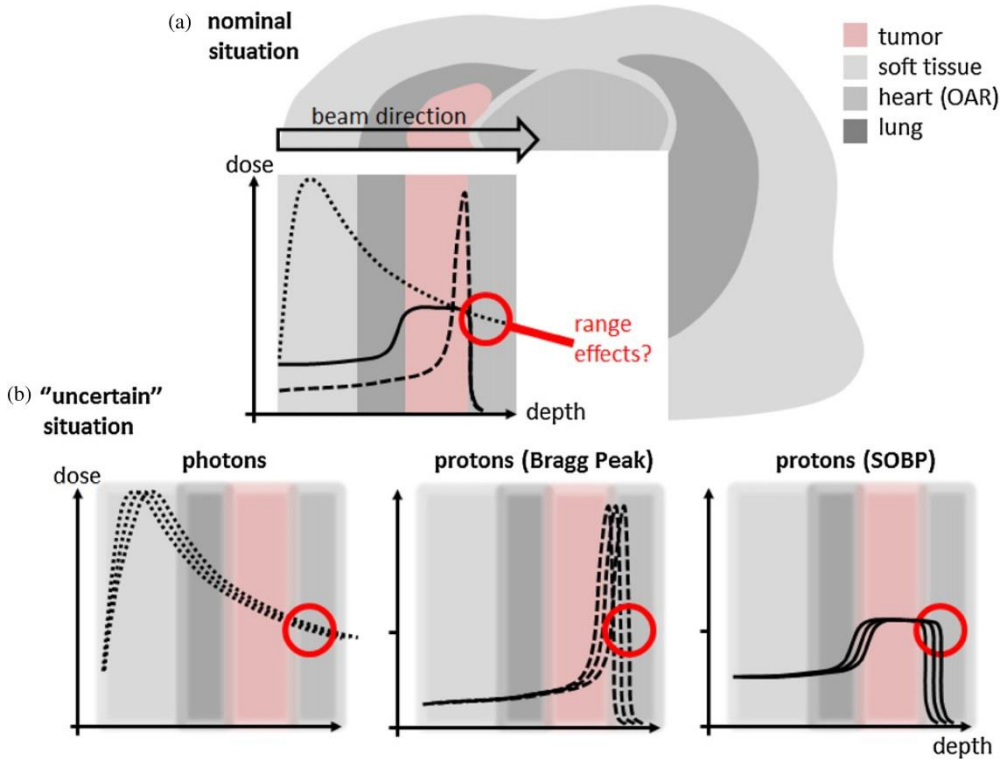

Figure 1.1 (a) Comparison between photon and proton beam dose delivery in the body. Photons (dotted line) reach a peak early on in their path and continue to deposit substantial portion of their energy in healthy cells before they reach the tumor. Mono-energetic protons (dashed line), on the other hand, deposit most of their energy in the tumor before they are stopped. SOBP proton beam (straight line) covers the entire cancer tissue and is the most common PBT method. (b) The effect of uncertainties in range for different methods **[5]**.

1.2 Compton Camera

One potential imaging device for real-time monitoring of the proton beam is a Compton Camera proposed by Todd et al. in 1974 **[6]**. The detection principle is demonstrated in **Figure 1.2**. The gamma photon emitted from the cancer tissue enters a scattering layer where it undergoes Compton Effect and produces a photon and an electron. The Compton photon is then detected in an absorption layer. Energy and momentum information from said photon helps reconstruct the initial gamma.

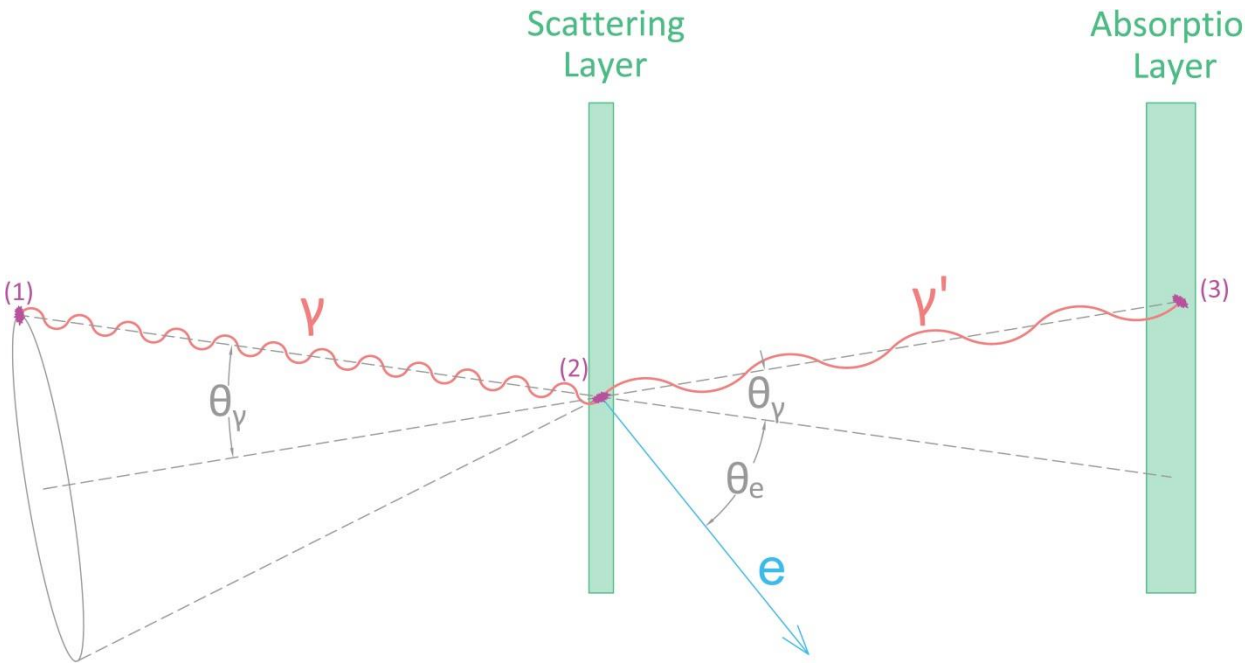

Figure 1.2 Principles of Compton Camera proposed by Todd et al. **[6]**. Incoming gamma (1) from the body undergoes Compton Scattering in the first layer of the detector (2). The second layer stops and detects the secondary photon (3).

Full reconstruction of the incident photon (P_γ) requires knowledge of two properties: Compton photon's angle (θ_γ) and energy $(E_{\gamma'})$. The former is related to the latter by **Equation 1.1** or alternatively **Equation 1.2** (See Section 2.5 for full description). θ_γ and $E_{\gamma'}$ are resolved in the absorber layer, while the scattering layer provides additional location and deposited energy information, which are used to eliminate background. The combination of these two parameters limits the location of the source to a cone with half angle of θ_γ as shown in **Figure 1.2**. The cone does not possess sharp edges due to uncertainties in energy and position. Multiple incident photons are then analyzed in a similar manner to pinpoint the location of the source statistically as shown in **Figure 1.3**.

$$E_{\gamma'} = \frac{E_\gamma}{1 + \frac{E_\gamma}{m_e c^2}(1 - cos\theta_\gamma)} \qquad \textbf{Eq. (1.1)}$$

$$cos\theta_\gamma = 1 + m_e c^2 \left(\frac{1}{E_\gamma} - \frac{1}{E_{\gamma'}}\right) \qquad \textbf{Eq. (1.2)}$$

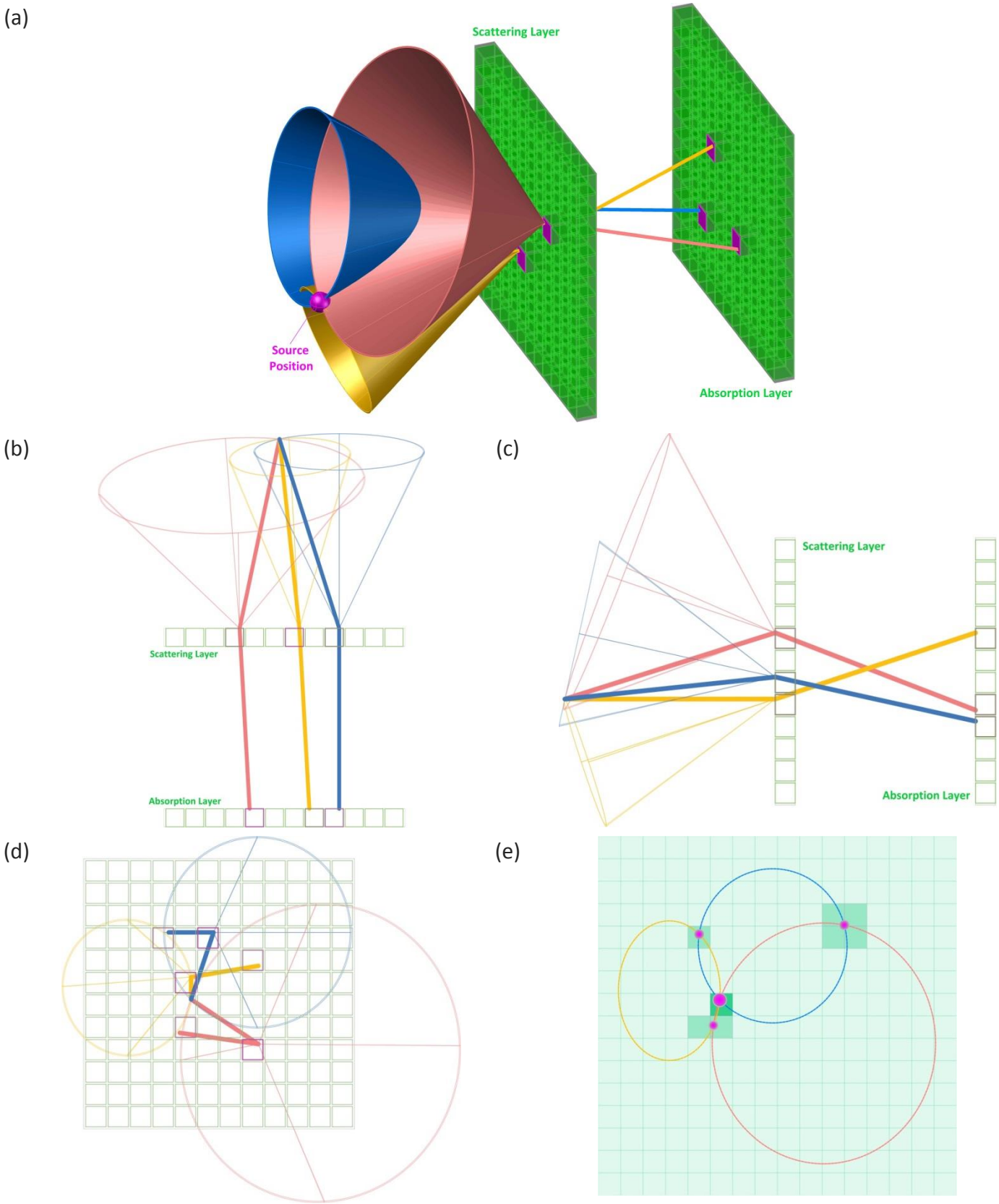

Figure 1.3 Determination of the source location in a Compton Camera. (a) 3D view of three photons interacting with the scattering and absorption layers. Reconstruction leads to three cones overlapping in a singular location. (b) Top view. (c) Side view. (d) Front view. (e) Statistical reconstruction of the source. Intersections of the cones are color coded with darkest bin having the highest probability of being the source location.

Measurements of photon's energy and position in two layer detectors have certain shortcomings. Simulations suggest that the Compton photon may not deposit its entire energy in the second detector (Absorption Layer), rendering a full reconstruction impossible **[7]**. Furthermore, uncertainties in the depth of interaction in the second layer (especially for thick scintillators) introduce resolution deterioration due to parallax **[8]**. Depth-of-Interaction techniques are necessary to correct the uncertainties **[9]**. Incident photon may, in addition, undergo multiple Compton scattering in the first layer, resulting in multiple energy depositions in the absorber layer. To that end, detection of the Compton electron's position and energy in the first layer may resolve the shortcomings. In case of partial absorption in the second layer, electron's information helps produce the Compton cone. When full absorption occurs, electron information adds to the location precision within the Compton cone. Peterson et al. proposed use of Cherenkov light for reconstruction of the electron due to Cherenkov light's advantageous rate and time resolution as well as parallax suppression **[10]**. Electron detection via Cherenkov light has been the focus of our team, as full reconstruction of the energy, interaction position, and momentum is a major leap towards making the Compton Camera a viable real-time imaging device for nuclear medicine.

1.3 Outline of the Experiment

This work examines determination of Compton electron's energy via coincidence detection of Cherenkov light. A radioactive source (^{90}Sr) is used to simulate the Compton electrons which enter a radiator material and produce Cherenkov light. The momentum information of the electron can be determined form the shape of the Cherenkov cone on the detector. Although determining the momentum information of the electron from the Geometry of the Cherenkov cone is within the capability of this experimental setup, it is beyond the scope of the current study. Successful correlation of Cherenkov light to electron energy will lead to the ultimate goal of Compton research group at University of Siegen. The schematics of the ultimate setup is demonstrated in **Figure 1.4**

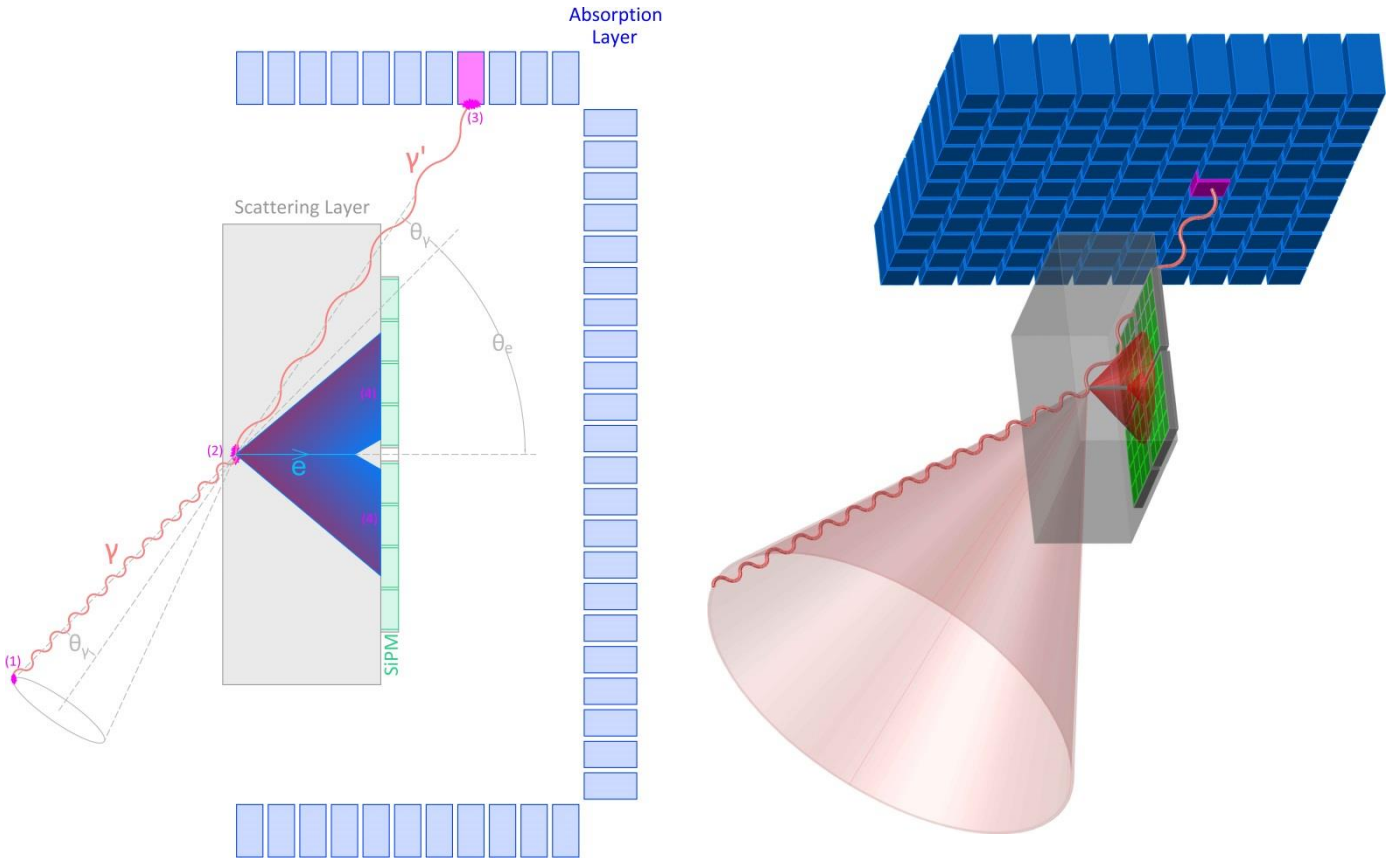

Figure 1.4 Determination of Compton electron's energy via coincidence detection of Cherenkov light in single photon detectors is the main focus of this work. The imaginary gamma emitted from a tumor (1) produces a secondary photon and an electron in the scattering layer, a 3.5x3.5x0.98 cm PMMA block (2). The Compton electron will be simulated by a radioactive source undergoing β^- decay. The electron creates Cherenkov light in the PMMA, which will be detected by an SiPM array (4). The number of Cherenkov photons will then be correlated against electron energy. The secondary photon information is shown merely for completion and is not within the scope of this work.

The ^{90}Sr source emits electrons in a spectrum with energies up to 2.278 MeV. The source is positioned in a way that it emits the electrons through its collimator. By placing an electromagnet after the source, only a narrow band around a specific energy reaches a collimator at the end of the path. The magnetic field bends electrons with a force proportional to the magnetic field strength and electron velocity. After the magnet, the beam is directed towards a collimator with varying opening gaps (between 1 to 5 mm) to further narrow down the electron energies. The beam eventually reaches a radiator (PolyMethyl MethAcrylate - PMMA) where it produces Cherenkov photons due to faster than light travel of charged electrons in PMMA. The Cherenkov photons are detected via an SiPM array. The setup is shown in **Figure 1.5**.

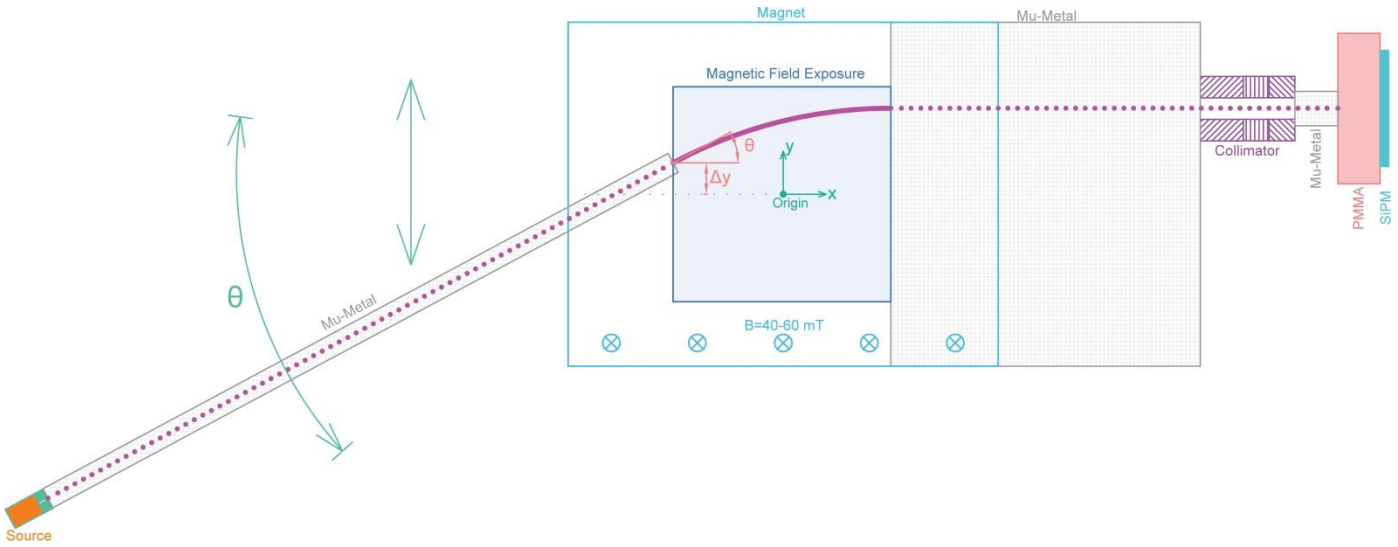

Figure 1.5 Schematics of the experimental setup used in this work.

The experiment builds a relation between photon count and electron energy which will be used to identify unknown electron energies in a Compton Camera. In addition, Cherenkov photons produce cone shapes in the detector. Analyzing the shape leads to identifying the angle of incoming electrons. Combined, Electron energy and angle information allows the reconstruction of the Compton electron in a Compton Camera.

The main objective of this study is to identify the energy of an unknown incoming electron by counting the number of Cherenkov photons it produces in the radiator. The angular information are presented, but not analyzed.

In Chapter two, the theory behind every physics aspect of the experiment is discussed. A description of the Silicon Photo Multiplier detectors, their function, and performance is presented in Chapter three. Chapter four details the design and development of the experimental setup. A detailed description of the electron trajectory and energy resolution is provided in Chapter five. The calibration of the detectors and data taking procedure are discussed in Chapter six. Analysis of the results is presented in Chapter seven.

2. Theory

2.1 Beta Decay Theory

The source of electrons for this study is β^- decay of Strontium-90 and its daughter nucleus Yttrium-90. With that in mind, a brief description of β decay is presented.

β decay occurs when an atomic nucleus emits a beta particle and is transformed to its isobar. In other words, a neutron (β^- decay) or a proton (β^+ decay) undergoes quark flavor change via emitting an intermediate vector boson, i.e., a $W^{\pm}$ boson, and becomes a proton or neutron respectively, creating a more stable ratio of protons to neutrons in the daughter nucleus.

$$p \longrightarrow n + e^+ + \nu_e \quad (\beta^+ \text{ decay})$$
$$n \longrightarrow p + e^- + \bar{\nu}_e \quad (\beta^- \text{ decay}) \qquad \textbf{Eq. (2.1)}$$

In β^- decay specifically, a down quark ($Q = -\frac{1}{3}\, e$) emits a W^- boson and becomes an up quark ($Q = +\frac{2}{3}\, e$) as demonstrated in **Figure 2.1**; "e" represents the elementary charge, i.e., the amount of charge of one electron; it is equivalent to 1.6022×10^{-19} Coulombs. The Beta decay is, therefore, governed by the electroweak force **[11]**. The W^- boson further decays to an electron e^- and an electron antineutrino $\bar{\nu}_e$.

$$d \longrightarrow u + e^- + \bar{\nu}_e \qquad \textbf{Eq. (2.2)}$$

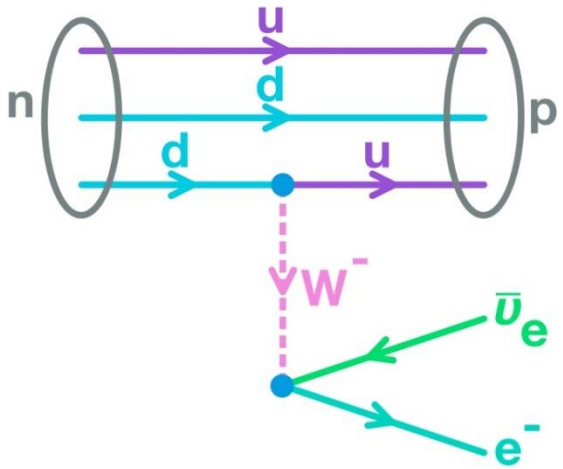

Figure 2.1 Feynman diagram for β^- decay of a neutron into a proton, an electron, and an electron antineutrino via a W^- boson emission.

The released energy (Q Value) of β^- decay is determined by comparing the mass of the parent and daughter nuclei:

$$Q_{\beta^-} = \left([mass\ of\ the\ parent\ nucleus] - [mass\ of\ the\ daughter\ nucleus] - m_e - m_{\bar{\nu}_e}\right).c^2 \quad \textbf{Eq. (2.3)}$$

$$Q_{\beta^-} = \left([M(Z,A) - Zm_e + B_e(Z)] - [M(Z+1,A) - (Z+1)m_e + B_e(Z+1)] - m_e - m_{\bar{\nu}_e}\right).c^2$$

$$\therefore\ Q_{\beta^-} \cong \left(M(Z,A) - M(Z+1,A)\right).c^2 \quad \textbf{Eq. (2.4)}$$

where Z stands for atomic number, A is the nucleon number (mass number), and m_e and c denote electron mass and speed of light respectively. $B_e(Z)$ is the correction made for the total binding energy of all the removed electrons, not applicable to this study **[12]**. $\mathrm{m}_{\bar{\nu}_e}$is the mass of the electron antineutrino which is ignored.

2.1.1 Strontium-90

Strontium-90 ($^{90}_{38}Sr_{52}$) has a half-life of $T_{1/2} = 29.91\ y$ and decays into the ground state of its isobar, Yttrium-90 with 100% branching ratio **[13]**. Hence, the released energy of the transition, roughly 546 keV, is completely transferred into the kinetic energy of electron and electron antineutrino **[11]**.

$$^{90}_{38}Sr_{52} \longrightarrow {}^{90}_{39}Y_{51} + e^- + \bar{\nu}_e \quad \textbf{Eq. (2.5)}$$

The atomic masses of Strontium-90 and Yttrium-90 are 89907727.870 μu and 89907141.749 μu respectively **[14].** The symbol u is the unified atomic mass unit, AKA Dalton. One Dalton is defined as $\frac{1}{12}$ of the atomic mass of one ^{12}C atom in its electronic and nuclear ground states and at rest. It is equivalent to $1.6605390666 \times 10^{-27}$kg.

$$\mathrm{m}_{^{90}Sr} = 89.90772787\ u \cong 1.49295294517377 \times 10^{-25}\ kg \quad \textbf{Eq. (2.6)}$$

$$\cong 8.37485145907506 \times 10^{10}\ \frac{eV}{c^2}$$

$$\mathrm{m}_{^{90}Y} = 89.907141749\ u \cong 1.49294321240558 \times 10^{-25}\ kg \quad \textbf{Eq. (2.7)}$$

$$\cong 8.37479686225198 \times 10^{10}\ \frac{eV}{c^2}$$

$$Q_{\beta^-} = \left(m_{^{90}Sr} - m_{^{90}Y}\right).c^2 \cong 545.968\ \text{keV} \qquad \textbf{Eq. (2.8)}$$

The calculated released energy matches the reference value of 545.967 keV reported by Huang et al. **[14]**. **Figure 2.2** demonstrates the decay scheme of ^{90}Sr.

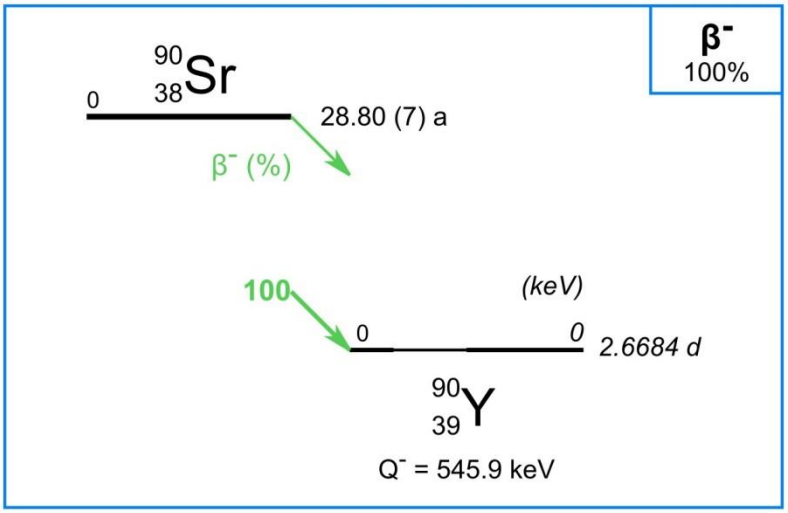

Figure 2.2 ^{90}Sr β$^-$ decay scheme **[15]**.

2.1.2 Yttrium-90

Yttrium-90 ($^{90}_{39}Y_{51}$) has a half-life of $T_{1/2} = 64\ h$ hours and undergoes β$^-$ decay into the ground state of $^{90}_{40}Zr_{50}$, a stable element, with a branching ratio of 99.9885% (**Equation 2.9**). In this case, the decay energy is 2278.5 keV **[13]**. In a negligible branch (0.0115%), Yttrium-90 decays into the excited state of Zirconium-90, which is followed by a 1760.74 keV γ emission (**Equation 2.10**) **[13]**. However, the latter occurs so rarely that it will be ignored in this study.

$$^{90}_{39}Y_{51} \longrightarrow {}^{90}_{40}Zr_{50} + e^- + \bar{\nu}_{e^-} \qquad \textbf{Eq. (2.9)}$$

$$\begin{cases} {}^{90}_{39}Y_{51} \longrightarrow {}^{90}_{40}Zr^*_{50} + e^- + \bar{\nu}_{e^-} \\ {}^{90}_{40}Zr^*_{50} \longrightarrow {}^{90}_{40}Zr_{50} + \gamma \end{cases} \qquad \textbf{Eq. (2.10)}$$

In a similar fashion to the previous section, the released energy of the β$^-$ decay can be determined. The atomic mass of Yttrium-90 and Zirconium-90 are 89907141.749 μu and 89904698.755 μu respectively **[14]**.

$$m_{^{90}Y} = 89.907141749\ u \cong 1.49294321240558 \times 10^{-25}\ kg \cong 8.37479686225198 \times 10^{10}\ \frac{eV}{c^2}$$ **Eq. (2.11)**

$$m_{^{90}Zr} = 89.904698755\ u = 1.49290264553582 \times 10^{-25}\ kg \cong 8.37456929881166 \times 10^{10}\ \frac{eV}{c^2}$$ **Eq. (2.12)**

$$Q_{\beta^-} = \left(m_{^{90}Y} - m_{^{90}Zr}\right).c^2 \cong 2275.634\ \text{keV}$$ **Eq. (2.13)**

The energy matches 2275.635 keV presented by Huang et al. **[14]**. **Figure 2.3** demonstrates the decay scheme.

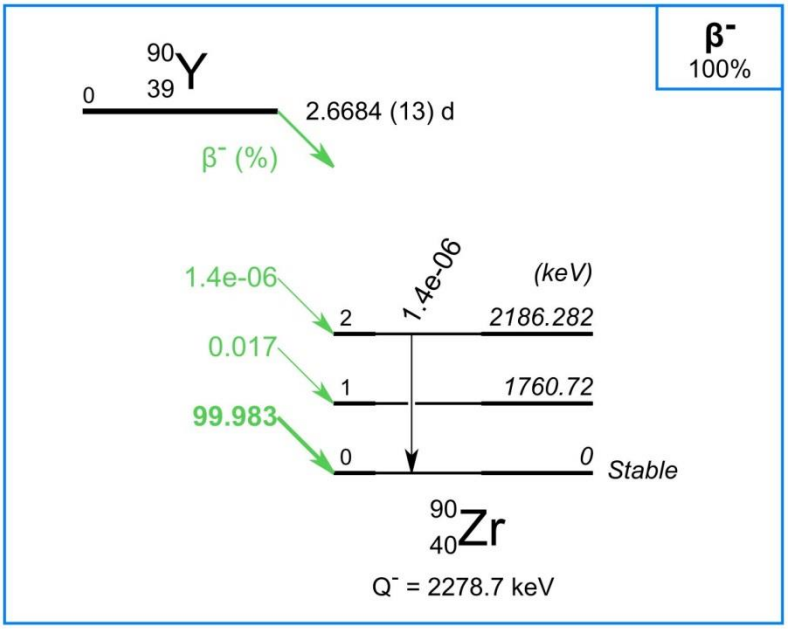

Figure 2.3 ^{90}Y β$^-$ decay scheme A **[15]**.

Table 2.1 outlines β$^-$ decay processes of both ^{90}Sr and ^{90}Y **[13]**. The digits after the letter β represent the ground or excited state of the parent and daughter nucleus respectively.

Table 2.1 β$^-$ decay of Strontium 90 and Yttrium 90 and their products **[13]**.

Parent	Daughter	Decay	Branching ratio	Energy (Q)	e^- ave.	e^- Max	$\bar{\nu}_{e^-}$ ave.	γ
$^{90}_{38}Sr_{52}$	$^{90}_{39}Y_{51}$	$\beta^-_{0,0}$	100%	546 keV	195.7 keV	546 keV	350.8 keV	0
$^{90}_{39}Y_{51}$	$^{90}_{40}Zr_{50}$	$\beta^-_{0,0}$	99.9885%	2275.6 keV	932.3 keV	2276 keV	1348 keV	0
$^{90}_{39}Y_{51}$	$^{90}_{40}Zr_{50}$	$\beta^-_{0,1}$	0.0115%	517.8 keV	-	517.8 keV	-	1760.7 keV

2.1.3 Energy Spectra

2.1.3.1 Relativistic Energy Momentum Relation

Einstein's theory of special relativity states that the laws of Physics are invariant (identical) in all frames of references and that the speed of light in vacuum is constant for all observers regardless of the motion of light source or observer **[16]**. Granted, a relation between relativistic energy and momentum can be attained.

$$\left.\begin{array}{c} E = mc^2 \\ m = \dfrac{m_0}{\sqrt{1-\left(\frac{v}{c}\right)^2}} = \dfrac{m_0}{\sqrt{1-\beta^2}} = \gamma m_0 \\ \beta = \dfrac{v}{c} \end{array}\right\} \Rightarrow \; m^2\left(1-\frac{v^2}{c^2}\right) = m_0^2 \quad \Rightarrow \quad m^2c^2 - m^2v^2 = m_0^2c^2 \qquad \textbf{Eq. (2.14)}$$

$$\Rightarrow \quad \boldsymbol{m^2c^4 - m^2v^2}c^2 = m_0^2c^4 \quad \Rightarrow \quad \boldsymbol{E^2 - p^2}c^2 = m_0^2c^4 \quad \Rightarrow \quad E = c\sqrt{p^2 + m_0^2c^2} \qquad \textbf{Eq. (2.15)}$$

$$E = E_{kin} + E_0 \quad \Rightarrow \quad \boldsymbol{m}c^2 = \boldsymbol{\gamma m_0}c^2 = E_{kin} + m_0c^2 \quad \Rightarrow \quad E_{kin} = (\gamma - 1)m_0c^2 \qquad \textbf{Eq. (2.16)}$$

$$\boldsymbol{E} = E_{kin} + E_0 \quad \Rightarrow \quad \boldsymbol{c}\sqrt{\boldsymbol{p^2} + \boldsymbol{m_0^2c^2}} = E_{kin} + m_0c^2 \quad \Rightarrow \quad E_{kin} = c\sqrt{p^2 + m_0^2c^2} - m_0c^2 \qquad \textbf{Eq. (2.17)}$$

$$E_{kin} = c\sqrt{p^2 + m_0^2c^2} - m_0c^2 \quad \Rightarrow \quad p = \frac{1}{c}\sqrt{E_{kin}(E_{kin} + 2m_0c^2)} = \frac{1}{c}\sqrt{E^2 - (m_0c^2)^2} \qquad \textbf{Eq. (2.18)}$$

where E, E_{kin}, and E_0 represent total energy, relativistic kinetic energy, and energy at rest of a particle respectively. m and m_0 are relativistic mass and mass at rest of the particle respectively. p stands for relativistic three-momentum of the particle, γ is the Lorentz factor, and c is the speed of light.

In the literature of relativity, the energy and momentum of a particle are often expressed in four-vector form. They are defined so that the length of a four-vector is invariant under a coordinate transformation. The invariance of the energy-momentum four-vector is associated with the fact that the rest mass of a particle is invariant under coordinate transformations. The length of this four-vector is the rest energy of the particle.

$$\vec{P} = \begin{bmatrix} E \\ p_x c \\ p_y c \\ p_z c \end{bmatrix} = \begin{bmatrix} E \\ \vec{p}c \end{bmatrix} \qquad \textbf{Eq. (2.19)}$$

$$\sqrt{\vec{P}.\vec{P}} = \sqrt{E^2 - (\vec{p}c)^2} = m_0 c^2 \qquad \textbf{Eq. (2.20)}$$

2.1.3.2 Conservation Laws of β^- decay

Both β^- decay schemes described by **Equations 2.5** and **2.9** are three-body decays. In such nuclear transmutations, the baryon number, the lepton number, angular momentum, and four-momentum are conserved.

Baryon number (**Equation 2.21**) does not change in case of β^- decay, as only quark flavor changes, i.e., the number of quarks and antiquarks remain the same.

$$\mathrm{B} = \frac{n_q - n_{\bar{q}}}{3} \qquad \textbf{Eq. (2.21)}$$

Lepton Number (**Equation 2.22)** is also conserved during β^- decay with the addition of electron antineutrino. All leptons are assigned the value of +1, and all antileptons are assigned the value of -1.

$$\mathrm{L} \equiv n_l - n_{\bar{l}} \qquad \textbf{Eq. (2.22)}$$

$$n \longrightarrow p + e^- + \bar{\nu}_e$$

$$L: \quad 0 \quad = \quad 0 \quad +1 \quad -1$$

For allowed decays, the net orbital angular momentum is zero, and only spin quantum numbers are considered. Electron and electron antineutrino are fermions with half-integer spins. Therefore, they may couple to total spin of 1 (parallel) or 0 (antiparallel).

In case of ^{90}Sr decay, the four-momentum conservation law, **Equation 2.23**, yields:

$$P_{Sr} = P_Y + P_e + P_{\bar{\nu}_e} \qquad \textbf{Eq. (2.23)}$$

$$\therefore \begin{bmatrix} \frac{E_{Sr}}{c} \\ \vec{p}_{Sr} \end{bmatrix} = \begin{bmatrix} \frac{E_Y}{c} \\ \vec{p}_Y \end{bmatrix} + \begin{bmatrix} \frac{E_{e^-}}{c} \\ \vec{p}_{e^-} \end{bmatrix} + \begin{bmatrix} \frac{E_{\bar{\nu}_e}}{c} \\ \vec{p}_{\bar{\nu}_e} \end{bmatrix} \qquad \textbf{Eq. (2.24)}$$

The parent nucleus is initially at rest. The kinetic energy of the recoil (daughter) nucleus is negligible but non-zero **[11]**. At worst (free neutron decay), the recoil proton can retain 0.05% of the Q value **[17]**. Assuming zero mass for the electron antineutrino, **Equation 2.24** becomes:

$$\therefore \begin{bmatrix} m_{0_{Sr}}c \\ 0 \end{bmatrix} = \begin{bmatrix} \sqrt{p_Y^2 + m_{o_Y}^2 c^2} \\ \vec{p}_Y \end{bmatrix} + \begin{bmatrix} \sqrt{p_{e^-}^2 + m_{o_{e^-}}^2 c^2} \\ \vec{p}_{e^-} \end{bmatrix} + \begin{bmatrix} |\vec{p}_{\bar{\nu}_e}| \\ \vec{p}_{\bar{\nu}_e} \end{bmatrix} \quad \textbf{Eq. (2.25)}$$

Equation 2.25 can be expanded into 2 equations:

$$\begin{cases} m_{0_{Sr}}c = \sqrt{p_Y^2 + m_{o_Y}^2 c^2} + \sqrt{p_{e^-}^2 + m_{o_{e^-}}^2 c^2} + |\vec{p}_{\bar{\nu}_e}| \\ \vec{p}_Y + \vec{p}_{e^-} + \vec{p}_{\bar{\nu}_e} = 0 \end{cases} \quad \textbf{Eq. (2.26)}$$

It has already been established that the energy yield or Q-value of the β^- decay is equivalent to the mass difference of the parent and daughter atoms (**Equation 2.3**). Rewriting **Equation 2.26** gives:

$$\begin{cases} \left(m_{0_{Sr}}c - m_{0_Y}c = \sqrt{p_Y^2 + m_{o_Y}^2 c^2} - m_{0_Y}c + \sqrt{p_{e^-}^2 + m_{o_{e^-}}^2 c^2} + |\vec{p}_{\bar{\nu}_e}|\right) \times \boldsymbol{c} \\ \vec{p}_Y + \vec{p}_{e^-} + \vec{p}_{\bar{\nu}_e} = 0 \end{cases} \quad \textbf{Eq. (2.27)}$$

$$\therefore \begin{cases} Q = E_{Y_{kin}} + E_{e^-} + |\vec{p}_{\bar{\nu}_e}|c \\ \vec{p}_Y + \vec{p}_{e^-} + \vec{p}_{\bar{\nu}_e} = 0 \end{cases} \quad \textbf{Eq. (2.28)}$$

Similarly, for ^{90}Y decay, we have:

$$\begin{cases} Q = E_{Zr_{kin}} + E_{e^-} + |\vec{p}_{\bar{\nu}_e}|c \\ \vec{p}_{Zr} + \vec{p}_{e^-} + \vec{p}_{\bar{\nu}_e} = 0 \end{cases} \quad \textbf{Eq. (2.29)}$$

In both cases, there exist four equations and five unknown variables (momentums of the daughter atom, electron, and electron antineutrino and the two angles between these three momentum vectors). Hence, a three-body decay always leads to continuous energy range for the beta particle, peaking at small energies and reaching β end-point energy of Q.

$$m_{o_{e^-}}c^2 \leq E_{e^-} \leq Q + m_{o_{e^-}}c^2 \quad \textbf{Eq. (2.30)}$$

$$0 \leq E_{kin_{e^-}} \leq Q \quad \textbf{Eq. (2.31)}$$

2.1.3.3 Fermi's Theory of Beta Decay

Fermi's golden rule treats the decay-causing interaction as a weak perturbation and predicts momentum and energy spectrum of the beta particle with the assumption that the mass of the neutrino is zero **[18]**. According to Fermi, the transition probability of beta decay is:

$$\lambda = \frac{2\pi}{\hbar}\left|V_{if}\right|^2 S(p_e, p_\nu)\ \rho\left(E_f\right)\ F(Z', p_e) \qquad \textbf{Eq. (2.32)}$$

where $\mathrm{V_{if}}\ (unit: eV)$ is the probability amplitude of the transition between the initial and final state; $S(p_e, p_\nu)$ denotes electron and electron antineutrino momentum dependence from forbidden transitions (if any). $\rho(E_f)$ represents density of the final state, i.e., the number of final states within the energy interval dE_f. Finally, $F(Z', p_e)$ is the Fermi function accounting for the daughter nucleus' coulomb field.

Nuclear Matrix Element M_{if}:

Treating the beta particle and the neutrino as free particles in a box of infinite size $(L \to \infty)$, where the potential is zero inside the box and infinite outside, the wave function of the free particles can be derived **[18]**.

$$\psi_{n_x,n_y,n_z}(x,y,z) = \left(\frac{2}{L}\right)^{\frac{3}{2}} sin(\frac{n_x \pi x}{L}) sin(\frac{n_y \pi y}{L}) sin(\frac{n_z \pi z}{L}) \qquad \textbf{Eq. (2.33)}$$

where n_i is the quantum number in the three-dimensional system ranging from 1 to infinity. Normalizing the wave functions yields the dimensionless nuclear matrix element M_{if}:

$$V_{if} = \frac{g M_{if}}{L^3} \qquad \textbf{Eq. (2.34)}$$

$$M_{if} \equiv < \psi_f \varphi_e \varphi_{\bar{\nu}} | V | \psi_i > \qquad \textbf{Eq. (2.35)}$$

where $g\ (unit: eV.fm^3)$ is a scalar denoting the strength of the beta transition. V is the potential coupling operator accounting for the transition from the initial quantum state ψ_i (normalized wave function of parent nucleus) to the final state $\psi_f, \varphi_e,\ and\ \varphi_{\bar{\nu}}$ (normalized wave functions of daughter nucleus, electron, and electron antineutrino respectively).

Forbidden Transition Correction Factor $S(p_e, p_\nu)$:

In section 2.1.3.2, it was established that the total spin of the emerging particles is either 0 or 1. In case of the former, if the total orbital angular momentum and spin are zero, the total angular momentum quantum number amounts to zero. Ergo, the nuclear spin and parity remain unchanged. In addition, the total angular momentum value matches the semi-classic angular momentum, which is a very small number.

$$s = o\,, l = 0 \quad \therefore \quad j = l + s = 0 \quad \therefore \quad \begin{cases} \Delta I = 0 \\ \Delta \pi = 0 \end{cases} \qquad \textbf{Eq. (2.36)}$$

$$pr = \frac{1}{c}\sqrt{E_{kin}(E_{kin} + 2m_0c^2)}r \cong 0 \qquad \textbf{Eq. (2.37)}$$

$$|\vec{j}| = \sqrt{j(j+1)}\hbar \qquad \textbf{Eq. (2.38)}$$

$$\therefore \quad pr \cong |\vec{j}| = 0 \qquad \textbf{Eq. (2.39)}$$

This is called the allowed Fermi transition. However, if the spin or the orbital angular momentum is not zero, the quantum mechanical total angular momentum number $|\vec{j}|$ becomes far larger than the semi-classical angular momentum. Such transitions are called forbidden. Forbidden decays are less likely to happen and tend to have longer half-life **[18]**. The term $S(p_e, p_\nu)$ in **Equation 2.32** accounts for such forbidden transitions via including electron and neutrino momentum dependence.

Density of the Final State $\rho(E_f)$:

The momentum of the free particle can also be determined from **Equation 2.32**.

$$p_i = \frac{n_i \pi \hbar}{L} \qquad \textbf{Eq. (2.40)}$$

n_i can be treated as continuous due to large L. Therefore, the number of final states in a sphere of thickness dn is given by:

$$dN = \frac{\pi}{2} n^2 dn \qquad \textbf{Eq. (2.41)}$$

Replacing quantum number n with momentum p returns:

$$dN = \frac{1}{2\pi^2}\frac{L^3}{\hbar^3}p^2 dp \quad \therefore \quad \frac{dN}{dE} = \frac{1}{2\pi^2}\frac{L^3}{\hbar^3}p^2\frac{dp}{dE} \qquad \textbf{Eq. (2.42)}$$

$$p = \frac{1}{c}\sqrt{E^2 - m_0c^2} \quad \therefore \quad dp = \frac{E}{c\sqrt{E^2 - m_0c^2}}dE = \frac{E}{pc^2}dE \qquad \textbf{Eq. (2.43)}$$

$$\therefore \quad \frac{dN}{dE} = \frac{1}{2\pi^2}\frac{L^3}{\hbar^3c^3}E\sqrt{E^2 - m_0c^2} \qquad \textbf{Eq. (2.44)}$$

$\frac{dN}{dE}$ is the density of the final state of the particles. For the electron and the electron antineutrino, the densities of final states are:

$$\frac{dN_e}{dE_e} = \frac{dN_e}{dE_{kin_e}} = \frac{1}{2\pi^2}\frac{L^3}{\hbar^3c^3}E_e\sqrt{E_e^2 - m_{e_0}^2c^4} = \frac{1}{2\pi^2}\frac{L^3}{\hbar^3c^3}(E_{kin_e} + m_{e_0}c^2)\sqrt{E_{kin_e}(E_{kin_e} + 2m_{e_0}c^2)} \qquad \textbf{Eq. (2.45)}$$

$$\frac{dN_\nu}{dE_\nu} = \frac{1}{2\pi^2}\frac{L^3}{\hbar^3c^3}E_\nu^2 \qquad \textbf{Eq. (2.46)}$$

Thus, the density of the final state of both particles is:

$$\rho(E_f) = \frac{dN_e}{dE_e}\frac{dN_\nu}{dE_\nu} = \frac{1}{2\pi^2}\frac{L^3}{\hbar^3c^3}(E_{kin_e} + m_{e_0}c^2)\sqrt{E_{kin_e}(E_{kin_e} + 2m_{e_0}c^2)}\frac{1}{2\pi^2}\frac{L^3}{\hbar^3c^3}E_\nu^2 \qquad \textbf{Eq. (2.47)}$$

Fermi Function $F(Z', p_e)$:

The Fermi function $F(Z', p_e)$ in **Equation 2.32** accounts for coulomb interaction of the daughter nucleus and beta particle. For β^- decay, the change in electron's wave function due to coulomb potential inside the daughter nucleus causes coulomb attraction of the beta particle. The effect manifests itself in terms of more lower energy electrons in the spectrum **[18]**. $F(Z', p_e)$ modifies the beta particle's energy spectrum to account for the coulomb interaction. Incorporating **Equations 2.34** and **2.47** into **Equation 2.32** yields the beta decay rate:

$$\lambda = \frac{1}{2\pi^3\hbar^7c^6}S(p_e, p_\nu)\,F(Z', p_e)\,g^2{M_{if}}^2(E_{kin_e} + m_{e_0}c^2)\sqrt{E_{kin_e}(E_{kin_e} + 2m_{e_0}c^2)}E_\nu^2 \qquad \textbf{Eq. (2.48)}$$

2.1.3.4 Beta Spectrum

Of particular interest is the number of beta particles $N(p_e)$ at final state, which determines the shape of the beta particle's energy spectrum **[18]**.

$$\begin{aligned} N(p_e)dp_e &= N(t)\frac{2\pi}{\hbar}S(p_e, p_\nu)\,F(Z', p_e)\,\frac{g^2{M_{if}}^2}{L^6}\frac{dN_e}{dp_e}\frac{dN_\nu}{dE_\nu}dp_e \\ &= \frac{1}{2\pi^3\hbar^7c}N(t)S(p_e, p_\nu)\,F(Z', p_e)g^2{M_{if}}^2p_e^2p_\nu^2dp_e \end{aligned} \qquad \textbf{Eq. (2.49)}$$

where N(t) denotes the number of beta emitters. **Equation 2.49** can be simplified into:

$$N(p_e)dp_e = \frac{C_0}{c} p_e^2 p_\nu^2 dp_e \qquad \textbf{Eq. (2.50)}$$

where C_0 is a constant representing all the terms that do not depend on electron and neutrino energies for an allowed transition. **Figures 2.4** demonstrates the shape of the electron's energy spectrum for ^{90}Sr and ^{90}Y β^- decay respectively **[15] [19]**. In both cases, the peak occurs at lower energies as discussed in Section 2.1.3.3 due to coulomb interaction of the daughter nucleus and beta particle.

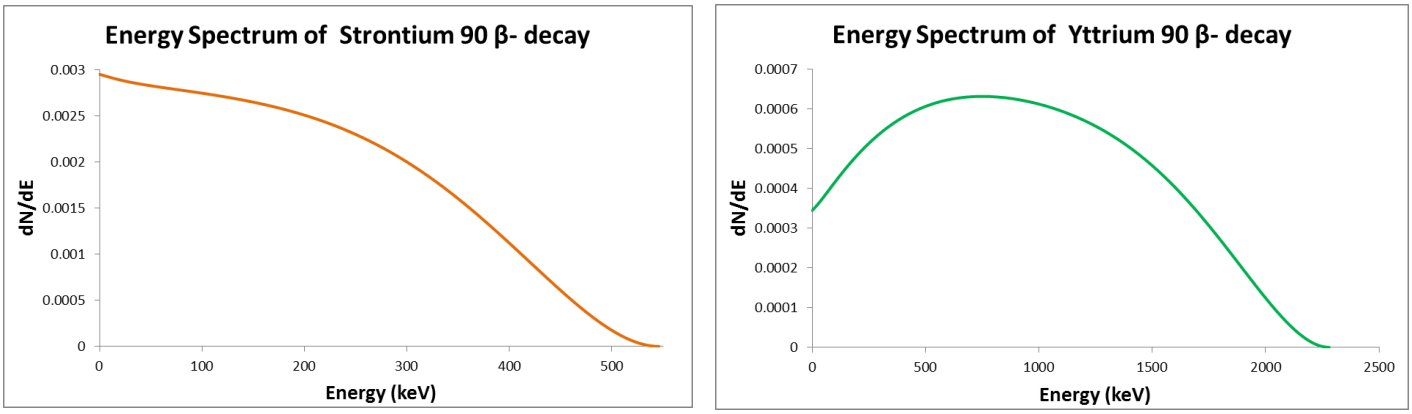

Figure 2.4 Beta spectrum of Strontium-90 (Left) and Yttrium-90 (Right) **[15] [19]**.

2.2 Electron Trajectory and Lorentz Force

The ^{90}Sr source produces electrons in a spectrum due to three-body decay. The aim is to measure the number of Cherenkov photons produced for a given electron energy. To do so, a narrow energy band of electron beam is needed. Despite the fact that producing a beam with a specific energy from ^{90}Sr is impossible, we can narrow the spectrum around a specific energy with an acceptable tolerance using an electromagnet.

Any charged particle traveling in a magnetic field experiences Lorentz Force tangent to its direction of motion. A particle (electron) with charge q_{e} and velocity $\vec{v}$ in an electric field $\vec{E}$ and a magnetic field $\vec{B}$ experiences an electromagnetic force $\vec{F}_{EM}$ **[16]**.

$$\vec{F}_{EM} = q_e(\vec{E} + \vec{v} \times \vec{B}) \qquad \textbf{Eq. (2.51)}$$

Centripetal force (Lorentz force) bends the electron in a circular motion. Assuming that electric field is zero and that the homogeneous $\vec{B}$ field is perpendicular to the electron trajectory at all time:

$$\left|\vec{F}_C\right| = \frac{\gamma m_0 v^2}{r} \qquad \textbf{Eq. (2.52)}$$

$$\left|\vec{F}_C\right| = \vec{F}_{EM} \quad \therefore \quad q_e v B = \frac{\gamma m_0 v^2}{r} \qquad \textbf{Eq. (2.53)}$$

$$\therefore \quad r = \frac{\gamma m_0 v}{q_e B} = \frac{p_e}{q_e B} \qquad \textbf{Eq. (2.54)}$$

where γ denotes the Lorentz factor, m_0 is the rest mass of the electron, and r is the bending radius of the trajectory. **Equation 2.54** enables prediction of the trajectory of electrons with different energies. In order to do so, one has to take into account the geometry of the experimental setup. From theory of special relativity:

$$\gamma = \frac{E_{kin}}{m_0 c^2} + 1 \qquad \textbf{Eq. (2.55)}$$

Therefore, less energetic electrons bend more (smaller bending radius) in the magnetic field (**Figure 2.5**).

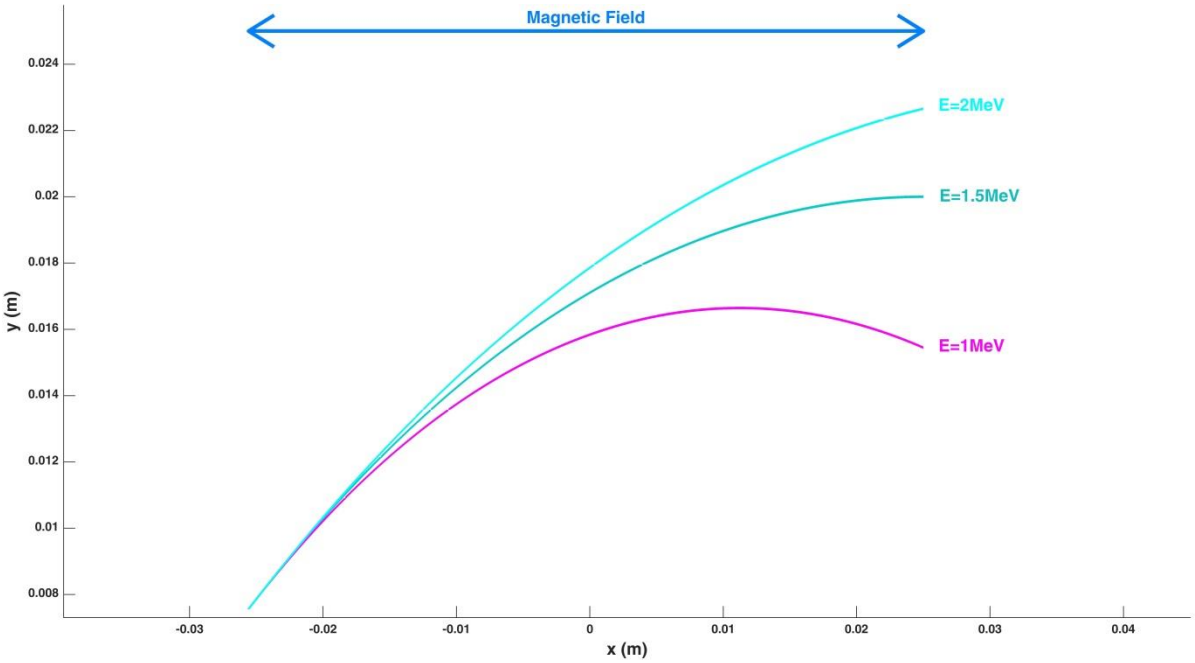

Figure 2.5 Trajectory of electrons with different energies for 60mT magnetic field strength.

The magnetic field covers an area with a length of 100mm and width of 80mm. However, the field is not constant in the entire region and diminishes around the edges. There exists a subsection where the field variation is negligible - homogeneous section (**Figure 1.5**). Detailed description of homogeneous section is provided in Section 4.2.3. Care must be taken that no electron leaves the homogeneous section of the magnetic field, i.e., the height of the trajectory must remain smaller than the width of the homogeneous section W_H $(40mm)$. The lowest energy relevant to a Compton Camera is 0.8 MeV. Assuming that 0.8 MeV electrons leave the source at an angle θ under a constant magnetic field B, the maximum height of the trajectory should be:

$$\gamma = \frac{E_{kin}}{m_0 c^2} + 1 \cong 2.565 \qquad \textbf{Eq. (2.56)}$$

$$v = \sqrt{1 - \left(\frac{1}{\gamma}\right)^2} \cong 0.921c \qquad \textbf{Eq. (2.57)}$$

$$r = \frac{\gamma m_0 v}{q_e B} = \frac{4.027 \times 10^{-3}}{B} \qquad \textbf{Eq. (2.58)}$$

$$\theta = arcsin\left(\frac{L_H}{r}\right) \qquad \textbf{Eq. (2.59)}$$

$$Maximum\ Height = r - rcos(\theta)\ \leq \boldsymbol{W_H} \qquad \textbf{Eq. (2.60)}$$

where L_H and W_H denote the length and width of the homogeneous section of the electromagnet (50 and 30 mm) respectively. For 40 mT magnetic field, the maximum height becomes 13.293 mm. For 60 mT, the maximum height becomes 22.342 mm. Having a large magnetic field is essential to achieving good energy resolution for higher energies. Therefore, highest possible magnetic field must be used. Energy resolution is discussed in details in Chapter 5.

Using Lorentz Force Law, a script is developed using MATLAB to predict the trajectory of electrons with energies ranging from 0.8 MeV to 2.2756 MeV with an increment of 0.2 MeV. **Figures 2.6** and **2.7** demonstrate the trajectory of electrons under 40mT and 60mT magnetic fields respectively. Electrons reach the end point at 20 mm above center, where the collimator and detector array are positioned. The starting angle and position varies depending on the energy requirement. The x-coordinates of the starting points are slightly different, as the rotation center of the source holder is located at x=-30mm. The geometry and angle/position mechanism are discussed in detail in Chapter 4.

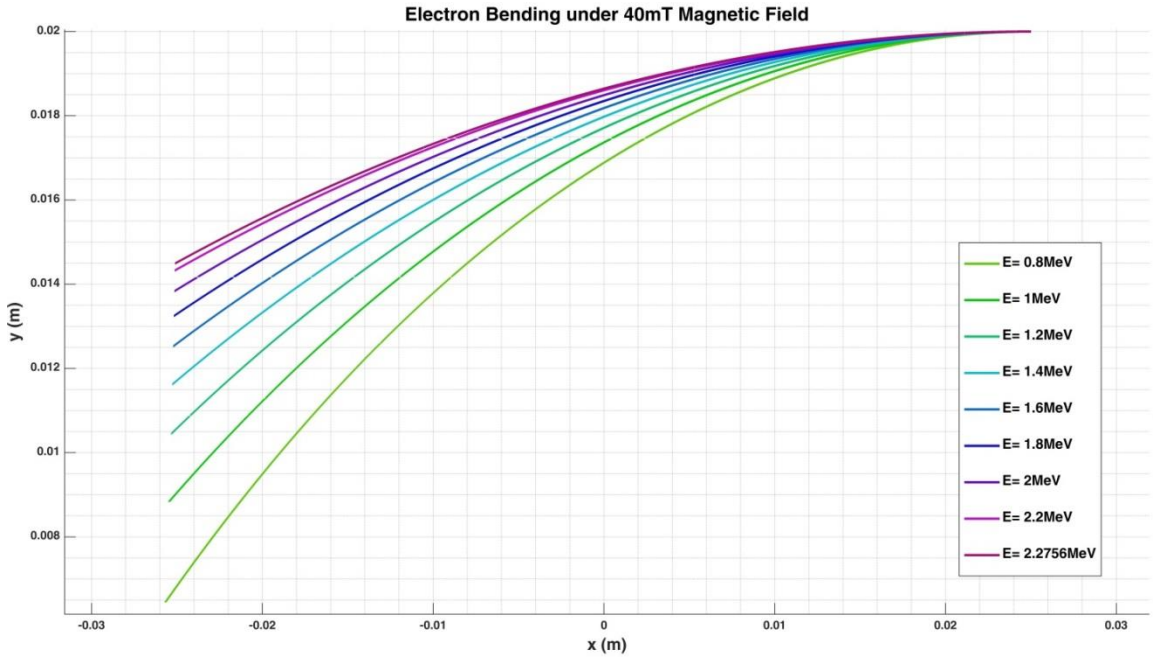

Figure 2.6 Electron trajectory under 40 mT magnetic field strength. Energies are color coded, i.e., green represents the lowest energy, and magenta represents the highest energy.

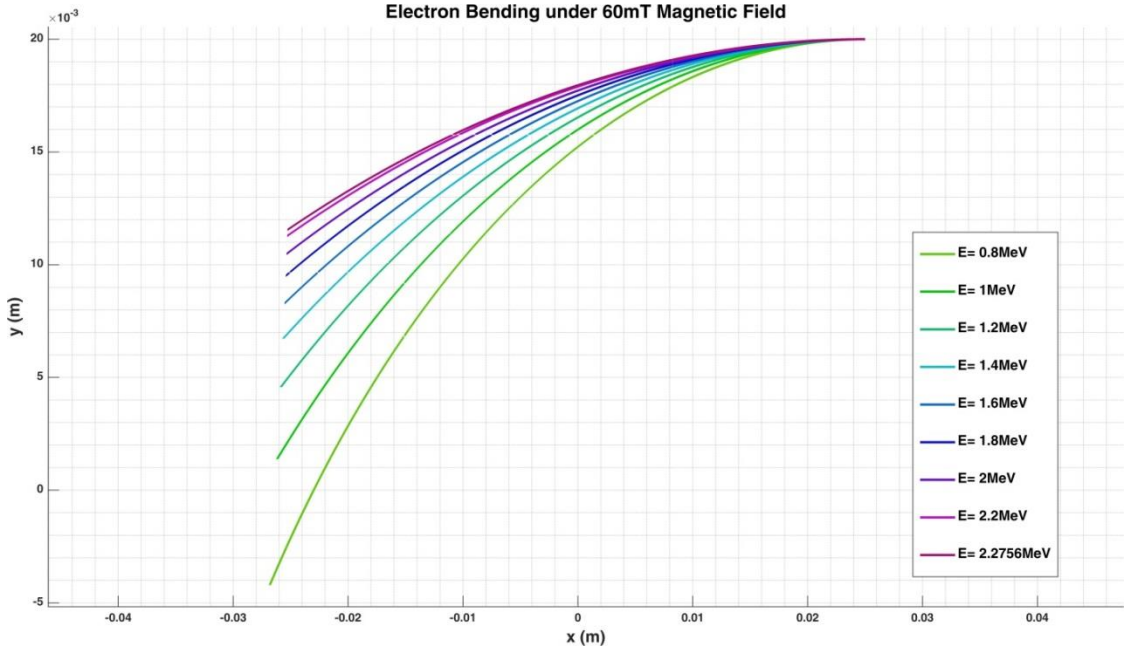

Figure 2.7 Electron trajectory under 60 mT magnetic field strength. Energies are color coded, i.e., green represents the lowest energy, and magenta represents the highest energy.

2.3 Electromagnet: Biot-Savart and Ampère's Circuital Laws

An electromagnet produces a magnetic field when current runs through its coils. The strength and direction of the magnetic field are determined by the Biot-Savart law, which states that at any point r, the magnetic field $\mathrm{d}\vec{\mathrm{B}}$ due to an element $\mathrm{d}\vec{\mathrm{l}'}$ of a current-carrying wire is given by **[16]**:

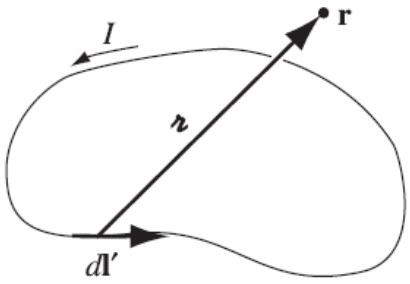

Figure 2.8 Biot Savart Law **[16]**.

$$d\vec{B}(r) = \frac{\mu_0}{4\pi} I \frac{d\vec{l'} \times \hat{r}}{|\vec{r}|^2} \qquad \Rightarrow \qquad B(r) = \frac{\mu_0}{4\pi} I \int \frac{d\vec{l'} \times \hat{r}}{|\vec{r}|^2} \qquad \textbf{Eq. (2.61)}$$

where $\mathrm{d}\vec{\mathrm{l}'}$ is the infinitesimal wire segment in the same direction as the current I, $\vec{r}$ is the vector that points from $\mathrm{d}\vec{\mathrm{l}'}$ to r, and $\hat{r}$ is the unit vector in the direction of $\vec{r}$.

In this work, an H-Magnet with an iron yoke made of ST52-3 steel ($\mu_{iron} \cong 1.26 \times 10^{-3}\ \frac{H}{m}$) is used. The iron yoke serves two distinct purposes: amplifying the magnetic field due to ferromagnetic properties of the iron and ensuring homogeneous magnetic field in the gap **[20]**. That is, the magnetic field tends not to leave the iron due to its high permeability. The gap provides a route for the field to travel and prevents magnetic saturation in the iron yoke **[16] [21] [22]**. **Figure 2.9** represents the front view and cross section of the magnet. Electrons will be travelling in a vacuum chamber in the x-y plane and bend due to the homogeneous magnetic field in z-direction.

Each of the two coils has “n” windings. The objective is to determine the required number of windings to produce a certain magnetic field strength when a specific current is set. The electromagnet should be able to produce up to 65mT (a 5mT headroom above operation field of 60mT) in the gap area where the electrons travel. The current should not be higher than 5A, as high currents can heat up the coils, potentially melting the resin holding the wires together and shorting the cupper wires. In addition, excess heat dissipation from the coils can negatively affect the experiment.

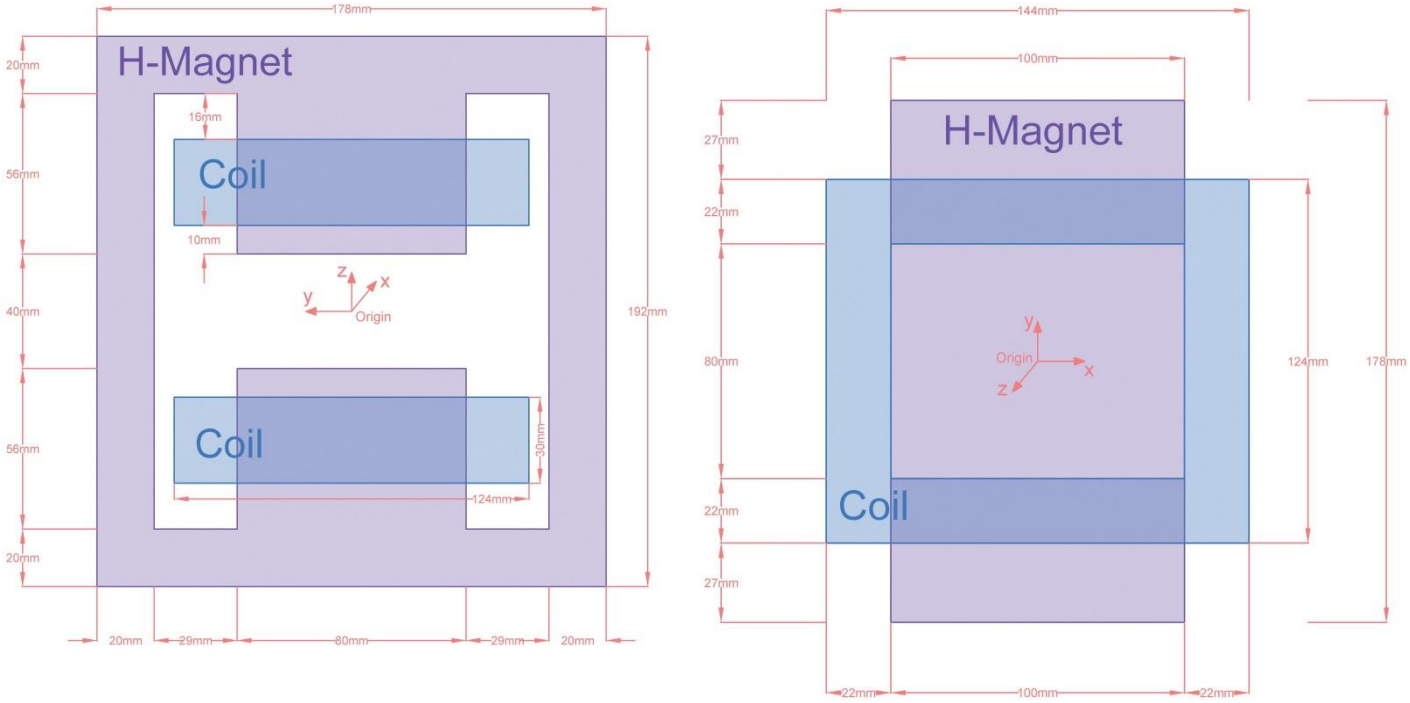

Figure 2.9 H-Magnet: Front view (Left) and cross section (Right).

Calculation of the magnetic field strength in the gap requires use of Ampère's Circuital Law, which states that the integrated magnetic field around a closed loop is related to the electric current passing through the loop **[16]**.

$$\oint \frac{\vec{B}}{\mu} . d\vec{l} = \frac{n\mu_0 I_{enc.}}{\mu_0} \qquad \textbf{Eq. (2.62)}$$

For an H-Magnet with two coils, the magnetic field produced at each point P in the Amperian loop shown in **Figure 2.10** is the combined effect of each wire segment of the two coils.

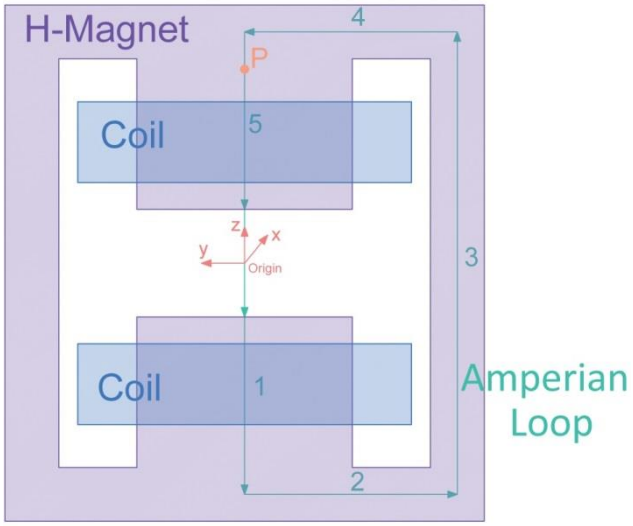

Figure 2.10 Amperian Loop.

$$\int \frac{\vec{B}_{p,1}}{\mu_{iron}}.d\vec{l}_1 + \int \frac{\vec{B}_{p,2}}{\mu_{iron}}.d\vec{l}_2 + \int \frac{\vec{B}_{p,3}}{\mu_{iron}}.d\vec{l}_3 + \int \frac{\vec{B}_{p,4}}{\mu_{iron}}.d\vec{l}_4 + \int \frac{\vec{B}_{p,5}}{\mu_{iron}}.d\vec{l}_5 + \frac{\vec{B}_{Gap}}{\mu_0} h_{Gap} = I_{enc.} \quad \textbf{Eq. (2.63)}$$

$$\Rightarrow \vec{B}_{Gap} = \frac{2\mu_0 nI}{h_{Gap}} - \frac{\mu_0}{h_{Gap}}\left(\int \frac{\vec{B}_{p,1}}{\mu_{iron}}.d\vec{l}_1 + \int \frac{\vec{B}_{p,2}}{\mu_{iron}}.d\vec{l}_2 + \int \frac{\vec{B}_{p,3}}{\mu_{iron}}.d\vec{l}_3 + \int \frac{\vec{B}_{p,4}}{\mu_{iron}}.d\vec{l}_4 + \int \frac{\vec{B}_{p,5}}{\mu_{iron}}.d\vec{l}_5\right) \quad \textbf{Eq. (2.64)}$$

A common practice is to assume a constant field B and nearly zero H-Field inside the iron yoke due to iron's high permeability. This assumption is fairly accurate due to the fact that permeability of the iron yoke can be as much as five orders of magnitude larger than permeability of air is. Assume a cylinder is placed at the intersection of the iron and the gap (**Figure 2.11**). Gauss's Law for magnetic flux demands:

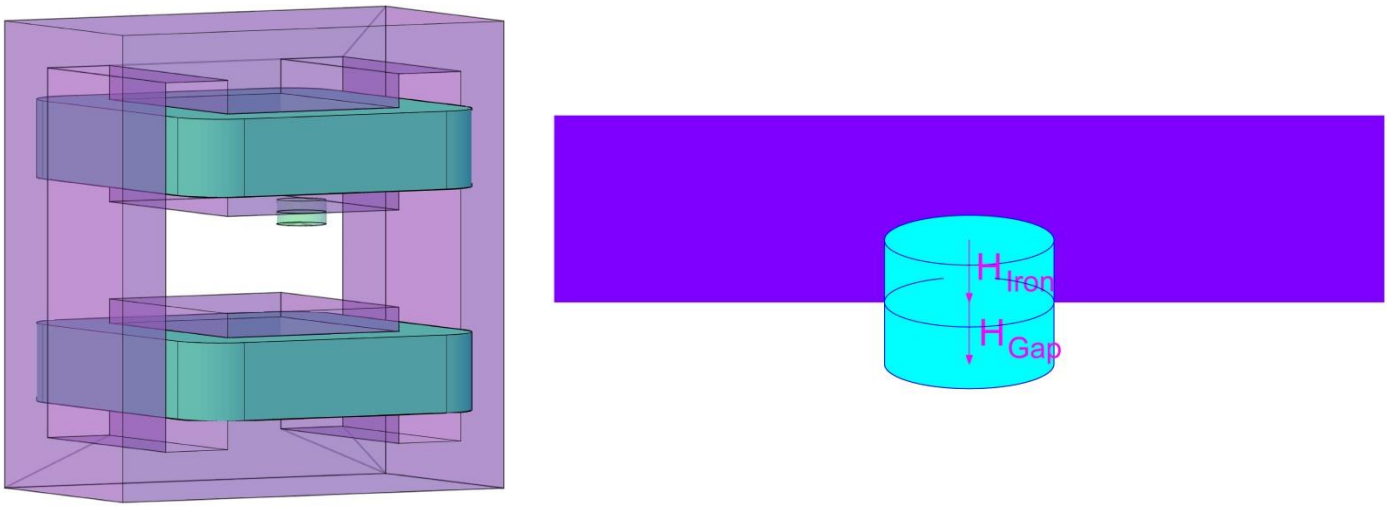

Figure 2.11 Demonstration of the Gauss' Law

$$\nabla \cdot \vec{B} = 0 \quad \therefore \quad \mu\nabla \cdot \vec{H} + \vec{H}\nabla \cdot \mu = 0 \quad \textbf{Eq. (2.65)}$$

Assuming the permeability of the iron yoke to be constant:

$$\mu\nabla \cdot \vec{H} = 0 \quad \therefore \quad \mu_{Iron}\vec{H}_{Iron} = \mu_0\vec{H}_{Gap} \quad \therefore \quad \vec{H}_{Iron} = \frac{\mu_0}{\mu_{Iron}}\vec{H}_{Gap} \quad \textbf{Eq. (2.66)}$$

Note that inside the iron, magnetic lines both parallel and perpendicular to the surface exist. However, only magnetic fields perpendicular to the surface survive outside the iron. For $\mu_{iron} \cong 1.26 \times 10^{-3}\ \frac{H}{m}$ and $\mu_0 \cong 1.26 \times 10^{-6}\ \frac{H}{m}$ **[23]**:

$$\frac{\mu_0}{\mu_{Iron}} \cong 0.001 \quad \Rightarrow \quad \vec{H}_{Iron} \approx 0 \quad \textbf{Eq. (2.67)}$$

Assuming that the magnetic field H inside the iron is nearly zero, the iron yoke material is magnetically linear, and the magnetic field in the gap is homogeneous, **Equation 2.64** is simplified to:

$$\vec{B}_{Gap} \approx \frac{2\mu_0 nI}{h_{Gap}} \quad , \quad \vec{H}_{Gap} = \frac{2nI}{h_{Gap}} \qquad \textbf{Eq. (2.68)}$$

For 65mT field strength and 5A current, this gives us a minimum winding number of 207. Nevertheless, we shall endeavor to calculate the magnetic field inside the iron to improve accuracy using Biot-Savart Law.

Figure 2.12 demonstrates dimensional parameters used in the calculations. The complete calculation is presented in **Appendix A**.

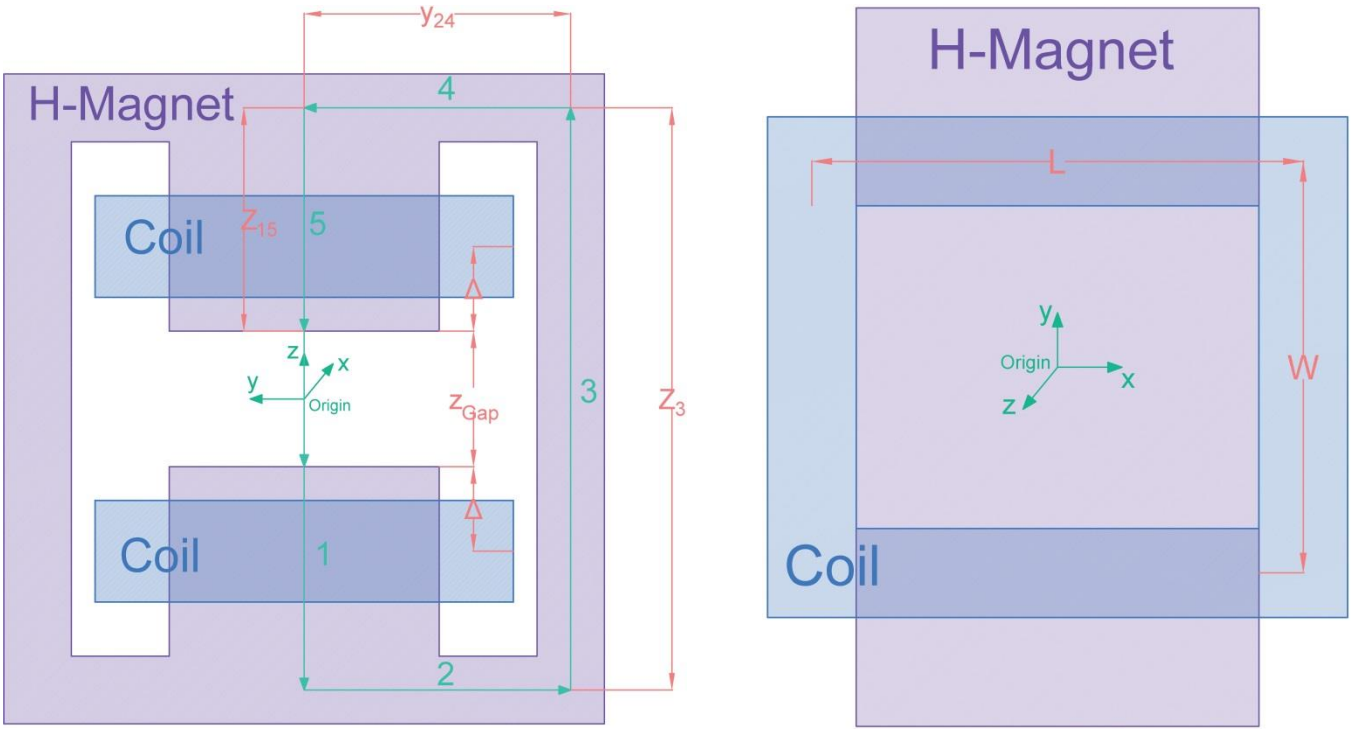

Figure 2.12 Parametric dimension of the magnet used in the calculations.

$$n\left(\int \frac{\vec{B}_{p,1}}{\mu_{iron}}.d\vec{l}_1 + \int \frac{\vec{B}_{p,2}}{\mu_{iron}}.d\vec{l}_2 + \int \frac{\vec{B}_{p,3}}{\mu_{iron}}.d\vec{l}_3 + \int \frac{\vec{B}_{p,4}}{\mu_{iron}}.d\vec{l}_4 + \int \frac{\vec{B}_{p,5}}{\mu_{iron}}.d\vec{l}_5\right) + \frac{\vec{B}_{Gap}}{\mu_0} h_{Gap} = I_{enc.} \qquad \textbf{Eq. (2.69)}$$

$$\Rightarrow \vec{B}_{Gap} = \frac{2\mu_0 nI}{h_{Gap}} - \frac{n\mu_0}{h_{Gap}}\left(\int \frac{\vec{B}_{p,1}}{\mu_{iron}}.d\vec{l}_1 + \int \frac{\vec{B}_{p,2}}{\mu_{iron}}.d\vec{l}_2 + \int \frac{\vec{B}_{p,3}}{\mu_{iron}}.d\vec{l}_3 + \int \frac{\vec{B}_{p,4}}{\mu_{iron}}.d\vec{l}_4 + \int \frac{\vec{B}_{p,5}}{\mu_{iron}}.d\vec{l}_5\right) \qquad \textbf{Eq. (2.70)}$$

where μ_0 is permeability of the medium within which the particle travels, h_{Gap} is the height of the gap (40 mm), $I_{enc.} \equiv nI$ is the current enclosed by the Amperian loop, and n is the number of windings in each coil. Note that $\vec{B}_p$ is not constant along the path and cannot be taken out of the first integral in **Equation 2.69**. The contribution of each section of the Amperian loop varies drastically based on position. For instance, sections 2, 3, and 4 produce magnetic field in both forward and opposite directions. The sum of all fields (the first five terms of the left-hand side of **Equation 2.69**) is a small yet nonzero value.

$$\Rightarrow \vec{B}_{Gap} = \frac{2\mu_0 nI}{h_{Gap}} \qquad \textbf{Eq. (2.71)}$$

$$-\frac{\boldsymbol{n\mu_0}}{\boldsymbol{h_{Gap}\mu_{iron}}} \times \left(\int_{-\frac{z_{Gap}}{2}}^{-\frac{z_{Gap}}{2}-z_{15}} \int_{-\tan^{-1}\frac{L}{W}}^{\tan^{-1}\frac{L}{W}} \frac{\frac{\mu_0 I \left(\frac{W}{2}\right)^2}{\pi}}{(\cos\theta)^2 \left(\left(\frac{W}{2}\tan\theta\right)^2 + \left(\frac{W}{2}\right)^2 + \left(z_p + \frac{z_{Gap}}{2} + \Delta\right)^2\right)^{3/2}} d\theta dz_p \right.$$

$$+ \int_{-\frac{z_{Gap}}{2}}^{-\frac{z_{Gap}}{2}-z_{15}} \int_{-\tan^{-1}\frac{L}{W}}^{\tan^{-1}\frac{L}{W}} \frac{\frac{\mu_0 I \left(\frac{W}{2}\right)^2}{\pi}}{(\cos\theta)^2 \left(\left(\frac{W}{2}\tan\theta\right)^2 + \left(\frac{W}{2}\right)^2 + \left(z_p - \frac{z_{Gap}}{2} - \Delta\right)^2\right)^{3/2}} d\theta dz_p$$

$$+ \int_{-\frac{z_{Gap}}{2}}^{-\frac{z_{Gap}}{2}-z_{15}} \int_{-\tan^{-1}\frac{W}{L}}^{\tan^{-1}\frac{W}{L}} \frac{\frac{\mu_0 I \left(\frac{L}{2}\right)^2}{\pi}}{(\cos\theta')^2 \left(\left(\frac{L}{2}\right)^2 + \left(\frac{L}{2}\tan\theta'\right)^2 + \left(z_p + \frac{z_{Gap}}{2} + \Delta\right)^2\right)^{3/2}} d\theta' dz_p$$

$$+ \int_{-\frac{z_{Gap}}{2}}^{-\frac{z_{Gap}}{2}-z_{15}} \int_{-\tan^{-1}\frac{W}{L}}^{\tan^{-1}\frac{W}{L}} \frac{\frac{\mu_0 I \left(\frac{L}{2}\right)^2}{\pi}}{(\cos\theta')^2 \left(\left(\frac{L}{2}\right)^2 + \left(\frac{L}{2}\tan\theta'\right)^2 + \left(z_p - \frac{z_{Gap}}{2} - \Delta\right)^2\right)^{3/2}} d\theta' dz_p$$

$$+ \int_{-y_{24}}^{0} \int_{-\tan^{-1}\frac{L}{2\left|\frac{W}{2}+y_p\right|}}^{\tan^{-1}\frac{L}{2\left|\frac{W}{2}+y_p\right|}} \frac{\frac{\mu_0 I \left|\frac{W}{2}+y_p\right| \left(z_p + \frac{z_{Gap}}{2} + \Delta\right)}{2\pi}}{\cos^2\theta \left(\left(\left|\frac{W}{2}+y_p\right|\tan\theta\right)^2 + \left(\frac{W}{2}+y_p\right)^2 + \left(z_p + \frac{z_{Gap}}{2} + \Delta\right)^2\right)^{3/2}} d\theta dy_p$$

$$+ \int_{-y_{24}}^{0} \int_{-\tan^{-1}\frac{L}{2\left|\frac{W}{2}+y_p\right|}}^{\tan^{-1}\frac{L}{2\left|\frac{W}{2}+y_p\right|}} \frac{\frac{\mu_0 I \left|\frac{W}{2}+y_p\right| \left(z_p - \frac{z_{Gap}}{2} - \Delta\right)}{2\pi} 1}{\cos^2\theta \left(\left(\left|\frac{W}{2}+y_p\right|\tan\theta\right)^2 + \left(\frac{W}{2}+y_p\right)^2 + \left(z_p - \frac{z_{Gap}}{2} - \Delta\right)^2\right)^{3/2}} d\theta dy_p$$

$$- \int_{-y_{24}}^{0} \int_{-\tan^{-1}\frac{L}{2\left|\frac{W}{2}-y_p\right|}}^{\tan^{-1}\frac{L}{2\left|\frac{W}{2}-y_p\right|}} \frac{\frac{\mu_0 I \left|\frac{W}{2}-y_p\right| \left(z_p + \frac{z_{Gap}}{2} + \Delta\right)}{2\pi}}{\cos^2\theta \left(\left(\left|\frac{W}{2}-y_p\right|\tan\theta\right)^2 + \left(\frac{W}{2}-y_p\right)^2 + \left(z_p + \frac{z_{Gap}}{2} + \Delta\right)^2\right)^{3/2}} d\theta dy_p$$

$$- \int_{-y_{24}}^{0} \int_{-\tan^{-1}\frac{L}{2\left|\frac{W}{2}-y_p\right|}}^{\tan^{-1}\frac{L}{2\left|\frac{W}{2}-y_p\right|}} \frac{\frac{\mu_0 I \left|\frac{W}{2}-y_p\right| \left(z_p - \frac{z_{Gap}}{2} - \Delta\right)}{2\pi}}{\cos^2\theta \left(\left(\left|\frac{W}{2}-y_p\right|\tan\theta\right)^2 + \left(\frac{W}{2}-y_p\right)^2 + \left(z_p - \frac{z_{Gap}}{2} - \Delta\right)^2\right)^{3/2}} d\theta\, dy_p$$

$$+\int_{-\frac{z_3}{2}}^{\frac{z_3}{2}}\int_{-\tan^{-1}\frac{L}{2\left|\frac{W}{2}+y_p\right|}}^{\tan^{-1}\frac{L}{2\left|\frac{W}{2}+y_p\right|}}\frac{\frac{\mu_0 I\left(\frac{W}{2}+y_p\right)^2}{4\pi}}{\cos^2\theta\left(\left(\left|\frac{W}{2}+y_p\right|\tan\theta\right)^2+\left(\frac{W}{2}+y_p\right)^2+\left(z_p+\frac{z_{Gap}}{2}+\Delta\right)^2\right)^{3/2}}d\theta dz_p$$

$$+\int_{-\frac{z_3}{2}}^{\frac{z_3}{2}}\int_{-\tan^{-1}\frac{L}{2\left|\frac{W}{2}+y_p\right|}}^{\tan^{-1}\frac{L}{2\left|\frac{W}{2}+y_p\right|}}\frac{\frac{\mu_0 I\left(\frac{W}{2}+y_p\right)^2}{4\pi}}{\cos^2\theta\left(\left(\left|\frac{W}{2}+y_p\right|\tan\theta\right)^2+\left(\frac{W}{2}+y_p\right)^2+\left(z_p-\frac{z_{Gap}}{2}-\Delta\right)^2\right)^{3/2}}d\theta dz_p$$

$$-\int_{-\frac{z_3}{2}}^{\frac{z_3}{2}}\int_{-\tan^{-1}\frac{L}{2\left|\frac{W}{2}-y_p\right|}}^{\tan^{-1}\frac{L}{2\left|\frac{W}{2}-y_p\right|}}\frac{\frac{\mu_0 I\left(\frac{W}{2}-y_p\right)^2}{4\pi}}{\cos^2\theta\left(\left(\left|\frac{W}{2}-y_p\right|\tan\theta\right)^2+\left(\frac{W}{2}-y_p\right)^2+\left(z_p+\frac{z_{Gap}}{2}+\Delta\right)^2\right)^{3/2}}d\theta dz_p$$

$$-\int_{-\frac{z_3}{2}}^{\frac{z_3}{2}}\int_{-\tan^{-1}\frac{L}{2\left|\frac{W}{2}-y_p\right|}}^{\tan^{-1}\frac{L}{2\left|\frac{W}{2}-y_p\right|}}\frac{\frac{\mu_0 I\left(\frac{W}{2}-y_p\right)^2}{4\pi}}{\cos^2\theta\left(\left(\left|\frac{W}{2}-y_p\right|\tan\theta\right)^2+\left(\frac{W}{2}-y_p\right)^2+\left(z_p-\frac{z_{Gap}}{2}-\Delta\right)^2\right)^{3/2}}d\theta dz_p$$

$$-\int_{-\frac{z_3}{2}}^{\frac{z_3}{2}}\int_{\tan^{-1}\frac{|y_p|-\frac{W}{2}}{\frac{L}{2}}}^{\tan^{-1}\frac{|y_p|+\frac{W}{2}}{\frac{L}{2}}}\frac{\frac{\mu_0 I\left(\frac{L}{2}\right)^2}{2\pi}}{(\cos\theta')^2\left(\left(\frac{L}{2}\right)^2+\left(\frac{L}{2}\tan\theta'\right)^2+\left(z_p+\frac{z_{Gap}}{2}+\Delta\right)^2\right)^{3/2}}d\theta' dz_p$$

$$-\int_{-\frac{z_3}{2}}^{\frac{z_3}{2}}\int_{\tan^{-1}\frac{|y_p|-\frac{W}{2}}{\frac{L}{2}}}^{\tan^{-1}\frac{|y_p|+\frac{W}{2}}{\frac{L}{2}}}\frac{\frac{\mu_0 I\left(\frac{L}{2}\right)^2}{2\pi}}{(\cos\theta')^2\left(\left(\frac{L}{2}\right)^2+\left(\frac{L}{2}\tan\theta'\right)^2+\left(z_p-\frac{z_{Gap}}{2}-\Delta\right)^2\right)^{3/2}}d\theta' dz_p\Bigg)$$

Using MATLAB, the full calculations for 65 mT and 5A yields n=217, 10 more windings on each coil compared to the approximation method. Comparison with approximation method reveals the small but non-zero contribution of iron yoke. Note that even the full calculation is based on oversimplifying a complex three-dimensional geometry to a single line and that the field in the gap is completely homogeneous. In reality, it only provides the field strength at an axis at the center of the gap and assumes it is homogeneous across the gap.

2.4 Synchrotron Radiation Energy Loss

When charged particles experience acceleration perpendicular to their direction of motion, they emit electromagnetic radiation. For instance, electrons traveling in a magnetic field experience Lorentz force normal to both the magnetic field and their direction of motion, leading to acceleration. This is always accompanied by electromagnetic radiation in the direction of motion from the particle **[24]**. For highly relativistic particles, this is referred to as synchrotron radiation. The phenomenon is observed in ring accelerators and charged particles of astronomical sources around a black hole (**Figure 2.13**).

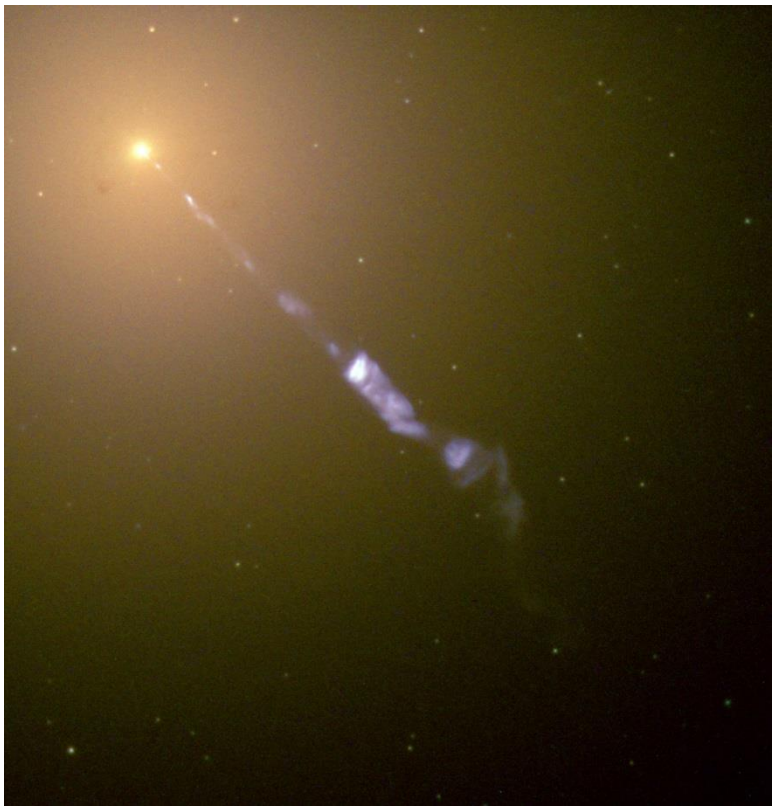

Figure 2.13 Black Hole-Powered Jet of Electrons and Sub-Atomic Particles Streams From Center of Galaxy M87 **[25]**. the visible light of the jet is due to Synchrtron radiation of electrons bending in the magnetic field of the jet.

The synchrotron radiation in the laboratory frame is forward-peaked around the electron direction and provides a very high-brightness X-ray source **[26]**. Synchrotron radiation is essentially the same basic physical process as bremsstrahlung, but with much higher energy photons (roughly X-ray energies). It is used for investigating the structure of materials, and synchrotron light sources.

However, Synchrotron radiation in the context of the current study could cause heating of components and produce backgrounds in the detector. In addition, the energy loss will reduce the accuracy of the experiment should the loss be significant. The rate of energy loss is related to the mass of the particle by

$\Delta E \propto \frac{1}{m^4}$. Given the relatively low mass of electrons, it is prudent to investigate whether or not synchrotron radiation energy loss bares significance in the current experiment.

The power radiated from an accelerated relativistic electron in a magnetic field is determined from Larmor's formula **[24] [27]**:

$$P = \frac{1}{4\pi\varepsilon_0}\frac{2{q_e}^2}{3c^3}a^2 \qquad \textbf{Eq. (2.72)}$$

where ε_0 denotes vacuum permittivity, q_e is the charge of the electron, and a is the acceleration of the particle. For the general case, one has to consider relativistic effects.

$$a = \frac{1}{m_0}\frac{dp_e}{d\tau} \qquad \textbf{Eq. (2.73)}$$

where m_0 is the rest mass of the electron, p_e is its momentum, and τ is the proper time from special relativity.

$$\tau = \frac{t}{\gamma} \quad \Rightarrow \quad d\tau = \frac{1}{\gamma}dt \qquad \textbf{Eq. (2.74)}$$

Combining **Equations 2.73** and **2.74** yields:

$$a = \frac{1}{m_0}\gamma\frac{d(\gamma m_0 v)}{dt} = \gamma^2\frac{dv}{dt} \qquad \textbf{Eq. (2.75)}$$

From **Equation 2.52**, we know that:

$$\left|\vec{F}_C\right| = \gamma m_0\frac{dv}{dt} = \frac{\gamma m_0 v^2}{r} \quad \Rightarrow \quad \frac{dv}{dt} = \frac{v^2}{r} \qquad \textbf{Eq. (2.76)}$$

Therefore:

$$a = \gamma^2\frac{dv}{dt} = \gamma^2\frac{v^2}{r} \qquad \textbf{Eq. (2.77)}$$

In the current experiment, the electrons are accelerated in a curved path with radius r due to centripetal (Lorentz) force (**Equation 2.53**). Expressing the bending radius in terms of speed and magnetic field strength (**Equation 2.54**), the power loss from **Equation 2.72** becomes:

$$\left|\vec{F}_C\right| = \vec{F}_{EM} \quad \therefore \quad q_e v B = \frac{\gamma m_0 v^2}{r} \qquad \textbf{Eq. (2.53)}$$

$$\therefore \quad r = \frac{\gamma m_0 v}{q_e B} \qquad \textbf{Eq. (2.54)}$$

$$\therefore \quad P = \frac{1}{4\pi\varepsilon_0}\frac{2{q_e}^2}{3c^3}\gamma^4\frac{v^4}{r^2} = \frac{{q_e}^2 v^4 \gamma^4}{6\pi\varepsilon_0 c^3 r^2} \qquad \textbf{Eq. (2.78)}$$

If an electron travels in an arc with δ radians, the synchrotron energy loss becomes:

$$\Delta E = P \times \frac{\delta \times r}{v} = \frac{\delta}{6\pi\varepsilon_0 c^3}\frac{{q_e}^2 v^3 \gamma^4}{r} \qquad \textbf{Eq. (2.79)}$$

From trigonometry, it can be understood that the angle δ and the initial electron angle θ in **Figure 2.14** are equivalent. Therefore, the energy loss can be determined in terms of electron's initial angle and kinetic energy.

$$\Delta E = \frac{\theta}{6\pi\varepsilon_0 c^3}\frac{{q_e}^2 v^3 \gamma^4}{r} \qquad \textbf{Eq. (2.80)}$$

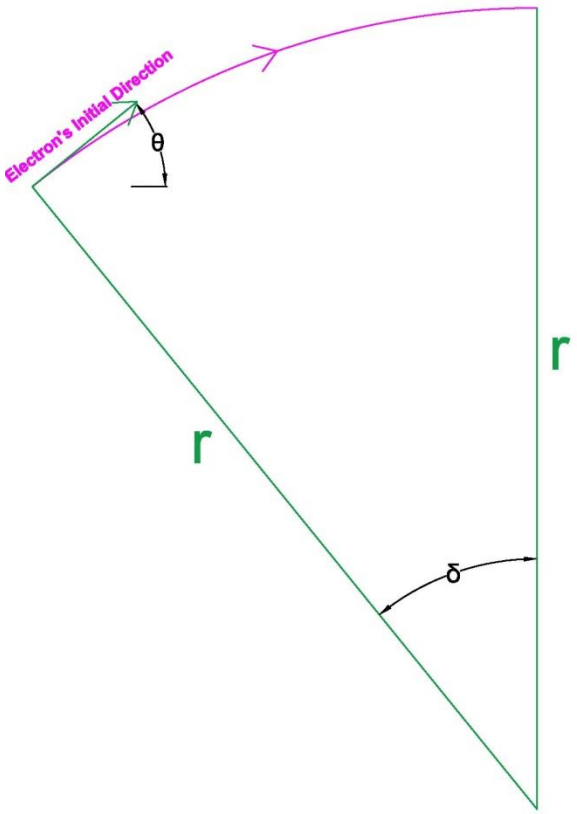

Figure 2.14 Initial angle of the electron (θ) and radians of the electron arc (δ) are equivalent.

Calculations indicate that the synchrotron radiation energy loss is negligible in the current experiment and can be safely ignored. The maximum synchrotron energy loss occurs for the highest energy (2.2785 MeV) at 0.77 μeV and 1.8 μeV for B=40mT and 60mT respectively. **Table 2.2** summarizes the outcomes of the calculations. **Figure 2.15** demonstrates the rise in synchrotron radiation energy loss as electron energy increases.

Table 2.2: Synchrotron Radiation Energy Loss based on Electrons' Kinetic Energy.						
Energy (MeV)	B=40mT			B=60mT		
	Starting Angle (°)	Average Radius (mm)	Synchrotron Energy Loss (MeV)	Starting Angle (°)	Average Radius (mm)	Synchrotron Energy Loss (MeV)
0.8	30.0	101.3	1.7E-13	50.2	67.4	4.2E-13
0.9	27.3	110.4	1.9E-13	44.5	73.5	4.8E-13
1	25.0	119.4	2.2E-13	40.1	79.5	5.4E-13
1.1	23.1	128.3	2.5E-13	36.7	85.4	6.1E-13
1.2	21.5	137.1	2.9E-13	33.8	91.3	6.8E-13
1.3	20.2	145.9	3.2E-13	31.5	97.2	7.6E-13
1.4	19.0	154.7	3.6E-13	29.5	103.0	8.4E-13
1.5	17.9	163.4	4.0E-13	27.7	108.8	9.3E-13
1.6	17.0	172.1	4.4E-13	26.2	114.6	1.0E-12
1.7	16.1	180.8	4.8E-13	24.8	120.4	1.1E-12
1.8	15.4	189.5	5.3E-13	23.6	126.1	1.2E-12
1.9	14.7	198.1	5.7E-13	22.5	131.9	1.3E-12
2	14.0	206.7	6.2E-13	21.5	137.6	1.4E-12
2.1	13.5	215.3	6.7E-13	20.6	143.4	1.5E-12
2.2	12.9	223.9	7.3E-13	19.7	149.1	1.7E-12
2.2756	12.6	230.4	7.7E-13	19.1	153.4	1.8E-12

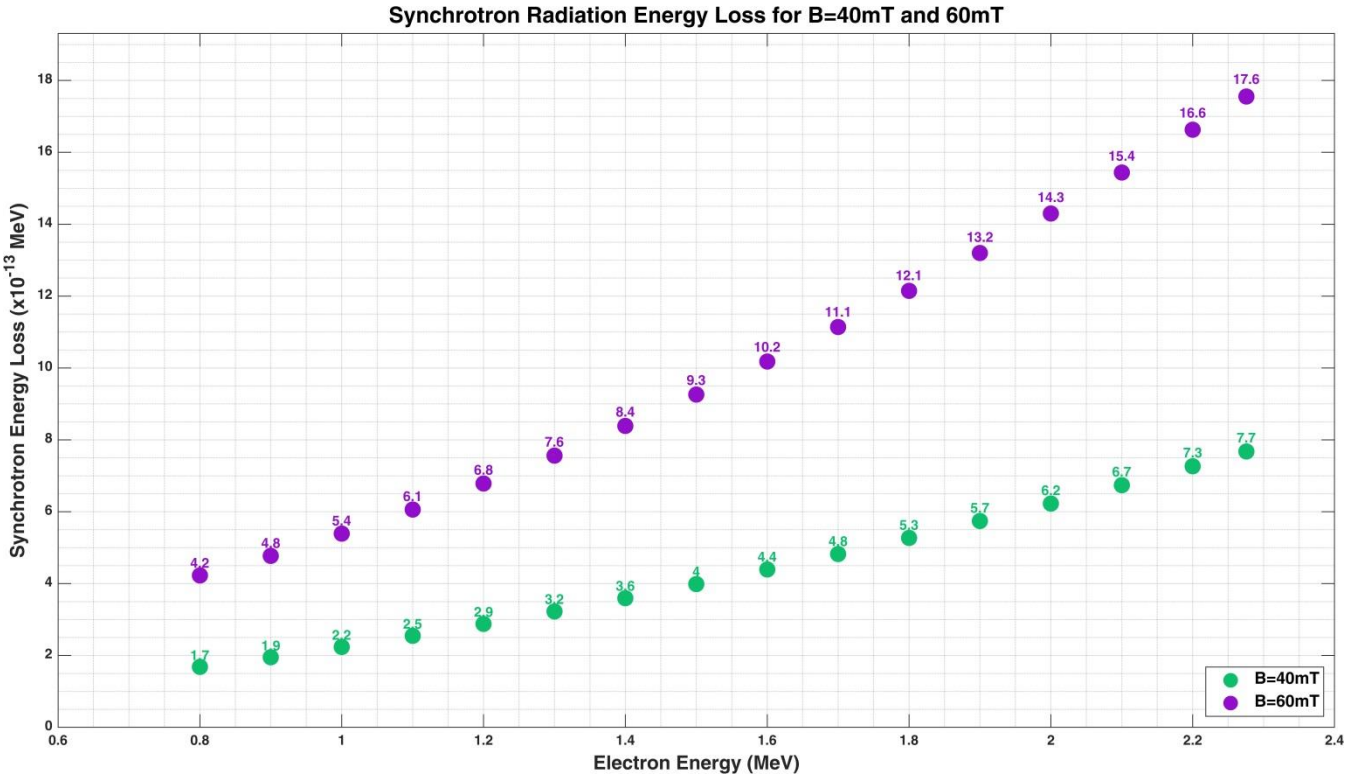

Figure 2.15 Synchrotron radiation energy loss of electrons based on their kinetic energy.

2.5 Compton Effect:

Interaction of photons with matter falls into one of the below categories:

1. Photoelectric effect
2. Compton scattering
3. Pair production
4. Thomson scattering
5. Rayleigh scattering

Photoelectric effect occurs when a photon deposits its entire energy to an atom, which subsequently emits a shell electron (**Figure 2.16-a**). In Compton scattering, a photon is elastically scattered off a shell electron, releasing it from the atom in the process (**Figure 2.16-b**); pair production is conversion of a photon to an electron-positron pair in the proximity of a nucleus or an electron (**Figure 2.16-c**). Based on the incoming photon's energy and atomic number of the nucleus, one of the above three processes become the dominant interaction (**Figure 2.17**). Below ionization threshold, Thomson and Rayleigh scattering, low-energy photons scattering off a free charge and atom respectively, are also possible.

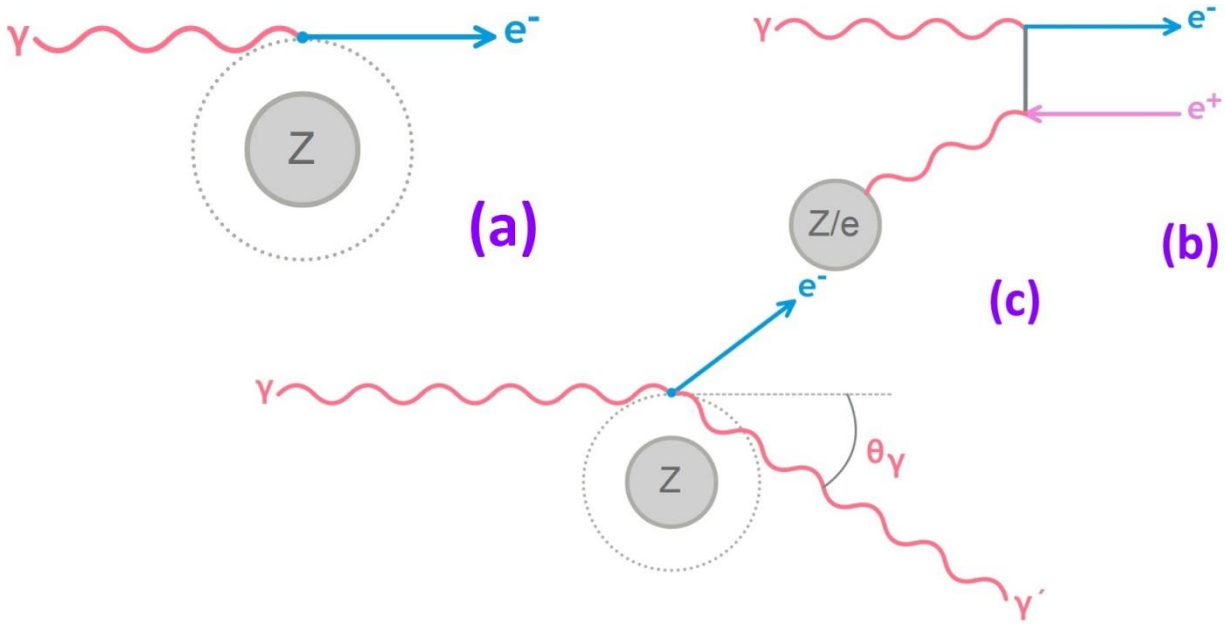

Figure 2.16 Kinematics of 3 major interactions of photons with mater: (a) Photoelectric effect, (b) Pair Production, and (c) Compton effect.

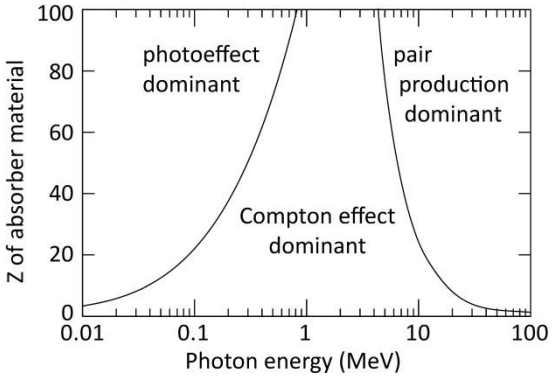

Figure 2.17 Regions in (Eγ,Z) plane where one of the three photon interaction processes are dominant **[28]**.

2.5.1 Compton Scattering: Kinematics

If a photon with energies in the range of a few keV to 30 MeV (depending on the atomic number of the absorber material) hit an electron at rest, the photon will be scattered. According to classical electromagnetism, the electron absorbs the photon, starts oscillating, and emits a photon with the same wavelength and intensity as the initial photon has. However, observations show that the emitted photon has greater wavelength and lower intensity. In 1923, Arthur Holly Compton at Washington University in St. Louis came up with a quantum explanation which earned him the 1927 Nobel Prize in Physics **[29]**. He treated the photon as a discrete particle, not a wave. He further assumed that the photon collides with a single electron elastically and solved the mathematical equation for conservation of energy and momentum.

Compton Effect will be discussed in detail in this section, as it is the source of the electrons in a Compton Camera. When the energy of the incoming photon is significantly larger than the binding energy of a shell electron of an atom, the electron is considered quasi-free. That is, the binding energy of the electron can be safely ignored compared to the energy of the incident photon **[24]**. In Compton scattering, a high energy photon is scattered off such electron. Depending on the scattering angle of the photon, a fraction of the energy is transferred to the quasi-free electron, releasing it from the nucleus. Using conservation of four-momentum (with unit of energy), a relation between scattering angle and electron energy can be obtained. Note that the following calculations are based on the assumption that the binding energy of the shell electron is far below incident photon's energy, i.e., quasi-free electron assumption. Let θ_γ and θ_e in **Figure 2.18** be the scattering angles of photon and electron respectively.

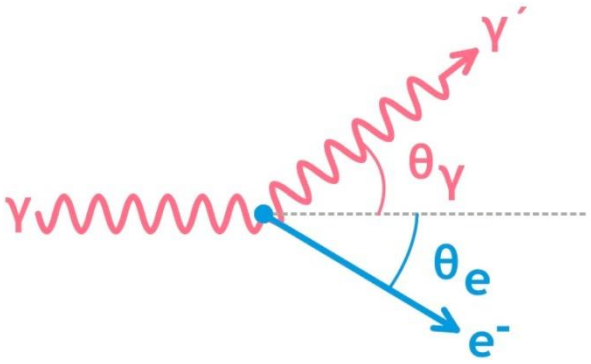

Figure 2.18 Diagram of Compton Scattering process.

$$P_\gamma + P_e = P_{\gamma'} + P_{e'} \qquad \textbf{Eq. (2.81)}$$

$$\begin{bmatrix} E_\gamma \\ \vec{p}_\gamma c \end{bmatrix} + \begin{bmatrix} E_e \\ 0 \end{bmatrix} = \begin{bmatrix} E_{\gamma'} \\ \vec{p}_{\gamma'} c \end{bmatrix} + \begin{bmatrix} E_{e'} \\ \vec{p}_{e'} c \end{bmatrix} \qquad \textbf{Eq. (2.82)}$$

$$\begin{bmatrix} E_\gamma \\ cp_\gamma \\ 0 \\ 0 \end{bmatrix} + \begin{bmatrix} m_e c^2 \\ 0 \\ 0 \\ 0 \end{bmatrix} = \begin{bmatrix} E_{\gamma'} \\ cp_{\gamma'} cos\theta_\gamma \\ cp_{\gamma'} sin\theta_\gamma \\ 0 \end{bmatrix} + \begin{bmatrix} E_{e'} \\ cp_{e'} cos\theta_e \\ -cp_{e'} sin\theta_e \\ 0 \end{bmatrix} \qquad \textbf{Eq. (2.83)}$$

Equation 2.83 can be broken down to 3 separate equations.

$$E_\gamma + m_e c^2 = E_{\gamma'} + E_{e'} \qquad \textbf{Eq. (2.84)}$$

$$p_\gamma = p_{\gamma'} cos\theta_\gamma + p_{e'} cos\theta_e \qquad \textbf{Eq. (2.85)}$$

$$p_{\gamma'} sin\theta_\gamma = p_{e'} sin\theta_e \qquad \textbf{Eq. (2.86)}$$

From **Equation 2.84**, we have:

$$E_{e'} - m_e c^2 = E_\gamma - E_{\gamma'} \quad \therefore \quad E_{kin,e'} = E_\gamma - E_{\gamma'} \qquad \textbf{Eq. (2.87)}$$

From Special Relativity:

$$E = c\sqrt{p^2 + m_0^2 c^2} \quad \therefore \quad \begin{cases} E_\gamma = cp_\gamma \\ E_{\gamma'} = cp_{\gamma'} \end{cases} \qquad \textbf{Eq. (2.88)}$$

Therefore:

$$E_{kin,e'} = c(p_\gamma - p_{\gamma'}) \qquad \textbf{Eq. (2.89)}$$

From **Equation 2.85**:

$$p_\gamma = p_{\gamma'}cos\theta_\gamma + p_{e'}cos\theta_e \quad \therefore \quad {p_{e'}}^2(cos\theta_e)^2 = (p_\gamma - p_{\gamma'}cos\theta_\gamma)^2 \qquad \textbf{Eq. (2.90)}$$

$$\Rightarrow \quad {p_{e'}}^2(cos\theta_e)^2 = {p_\gamma}^2 + {p_{\gamma'}}^2(cos\theta_\gamma)^2 - 2p_\gamma p_{\gamma'}cos\theta_\gamma \qquad \textbf{Eq. (2.91)}$$

From **Equation 2.86**:

$$p_{\gamma'}sin\theta_\gamma = p_{e'}sin\theta_e \quad \therefore \quad {p_{e'}}^2(sin\theta_e)^2 = {p_{\gamma'}}^2(sin\theta_\gamma)^2 \qquad \textbf{Eq. (2.92)}$$

Adding **Equations 2.91** and **2.92**:

$${p_{e'}}^2 = {p_\gamma}^2 + {p_{\gamma'}}^2 - 2p_\gamma p_{\gamma'}cos\theta_\gamma \qquad \textbf{Eq. (2.93)}$$

According to Special Relativity:

$${p_{e'}}^2 = \frac{1}{c^2}E_{kin,e'}\left(E_{kin,e'} + 2m_e c^2\right) \qquad \textbf{Eq. (2.94)}$$

Replacing $\mathrm{E_{kin,e'}}$ from **Equation 2.89** yields:

$${p_{e'}}^2 = \frac{1}{c^2}c\left(p_\gamma - p_{\gamma'}\right)\left(c\left(p_\gamma - p_{\gamma'}\right) + 2m_e c^2\right) = {p_\gamma}^2 + {p_{\gamma'}}^2 - 2p_\gamma p_{\gamma'} + 2m_e c\left(p_\gamma - p_{\gamma'}\right) \qquad \textbf{Eq. (2.95)}$$

Equating **Equation 2.93** and **2.95**:

$${p_\gamma}^2 + {p_{\gamma'}}^2 - 2p_\gamma p_{\gamma'} + 2m_e c\left(p_\gamma - p_{\gamma'}\right) = {p_\gamma}^2 + {p_{\gamma'}}^2 - 2p_\gamma p_{\gamma'}cos\theta_\gamma \qquad \textbf{Eq. (2.96)}$$

$$\therefore \quad p_\gamma p_{\gamma'} - m_e c\left(p_\gamma - p_{\gamma'}\right) = p_\gamma p_{\gamma'}cos\theta_\gamma \qquad \textbf{Eq. (2.97)}$$

$$\therefore \quad p_{\gamma'} = \frac{m_e c p_\gamma}{m_e c + p_\gamma(1 - cos\theta_\gamma)} = \frac{p_\gamma}{1 + \frac{p_\gamma}{m_e c}(1 - cos\theta_\gamma)} \qquad \textbf{Eq. (2.98)}$$

Expressing **Equation 2.98** in energy form:

$$E_{\gamma'} = \frac{E_\gamma}{1 + \frac{E_\gamma}{m_e c^2}(1 - cos\theta_\gamma)} \qquad \textbf{Eq. (2.99)}$$

The electron's total energy and kinetic energy become:

$$E_{e'} = E_\gamma - E_{\gamma'} + m_e c^2 = E_\gamma\left(1 - \frac{1}{1 + \frac{E_\gamma}{m_e c^2}(1 - cos\theta_\gamma)}\right) + m_e c^2 \qquad \textbf{Eq. (2.100)}$$

$$E_{kin,e'} = E_\gamma\left(1 - \frac{1}{1 + \frac{E_\gamma}{m_e c^2}(1 - cos\theta_\gamma)}\right) \qquad \textbf{Eq. (2.101)}$$

Figure 2.19 shows the relation between electron and incident photon energy for different scattering angles. At higher energies and scattering angles, the electron receives a larger portion of the incident photon's energy, yet it never receives the entirety of it, as shown in **Equation 2.101**.

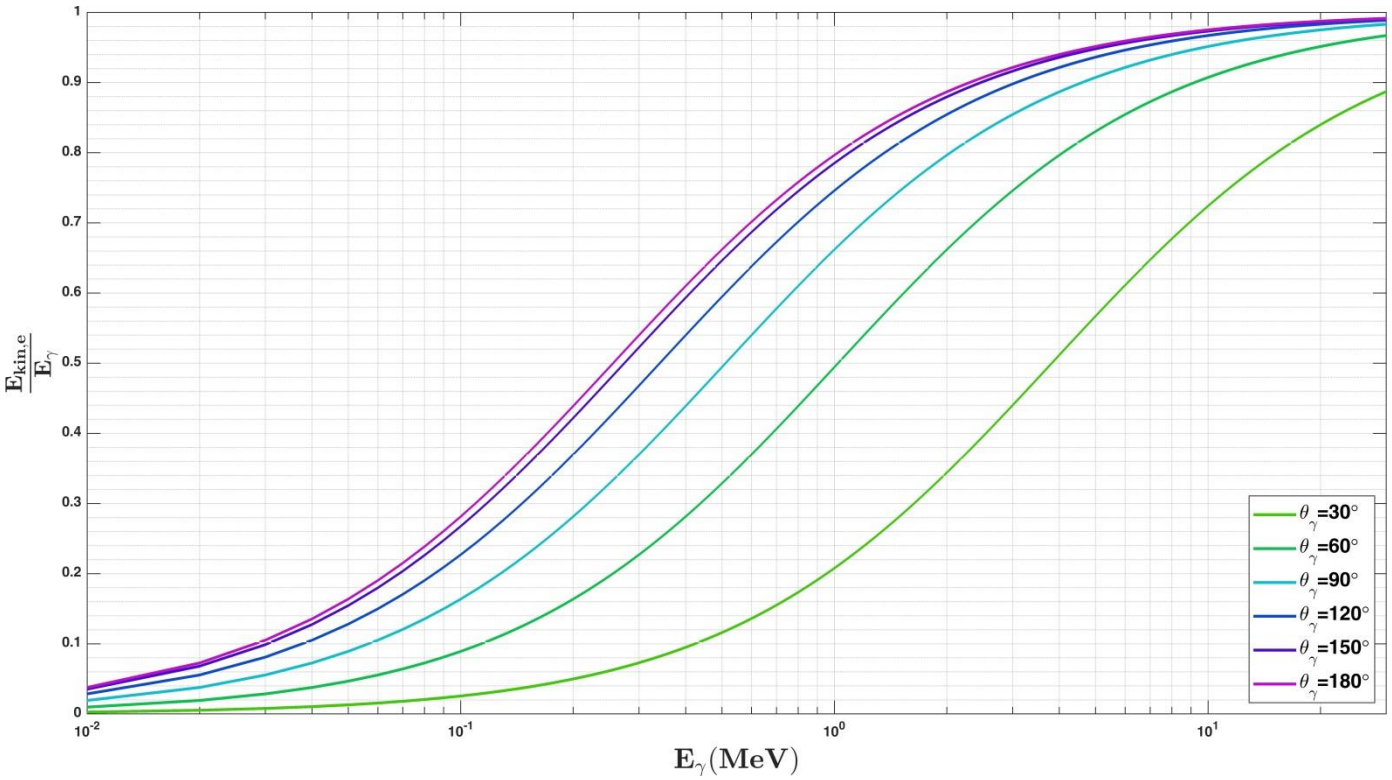

Figure 2.19 Normalized energy transfer to electrons versus incident photon energy at different scattering angles.

At any given incident photon energy, the electron energy is a function of the scattering angle θ_γ. The derivative of **Equation 2.101** indicates that the function has two extrema: a minimum at $\theta_\gamma = 0$ and a maximum at $\theta_\gamma = \pi$.

$$\frac{dE_{kin,e'}}{d\theta_\gamma} = \frac{E_\gamma sin\theta_\gamma}{\left(1 + \frac{E_\gamma}{m_e c^2}(1 - cos\theta_\gamma)\right)^2} \qquad \textbf{Eq. (2.102)}$$

Figure 2.20 shows electron energy distribution as a function of the photon's scattering angle. The dotted line represents the Cherenkov threshold, above which electrons produce Cherenkov photons in the radiator medium with refractive index of 1.49 (PMMA). The colored band indicates the measurable energy range of the current study. In this range, electron and photon scattering angles are between 0 to 34 and 35 to 180 degrees respectively for 2MeV incident photon. For higher energies, electron and photon scattering angles change between 26 to 8 and 2 to 22 degrees respectively.

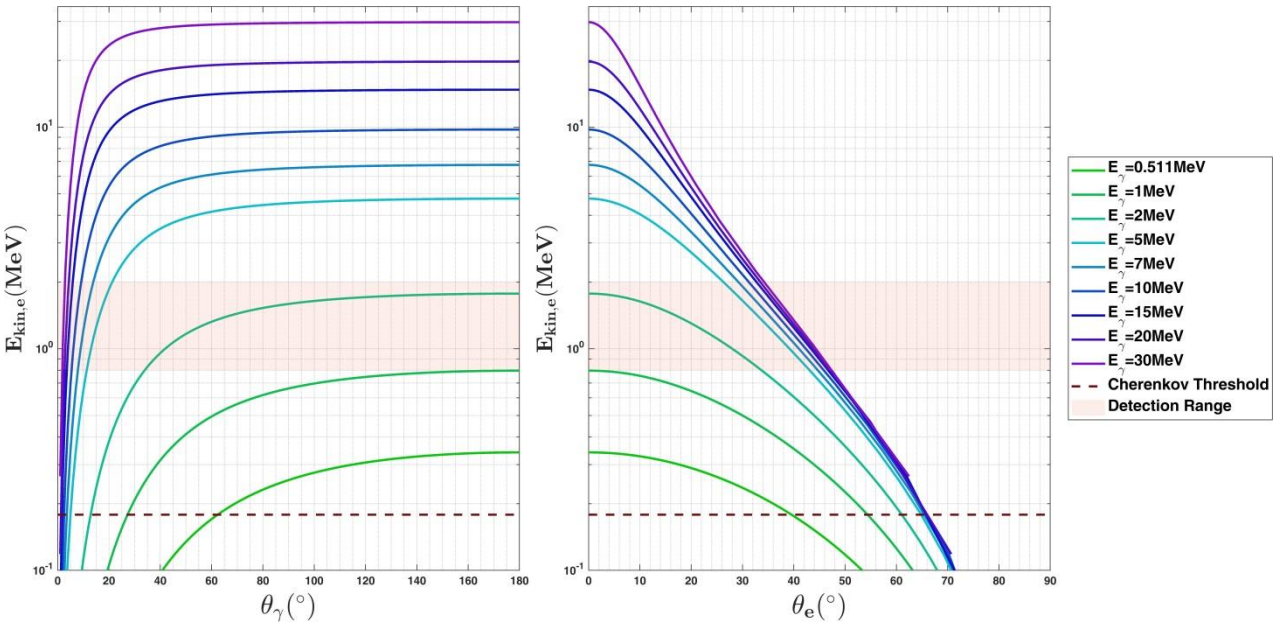

Figure 2.20 Energy received by the electron as a function of photon's scattering angle (left) and electron's scattering angle (right). The dotted lines represent minimum electron energy required to create Cherenkov light in a PMMA with refractive index of 1.49. the horizontal bands indicate the range of electron energies which can be detected by current setup through Cherenkov radiation.

Maximum energy is always attained at 180 degrees at which the photon back scatters. Therefore, maximum electron energy always occurs when incident photon back scatters.

$$E_{kin,e',Max} = E_\gamma\left(1 - \frac{1}{1 + \frac{2E_\gamma}{m_e c^2}}\right) \qquad \textbf{Eq. (2.103)}$$

Electron and photon scattering angles are not independent. From **Equations 2.85** and **2.86**:

$$p_{e'} = p_{\gamma'}\frac{sin\theta_\gamma}{sin\theta_e} \quad \therefore \quad p_\gamma = p_{\gamma'}cos\theta_\gamma + p_{\gamma'}sin\theta_\gamma\frac{cos\theta_e}{sin\theta_e} \qquad \textbf{Eq. (2.104)}$$

$$\therefore \quad E_\gamma = E_{\gamma'}cos\theta_\gamma + E_{\gamma'}sin\theta_\gamma\frac{cos\theta_e}{sin\theta_e} \qquad \textbf{Eq. (2.105)}$$

$$\therefore \quad \frac{E_\gamma}{E_{\gamma'}}\left[= 1 + \frac{E_\gamma}{m_e c^2}\left(1 - cos\theta_\gamma\right)\right] = cos\theta_\gamma + sin\theta_\gamma\frac{cos\theta_e}{sin\theta_e} \qquad \textbf{Eq. (2.106)}$$

$$\therefore \quad \frac{1 + \frac{E_\gamma}{m_e c^2}\left(1 - cos\theta_\gamma\right) - cos\theta_\gamma}{sin\theta_\gamma} = \frac{cos\theta_e}{sin\theta_e} \quad \therefore \quad tan\theta_e = \frac{sin\theta_\gamma}{\left(1 - cos\theta_\gamma\right)} \times \frac{1}{\left(1 + \frac{E_\gamma}{m_e c^2}\right)} \qquad \textbf{Eq. (2.107)}$$

$$\therefore \quad tan\theta_e = \frac{2sin\frac{\theta_\gamma}{2}cos\frac{\theta_\gamma}{2}}{\left(1 - 1 + (sin\frac{\theta_\gamma}{2})^2\right)} \times \frac{1}{\left(1 + \frac{E_\gamma}{m_e c^2}\right)} \qquad \textbf{Eq. (2.108)}$$

$$\therefore \quad tan\theta_e = \frac{cot\frac{\theta_\gamma}{2}}{\left(1 + \frac{E_\gamma}{m_e c^2}\right)} \qquad \textbf{Eq. (2.109)}$$

Figure 2.21 shows the relation between the two scattering angles. At higher incident energies, electrons tend to scatter in forward direction. Note that electron scattering angle never goes beyond 90 degrees. Successful detection of Cherenkov photons requires electron scattering angles below 20, ideally covering a large photon scattering range. For instance, 2MeV incident photons produce such electrons with photon scattering angles spanning roughly from 60-180 degrees. Larger incident energies produce wider spans and better electron scattering angles, but at the cost of a lower cross section.

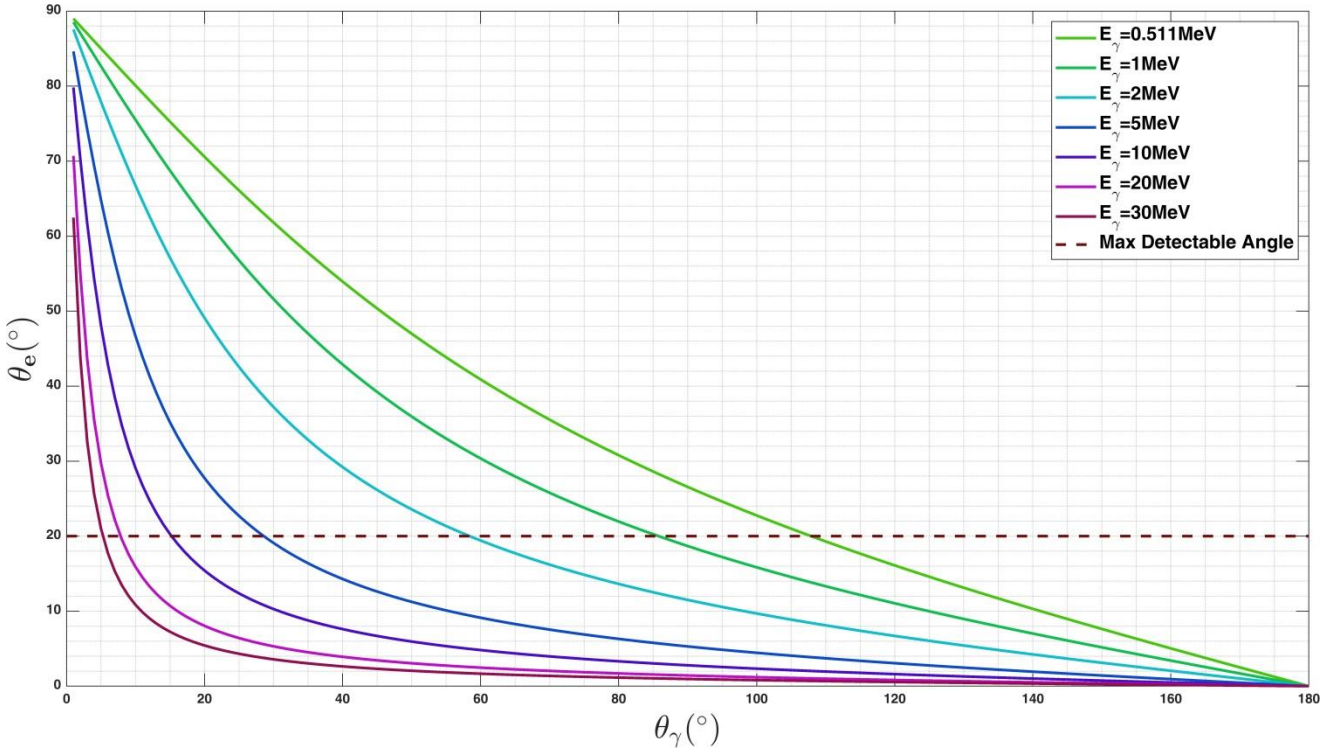

Figure 2.21 Inter-dependencies of electron and photon scattering angles in Compton scattering for various incident energies.

2.5.2 Compton Scattering: Cross Section of Free Electrons

The cross section of Compton scattering per (quasi-)free electron has been formulated by Klein and Nishina **[28]** by solving Dirac equation for the electron (quantum electrodynamics). Differential cross section per unit solid angle $\mathrm{d}\Omega$ for the number of photons scattered at the angle θ_γ is:

$$\frac{d\sigma_c}{d\Omega} = \frac{{r_e}^2}{2\left[1+\alpha(1-cos\theta_\gamma)\right]^2}\left(1+(cos\theta_\gamma)^2+\frac{\alpha^2(1-cos\theta_\gamma)^2}{1+\alpha(1-cos\theta_\gamma)}\right) \qquad \textbf{Eq. (2.110)}$$

where $\alpha = \frac{E_\gamma}{m_e c^2}$ and $\mathrm{r_e}$ is the classical electron radius $\left(\mathrm{r_e} = \frac{1}{4\pi\epsilon_0}\frac{e^2}{m_e c^2} \cong 2.82\ fm\right)$. **Figure 2.22** shows the cross section in polar and Cartesian coordinates.

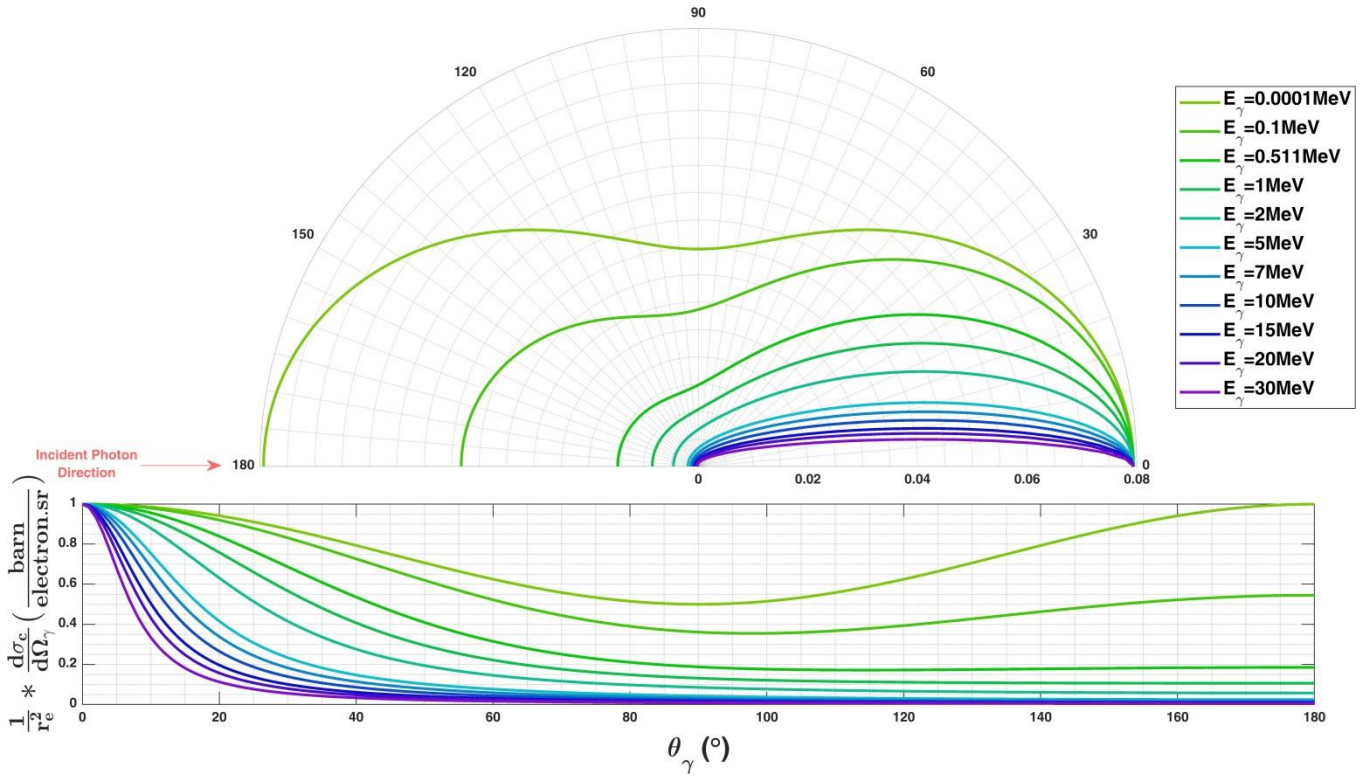

Figure 2.22 Differential cross section per unit solid angle for the number of photons scattered at the angle θ_γ according to Klein- Nishina formula in polar (top) and Cartesian (bottom) coordinates. The unit of cross section in both coordinates is barn-per-electron-per-steradian.

Similarly, Differential cross section per unit solid angle for the number of free electrons scattered at the angle θ_e can be written **[30]**. **Figure 2.23** demonstrates the cross section.

$$\frac{d\sigma_c}{d\Omega_e} = \frac{d\sigma_c}{d\Omega}\frac{d\Omega}{d\Omega_e} = \frac{(1+\alpha)^2(1-cos\theta_\gamma)^2}{(cos\theta_e)^3}\frac{d\sigma_c}{d\Omega} \qquad \textbf{Eq. (2.111)}$$

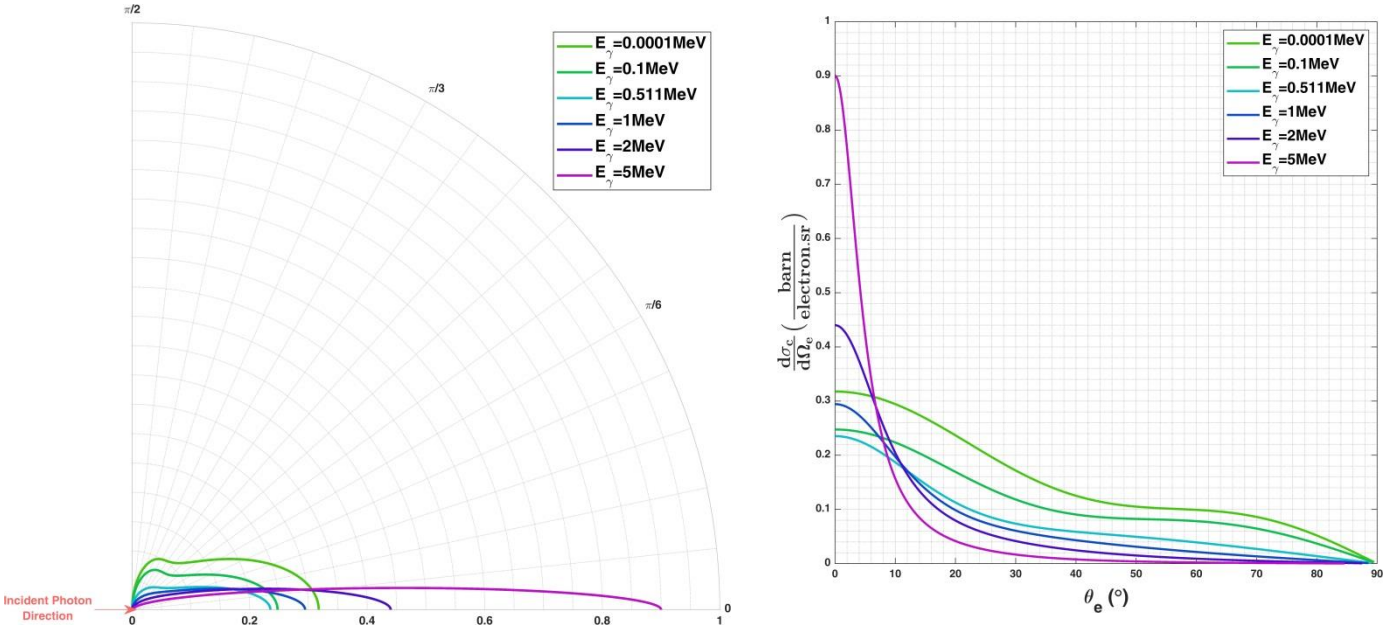

Figure 2.23 Differential cross section per unit solid angle for the number of electrons scattered at the angle θ_e.

The differential cross section for giving a free electron a recoil energy in the interval between $E_{kin,e}$ and $E_{kin,e} + dE_{kin,e}$ is given by **[28]**:

$$\frac{d\sigma_c}{dE_{kin,e}} = \frac{\pi {r_e}^2}{\alpha^2 m_e c^2}\left[2 + \frac{\beta^2}{\alpha^2(1-\beta)^2} + \frac{\beta}{1-\beta}\left(\beta - \frac{2}{\alpha}\right)\right] \qquad \textbf{Eq. (2.112)}$$

where $\beta = \frac{E_{kin,e}}{E_\gamma}$. **Equation 2.112** reveals the dependence of Compton cross section on recoil energy of the electron as shown in **Figure 2.24**.

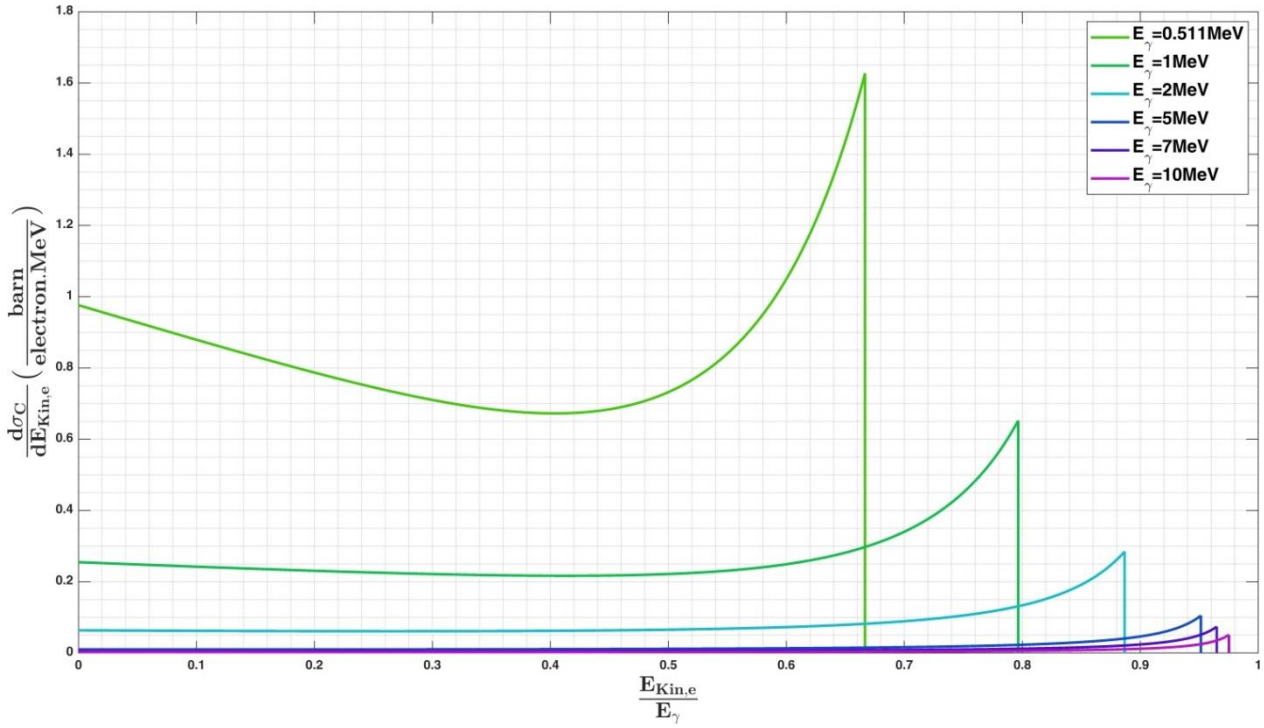

Figure 2.24 Dependence of Compton cross section on recoil energy of the electron.

The relation between cross section and recoil energy reveals useful information regarding the energy distribution. The Compton Effect involves all scattering angles from 0 to 180 degrees, bringing about transfer of a continuum of energies from zero to $\mathrm{E_{kin,e,Max}}$ to the electron. Maximum energy transfer to the electron occurs at $\theta_\gamma = \pi$ as discussed before (**Figure 2.25**). The sudden drop after $\mathrm{E_{kin,e,Max}}$ is known as the Compton edge, after which no further energy can be transferred to the free electron.

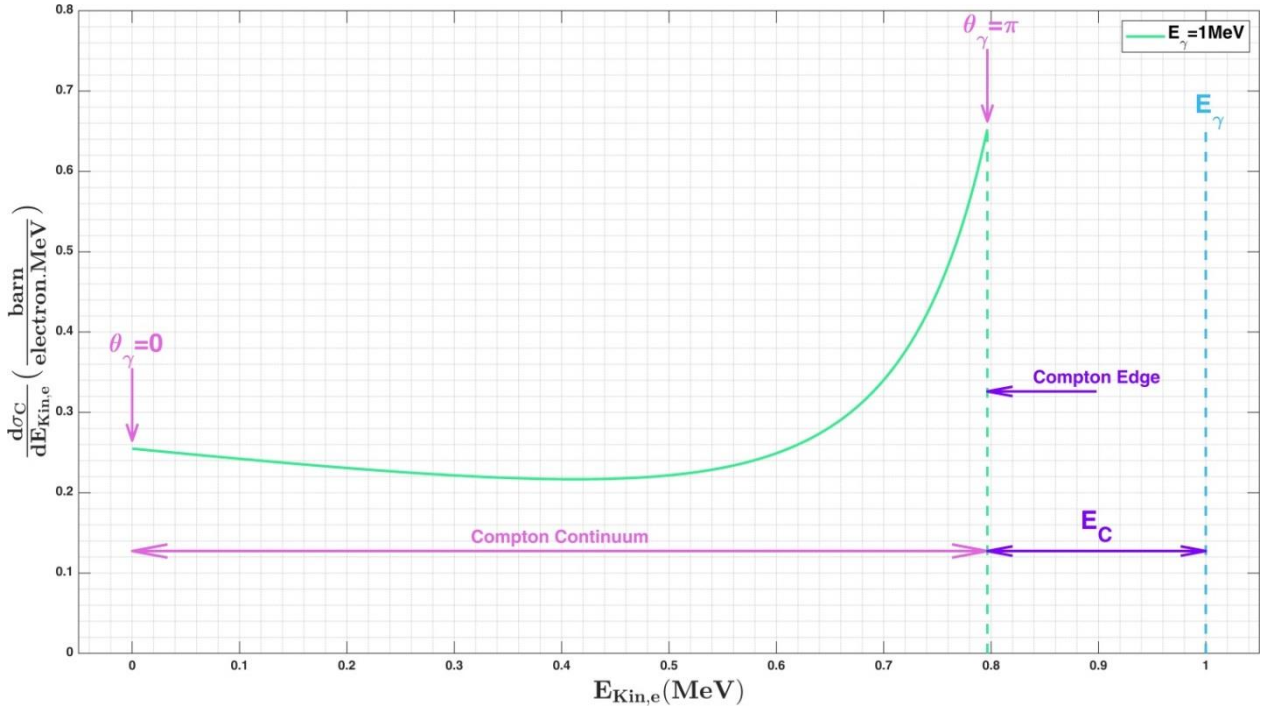

Figure 2.25 Compton continuum from $\theta_\gamma = 0$ to 180 degrees, where Compton edge occurs. E_c represents energy of the back-scattered photon.

Integration of Klein–Nishina formula over the entire solid angle yields the total Compton cross section per free electron **[28]**.

$$\sigma_c = 2\pi {r_e}^2 \left[\left(\frac{1+\alpha}{\alpha^2}\right)\left(\frac{2(1+\alpha)}{1+2\alpha} - \frac{1}{\alpha} ln(1+2\alpha)\right) + \frac{1}{2\alpha} ln(1+2\alpha) - \frac{1+3\alpha}{(1+2\alpha)^2}\right] \qquad \textbf{Eq. (2.113)}$$

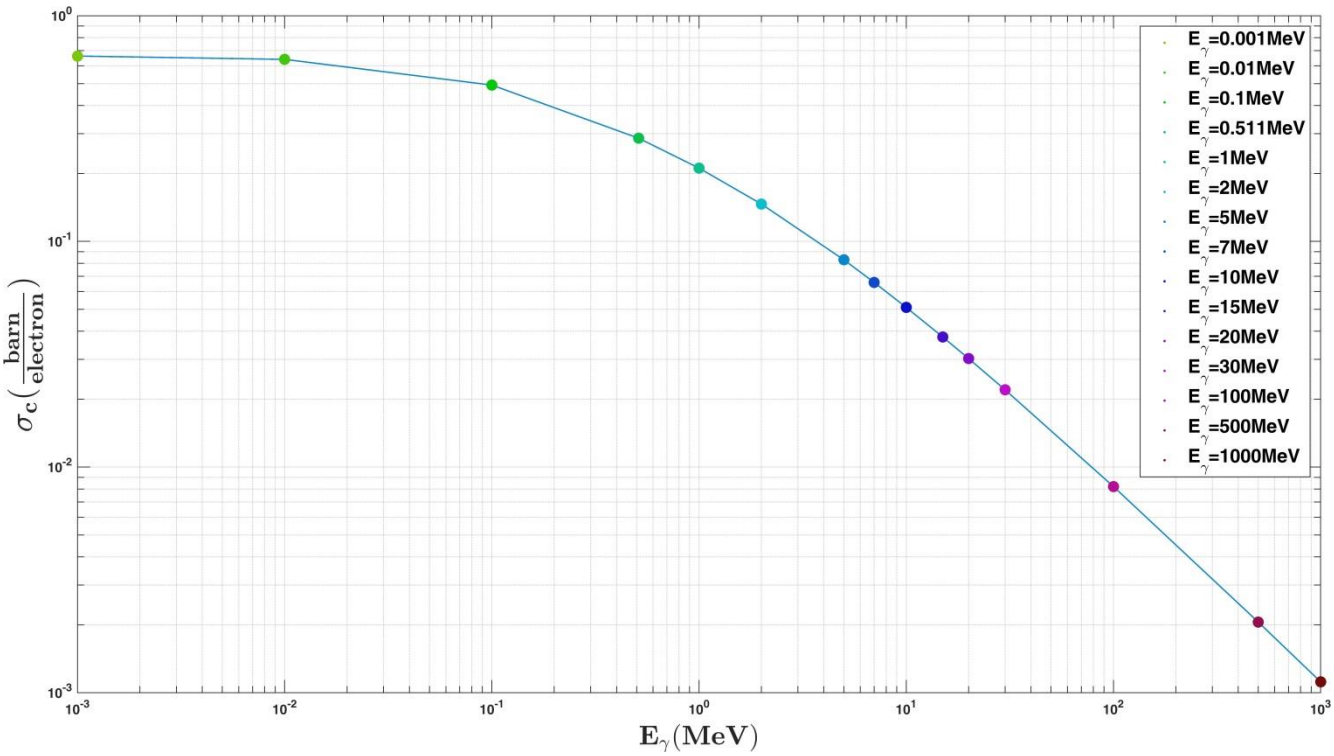

Figure 2.26 Total cross section of the number of photons removed from the original beam.

2.5.3 Cross Section of shell electrons:

So far, the Compton cross section for free electrons have been calculated. We considered the electrons quasi-free based on the assumption that the incident photon's energy is much larger than the binding energy of the electron. This assumption is fairly accurate for incident photon energies of 0.5MeV and higher. The caveat to **Figure 2.26** is that Compton cross section of bound electrons tends to drop close to the lower energies where Thomson and Rayleigh scatterings become dominant as shown in **Figure 2.27 [28]**.

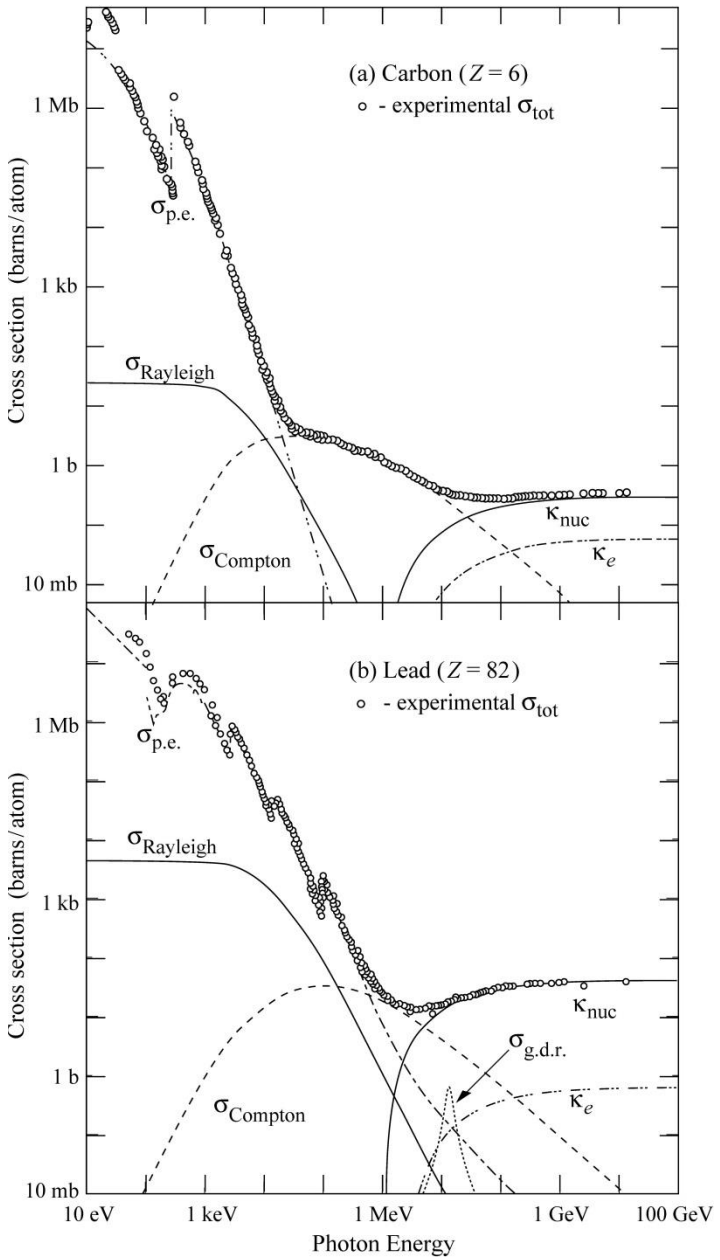

Figure 2.27 Reduction in total Compton cross section due to binding energy of the electrons at low incident photon energies in carbon (top) and lead (bottom) **[31]**.

2.6 Cherenkov Effect

When charged particles traverse a dielectric medium with a phase velocity greater that the speed of light in a medium ($\frac{c}{n}$), an electromagnetic emission known as Cherenkov radiation is ensued (n: refractive index of the medium). The phenomenon was first discovered and reported by Pavel Cherenkov in 1934 **[32]**. His colleagues, Tamm and Frank, later theoretically interpreted Cherenkov radiation using theory of special relativity in 1937 **[33]**. The trio shared the Nobel Prize for their efforts in 1958 **[34]**.

2.6.1 Cherenkov Theory

When charged particles travel through an electrically polarizable matter (dielectric), the atoms in the vicinity of the particles elliptically stretch and form electric dipoles via electromagnetic interaction with the charged particles. If the phase velocity of the charged particles are smaller than ($\frac{c}{n}$), the polarization is symmetric along particle's trajectory as well as in azimuth (**Figure 2.28-a**), provided the medium is isotropic. The perturbation decays (atoms relax back to their original shape and arrangement) as the particles move past them. Therefore, no net dipole field is produced. When the phase velocity is greater than ($\frac{c}{n}$), however, the dipoles are only symmetric azimuthally, as dipole formation rate equals the speed of light in the medium, which is smaller than the velocity of the particle (**Figure 2.27-b**). The dipoles cannot develop and relax at the same speed as the particle's phase velocity is. This leads to a non-zero dipole field, which releases its energy in the form of an electromagnetic pulse.

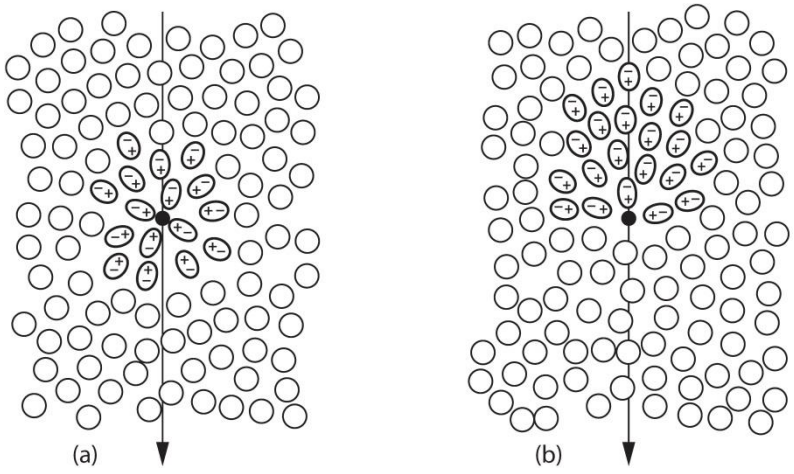

Figure 2.28 Cherenkov Effect. (a) Charged particle's phase velocity is smaller than $\frac{c}{n}$; polarization is spherically symmetric. (b) Charged particle's phase velocity is larger than $\frac{c}{n}$; the dipoles do not have enough time to form in front of the particle, as their formation rate is $\frac{c}{n}$ **[24]**.

When $v \geq \frac{c}{n}$, the electromagnetic waves, generated following the decay of the perturbations, interfere according to the Huygens-Fresnel principle. That is, the EM wave propagates spherically from particle's location at each moment, and under a certain angle θ_c, they interfere constructively with the next wave. The pattern is demonstrated in **Figures 2.29-b** and **2.30**.

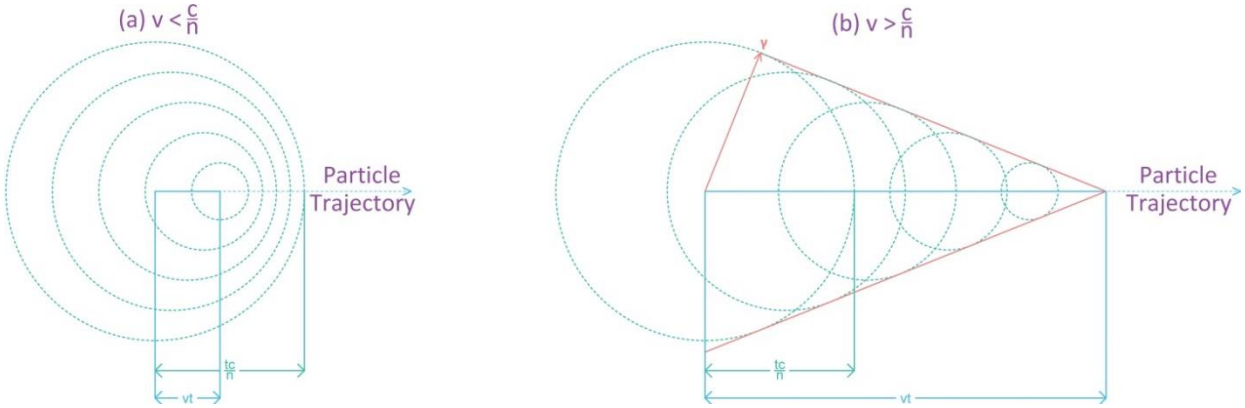

Figure 2.29 (a) The charged particle travels slower than speed of ligh in the medium, and no net dipole field is created. (b) The charged particle travels faster than light in the medium. Constructive interference of dipole fileds amounts to Cherenkov radiation at a specific angle.

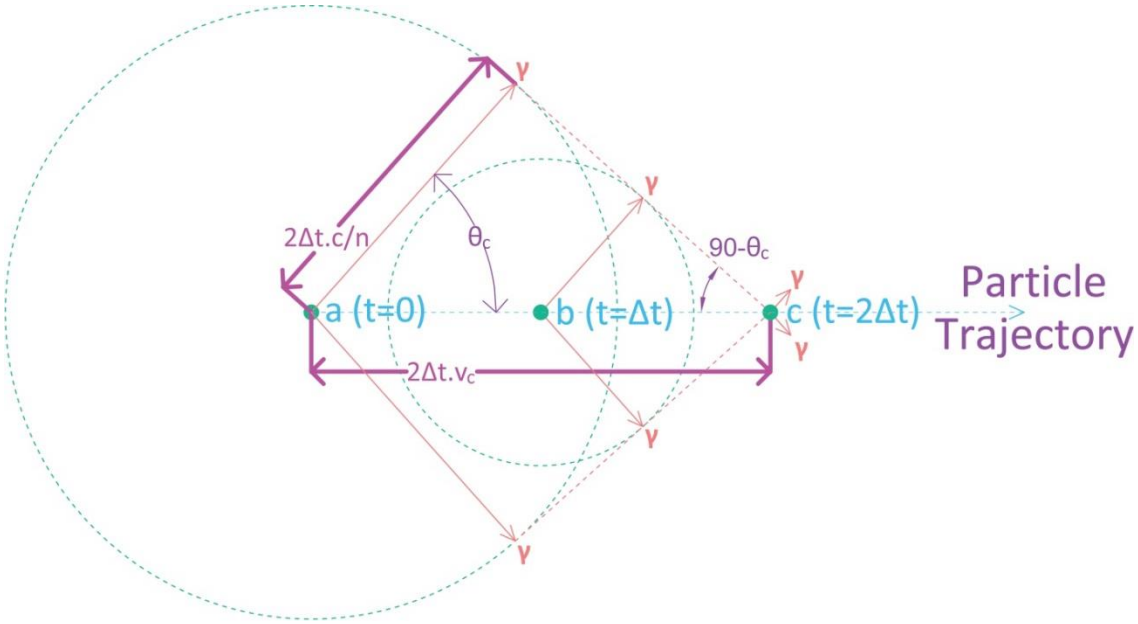

Figure 2.30 Consider the EM emission at points (a), (b), and (c) as the particle passes through each point with faster than light speed in the medium ($v_c > \frac{c}{n}$). At point (a), the particle emits EM waves spherically which propagates with speed of light in the medium ($\frac{c}{n}$). At point (b), the particle has already traveled the distance $\Delta t. v_c$, whereas the wave from point (a) has traveled the distance $\Delta t \cdot \frac{c}{n}$. Similarly, at point (c), the particle and the first wave have traveled $2\Delta t \cdot v_c$ and $2\Delta t \cdot \frac{c}{n}$ respectively. At the same time, the wave emitted from point (b) has only traveled $\Delta t \cdot v_c$. The pattern repeats itself until either the particle exits the medium or slows down to lower than light speed in the medium. The EM waves interfere constructively at angle θ_c.

2.6.2 Cherenkov Angle and Threshold

The Cherenkov angle can be deduced from **Figure 2.31**. Assume an electron has energy and momentum E_0 , $\vec{p}_0$ at point a. It emits a photon with energy $\hbar k$, after which its energy and momentum become E , $\vec{p}$ respectively. The recoil effect of photon emission is depicted in **Figure 2.31-a** with exaggerated deviation of the electron after Cherenkov emission. Due to symmetry of photon emissions, θ_e is ignored. It has been shown that including θ_e has an insignificant effect on calculation of the Cherenkov angle **[35]**. Using conservation of four-momentum in energy units:

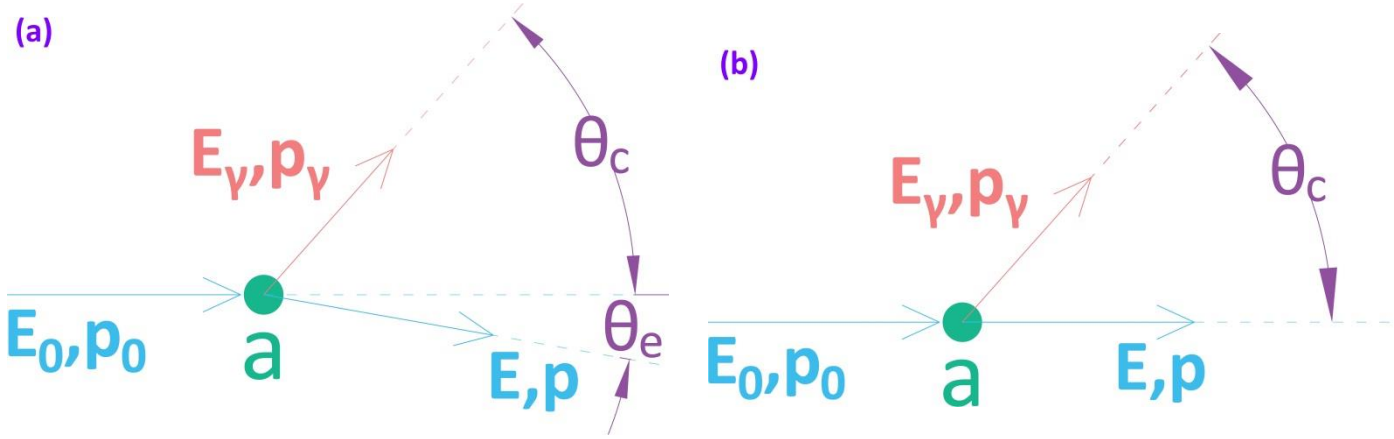

Figure 2.31 (a) Initial and final states of Cherenkov effect with exaggerated electron angle. (b) The states are shown with electron angle ignored due to symmetric emission.

$$P_0 = P_\gamma + P \quad \therefore \quad \begin{bmatrix} E_0 \\ \vec{p}_0 c \end{bmatrix} = \begin{bmatrix} E_\gamma \\ \vec{p}_\gamma c \end{bmatrix} + \begin{bmatrix} E \\ \vec{p} c \end{bmatrix} \qquad \textbf{Eq. (2.114)}$$

$$\begin{bmatrix} E_0 \\ p_0 c \\ 0 \\ 0 \end{bmatrix} = \begin{bmatrix} E_\gamma \\ p_\gamma c \cos\theta_c \\ p_\gamma c \sin\theta_c \\ 0 \end{bmatrix} + \begin{bmatrix} E \\ pc\cos\theta_e \\ -pc\sin\theta_e \\ 0 \end{bmatrix} \qquad \textbf{Eq. (2.115)}$$

$$\begin{cases} E_0 = c\sqrt{{p_0}^2 + {m_0}^2 c^2} \\ E_\gamma = \hbar\omega \\ E = c\sqrt{p^2 + {m_0}^2 c^2} \end{cases} \qquad \begin{cases} p_0 = mv = \gamma m_0 \beta c = \dfrac{m_0 \beta c}{\sqrt{1-\beta^2}} \\ p_\gamma = \hbar k_n = \dfrac{n\hbar\omega}{c} \\ p = unknown \end{cases} \qquad \textbf{Eq. (2.116)}$$

$$\vec{p}_0 - \vec{p}_\gamma = \vec{p} \quad \therefore \quad {p_0}^2 + {p_\gamma}^2 - 2p_0 p_\gamma cos\theta_c = p^2 \qquad \textbf{Eq. (2.117)}$$

$$\therefore \quad p^2 = {p_0}^2 + \left(\frac{n\hbar\omega}{c}\right)^2 - 2p_0 \frac{n\hbar\omega}{c} cos\theta_c \qquad \textbf{Eq. (2.118)}$$

$$E = E_0 - E_\gamma \quad \therefore \quad \sqrt{p^2 + {m_0}^2c^2} = \sqrt{{p_0}^2 + {m_0}^2c^2} - \frac{\hbar\omega}{c} \qquad \textbf{Eq. (2.119)}$$

$$p^2 + {m_0}^2c^2 = {p_0}^2 + {m_0}^2c^2 + \left(\frac{\hbar\omega}{c}\right)^2 - 2\sqrt{{p_0}^2 + {m_0}^2c^2}\frac{\hbar\omega}{c} \qquad \textbf{Eq. (2.120)}$$

$$p^2 = {p_0}^2 + \left(\frac{\hbar\omega}{c}\right)^2 - 2\sqrt{{p_0}^2 + {m_0}^2c^2}\frac{\hbar\omega}{c} \qquad \textbf{Eq. (2.121)}$$

Substituting p^2 from **Equation 2.121** to **Equation 2.118**:

$${p_0}^2 + \left(\frac{n\hbar\omega}{c}\right)^2 - 2p_0\frac{n\hbar\omega}{c}cos\theta_c = {p_0}^2 + \left(\frac{\hbar\omega}{c}\right)^2 - 2\sqrt{{p_0}^2 + {m_0}^2c^2}\frac{\hbar\omega}{c} \qquad \textbf{Eq. (2.122)}$$

$$\therefore \quad (n^2 - 1)\left(\frac{\hbar\omega}{c}\right)^2 = \frac{\hbar\omega}{c}\left(2np_0cos\theta_c - 2\sqrt{{p_0}^2 + {m_0}^2c^2}\right) \qquad \textbf{Eq. (2.123)}$$

$$\therefore \quad 2np_0cos\theta_c = 2\sqrt{{p_0}^2 + {m_0}^2c^2} + (n^2 - 1)\frac{\hbar\omega}{c} \qquad \textbf{Eq. (2.124)}$$

$$\therefore \quad cos\theta_c = \frac{1}{n}\sqrt{\frac{{p_0}^2 + {m_0}^2c^2}{{p_0}^2}} + \frac{(n^2 - 1)}{2np_0}\frac{\hbar\omega}{c} \qquad \textbf{Eq. (2.125)}$$

Substituting p_0 and $\frac{n\omega}{c}$ from **Equation 2.116**:

$$cos\theta_c = \frac{1}{n}\sqrt{1 + \frac{1 - \beta^2}{\beta^2}} + \frac{(n^2 - 1)\hbar\omega}{2n\gamma m_0\beta c^2} \qquad \textbf{Eq. (2.126)}$$

$$cos\theta_c = \frac{1}{n\beta} + \frac{(n^2 - 1)\hbar\omega}{2n\gamma m_0\beta c^2} \qquad \textbf{Eq. (2.127)}$$

The second term accounts for the recoil effect of the photon and is usually ignored due to its insignificant contribution. For instance, for a 1MeV electron moving in a PMMA with $n = 1.49$ emitting a Cherenkov photon with average wavelength of 420nm, the first and second term are roughly 0.78 and 1.41×10^{-6} respectively.

$$cos\theta_c = \frac{1}{n\beta} + \frac{\hbar k_n}{2p_0}\left(1 - \frac{1}{n^2}\right) \cong 0.78 + 1.41 \times 10^{-6} \quad \therefore \quad \theta_c \cong 38.67° \qquad \textbf{Eq. (2.128)}$$

Equation 2.127 holds under the following conditions:

1. Charged particles' velocity is larger than the speed of light in the medium $v > \frac{c}{n}$.
2. The radiator is transparent in optical and possibly UV regions. The length of the radiator must also be much larger than the wavelength of the photons for interference to occur.

The Cherenkov threshold corresponds to the onset of Cherenkov radiation, where the particle's speed increases beyond $\frac{c}{n}$. From **Equation 2.127**:

$$cos\theta \leq 1 \quad \therefore \quad \beta \geq \frac{1}{n} \quad \therefore \quad \beta_{th} = \frac{1}{n} \qquad \textbf{Eq. (2.129)}$$

The Cherenkov angle is zero at threshold, and increases with speed of the particle. As the speed of the particle increases up to speed of light in vacuum, the emission angle asymptotically reaches its maximum.

$$\theta_{max} = \lim_{\beta \to 1} \theta_c = cos^{-1} \frac{1}{n} \qquad \textbf{Eq. (2.130)}$$

At a fixed emission wavelength, the photons form a sharp cone with half angle θ_c. No emission occurs inside or outside the cone. However, dependence of refractive index on wavelength introduces an uncertainty to θ_c, which changes the shape of the cone's imprint on the detector as a hollow circle instead of a sharp circle (**Figure 2.32**). Detailed description of this Cherenkov angle spreading in dispersive medium is presented in **[35]**.

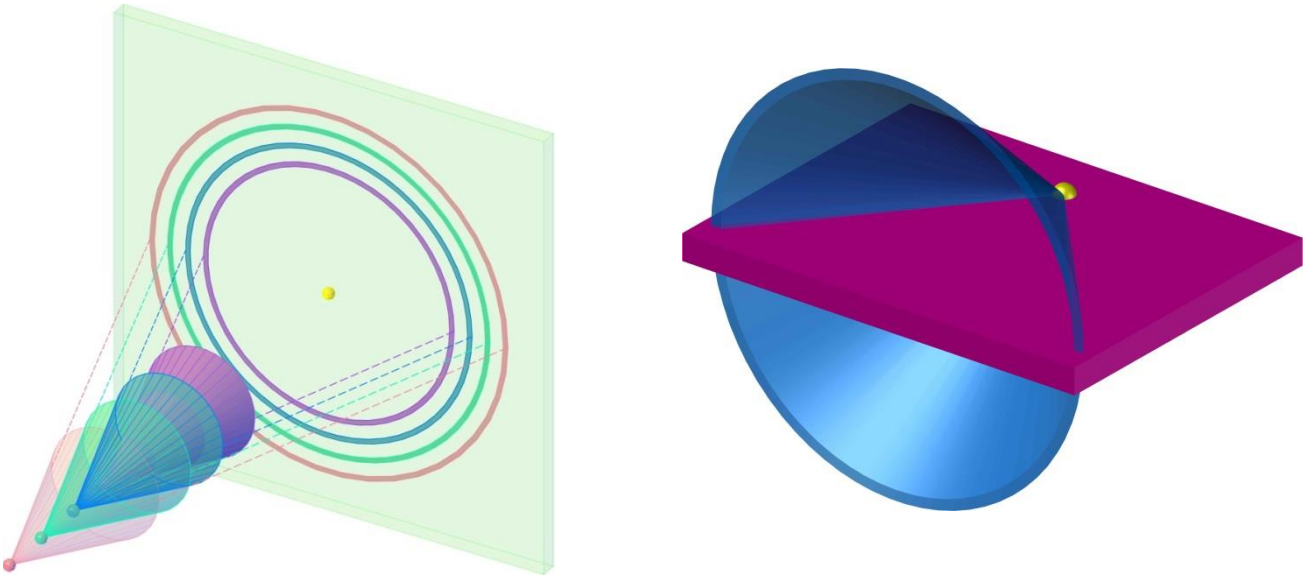

Figure 2.32 As a charged particle travels throught the radiator, it emits Cherenkov photons in a cone shape. The emission of the photons from different starting points produces hollow circles on the detector. This pattern continues until either the speed of the particle drops below the threeshold limit or the particle leaves the radiator.

Real media always exhibit dispersion, and radiation only occurs for wavelengths which meet the requirement of $\beta n(\omega) > 1$. **Figure 2.33** shows dispersion curve for a media transparent in visible range **[28]** and **[36]**. Emission at $n(\omega) < 1$ is always forbidden. Transition from normal to anomalous dispersion signifies the beginning of absorption bands for which no radiation occurs. Emission bands involve certain ranges of X-ray, from near UV to near IR, far IR, and radio wavelengths. The region of interest for current study is visible range and parts of the UV wavelengths which allow Cherenkov emission, i.e., $300nm \leq \lambda \leq 1000nm$.

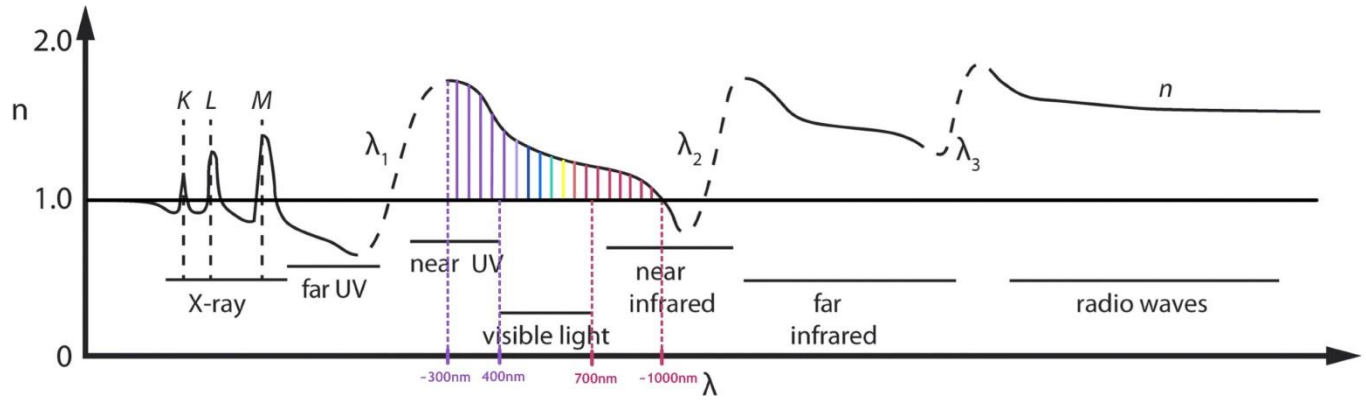

Figure 2.33 Dispersion relation for a typical optically transparent media. Regions of anomalous dispersion for which $\frac{dn}{d\omega} > 1$ are shown as dashed black lines.

Relying on the Cherenkov angle alone to determine the energy has limited precision. The angle increases rapidly with energy and saturates very close to θ_c as shown in **Figure 2.34**. This underscores the importance of photon yield measurement in experimental setups.

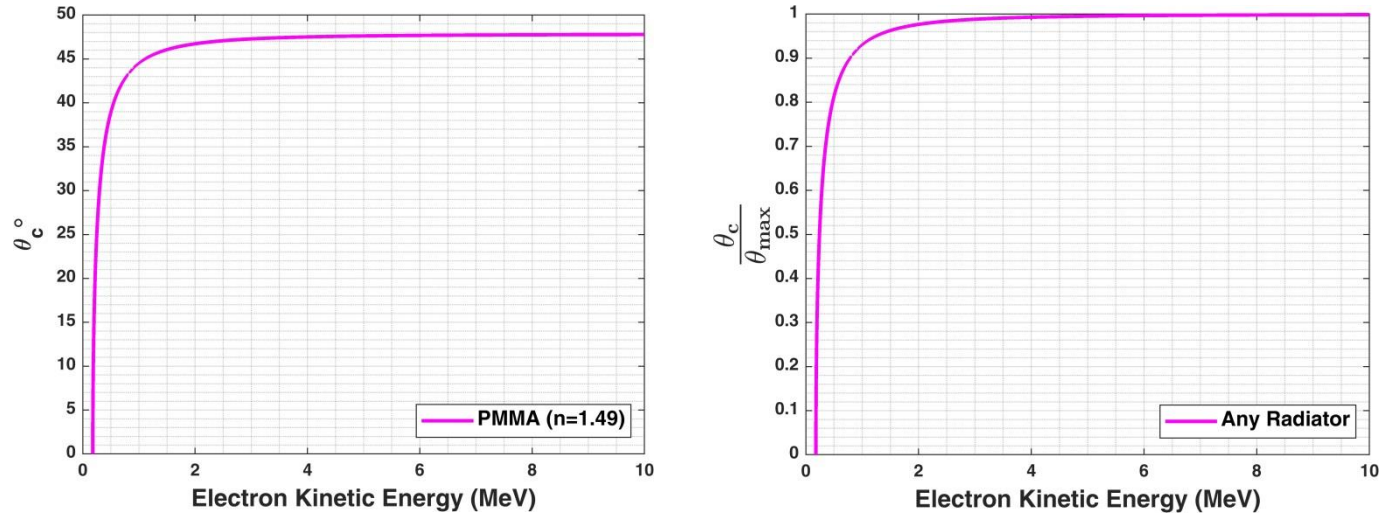

Figure 2.34 (Left) Cherenkov angle for electrons ranging from threshold energy to 10MeV traveling in PMMA with n=1.49. (Right) $\frac{\theta_c}{\theta_{max}}$ for the same range in any radiator. The ratio saturates to 98% already at 3MeV. The dynamic range limitation makes it difficult to determine energy solely based on Cherenkov angle.

2.6.3 Cherenkov Energy Spectrum

The Energy distribution of the emitted Cherenkov photons is:

$$\frac{d^2E}{d\omega dx} = \frac{z^2e^2}{4\pi\epsilon_0 c^2}\omega\left(1 - \frac{1}{\beta^2 n^2(\omega)}\right) \qquad \textbf{Eq. (2.131)}$$

where z is the atomic number of the medium. Integrating over a specific frequency interval $[\omega_1, \omega_2]$ yields emitted Cherenkov photon energy per path length:

$$\frac{dE}{dx} = \frac{z^2e^2}{4\pi\epsilon_0 c^2}\int_{\omega_1}^{\omega_2}\omega\left(1 - \frac{1}{\beta^2 n^2(\omega)}\right)d\omega \qquad \textbf{Eq. (2.132)}$$

This energy is equal to the energy loss of the charged particle through radiation and is quite small ($\approx 1\frac{\text{keV}}{cm.particle}$) in magnitude. It is, however, possible to detect due to emission of large number of low-energy Cherenkov photons emitted **[35]**. To calculate the photon yield, one must transform the left-hand side of **Equation 2.132** to reflect number of photons, instead of their energy.

$$E = N\hbar\omega \quad \therefore \quad \frac{dN}{dE} = \frac{1}{\hbar\omega} \qquad \textbf{Eq. (2.133)}$$

$$\frac{dN}{dx} = \frac{dE}{dx}\times\frac{dN}{dE} = \frac{z^2e^2}{4\pi\epsilon_0 c^2}\int_{\omega_1}^{\omega_2}\frac{\omega}{\hbar\omega}\left(1 - \frac{1}{\beta^2 n^2(\omega)}\right)d\omega = \frac{z^2\alpha}{c}\int_{\omega_1}^{\omega_2}\left(1 - \frac{1}{\beta^2 n^2(\omega)}\right)d\omega \qquad \textbf{Eq. (2.134)}$$

where $\alpha = \frac{e^2}{4\pi\epsilon_0\hbar c}$ is the fine-structure constant. Rewriting Equation above in terms of wavelength:

$$\omega = \frac{2\pi c}{\lambda} \quad \therefore \quad d\omega = -\frac{2\pi c}{\lambda^2}d\lambda \qquad \textbf{Eq. (2.135)}$$

$$\frac{dN}{dx} = -2\pi z^2\alpha\int_{\lambda_1}^{\lambda_2}\left(1 - \frac{1}{\beta^2 n^2(\lambda)}\right)d\lambda = 2\pi z^2\alpha\int_{\lambda_2}^{\lambda_1}\left(1 - \frac{1}{\beta^2 n^2(\lambda)}\right)\frac{d\lambda}{\lambda^2} \qquad \textbf{Eq. (2.136)}$$

Derivative of **Equation 2.136** is an expression of photon yield per wavelength per distance:

$$\frac{d^2N}{d\lambda dx} = \frac{2\pi z^2 \alpha}{\lambda^2}\left(1 - \frac{1}{\beta^2 n^2(\lambda)}\right) \qquad \textbf{Eq. (2.137)}$$

With the assumption of constant average refractive index $n(\lambda) \cong \bar{n}$ and average frequency $\bar{\omega} = \frac{\omega_1 + \omega_2}{2}$ over the frequency interval $[\omega_1\ \omega_2]$, an expression can be obtained for the integral. Substituting $\left(1 - \frac{1}{\beta^2 \bar{n}^2}\right)$ with $\sin^2 \theta_c$:

$$\frac{dN}{dx} \cong 2\pi z^2 \alpha \int_{\lambda_2}^{\lambda_1} \left(1 - \frac{1}{\beta^2 \bar{n}^2}\right) \frac{d\lambda}{\lambda^2} \qquad \textbf{Eq. (2.138)}$$

$$\therefore \quad \frac{dN}{dx} = 2\pi z^2 \alpha \sin^2 \theta_c \left(\frac{1}{\lambda_1} - \frac{1}{\lambda_2}\right) \qquad \textbf{Eq. (2.139)}$$

Integrating **Equation 2.139** over the total length of the medium (L) yields the number of Cherenkov photons produced by a single charged particle.

$$N = \int_0^L 2\pi z^2 \alpha \sin^2 \theta_c \left(\frac{1}{\lambda_1} - \frac{1}{\lambda_2}\right) dx = 2\pi z^2 \alpha \sin^2 \theta_c \left(\frac{1}{\lambda_1} - \frac{1}{\lambda_2}\right) L \qquad \textbf{Eq. (2.140)}$$

Integration of **Equation 2.137** over the path length determines the dependence of photon yield to the wave length in general as shown in **Figure 2.35**.

$$\frac{dN}{d\lambda} = \frac{2\pi z^2 \alpha}{\lambda^2} \sin^2 \theta_c\, L \qquad \textbf{Eq. (2.141)}$$

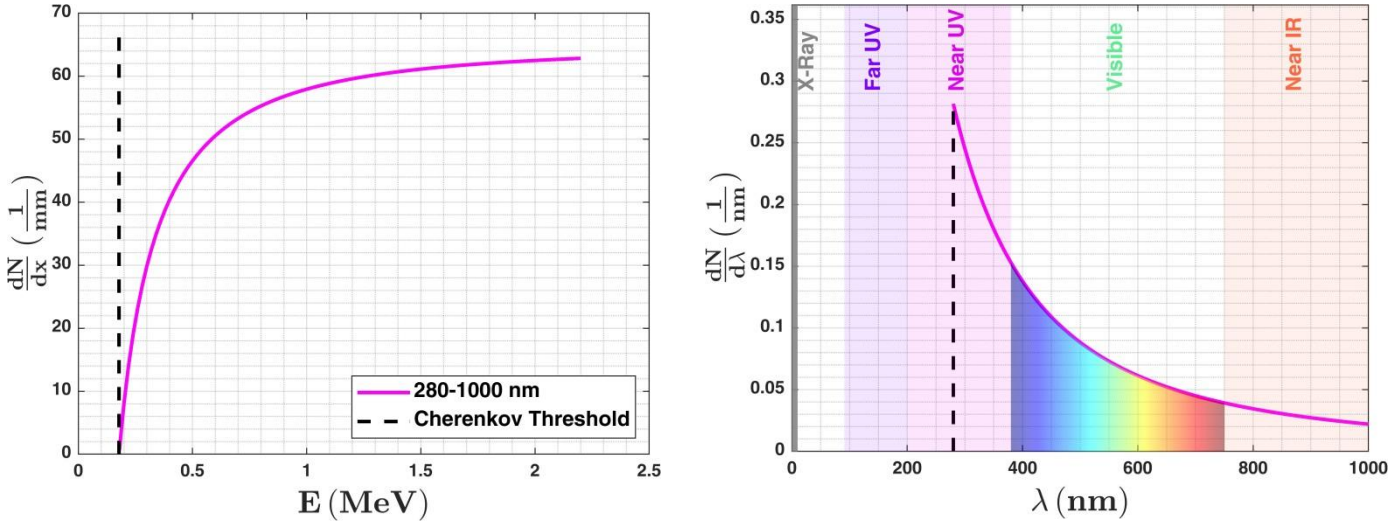

Figure 2.35 Dependence of photon yield on frequency and wavelength. Inclusion of UV range into **Equation 2.140** significantly increases the photon yield due to the power relation. At near UV, the Cherenkov emission is cut off due to onset of anomalous dispersion shown with dashed line. Extension of the emission to the near infrared has very limited effect on the overall yield.

2.6.4 Cherenkov Photon Yield

Equation 2.140 does not reflect the reality of Cherenkov radiation. As electrons travel through a radiator, they experience energy loss through ionization, excitation, bremsstrahlung, and Cherenkov radiation. In case of electrons, in particular, the energy loss is significant compared to heavy charged particles. For instance, Møller scattering or Bremsstrahlung can reduce electron's kinetic energy by 50% all the way up to 100%. This introduces a stopping power related range to the charged particle. Determination of range of a charged particle is a statistical process, where individual particle's range may differ significantly from its mean value. This is known as range straggling **[35]**. The range can be calculated from:

$$R = \int_{E}^{m_0 c^2} \frac{dE}{dE/dx} \qquad \textbf{Eq. (2.142)}$$

Since only kinetic energy can be transferred in interactions, the upper limit of the integral is always the mass-at-rest of the charged particle. Determination of range of electrons in absorbers is much more difficult than for heavier charged particles. Due to their small mass, elastic and inelastic scattering can substantially change the electrons' direction so much so that backscattering contributes significantly to the total loss of an electron beam.

In this work, ESTAR database provided by NIST **[37]** is used to estimate the overall energy loss of charged particles in different radiators. ESTAR adopts Bethe theory **[38]** for collision related energy losses with density effect corrections from Sternheimer **[39] [40]**. The collision energy loss is reported to have 1 to 2%

uncertainty at electron energies above 100keV. Theoretical Bremsstrahlung cross sections from Seltzer and Berger **[41]** in combination with numerical results from Pratt et al. **[42]** are used for radiated energy loss with uncertainties between 2 to 5%.

In order to calculate the total number of Cherenkov photons emitted from a PMMA with length L, the following algorithm is implemented. The electrons enter the medium with their initial energy. The path length required for the electron to lose ΔE is calculated from **[37]** using **Equation 2.143**.

$$\Delta x_i = \frac{\Delta E}{dE_i/dx} \qquad \textbf{Eq. (2.143)}$$

Choosing a small step size for ΔE, we can assume the energy loss remains constant. The photon yield then becomes:

$$\frac{dN_i}{dx} = 2\pi z^2 \alpha \, sin^2 \, \theta_c \left(\frac{1}{\lambda_2} - \frac{1}{\lambda_1}\right) \qquad \textbf{Eq. (2.144)}$$

$$N_i = \int_0^{\Delta x_i} 2\pi z^2 \alpha \, sin^2 \, \theta_c \left(\frac{1}{\lambda_2} - \frac{1}{\lambda_1}\right) dx = 2\pi z^2 \alpha \, sin^2 \, \theta_c \left(\frac{1}{\lambda_2} - \frac{1}{\lambda_1}\right) \Delta x_i \qquad \textbf{Eq. (2.145)}$$

This process continues until either we reach the end of the radiator or the energy of the electron drops below Cherenkov threshold. The total number of photons produced, therefore, becomes the sum of all steps:

$$N = \sum_i N_i \qquad \textbf{Eq. (2.146)}$$

Figure 2.36 shows the photon yields of electrons with different energies in a 9.8mm PMMA based on the algorithm used. **Figure 2.37** shows the range of electrons in the PMMA. A 1MeV electron is, for instance, expected to produce nearly 160 photons before it is stopped at 4.4mm, while 2MeV electron will produce 447 electrons and travels 8.2 mm before it is stopped.

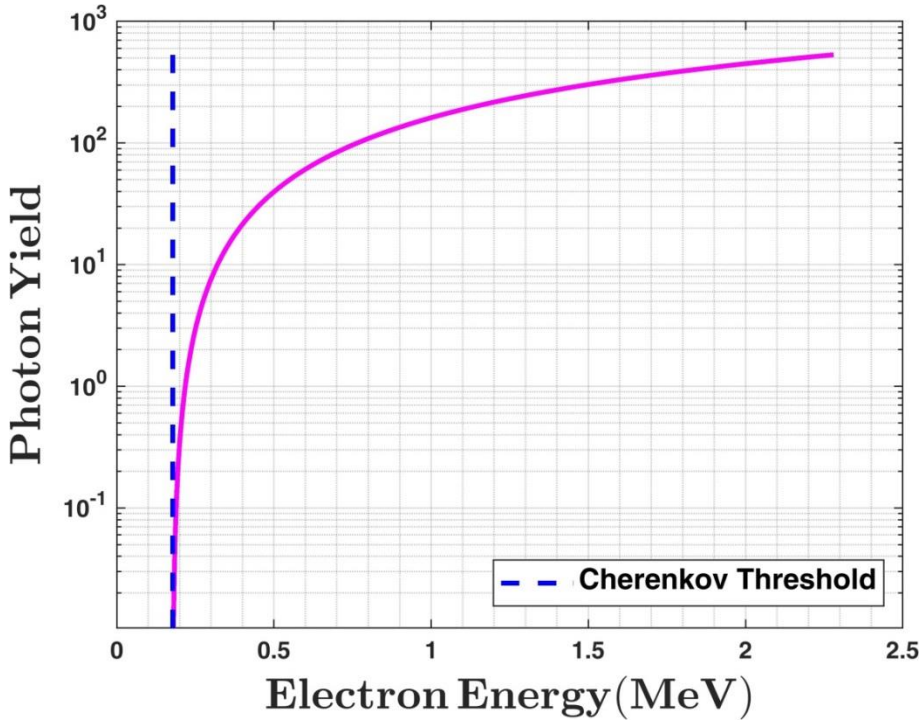

Figure 2.36 Photon Yield of Electrons with energies from Cherenkov Threshold to 2.2 MeV. The electrons are traveling in 9.8mm of PMMA with refractive index of 1.49. The wavelength is cut to 280-1000nm. Photon yield increases logarithmically with energy as radiator's length increases.

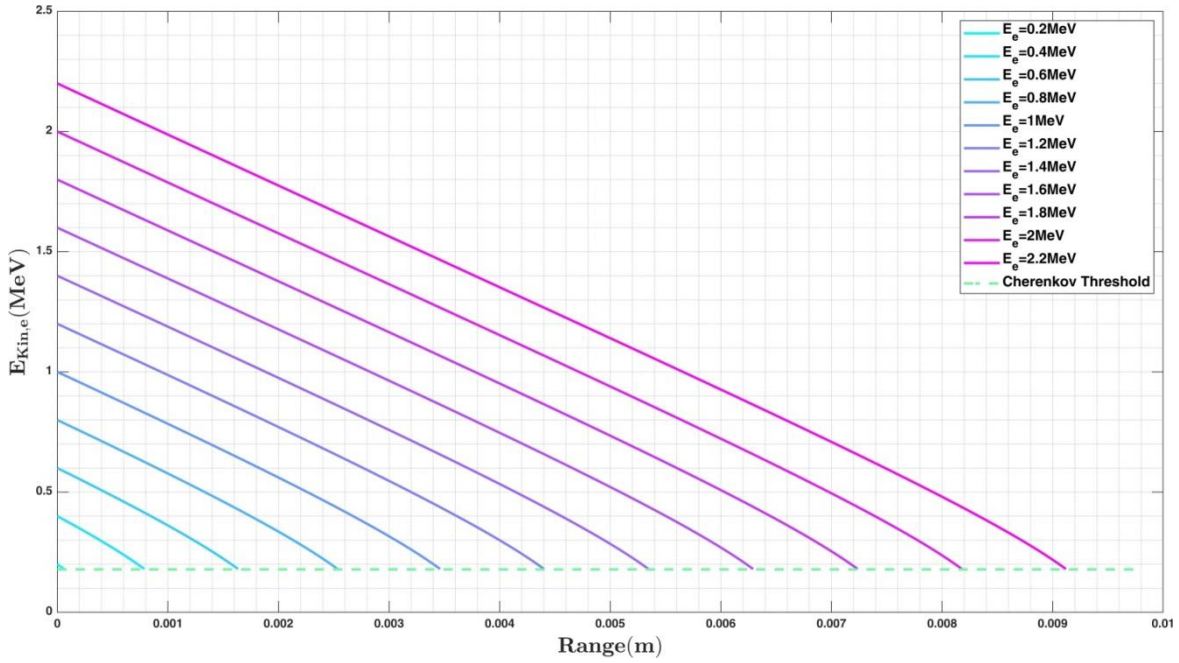

Figure 2.37 Range of electrons with different energies in PMMA with n=1.49 and 9.8mm length. The electrons lose energy based on their remaining energy. Energy loss is calculated from the stopping power $\frac{dE}{dx}$ estimated from ESTAR **[37]**. Electrons either exit the radiator with energies above Cherenkov threshold or lose energy below the threshold. For electrons up to 2.2 MeV, the stopping power is large enough to drain the charged particles' energy below the threshold.

3. Silicon PhotoMultipliers

Silicon Photomultipliers (SiPM) are single-photon detectors based on Single-Photon Avalanche Diodes (SPAD). An SiPM channel houses tens of thousands of SPADs on a silicon substrate. SiPMs operate on Geiger mode and require far less bias voltage than PhotoMultiplier Tubes. The SiPM used in current experiment is an 8x8 Hamamatsu S13361-3075AS. A brief introduction into SiPMs followed by operation principles of the detector used in this experiment are provided in this chapter.

3.1 p-n Junction

Silicon PhotoMultiPliers are made of semiconductor materials. The most common semiconductor materials, in order of prevalence are Silicon (Si), Germanium (Ge), and Gallium-Arsenide binary compound (GaAs). Silicon and other atoms of group IV elements have four valence electrons in their outer shell. When combined in a lattice, the discrete energy states of individual atoms combine and form valence and conduction energy bands, which are separated by a band gap. Each valence electron forms a covalent bond with its counterpart from a neighboring atom. At absolute zero, all covalent bonds are intact, and no valence electron ventures from the valence band into the conduction band. As temperature increases, valence electrons receive enough thermal energy to jump from the valence band into the conduction band, creating electron-hole pairs. Electrons in the conduction band travel within the crystal lattice freely, turning the material from an insulator into a conductor (See **Figure 3.1**). Same is true in case of holes, as they receive electrons from adjacent atoms.

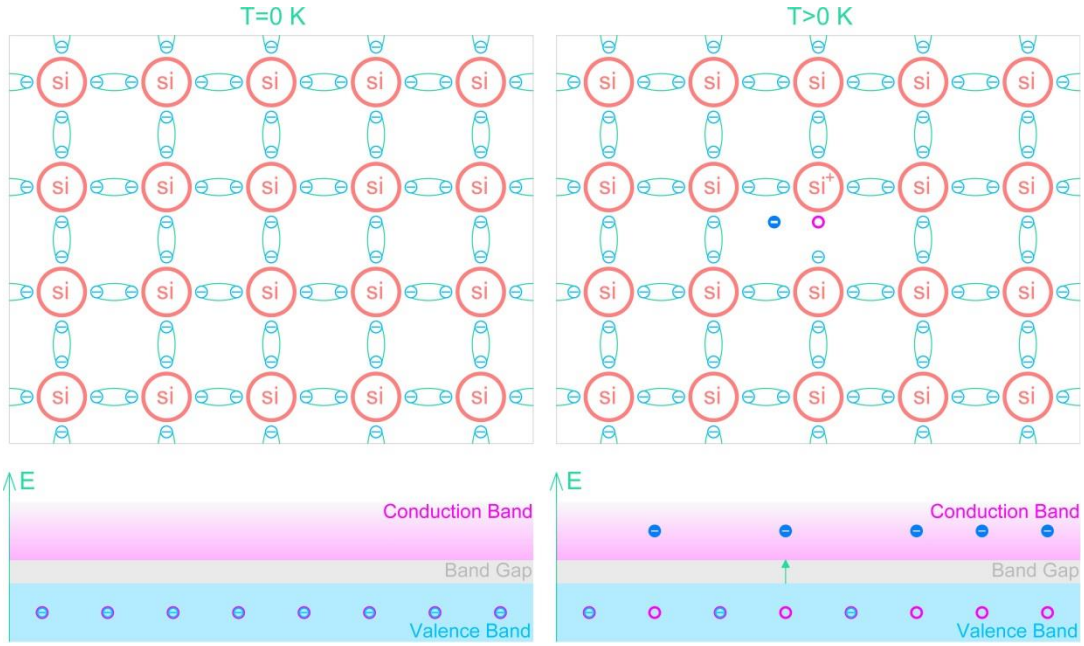

Figure 3.1 Pure silicon lattice at T=0 K (left) and T>0 K (right). Energy bands are shown below the lattice structure. At T>0 K, some of the covalent bonds break down due to thermal energy, releasing electrons into the conduction band.

The amount of energy needed to transfer electrons to the conduction band equals the height of the band gap. The band gaps for Silicon and Germanium at room temperature are 1.12 and 0.67 eV respectively and decreases with higher temperatures **[43]**. The number of holes in the valence band is identical to the number of electrons in the conduction band. This type of pure silicon lattice is known as intrinsic silicon and has a very high resistivity to current.

In order to increase electric conductivity, the lattice must contain more free electrons and holes at room temperature. To do so, the silicon lattice is infused (doped) with impurities from group III and group V elements to create p-type and n-type semiconductors respectively. In a p-type, silicon is doped with boron or aluminum impurities, which have three valence electrons in their outer shell. The trivalent bond in silicon lattice turns the impurity into an acceptor of a shell electron, creating a hole in the process. In an n-type, the impurity is a pentavalent atom, forming four covalent bonds with neighboring silicon atoms and donating a free electron. The free electrons jump to the conduction band upon gaining thermal energy and become charge carriers. In other words, all atoms in the lattice share the same conduction and valence band. Therefore, electrons in the conduction band and holes in the valence band can move freely within the lattice. The process is demonstrated in **Figure 3.2**.

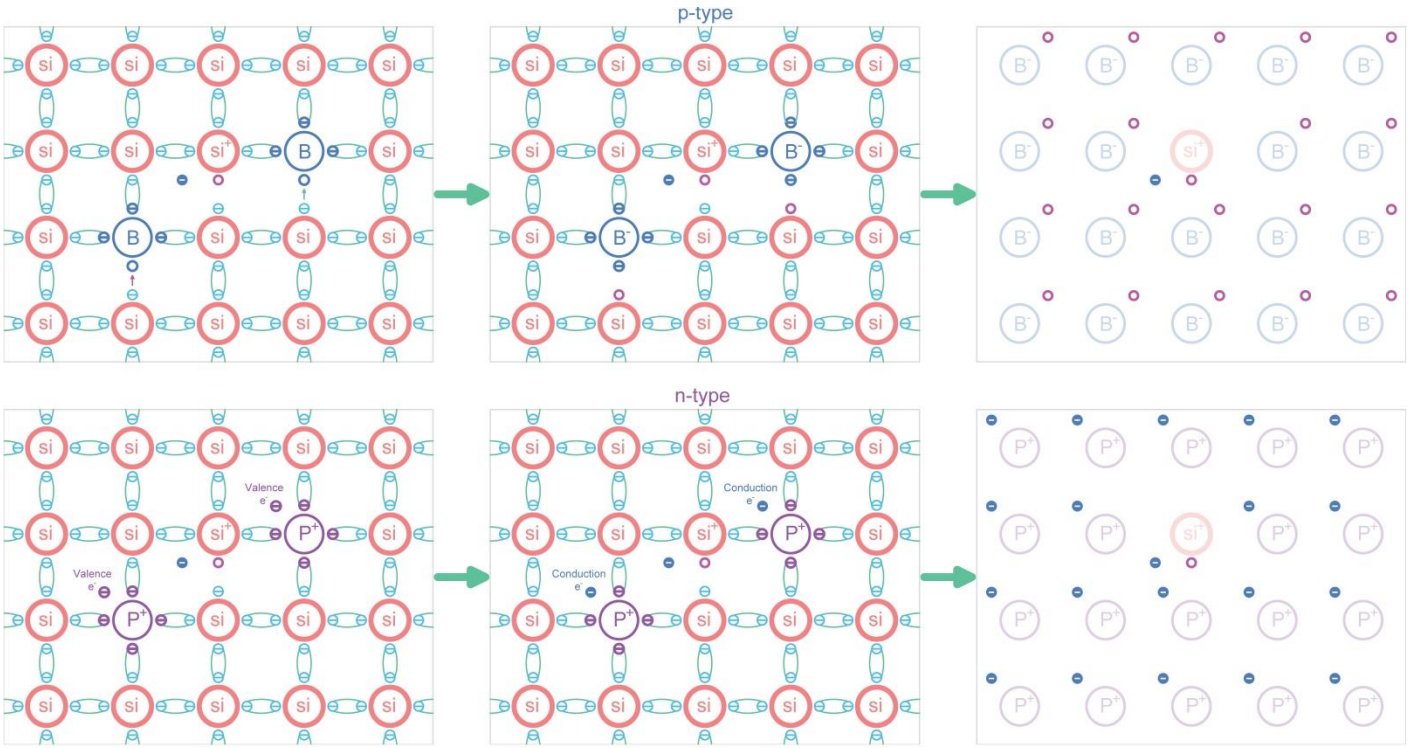

Figure 3.2 p-doped (top) silicon lattice has majority holes and minority electrons, whereas n-doped (bottom) silicon lattice has majority electrons and minority holes. Note that acceptor and donor atoms are immobile and cannot move. It is only the charge carriers (electrons and holes) that are moving freely. Dopant concentration is exaggerated. In reality, the concentration is around 10^{13} to 10^{18} $\frac{\text{atoms}}{cm^3}$. For reference, there are approximately 5×10^{22} $\frac{\text{atoms}}{cm^3}$ in a silicon lattice [1].

The building block of an SiPM is a p-n junction, made up of connecting an n-type and a p-type semiconductor together. Once combined, the majority conduction electrons from the n-type and the majority valence holes from the p-type diffuse towards the opposite side in order to recombine (see **Figure 3.3**). The recombination only occurs in close proximity to the junction and depletes the region of majority carriers, while the immobile, ionized acceptor and donor atoms remain. The impurity atoms in the depletion region form an electrical field which gradually prevents further diffusion of charged carriers across the junction until the electric field magnitude becomes equal to the electrical attraction of opposite charge carriers, at which point equilibrium is reached between electric field and carrier diffusion. The electric field is not uniform; it peaks at the junction where oppositely charged stationary ions are closest and tapers off near the boundaries of the depletion region (**Figure 3.4**).

[1] Atomic weight and density of silicon are 28.09 $\frac{g}{cm^3}$ and 2.33 $\frac{g}{cm^3}$ respectively. Assuming Avogadro constant to be 6.022×10^{23}, density of silicon atoms becomes $\frac{2.33\,\frac{g}{cm^3} \times 6.022 \times 10^{23}}{28.09\,\frac{g}{cm^3}} \cong 6.022 \times 10^{23}$ **[71]**.

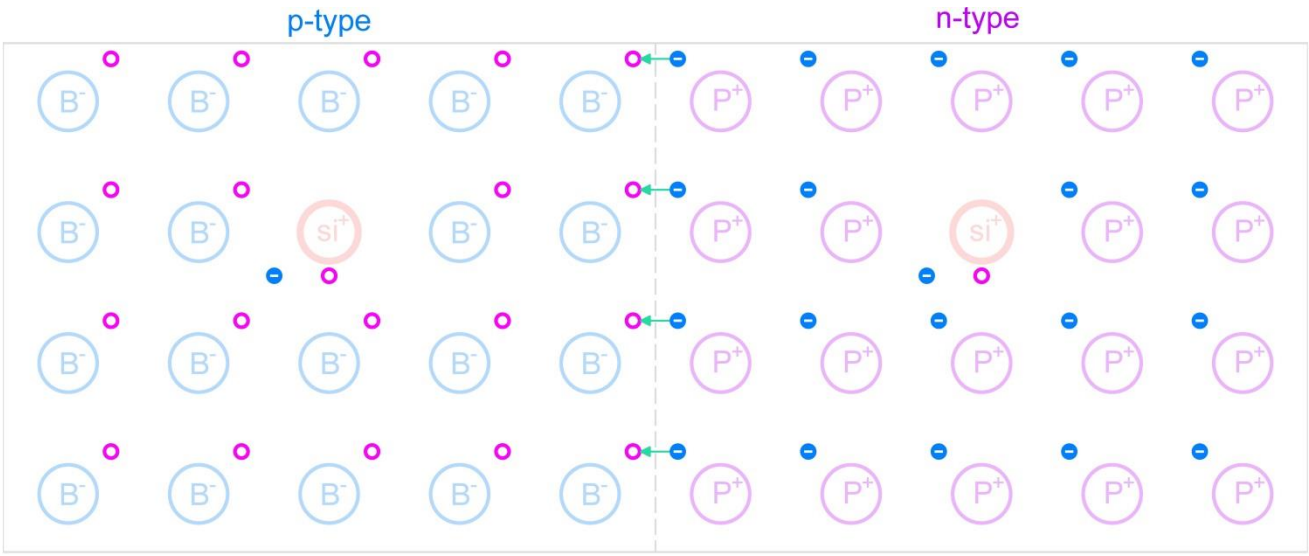

Figure 3.3 Juxtaposition of an n-type and p-type silicon lattice. In the p-n junction vicinity, majority electrons from n-type and majority holes from the p-type diffuse towards each other to recombine.

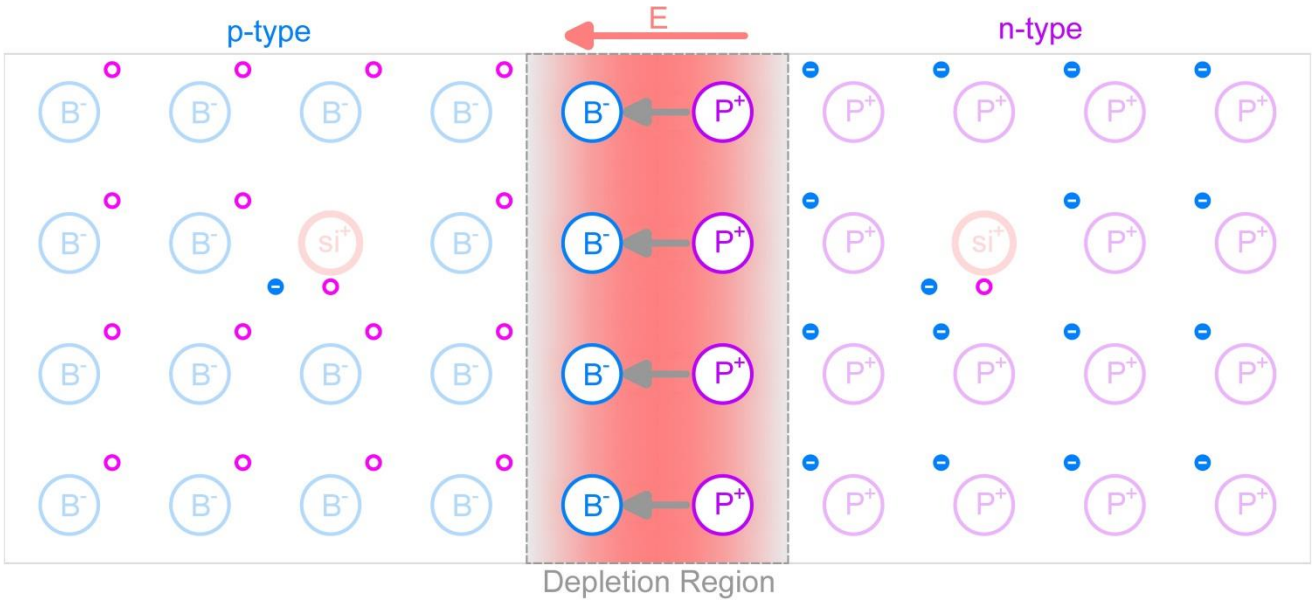

Figure 3.4 Formation of depletion region in p-n junction. Diffusion of charged carriers does not stop immediately. Conduction electrons which try to diffuse to the p side experience electric repulsion from negative immobile ions in the depletion region. Same occurs between valence holes and positive ions to the point where the electric repulsion of the ions grows equal in magnitude to the attraction of charged carriers is, at which point diffusion stops altogether.

Figure 3.5-a shows a p-n junction's energy band. p-type semiconductors have slightly higher energy bands than the n-type has, as trivalent dopants exert less force on the outer shell electrons **[44]**. Once the p-n junction is formed, high energy conduction electrons from the n-region diffuse into the lower energy part of the conduction band of the p-region, only to rapidly lose energy and drop into the valence band of the p-region. The diffusion of free electrons triggers the formation and expansion of the depletion region. As

the free electrons diffuse to the p-region, the n-region's conduction energy level drops to the point where the overlap between conduction bands of the two regions is reduced to zero (**Figure 3.5-b**). This signifies the equilibrium at which there are no free electrons in the conduction band of the n-region with enough energy to cross the junction. The valence band of the n-region drops in energy level as well since the band gap always remains constant.

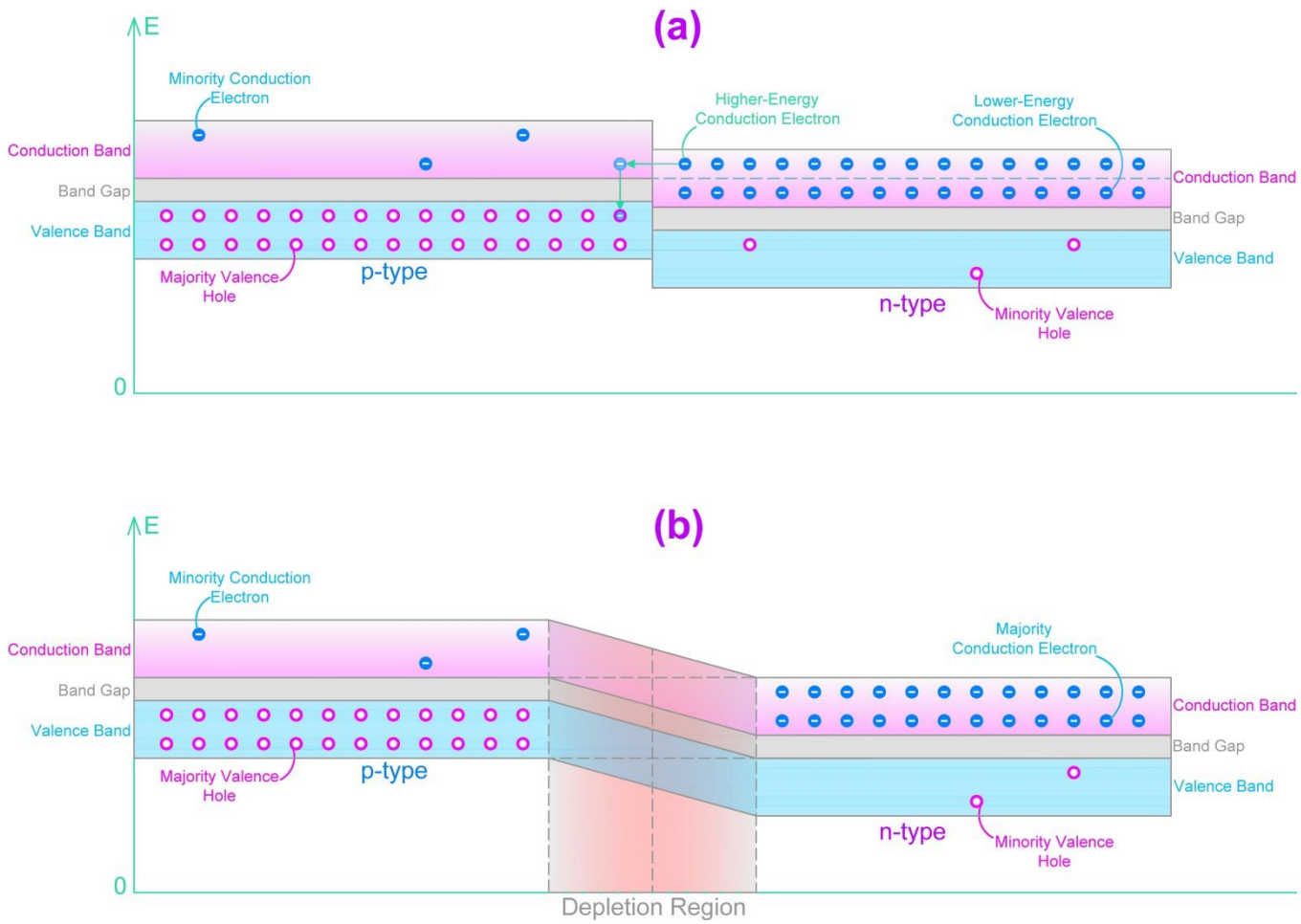

Figure 3.5 Energy band transformation during depletion region formation of a p-n junction. (a) Juxtaposition of p-type and n-type silicon. The overlap in conduction band facilitates diffusion of conduction electrons. (b) Upon diffusion of enough conduction electrons, the overlap closes, and the p-n silicon reaches equilibrium.

3.2 Signal Generation in p-n Junctions

If energies higher than the energy band gap is provided (through thermal excitation or photoelectric effect) to a valence electron in the depletion region, the electron transitions into the conduction band and leaves a hole behind. Due to the electric field, the electron and the hole drift to the N side and the P side respectively (See **Figure 3.6**). If a closed circuit is formed between N and P regions, the accumulated electrons and holes travel through the wire and recombine, creating photoelectric current. The electric

signal, in this case, is proportional to the number of events occurred. In other words, this system has a gain of one. This phenomenon also occurs outside the depletion region, but the electron-hole pair recombines quickly, due to absence of electric field outside the depletion region.

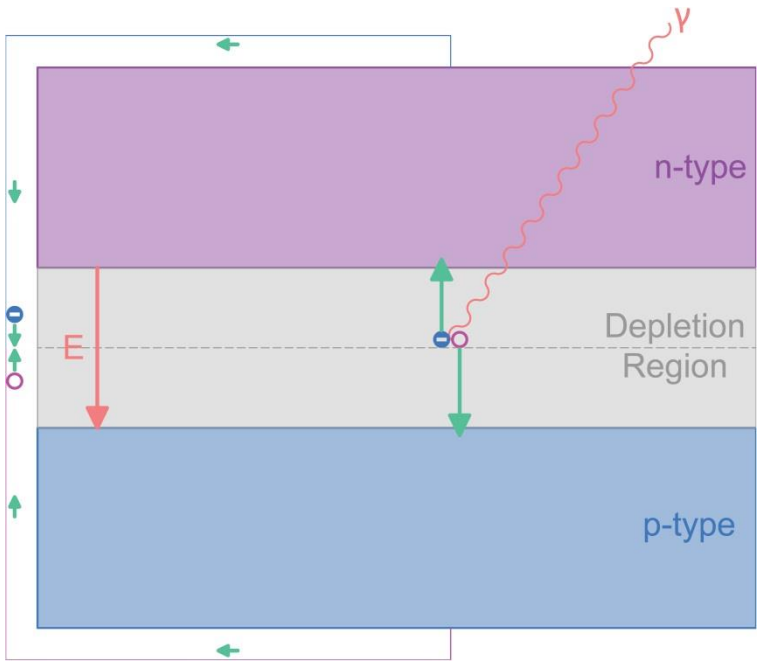

Figure 3.6 Incoming photon creates an electron-hole pair in the depletion region. The electric field separates the charge carriers to opposite sides. When N and P sides are externally connected, The charge carriers travel through the wire and recombine, creating a signal.

In the absence of external voltage, the small signal (electron-hole recombination) cannot be interpreted without amplification, which comes at the expense of increased noise. Also, the depletion zone encompasses a very small portion of the p-n unit, which limits the photo absorption capability of the detector **[44]**. The solution is applying reverse bias voltage. The reverse bias voltage (**Figure 3.7**) is in the same direction as the diffusion voltage V_D. Therefore, diffusion rate of majority holes from p-side to n-side and majority electrons from n-side to p-side decreases, which in turn substantially diminishes the diffusion current. As a reference, 1V is enough to completely stop the diffusion current $(I_D \approx 0)$. Upon applying reverse bias, free electrons from the external current try to cross the depletion region from p-side to n-side, but they are repelled by the negative side of the depletion region. Hence, they recombine with majority valence holes, expanding the depletion region in the process. The same occurs for the holes trying to cross the depletion region from n-side to p-side. They recombine with majority conduction electrons and expand the depletion region on the n-side. This process also amplifies the electric field in the depletion region, which means electron-hole pairs produced in the depletion region diffuse easier. When there is no signal, a reverse biased p-n diode draws a very small and constant current known as drift current or saturation current which is induced by thermal excitation of minority holes and minority free electrons.

The drift current highly depends on temperature and is independent of electric field in the depletion region.

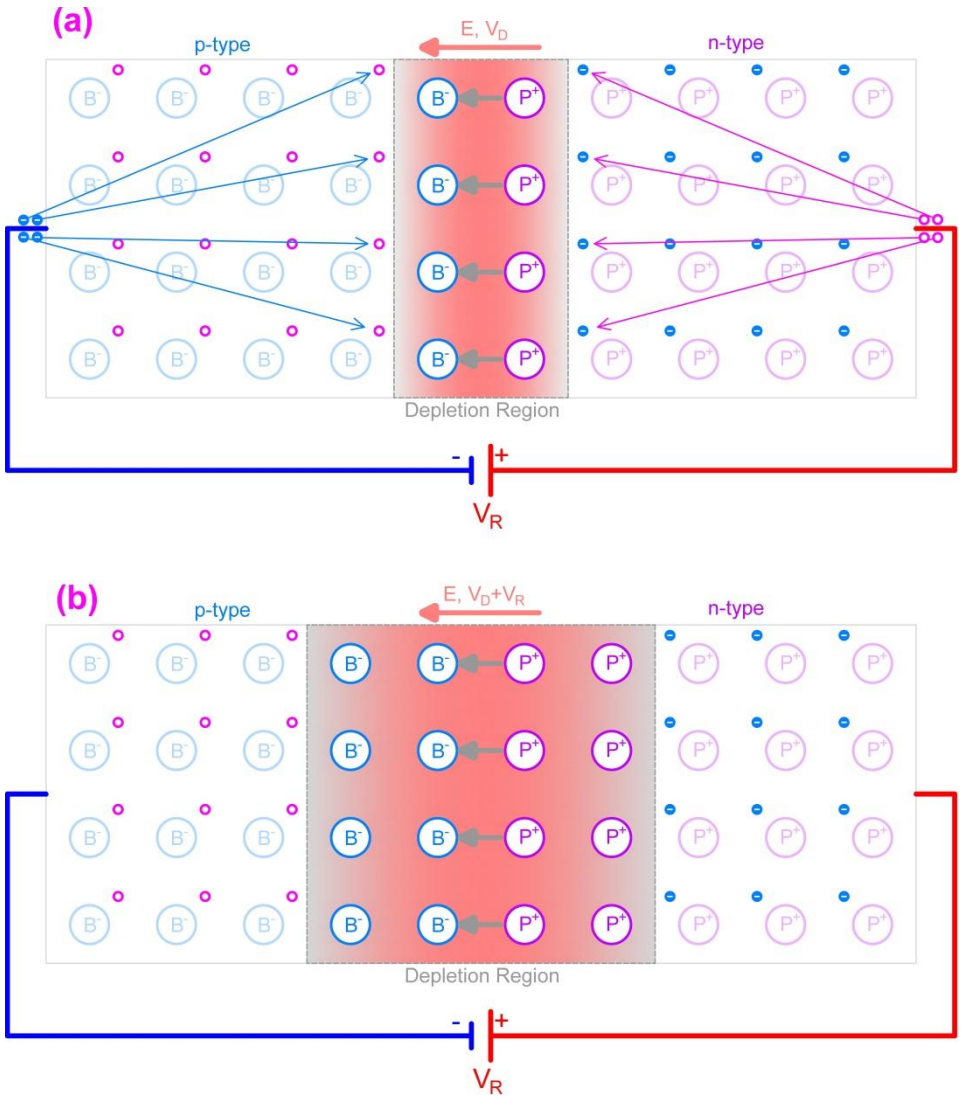

Figure 3.7 Reverse biased p-n junction. (a) Free electrons and holes from the external current try to cross the depletion region, but they are repelled by the electric charge of the immobile ions. (b) They eventually combine with majority charge carriers near th depletion zone, expanding it in the process.

At reverse bias mode, the current drawn from the circuit equals the drift current, which is negligible $(10^{-18}\ to\ 10^{-12}\ A)$. However, at certain reverse bias voltage, the electric field becomes so strong that minority free electrons, crossing the junction, or free electrons from electron-hole pairs, produced within the depletion region, gain sufficient kinetic energy from the electric field to ionize the atoms they collide with, releasing extra carriers. The ionization energy equals the band gap energy of silicon, which is roughly 2 eV. Under the influence of the electric field, these carriers liberate additional carriers through ionization collision. The ionization and carrier release keeps repeating analogous to an avalanche. In this case, the current flowing through the circuit is linearly proportional to the applied voltage with a slope equal to the

gain of the diode as shown in **Figure 3.8**. This is the principal operation of Avalanche Photodiodes (APD). A typical APD has a gain of 100 **[44]**.

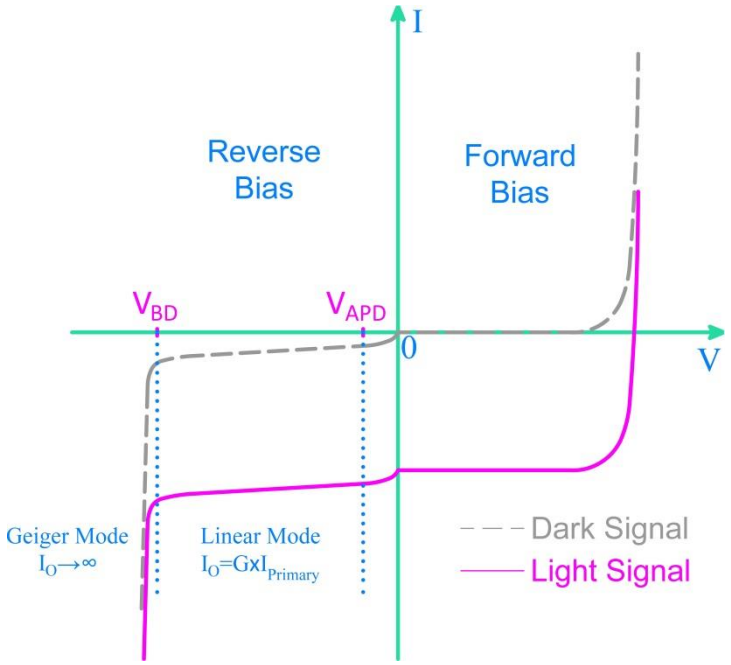

Figure 3.8 Breakdown voltage marking the start of Geiger mode operation. In reverse bias mode, the current is linearly proportional to the voltage up to breakdown point. This is true for both minority carriers created through thermal excitation (dark signal) and electron-hole pairs created through photoelectric effect in the depletion zone (Light Signal). Beyond breakdown voltage, the proportianality is lost, the diode operates in Geiger mode **[44]**.

3.3 Single-Photon Avalanche Diode (SPAD)

A single SiPM channel houses tens of thousands of p-n diodes called Single-Photon Avalanche Diodes (SPAD). Each SPAD is a Geiger Avalanche Photodiode (G-APD), working above breakdown bias voltage. Below breakdown voltage, only free electrons carriers have enough energy to cause impact ionization, and the signal is linearly proportional to the reverse bias voltage. Beyond breakdown voltage, however, holes and secondary photons also create additional carriers through impact ionization **[45]**. In this case, the silicon breaks down and becomes conductive, and a single charge carrier becomes capable of creating a self-sustaining avalanche so large that it cannot be stopped by itself and requires high-ohmic serial quenching resistors to reset the diode. Due to their high gain, SPADs create binary signals that are no longer proportional to the number of original carrier crossing. In other words, the p-n diode becomes a Geiger mode detector only registering absence or existence of signal, and energy information of the signal is lost. The threshold voltage at which Geiger mode takes effect is known as the breakdown voltage, which is the key characteristic of an SiPM photo detector.

Each Single-Photon Avalanche Photo Diode (SPAD) can be fabricated as P-on-N or N-on-P type, as shown in **Figure 3.9**. N-on-P SPADs have a P layer sandwiched between highly doped N and P layers (known as N^+ and P^+). The area of the N^+ region is much smaller than the P region is. Therefore, the P-side of the depletion region becomes far larger than the N-side is and captures more photon interactions. Free electrons, in general, have a higher probability of initiating an avalanche than holes do, provided they are created in the P-region of the depletion region. Furthermore, the longer the charge carrier's path in the depletion region, the more impact ionization it causes. In other words, a sustained avalanche depends on how far a free electron can travel within the depletion layer before it is absorbed and recombined as well as whether or not it crosses the p-n junction, where the electric field is at its peak. Therefore, photons interacting in the P-region of the depletion region create free electrons which accelerate in the electric field and create avalanche. The holes simply drift towards the P+ region and have a lower chance of creating an avalanche, as they do not cross the junction. This increases detection efficiency of the longer wavelengths at the expense of the shorter wavelengths, as longer wavelength photons tend to travel deeper into the diode before interacting with atoms due to photoelectric effect.

P-on-N SPADs have the opposite structure (an N layer sandwiched between highly doped P^+ and N^+ layers). They are designed with the focus of free electrons, created in the P side of the depletion layer, crossing the junctions, having the maximum path length inside the depletion region, and producing the avalanche. P-on-N SPADs are more efficient in detecting shorter wavelengths at the expense of longer wavelengths, as shorter wavelength photons tend to interact with the diode very close to the surface. Typical gain of a SPAD operating in Geiger mode is around 10^6 **[46]**.

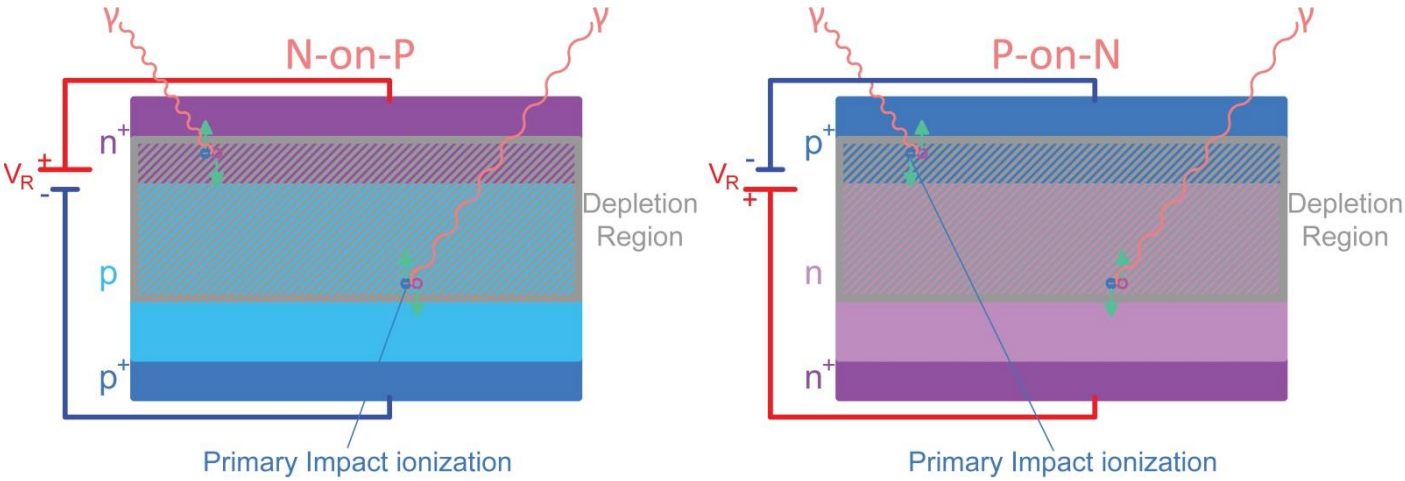

Figure 3.9 N-on-P and P-on-N SPADs. N-on-P SPADs (Left) are designed with focus on free electrons produced in the P side of the depletion region creating avalanche. Longer wavelengths tend to interact deeper into the diode, where the free electrons from the electron-hole pair have longer path length in the depletion region. P-on-N SPADs (right) also focus on free electrons, created by shorter wavelength photons, being the primary cause of avalanche.

3.4 Operation Principles of SPADs

As discussed, SPADs have three distinct operation modes based on in reverse bias voltage. Photodiode operation mode involves very low reverse bias voltage; in this case, there is no avalanche, and electron-hole pairs create a current proportional to the intensity of the impinging photons.

In avalanche mode, the voltage is increased to the point where free electrons from the electron-hole pair create additional electron-hole pairs through impact ionization. The resulting current is still proportional to incident photon intensity with a gain in the range of 100.

In Geiger mode, the bias voltage is increased beyond breakdown point, where both free electrons and holes contribute to avalanche due to very large electric field in the depletion region $\left(> 10^5 \frac{V}{cm}\right)$ **[47]**. The resulting current is no longer proportional to the original incident photon, and the avalanche cannot be self-quenched. Without quenching, the diode cannot detect subsequent photons.

The quenching is achieved via a high-ohm series resistor (R_q), which limits the current discharged by the diode during breakdown. **Figure 3.10** demonstrates the equivalent electrical circuit of a single SPAD and how quenching is performed. Absence of signal is analogous to the conceptual switch being open (**Figure 3.10-a**). In this case, the reverse bias voltage (V_{bias}) asymptotically charges the diode's capacitor (C_d) to V_{bias} through an RC circuit. That is, the initial voltage across the diode's capacitor and the quenching resistor (R_q) are V_{bias} and 0 respectively. As the diode's capacitor reaches equilibrium with the bias voltage, the voltage across the quenching resistor (R_q) as well as the current through the circuit exponentially decays.

$$V_{bias} = \frac{1}{C_d}\int_0^t i_q(\tau)d\tau + R_q i_q(t) \qquad \textbf{Eq. (3.1)}$$

$$\therefore \quad \begin{cases} v_d(t) = V_{bias}\left(1 - \frac{1}{e^{\frac{t}{\tau}}}\right) \\ i_q(t) = \frac{V_{bias}}{R_q}\left(\frac{1}{e^{\frac{t}{\tau}}}\right) \end{cases} \qquad \textbf{Eq. (3.2)}$$

where $\tau = R_q C_d$ is the time constant of the RC circuit. Production of an electron-hole in the depletion region through either thermal excitation or incident photon closes the conceptual switch. Once the switch is closed, the diode's capacitance begins to discharge through SPAD's serial resistance (R_s). In this case, the circuit involves two opposing current loops.

$$bottom\ loop: \quad V_{bias} - V_d = R_q i_q(t) \quad \therefore \quad i_q(t) = \frac{V_{bias} - V_d}{R_q} \qquad \textbf{Eq. (3.3)}$$

$$top\ loop: \quad V_d - V_{bd} = R_s i_s(t) \quad \therefore \quad i_s(t) = \frac{V_d - V_{bd}}{R_s} \qquad \textbf{Eq. (3.4)}$$

This means that the current through the diode's capacitor (I_d) is comprised of two opposing components: the bottom component which recharges C_d and the top component which discharges C_d. From Kirchhoff's junction rule, net I_d becomes:

$$I_d = i_q(t) - i_s(t) = \frac{V_{bias} - V_d}{R_q} - \frac{V_d - V_{bd}}{R_s} \qquad \textbf{Eq. (3.5)}$$

R_s is not constant and decreases in value during the avalanche, as the charge carrier multiplication in breakdown mode turns the diode into a conductor. The discharge prompts a surge in current flow through R_s, causing a voltage across diode's capacitance (V_d) to decay towards breakdown voltage (V_{bd}). Decline in V_d weakens the avalanche, which in turn increases R_s and decreases current across R_s. However, only when i_q is smaller than i_s can this process lead to quenching. Otherwise, the reverse bias voltage sustains a continuous avalanche. Therefore, R_s should be large enough so that i_q cannot sustain the discharge of C_d. Once the discharge is exhausted, the avalanche is quenched, and the conceptual switch reopens. This allows the reverse bias voltage V_{bias} to recharge V_d voltage from V_{bd} back to V_{bias}, recovering the diode for the next photon detection. The voltage recharge from V_{bd} to V_{bias} is known as the overvoltage (V_{ov}) **[46]**.

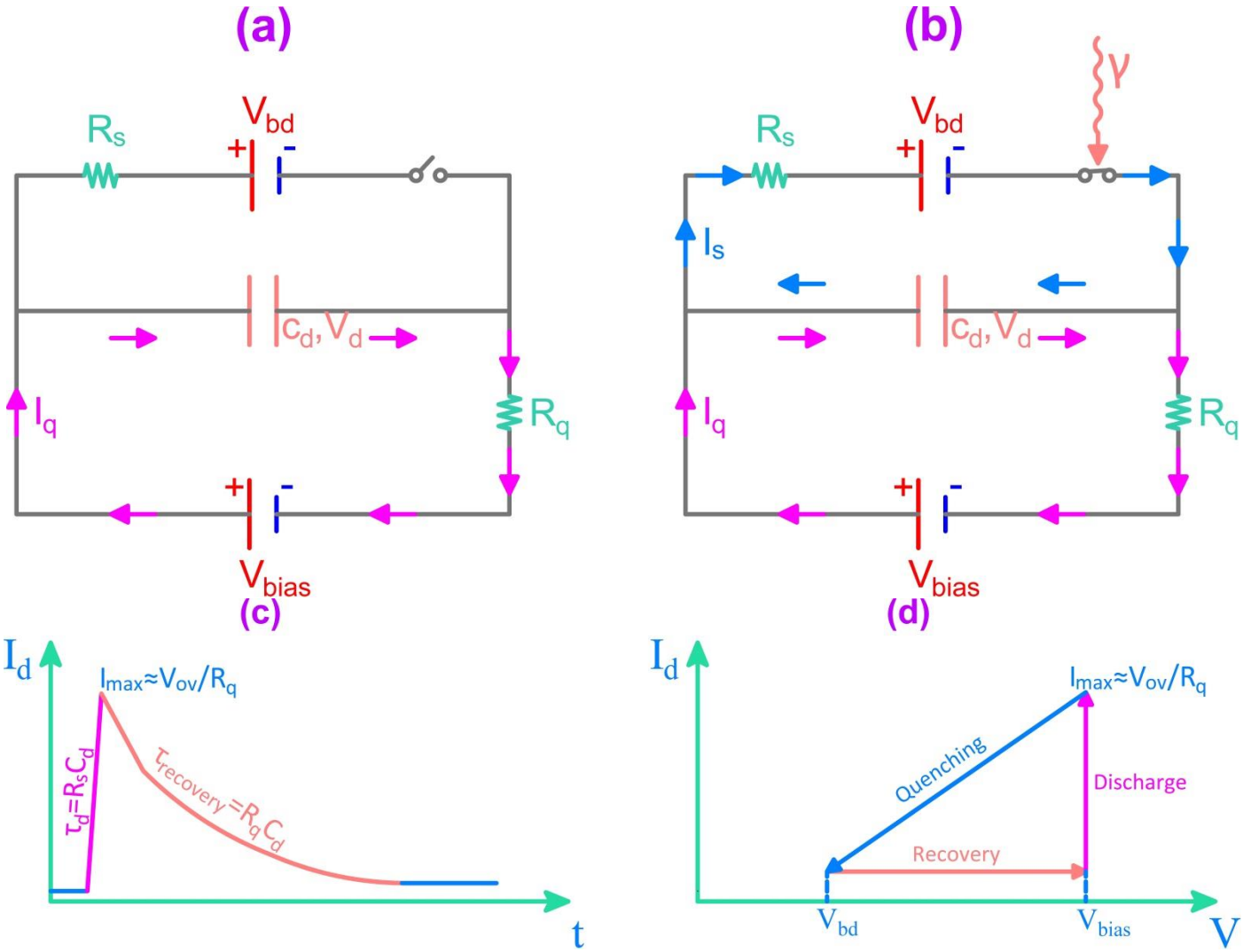

Figure 3.10 Equivalent circuit of a single SPAD in the absence of a signal (a) and when an electron-hole pair is created in the depletion region (b). The conceptual output pulse is demonstrated in (c) and (d).

C_d's discharge and recharge (recovery) time are characterized by time constants $\tau_d = R_s C_d$ and $\tau_{recovery} = R_q C_d$ respectively. Given the difference in values of R_s and R_q, the recovery time of the diode, during which time the SPAD is not operational, is much larger than the discharge time. In order to reduce the recovery time, the net capacitance of the diode can be reduced by introducing a smaller capacitor in series with C_d, as shown in **Figure 3.11**. The additional capacitor in the equivalent circuit translates to introducing an RC high-pass filter component in SPAD circuit. In this case, the discharge and recovery times of the SPAD become:

$$\tau_d = R_s \frac{1}{\frac{1}{C_d} + \frac{1}{C_q}} \qquad \textbf{Eq. (3.6)}$$

$$\tau_{recovery} = R_q \frac{1}{\frac{1}{C_d} + \frac{1}{C_q}} \qquad \textbf{Eq. (3.7)}$$

In other words, both discharge and recovery times are decreased, albeit at the expense of reduced gain (gain is proportional to diode's capacitance). This is beneficial for situations where photon detection requires a very high timing resolution such as Cherenkov radiators. The difference in response time is demonstrated in **Figure 3.11** for a 3x3mm Hamamatsu SPAD **[46]**.

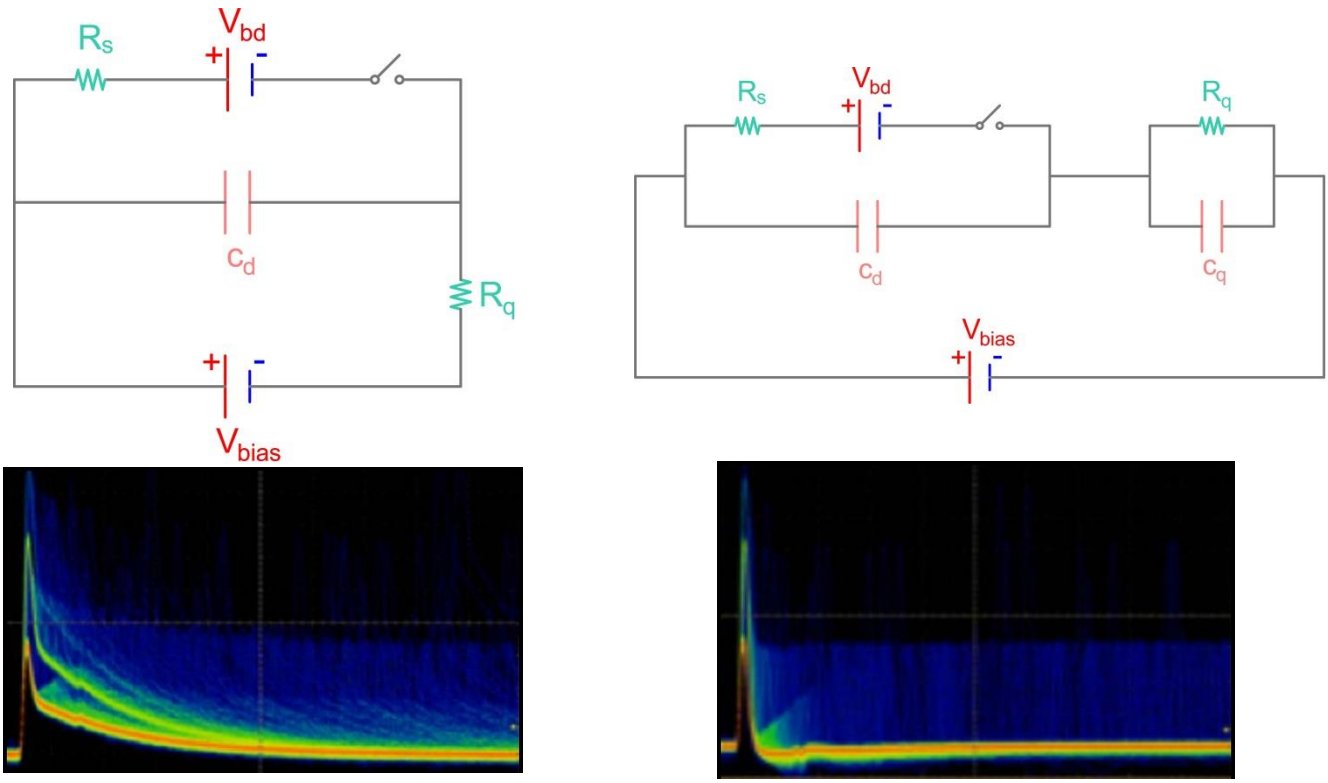

Figure 3.11 The effect of decreasing net capacitance of the diode on its discharge and recovery time. Equivalent circuit of a SPAD with (right) and without (left) an additional serial capacitance. The corresponding output signals over time **[46]** are shown under each circuit.

3.5 SiPM Structure

As mentioned previously, SPADs are single photon detectors. Their high gain (10^5-10^6) and low voltage requirements compared to PhotoMultiplier Tubes (PMT) makes them attractive candidates for low light applications. Other advantages of SPADs include linear dependence of gain on diode capacitance compared to power relation in PMTs, insensitivity to external magnetic field, and higher signal-to-noise ratio **[45]**.

However, a single SPAD cannot detect more than a single photon, has a non-linear response, and is non-operational during its recovery time. To overcome these shortcomings, a matrix of SPADs, known as pixels or microcells, are connected in parallel and placed in a monolithic silicon crystal. This arrangement is known as Silicon PhotoMultiplier (SiPM) or Multi-Pixel Photon Counter (MPPC).

Each microcell houses its own quenching resistor, as shown in **Figure 3.12**, and shares the same cathode and reverse bias voltage with other microcells. The quenching resistors are commonly made from poly-silicon or thin metal film **[48]** and, along with bias metal grid, constitute the optically dead area. The fill factor of a typical SiPM is between 20 and 80%, depending on microcell size (also known as cell pitch), which varies between 10 µm and 100 µm. The number of microcells connected in parallel in a single SiPM channel ranges from several hundreds to several tens of thousands, which yields an active area of 1 mm^2 to 6 mm^2 per channel **[46]**. The optical area is coated with thermally grown silicon dioxide (SiO_2) and silicon nitride (SiN_x), which acts as anti-reflective coating (ARC) **[49]**. Each microcell is optically isolated from others using trenches as shown in **Figure 3.12** to minimize cross talk.

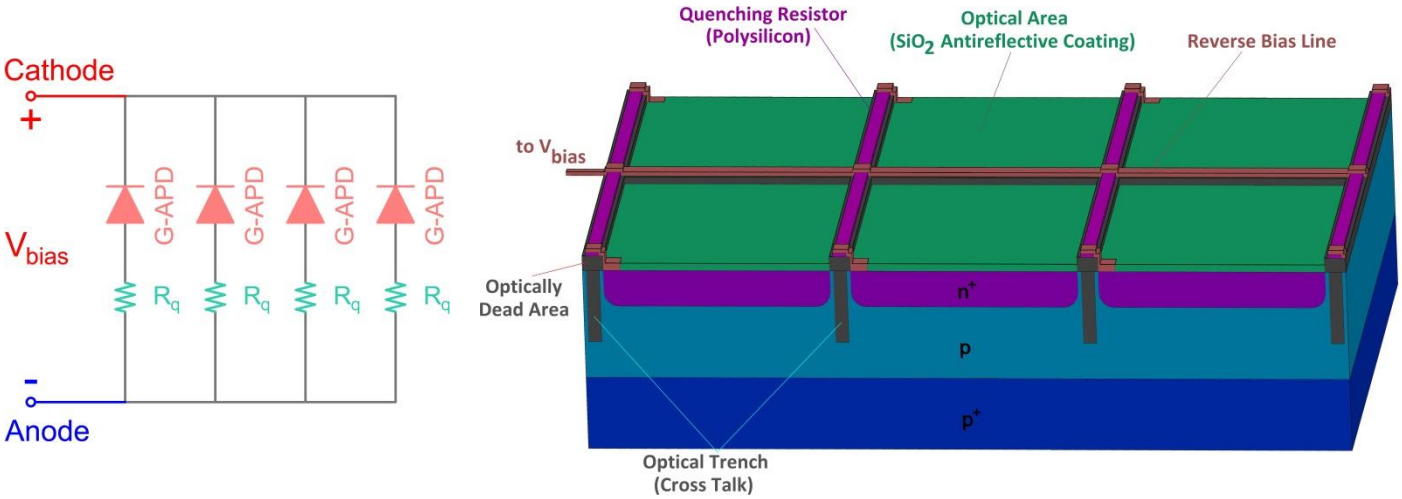

Figure 3.12 SPAD parallel connections in an N-on-P SiPM. Electrical diagram is shown on the left, and geometric structure is shown on the right.

Each microcell acts independently of other microcells. That is, when a microcell receives a photon, it creates a signal and goes into recovery. At the same time, all other microcells in the SiPM channel are reverse biased and ready to receive signal. The overall signal amplitude of an SiPM channel, therefore, is proportional to the number of microcells that receive photons. For instance, when an SiPM channel with 400 SPADs receives three photons (**Figure 3.13**), the signal amplitude is proportional to three photo-electron or "pe" signals.

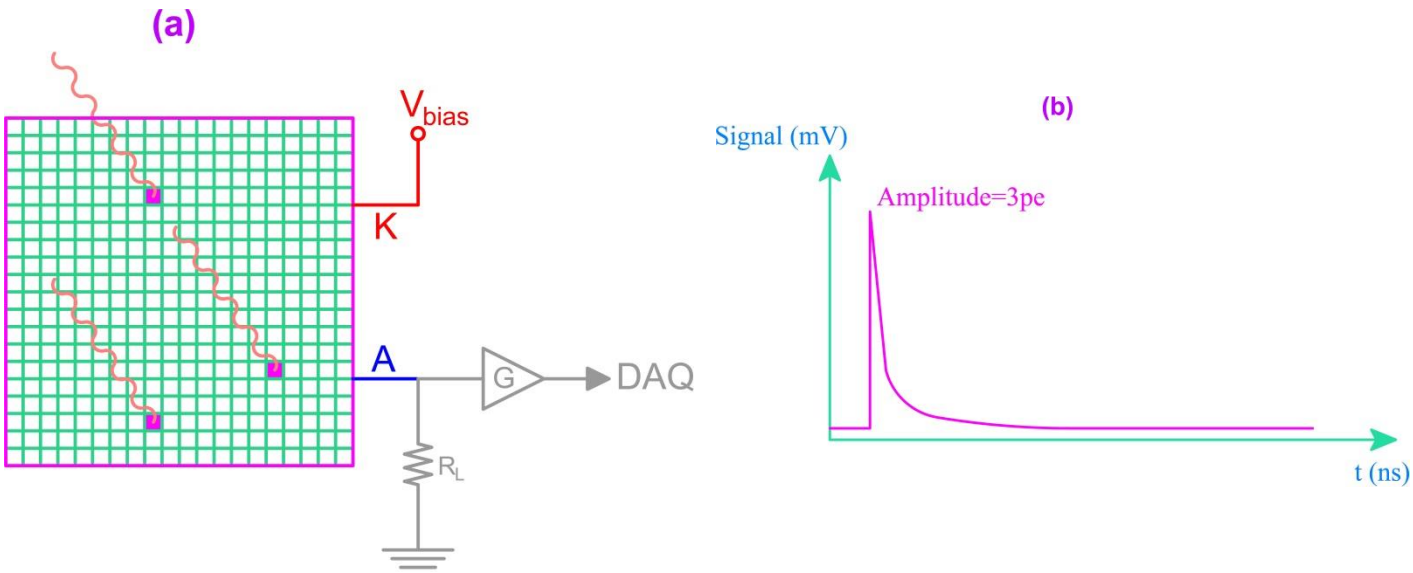

Figure 3.13 A 400-pixel SiPM channel with common cathode and output anode. The signal amplitude is proportional to the number of photons received by individual microcells. In this particular SiPM, signal travels from anode to an amplifier and eventually to the data acquisition system (DAQ). Adapted from **[50]**.

3.6 SiPM Characteristics

3.6.1 Breakdown

Breakdown is the reverse bias voltage above which SiPM operates in Geiger mode as shown in **Figure 3.8**. At breakdown, the gain is negligible, and the amount of additional voltage above breakdown determines the performance of the SiPM in terms of gain, detection efficiency, dark count, and crosstalk probability. Breakdown voltage has a linear relation with temperature **[46] [51]**.

$$V_{br} = A \cdot T + C \qquad \textbf{Eq. (3.8)}$$

where A is the temperature coefficient, T is the real-time temperature of the SiPM, and C is the breakdown voltage at 0 °C. For S13361-3075AS Hamamatsu SiPM, A and C are $54\ \frac{mV}{^\circ C}$ and $51.51\ V$ respectively **[46]**.

3.6.2 Gain

The number of impact ionizations during an avalanche determines the gain of an SiPM. Gain is defined as the ratio of total amount of charge collected at the terminal of the microcell (Q) over elementary charge

(e). Q can be approximated as $I_{max}\tau_{recovery}$ as shown in **Figure 3.10-c**. further, I_{max} and $\tau_{recovery}$ can be approximated as $\frac{V_{ov}}{R_q+R_s}$ and R_qC_d respectively **[46]**. Given that $R_q \gg R_s$:

$$G = \frac{Q}{e} \cong \frac{I_{max}\tau_{recovery}}{e} \cong \frac{1}{e} \cdot \frac{R_q}{R_q + R_s} V_{ov}C_d \cong \frac{1}{e} \cdot V_{ov}C_d \qquad \textbf{Eq. (3.9)}$$

Therefore, gain depends on pixel capacitance and overvoltage as shown in **Figure 3.14**. Pixel capacitance depends on the size of microcells and is constant. Overvoltage changes with temperature, as breakdown voltage increases with the increase of temperature. In order to maintain a constant gain, the bias voltage must be adjusted to ensure that the overvoltage is constant. When the bias voltage is fixed, the gain decreases with the increase of temperature. The gain of SiPMs is in the range of 10^5 to 10^6.

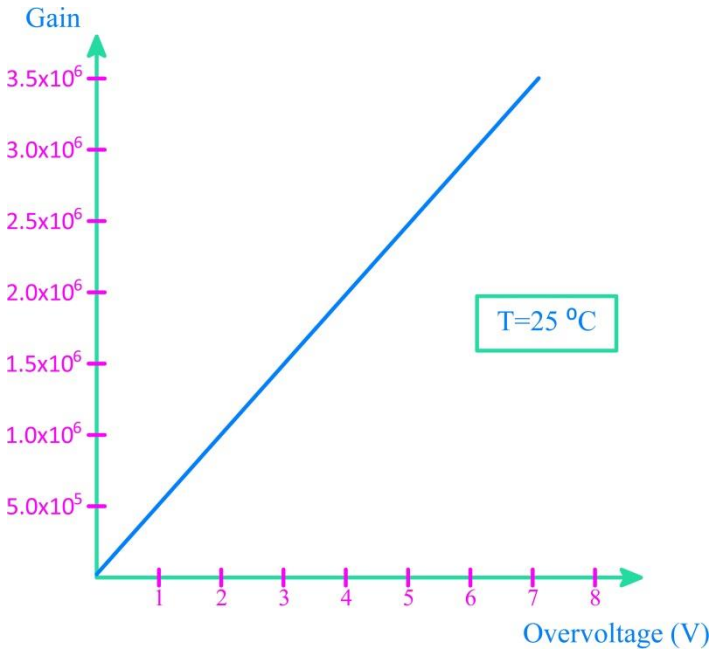

Figure 3.14 Relation between gain and overvoltage at T=25 °C for S13361-3075AS Hamamatsu SiPM **[46]**.

3.6.3 Photon Detection Efficiency (PDE)

PDE is defined as the probability that an SiPM produces an output signal in response to an incident photon. It is dependent on incident photon wavelength, over-voltage, and fill factor of the SiPM **[51]**.

$$PDE = f\eta_{QE}P_G \qquad \textbf{Eq. (3.10)}$$

where f is the geometric fill factor, η_{QE} is quantum efficiency, and P_G is the probability of Geiger discharge.

The geometric fill factor refers to the percentage of photosensitive area of a microcell compared to its entire area. Microcells with larger sizes (larger pixel pitch) have higher fill factors, and therefore larger PDEs. Quantum efficiency is the probability that an incident photon creates an electron-hole pair in a specific part of the depletion layer, where electric field forces the carriers to cross the junction and create an avalanche. As discussed before, N-on-P and P-on-N SPADs are designed to detect longer wavelength and shorter wavelength photons respectively. Therefore, quantum efficiency is highly dependent on incident photon wavelength. η_{QE} also increases with temperature, as increased phonon vibrations makes more conduction electrons and valence holes available for avalanche. These newly release carriers contribute to both photo-signal and dark signal.

The probability of a Geiger discharge depends on the overvoltage. At reverse bias voltages above breakdown, the electric field in the depletion region, width of the avalanche region, and ionization energy of the charged carriers increase with overvoltage, rising the probability of Geiger avalanche. However, increased overvoltage also increases dark count rate and cross talk probability. Temperature rise decreases Geiger avalanche probability, countering its positive effect on quantum efficiency. The overall effect of temperature on PDE depends on which of the two factors is dominant at any temperature. **Figure 3.15** shows the dependence of PDE on overvoltage and incident photon wavelength.

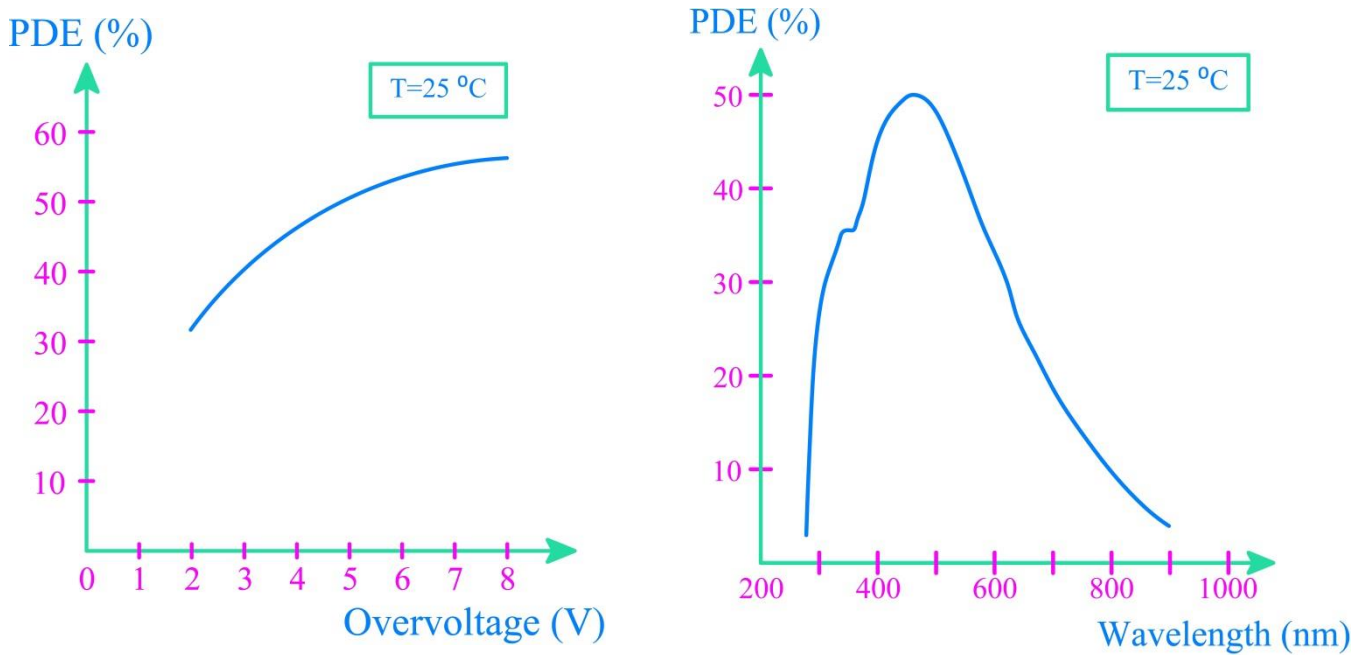

Figure 3.15 Relation between PDE and overvoltage (Left) and incident photon wavelength (Right) for S13361-3075AS Hamamatsu SiPM **[46]**. Both graphs show the relation at T=25 °C.

3.6.4 Dark Count Rate (DCR)

Dark count is considered noise, as it is not related to a photo-signal. The dark count rate increases with overvoltage as discussed. Dark count rate also increases with temperature since phonon vibrations rise

with temperature. For low light detection, it is imperative to keep the temperature as low as possible in order to trigger the SPADs at 1 photoelectron signal amplitude level. Dark count is reduced by roughly half for every 10 °C decrease in temperature. Increasing the discriminator level by 1 pe reduces dark count by one order of magnitude **[46]**. Discriminator is a programmable feature of data acquisition that allows signal collection at amplitudes above a specific pe level. **Figure 3.16** demonstrates the dependencies of DCR on overvoltage, temperature, and discriminator level for a Hamamatsu SiPM.

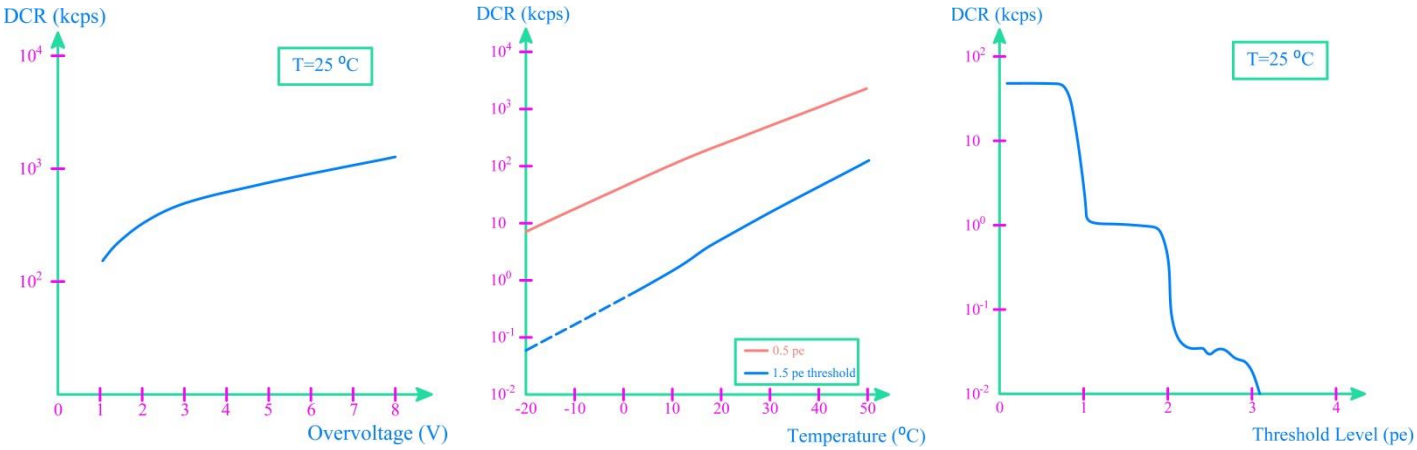

Figure 3.16 Dark count rate relation with overvoltage, temperature, and discriminator level for S13361-3075AS Hamamatsu SiPM **[46]**.

3.6.5 Afterpulse

Afterpulse is another type of noise prevalent in SiPMs and PMTs **[11]**. In SiPMs they are produced when part of the avalanching carriers are trapped in impurity atom's energy levels and are released after a delay, creating a subsequent avalanche. If the delay time is smaller than the triggered SPAD's recovery time, the signal from the afterpulse will have an amplitude smaller than 1 pe. However, if the carriers are released after the recovery, the afterpulse signal will be indistinguishable from a full 1 pe signal amplitude. In the case of the former, a pulse-height analysis is needed to remove afterpulse background from the signal, whereas the latter cannot be excluded in cases where the rate of incoming photons is unknown. **Figure 3.17** demonstrates the afterpulse in a Hamamatsu SiPM **[46]**. Afterpulse increases with higher overvoltage values.

3.6.6 Optical Crosstalk

Avalanche carriers may undergo three distinct processes in the depletion layer. These processes, in order of likelihood, are impact ionization, elastic scattering collision, and photon emission. Impact ionization is

the only process that leads to avalanche. Elastic scattering brings about energy loss in the form of heat due to increased phonon vibration. The least likely process is when charge carriers lose their energy in the form photon emission. This phenomenon was first observed in 1955 in General Electric Research Laboratory, where a reverse biased silicon p-n junction emitted weak yellow light **[52]**. Hot carrier relaxation in SPADs prompts photon emission in a broad spectrum. However, the physics mechanism behind the emission is still a debated issue **[53]**. The emitted photon may travel to an adjacent pixel and trigger an avalanche process, creating a signal known as optical crosstalk.

Crosstalk can be classified into two types (**Figure 3.18**): prompt crosstalk and delayed crosstalk. In case of the former, the photon creates an electron-hole pair within the depletion region of a neighboring pixel. The carrier pair triggers an avalanche and creates a pe signal identical to the original pixel almost simultaneously. The latter occurs when the photon creates charge carriers outside the depletion region of the neighboring cell. In this case, avalanche only occurs if the charge carriers successfully diffuse to the depletion region and avoid recombination. The diffusion introduces a delay in order of tens of nanoseconds **[46]** between the secondary crosstalk signal and the original, genuine signal. Prompt crosstalk cannot be excluded from genuine signal, whereas delayed crosstalk can be discriminated against using time-delay filtering algorithms.

The intensity of crosstalk increases when the distance between adjacent pixels are reduced, which limits the matrix density of an SiPM channel **[54]**. Crosstalk can occur for both dark and photo-signals (**Figure 3.19**). Introducing optical trenches, as shown in **Figure 3.12**, between individual pixels can reduce crosstalk but not eliminate it. Increasing overvoltage amplifies crosstalk probability. Hence, crosstalk is the primary source of noise in SiPMs and the most important inhibiting factor for overvoltage.

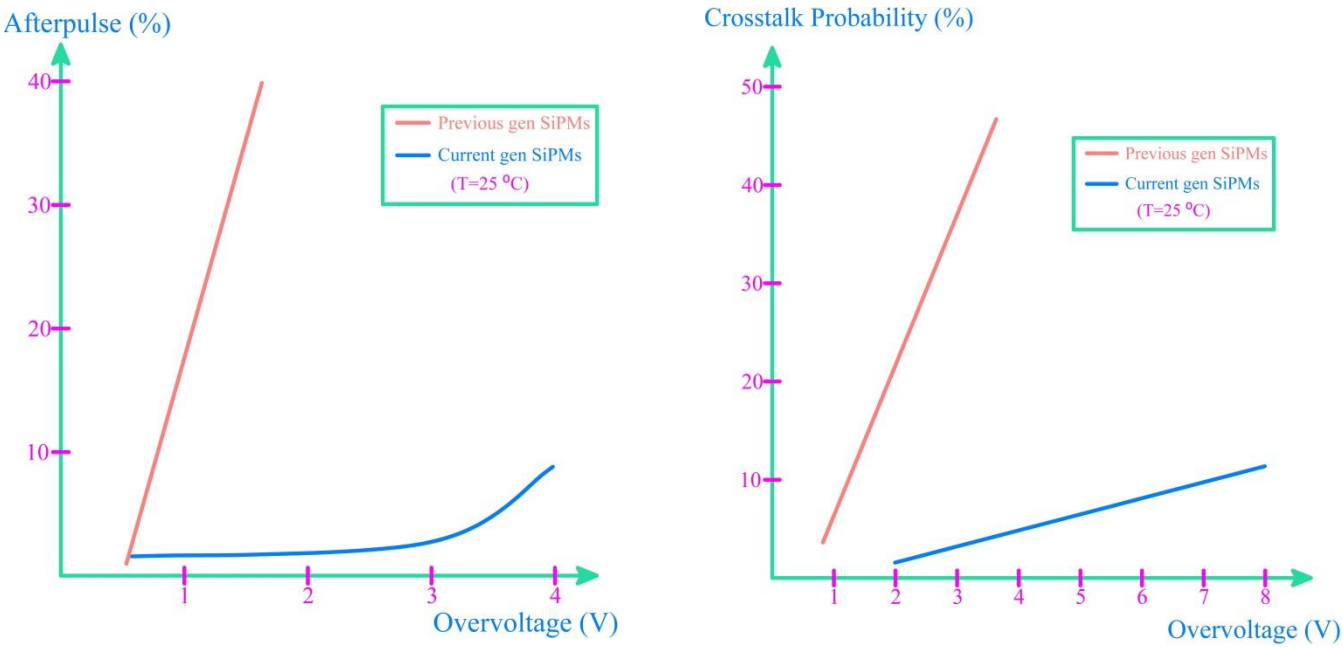

Figure 3.17 Change in afterpulse (left) and cross talk (right) with increase in overvoltage. The new generation of SiPMs are less dependent on overvoltage. Adapted from **[46]**.

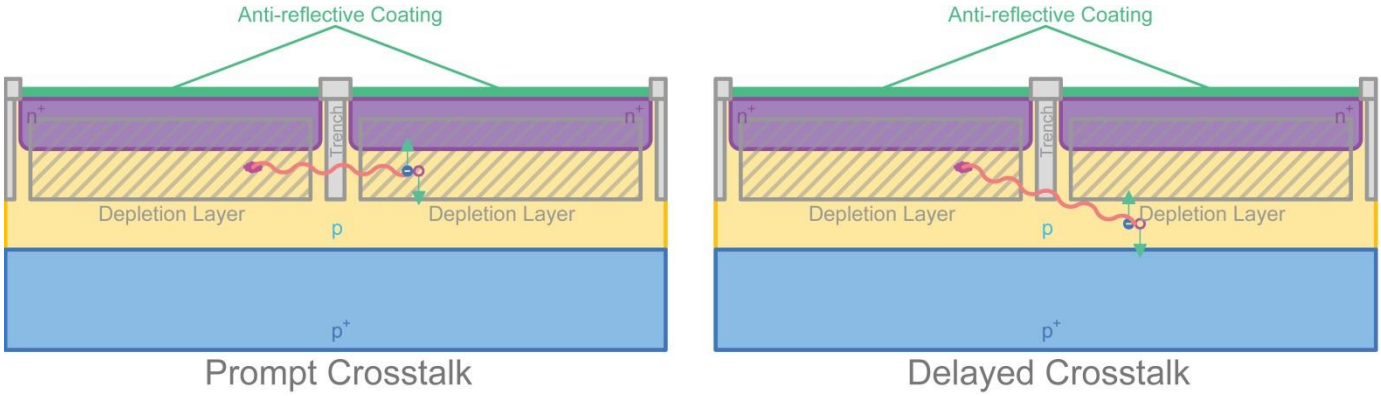

Figure 3.18 Prompt and delayed cross talk.

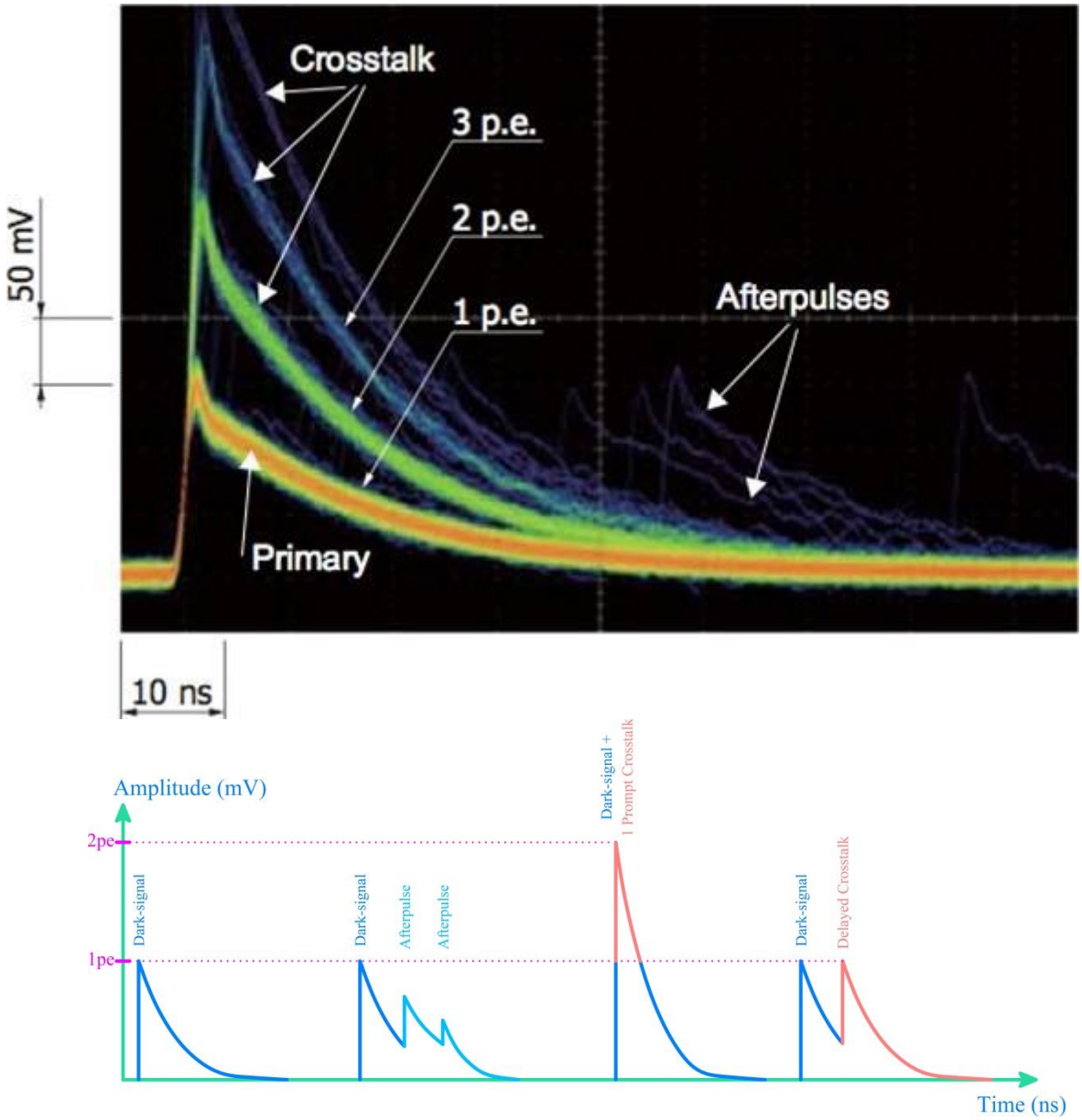

Figure 3.19 Output wave form of a 1pe dark signal with cross talk and afterpulse when the SiPM channel is in complete darkness. The density of the lines represents the frequency of occurance of each signal. In the absence of cross talk, the signal will be only dark 1pe waves. When a prompt cross talk occurs, the signal height is changed to 2pe. Additional cross talks create waveforms with 3pe, 4pe, etc. amplitudes. All waves that are not 1 pe are due to cross talk and afterpulse. The delayed afterpulses have lower amplitudes, as they occur during recovery time of the pixels.

4. Design and Development

4.1 Outline

In order to detect the Cherenkov photons and associate them with electrons of a specific energy, an electron beam with either a single energy or a small energy band is required. That is, energy and directional information of electrons can only be deduced from the Cherenkov photons when the incident beam does not have a wide spectrum. To that end, we designed a setup that bends electron beams from ^{90}Sr beta decay in a magnetic field and only captures specific energies with an acceptable resolution. The overall setup is shown in **Figure 1.5**.

The electrons produced from β^- decay of ^{90}Sr and its daughter nucleus ^{90}Y travel through a mu-metal until they reach the homogeneous magnetic field of an electromagnet. The electrons then travel through another mu-metal conduit until they reach a collimator, which narrows the beam's energy further. The beam that exits the collimator contains a narrow band of energy around a single intended energy. The filtered beam enters a PMMA radiator, where it produces Cherenkov light, which will be captured and counted by a 64-channel SiPM. The mu-metals ensure the electrons are not exposed to stray magnetic fields outside the homogeneous section of the magnet. In order to minimize interaction between electrons and air, the entire setup until the PMMA must operate in vacuum. A device must be designed to adjust the location and angle of the source with respect to the setup for different energies.

The SIPM modules must be kept at subzero temperatures during operation in order to minimize thermally induced photoelectrons as discussed in Chapter 3. The readout system is comprised of an ASIC (Application Specific Integrated Circuit) for coincidence detection, and an FPGA (Field Programmable Gate Array) for reference clock, logic functions, and communication to the computer. The design and implementation of each component is discussed in this chapter.

4.2 Electromagnet

4.2.1 Coil Winding and Geometry

As discussed in Section 2.3, the electromagnet needs to provide at least 65mT field. For safety purposes, we limited the current to a maximum of 5A. Calculations from Section 2.3 revealed that this translates to 217 windings for an H-magnet with an ST52-3 steel iron yoke ($\mu_{iron} \cong 1.26 \times 10^{-3}$). To be on the safe side, 234 windings were used with ϕ1.5mm enamelled copper wire. This, in theory, should produce 70.04mT in the gap under 5A constant current load. We will investigate how closely the measured field resembles the theory.

Orthocyclic winding method with equal turns at each layer is chosen for coil winding, as it provides an optimal fill factor (~91%) for round wires **[55]**. In addition, each layer provides grooves for the next layer, creating a self-guiding wire feed during the winding. **Figure 4.**1 demonstrates orthocyclic winding schematics. The self-guiding ability of the wire, however, requires that the wire guide makes a step with the size of the wire's diameter at the end of each layer. The coil winding were performed in the mechanical workshop at ENC Campus, University of Siegen under the supervision of the director of the workshop, Uwe Krüger. The mounting and rotary device for the winding are depicted in **Figure 4.2**. The end product is shown in **Figure 4.3**.

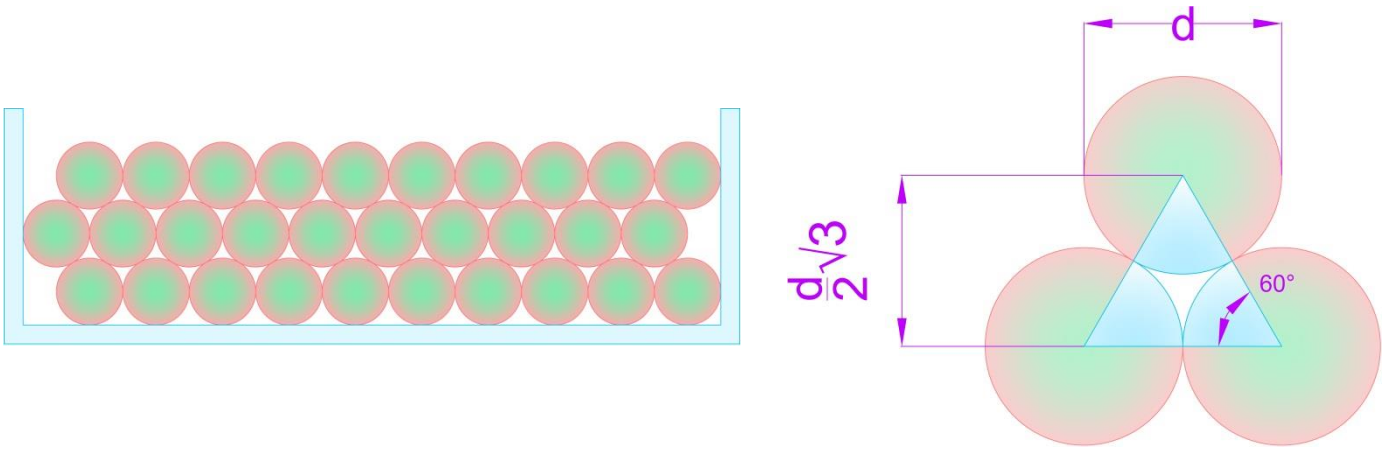

Figure 4.1 Orthocyclic winding is the most space-filling method for round wires. Adapted from **[55]**.

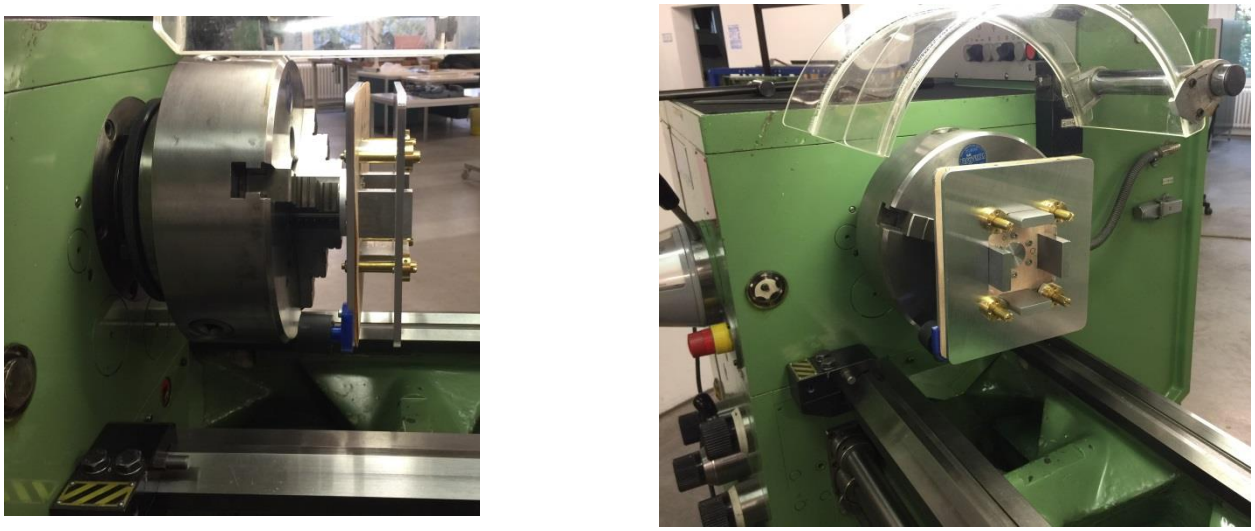

Figure 4.2 The coil frame mounted on winding spindle of a winding machine. The winding frame along with wire guide (not shown in the figure) ensures orthocyclic winding.

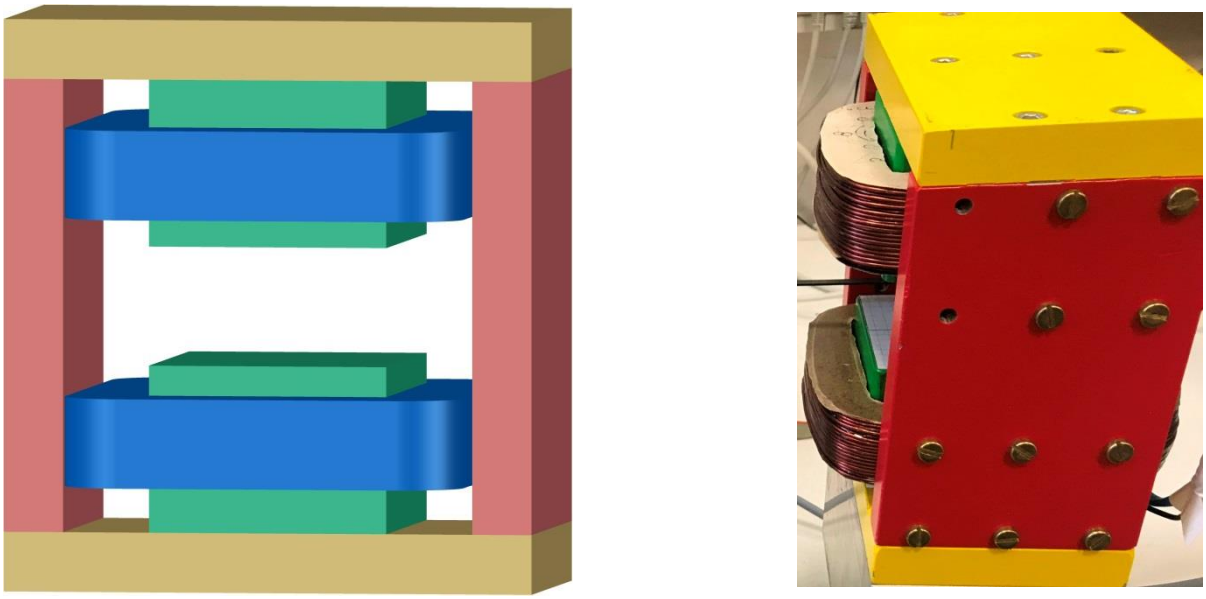

Figure 4.3 Electromagnet: Design (Left) and end product (Right)

4.2.2 Electromagnet Calibration

In order to produce different fields with the magnet, power requirements of the magnet must be known. To that end, the following setup is used to calibrate the magnet. A Rohde & Schwarz NGP824 provides constant current power to each coil in the magnet. The magnetic field is measured at various locations inside the gap using a PHYWE teslameter. The output of the teslameter (voltage signal) is read by a PeakTech 4360 digital multimeter and sent to a PC where the data is read and stored via LabVIEW. The Schematics of the calibration setup is shown in **Figure 4.4**.

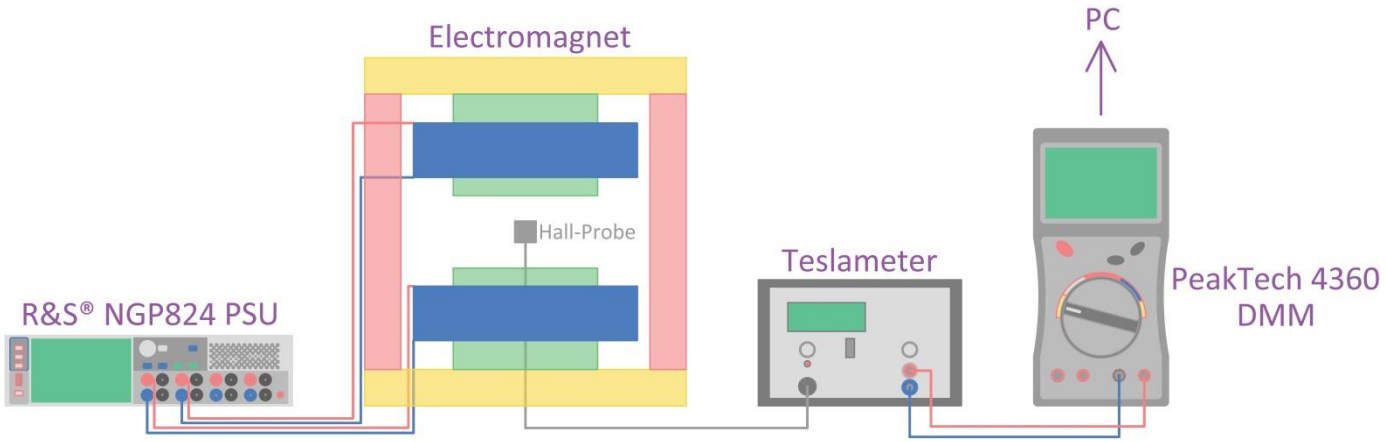

Figure 4.4 Schematics of the calibration setup

4.2.2.1 Multimeter Calibration:

The resolution and accuracy of the multimeter is tested via direct voltage signals from the power supply. The signal was increased with the increment of 1mV (resolution of the power supply), and perfect coordination was observed in the multimeter.

4.2.2.2 Multimeter vs. Teslameter Calibration:

In order to properly quantify the output of the multimeter, it has to be calibrated against the teslameter output shown on its display.

First, the coils in the electromagnet are attached to two separate channels of the power supply. The tangential Hall probe is placed at the center of the gap (0,0,0), and the power delivered to both channels are increased gradually in a constant current regime. Current at both channels are kept identical during each measurement and are increased by 0.1 A for each increment from 0A to 4.9A. At each step, the output of the teslameter and multimeter are stored. Using linear least-square method, a fit was applied to the multimeter output as a function of teslameter output from the dataset. The fit results indicate a relation described in **Equation 4.1**.

$$B(mT) = 0.1005(\pm 10^{-4}) \times M(mV) + 0.03402(\pm 0.04328) \qquad \textbf{Eq. (4.1)}$$

The fit results are then linearly refitted to $T = \alpha I$ to determine the power setting for each field. The second fit yielded the relation shown in **Equation 4.2**. The results are shown in **Figure 4.5**.

$$B(mT) = 13.4258(\pm 0.0587) \times I(A) \qquad \textbf{Eq. (4.2)}$$

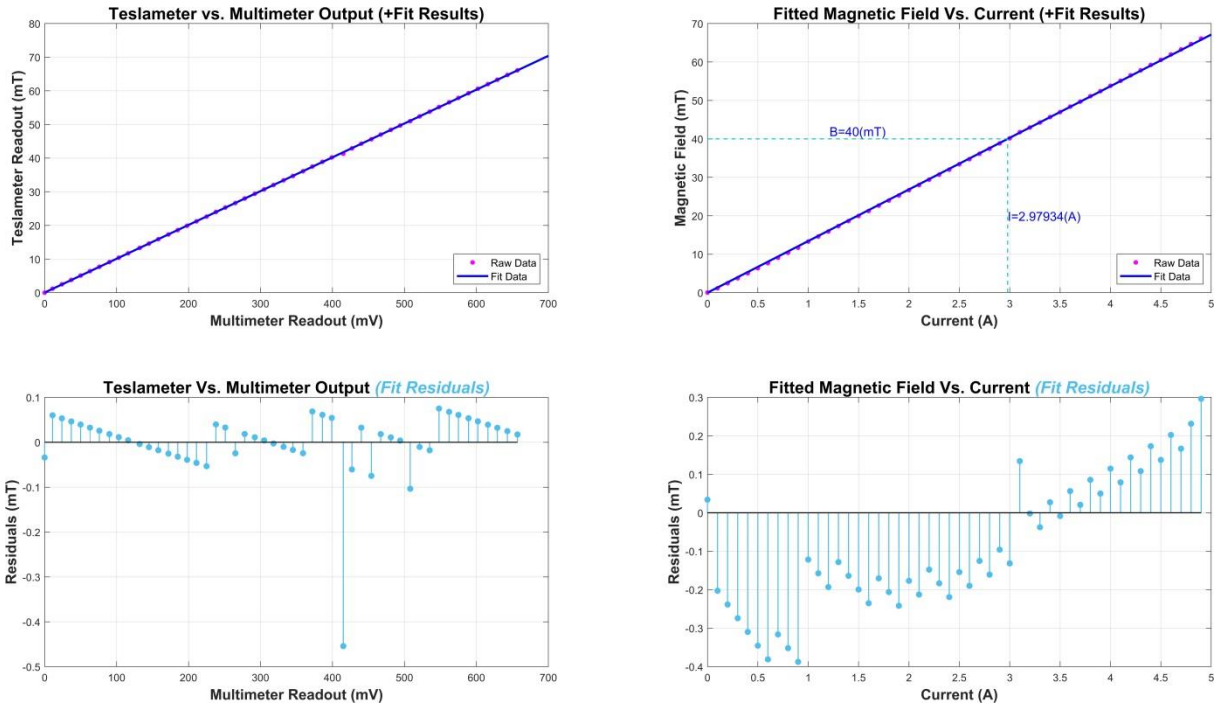

Figure 4.5 Left: Calibration of teslameter against multimeter. Right: Fitted magnetic field vs. current. Residuals of each fit function are shown below the graphs.

In addition, the voltage and current of each coil are logged during each measurement in order to find a fit function which represents the V-I relation between the two. The fit yielded resistance values of 1.2577(±0.0044)Ω and 1.3175(±0.0027)Ω for the coils. It was assumed that resistance remains constant during a potential difference of up to 8 V and a current of up to 5 A. That is, we assumed that a temperature increase in this particular span of voltage and current does not affect resistance. The experiment was run three times to investigate any discrepancy. **Figure 4.6** demonstrates the V-I relation for both coils. **Figure 4.7** shows resistance variations during measurement.

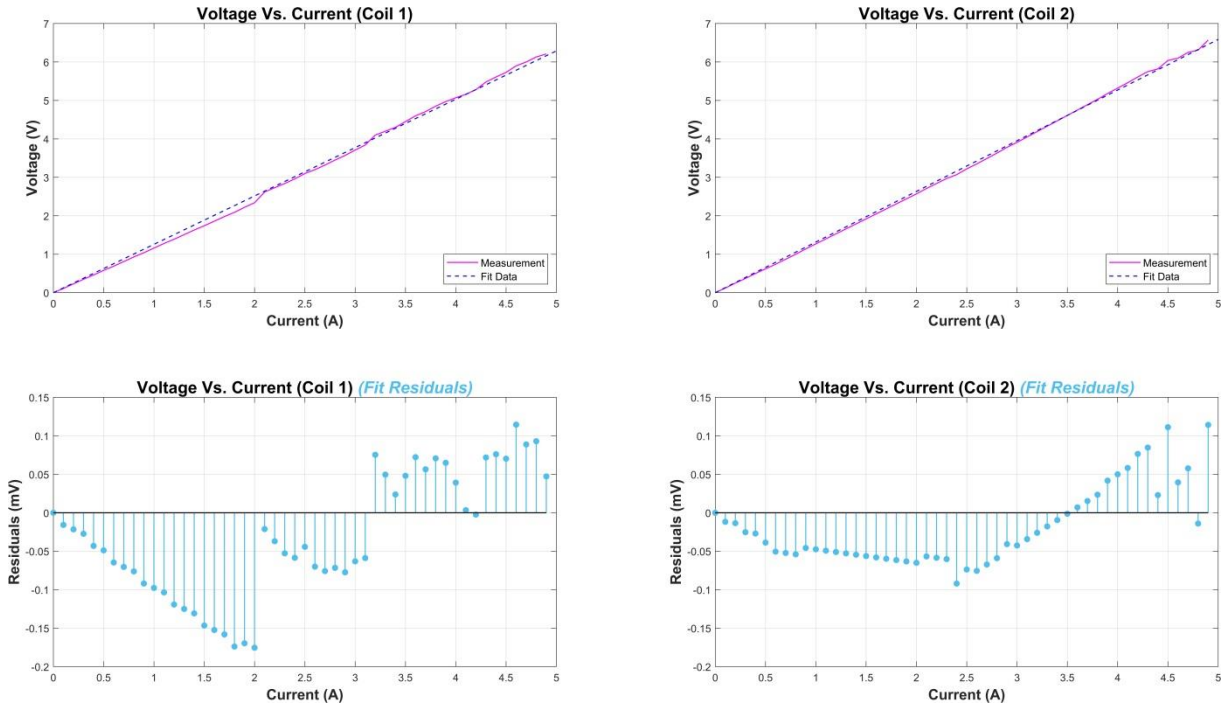

Figure 4.6 Voltage vs. Current for Channels 1 (Left) and 2 (Right) of the power supply.

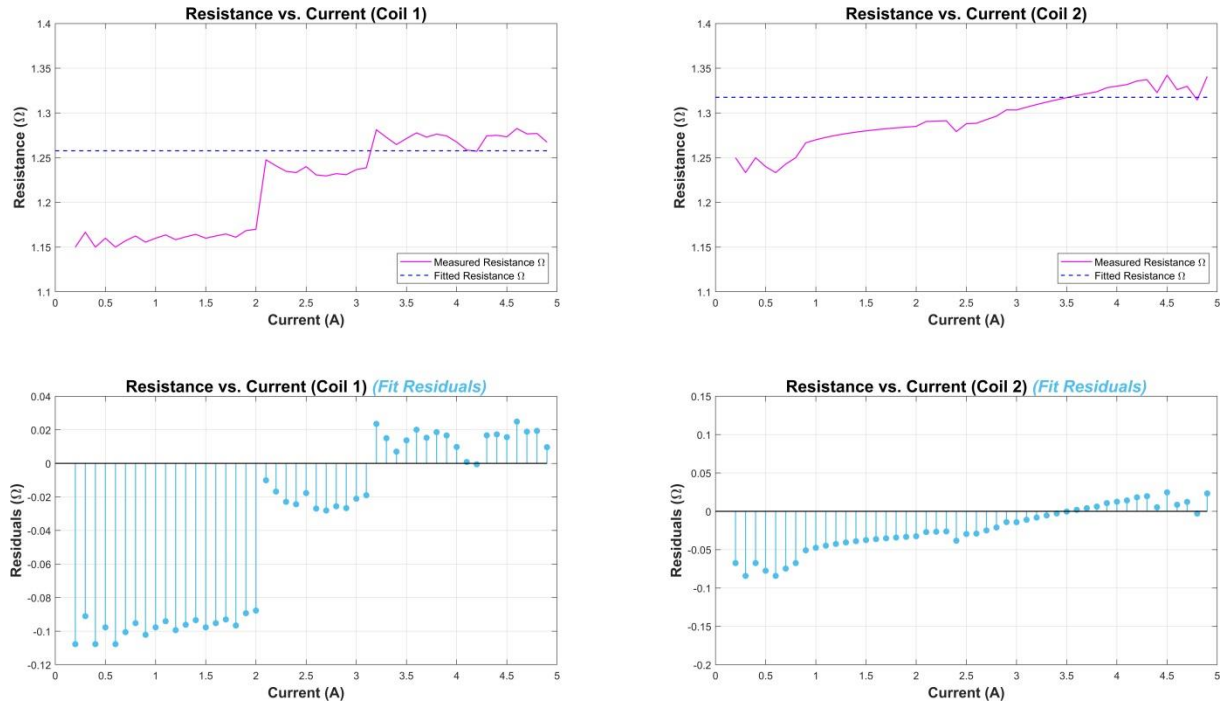

Figure 4.7 Resistance vs. Current for Channels 1 (Left) and 2 (Right) of the power supply.

Voltage and resistance deviations at certain currents are more pronounced in coil 1 (bottom coil), creating uncertainties in the readout. This is due to the fact that there was a complication in the coil winding of the coil, for which additional wire had to be soldered to make both coils identical in number of windings. This manifested itself in the form fluctuations in voltage at certain currents for the bottom coil (Channel 1). Nevertheless, given that current was kept constant, fluctuations did not carry over to the magnetic field output readout. Indeed at any given current (even with voltage fluctuations), we observed a solid

unchanging value at both Teslameter and Multimeter. Therefore, we decided to ignore the error and proceed with the experiment. Nevertheless, it is imperative that the bottom coil is rewound for future use, as the voltage fluctuations are pronounced and erratic.

4.2.3 Magnetic Profile

So far, we have assumed that all B-fields in the gap of the H-magnet are transverse, i.e., no planar B-filed is present. This assumption is true only at the center of long magnets. Another assumption is that the transverse field is constant across the gap and drops to zero at the edge of the gap. This is known as hard-edge approximation. In reality, planar B-fields are present at the edges, and the magnitude of the transverse field diminishes at fringes. The remedy is usually introducing an effective length at which the field is assumed constant as shown in **Figure 4.8 [56]**.

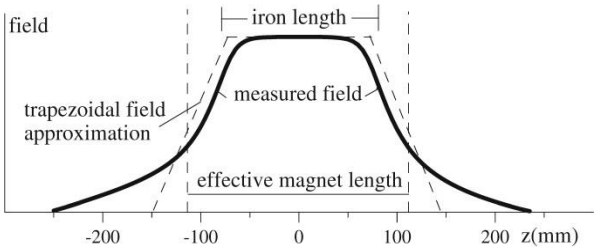

Figure 4.8 Hard-edge approximation with the introduced effective magnetic length for a quadrupole magnet. The area under the solid black curve and the area under the dashed trapezoid are identical **[56]**.

Given the required precision of the experiment, using an effective field is not tenable. In order to find a feasible method, the transverse B-field profile needs to be determined. To that end, the following procedure was implemented.

Three separate elevations (z=0, z=+5mm, & z=+10mm) are examined as shown in **Figure 4.9**. For each level, the tangential Hall-probe of the teslameter is mounted on a 3-axis, programmable step motor, which is programmed to follow the paths shown in **Figure 4.10** at 1000 steps per second using PASCAL and C. Each step translates to 0.13 μm. The step motor sweeps the region covering a quarter of the magnetic gap shown in **Figure 4.9**. Due to symmetry, it is assumed that the field is identical in the remaining quarters. The power supply is set to 5A constant current, and the multimeter reads the field every 5 seconds. Therefore, given the frequency, there are 3 or more readings per each millimeter. The test bench is shown in **Figure 4.11**.

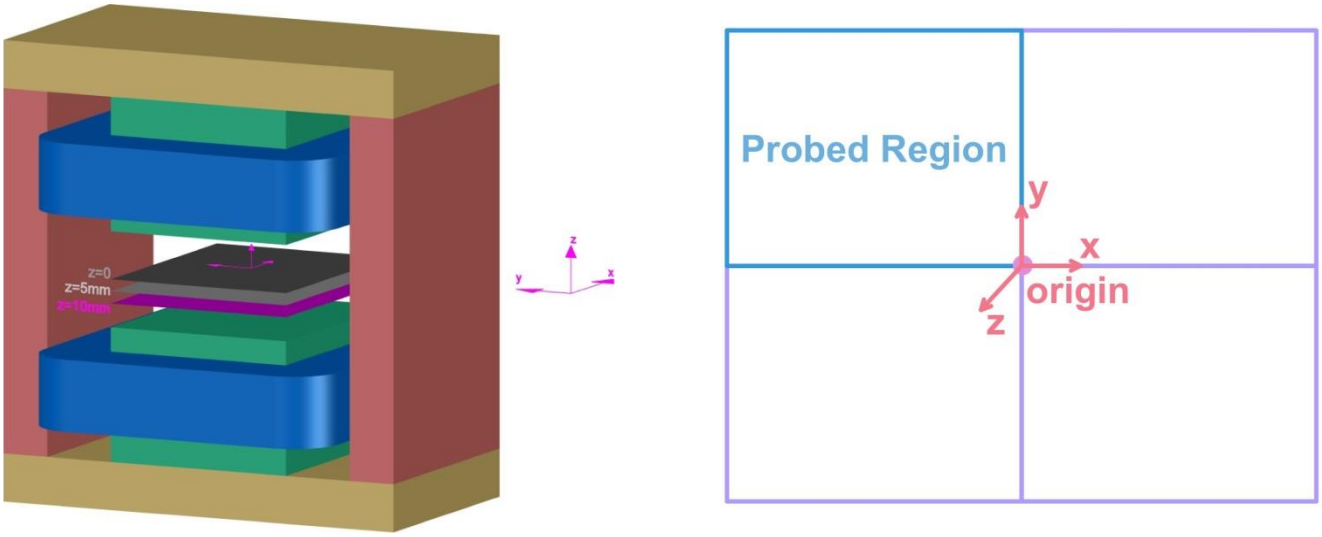

Figure 4.9 Left: The Hall probe sweeps three separate planes with elevations 0, 5mm, and 10mm. Right: The region probed by the teslameter is shown in blue. The magnetic field is assumed symmetric, and the remaining regions are estimated accordingly.

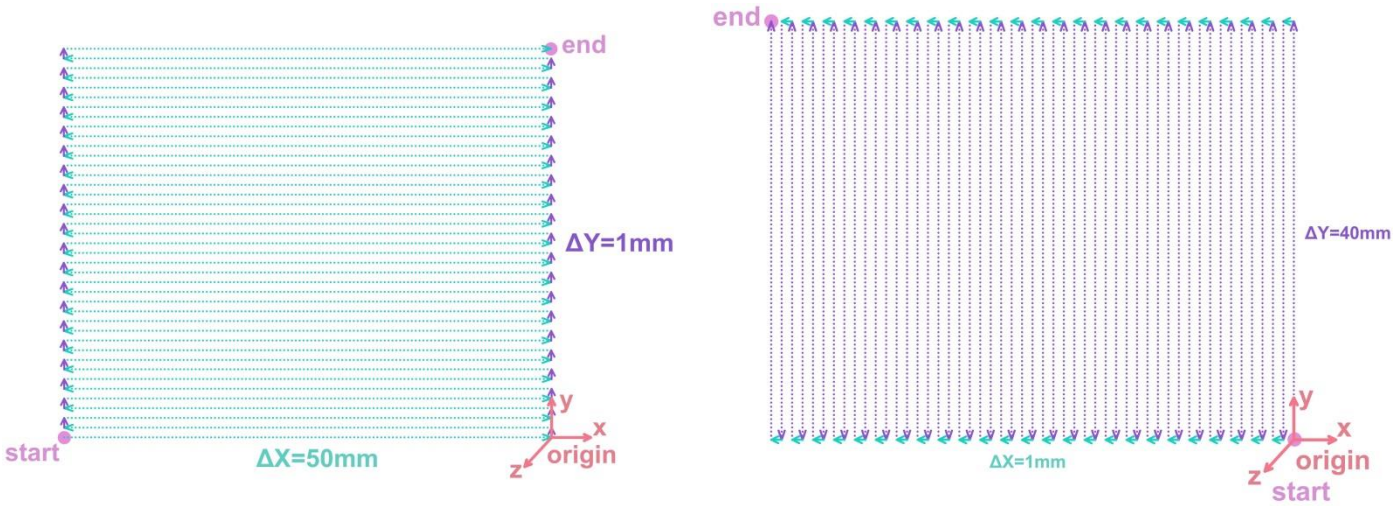

Figure 4.10 The step motor sweeps throught a quarter of the gap in the sequance shown for three separate elevations to determine the magnetic profile.

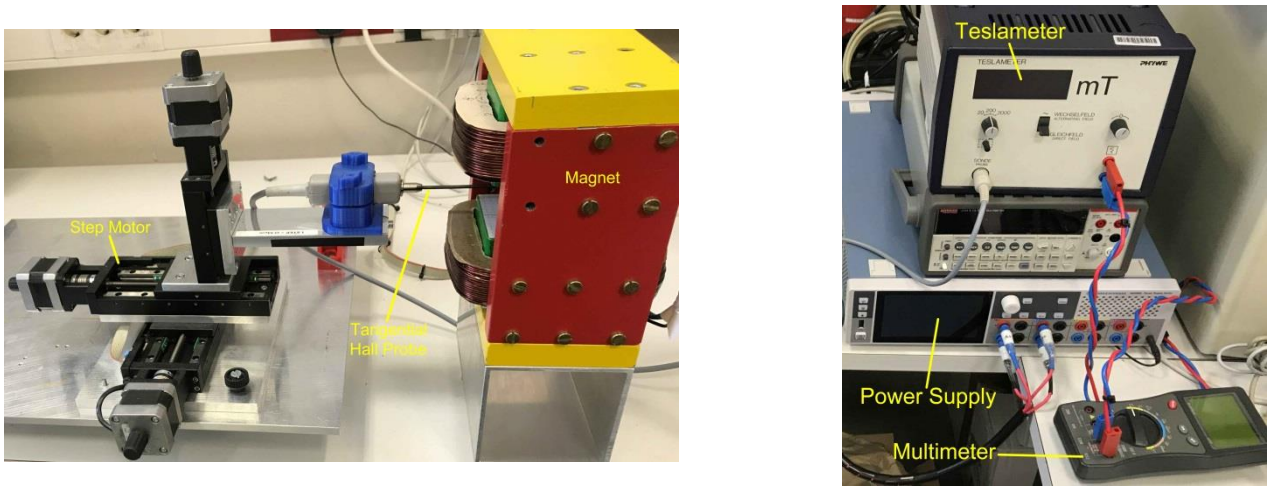

Figure 4.11 Schematics of the test bench.

The discrete points in the measurement are used to fit a surface profile of the magnet using linear interpolation. The following procedure was implemented to acquire the fit. First, the data points which were taken every 5 seconds are converted to coordinates based on the frequency of the step motors. The sweeps along the X-direction and Y-direction in **Figure 4.10** were programmed with 1000Hz frequency and the 2-mm jumps between the paths were set to 8000. Using the frequency, the location of each data point was identified mathematically. The motors' circuit is analog and lacks any closed loop system to check if the number of steps taken correspond to the input, which introduces errors to the measurements. To ensure the accuracy of the coordinates, the data was plotted, and corrections to the frequencies were applied prior to the fit using the fact that the magnetic field should be the highest at the end of the each sweep. The corrected frequencies were 949Hz for the sweeps along X-direction and 948Hz along the Y-direction. That is, the step motors missed around 5% of the steps.

Next, the data points for the other three regions shown in **Figure 4.9** were extrapolated. Finally, 2 separate fits are applied to each of the four regions shown in **Figure 4.9**: one for x-direction and one for y-direction sweep. The fit is performed using piecewise cubic interpolation with 1700 coefficients on average and standard deviations of 14.53 and 12.12 respectively. **Figure 4.12** shows the result of the fit. Note that when the probe is placed in higher elevations, maximum value for magnetic field slightly increases. If we define a homogenous region as an area within which the field difference between each point and center remains below 0.5mT, the homogeneous region becomes larger with elevation.

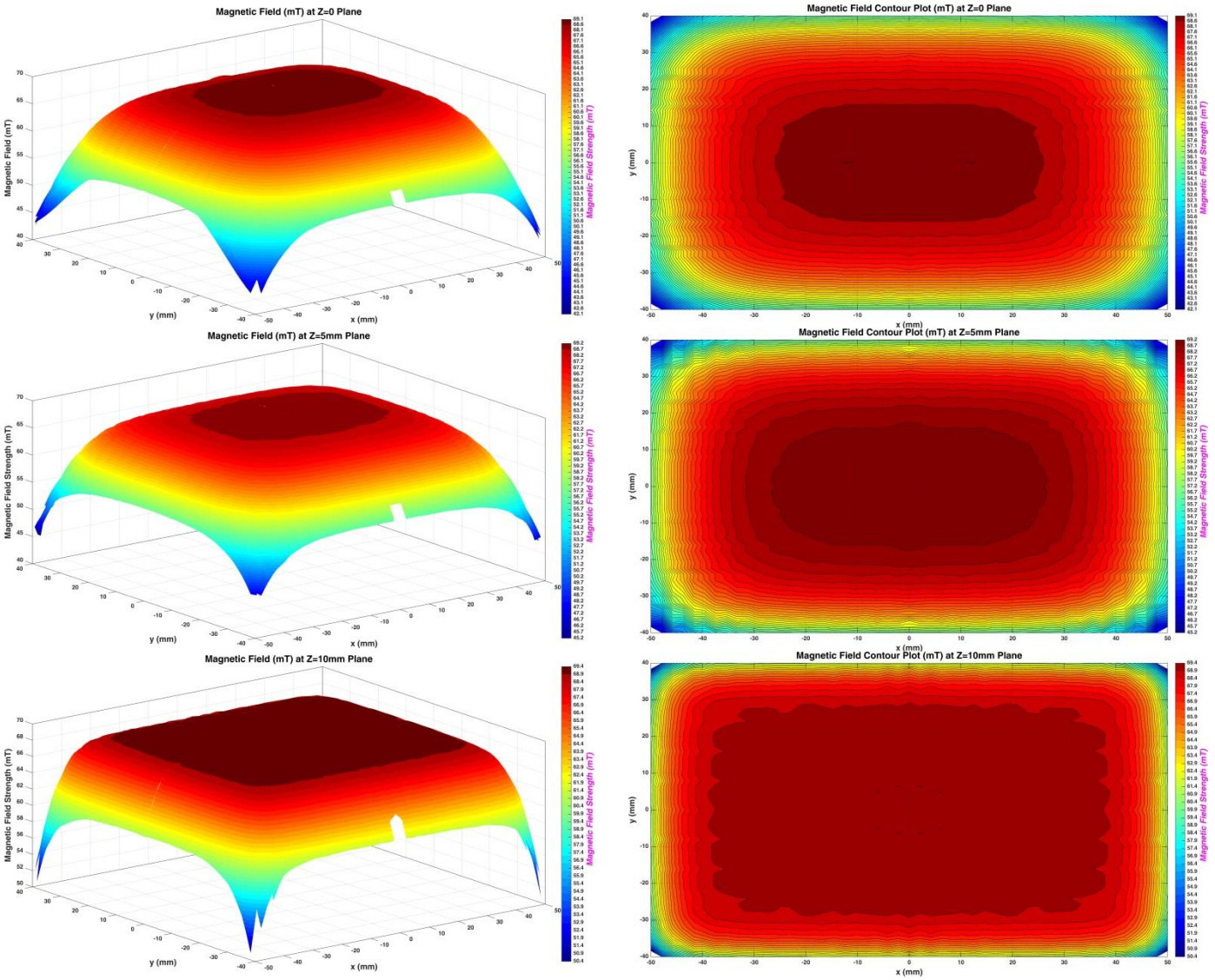

Figure 4.12 Left: 3D Magnetic profile at z=0, z=5mm, and z=10mm. Right: Contour plots for the three elevations.

Ideally, the setup should run at z=10mm. As shown in **Figure 4.13**, the homogenous region is much larger and magnetic field changes less drastically at z=10. However, the experimental design does not allow room to elevate the setup, and the actual experiment is run at z=0. The future upgrades to the setup, nevertheless, should accommodate z=10mm elevation.

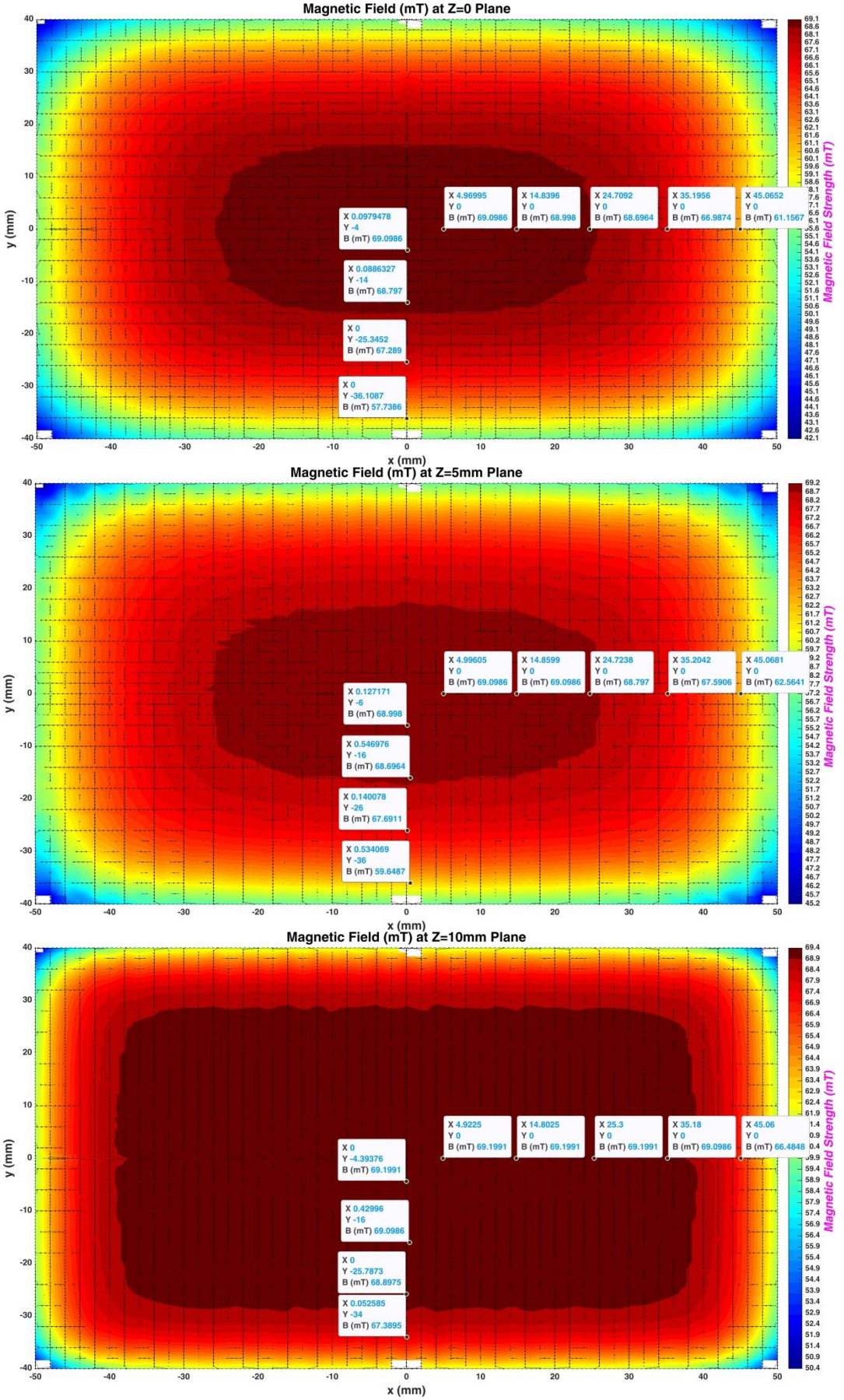

Figure 4.13 Magnetic field profile for z=0, z=5mm, and z=10mm elevations. Z represents the magnetic field in mT.

Given the profile shown in **Figure 4.13**, it is important to limit the area in which the electron is exposed to the magnetic field to 25mm from the center in x direction and 20mm from the center in y-direction. This is the area within which variation of magnetic field is below 0.5mT. It is still prudent to use the profile instead of an average constant value for the field. The main experiment will run at 40-60mT. Therefore, two more sets of measurements are carried out at 40mT and 60mT using currents that we determined from fits in Section 4.2.2. In addition, a fit is evaluated between 40mT and 60mT magnetic field profile. Fit results indicate a perfect linear dependence. For instance, multiplying 40mT magnetic field with 1.5 gives the 60mT field profile with 95% confidence. In other words, using the new fit function, the setup can run at any magnetic field between 40mT and 60mT. **Figure 4.14** show the results. The MATLAB program creates two profiles for 40mT and 60mT with three entries: x and y locations and corresponding magnetic field. In addition, it gives the linear fit results to be used in the experiment for any magnetic field between 40mT and 60mT. This way, the electron is exposed to a more realistic magnetic field in its trajectory.

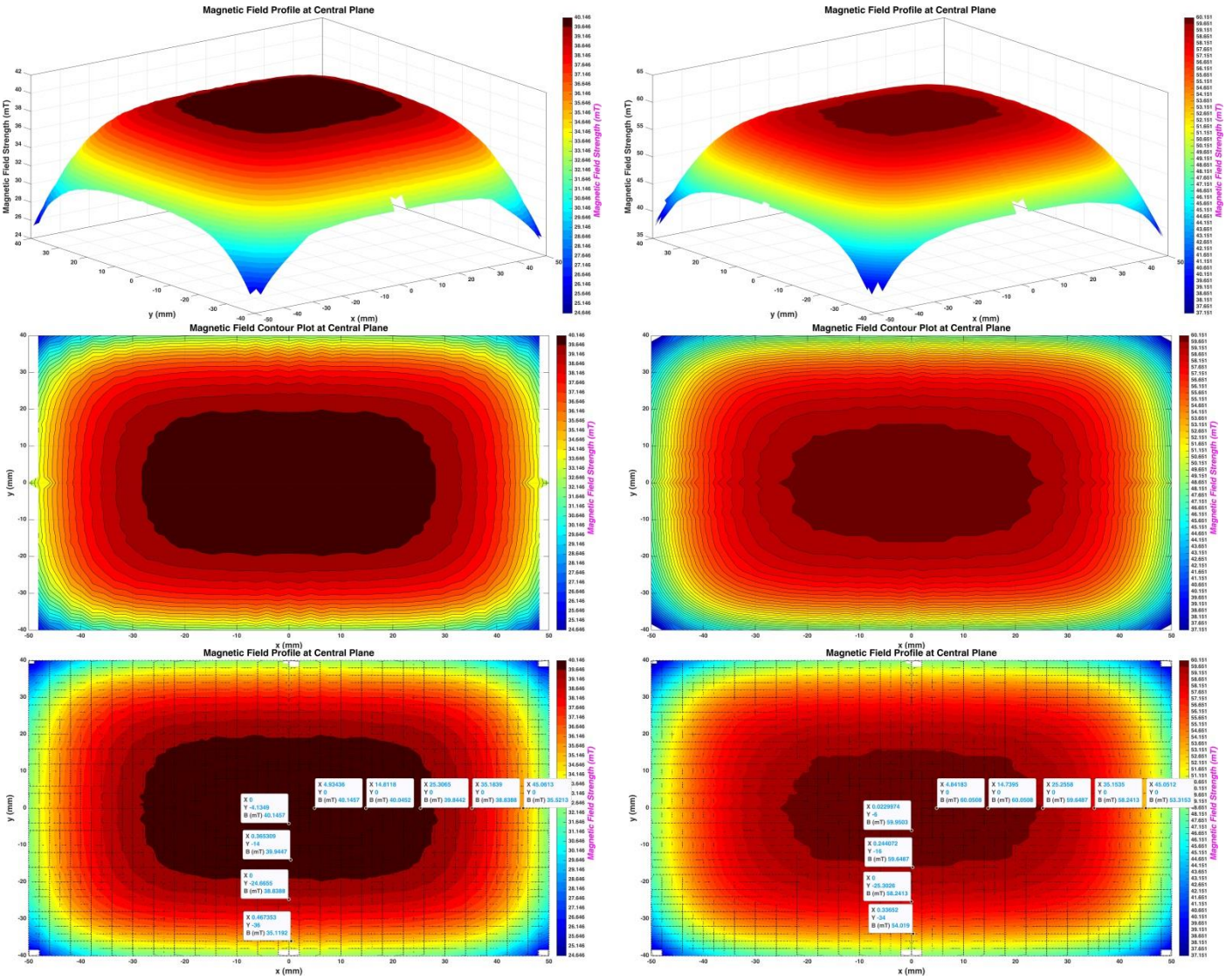

Figure 4.14 Magnetic profile at 40mT (Left) and 60mT (Right). 2D profile, contour, and data points are shown from top to bottom respectively.

4.2.4 Magnetic Hysteresis

When a ferromagnetic material is exposed to external magnetic field, electron spin dipoles align themselves with the field very strongly, augmenting the external field. The degree of magnetization $\overrightarrow{\mathrm{M}}$ of a ferromagnet is characterized by magnetic susceptibility χ_m **[57]**:

$$\vec{M} = \chi_m \vec{H} \qquad \textbf{Eq. (4.3)}$$

$$\vec{B} = \mu_0 \vec{H} + \mu_0 \vec{M} = (1 + \chi_m)\mu_0 \vec{H} \qquad \textbf{Eq. (4.4)}$$

Where $\overrightarrow{\mathrm{M}}$ is the magnetization or magnetic response of the ferromagnet $\left(\frac{A}{m}\right)$, $\overrightarrow{\mathrm{H}}$ is the driving magnetic influence from external field on the ferromagnet independent of the material's magnetic response $\left(\frac{A}{m}\right)$, and μ_0 is the vacuum permeability $\left(\frac{N}{A^2}\right)$.

When the external field is removed from a material, ferromagnets retain some magnetization due to the fact that some of the dipoles remain aligned. This residual magnetization manifests itself in terms of non-zero B-field when the external field is zero. This is known as magnetic hysteresis, and the residual field is called remanent magnetization **[58]**.

Hysteresis usually occurs when the external field is large enough to cause magnetic saturation in the material. H-magnets are designed to counteract saturation to some degree. In this work, we use up to 5A on each coil, which corresponds to 69.1mT. It is crucial to ensure that this amount of magnetic field does not exceed beyond the ferromagnet's saturation threshold. In order to investigate hysteresis in the electromagnet, the current on the power supply on both channels attached to the coils are programmed to ramp up from 0 to 5A with increment of 0.1A each 10 seconds followed by ramp down from 5A to 0 with the same settings. The procedure is repeated 10 times, while the Hall probe is positioned at the center of the magnet and the teslameter output is recorded by the multimeter every 5 seconds. As shown in **Figure 4.15**, the electromagnet shows 1.14mT of residual magnetization due to hysteresis. Demagnetization of ferromagnets requires applying magnetic fields in opposite direction. The power supply is therefore programmed to apply a sequence of forward and reverse currents to the electromagnet in order to "zero" its magnetization before each use.

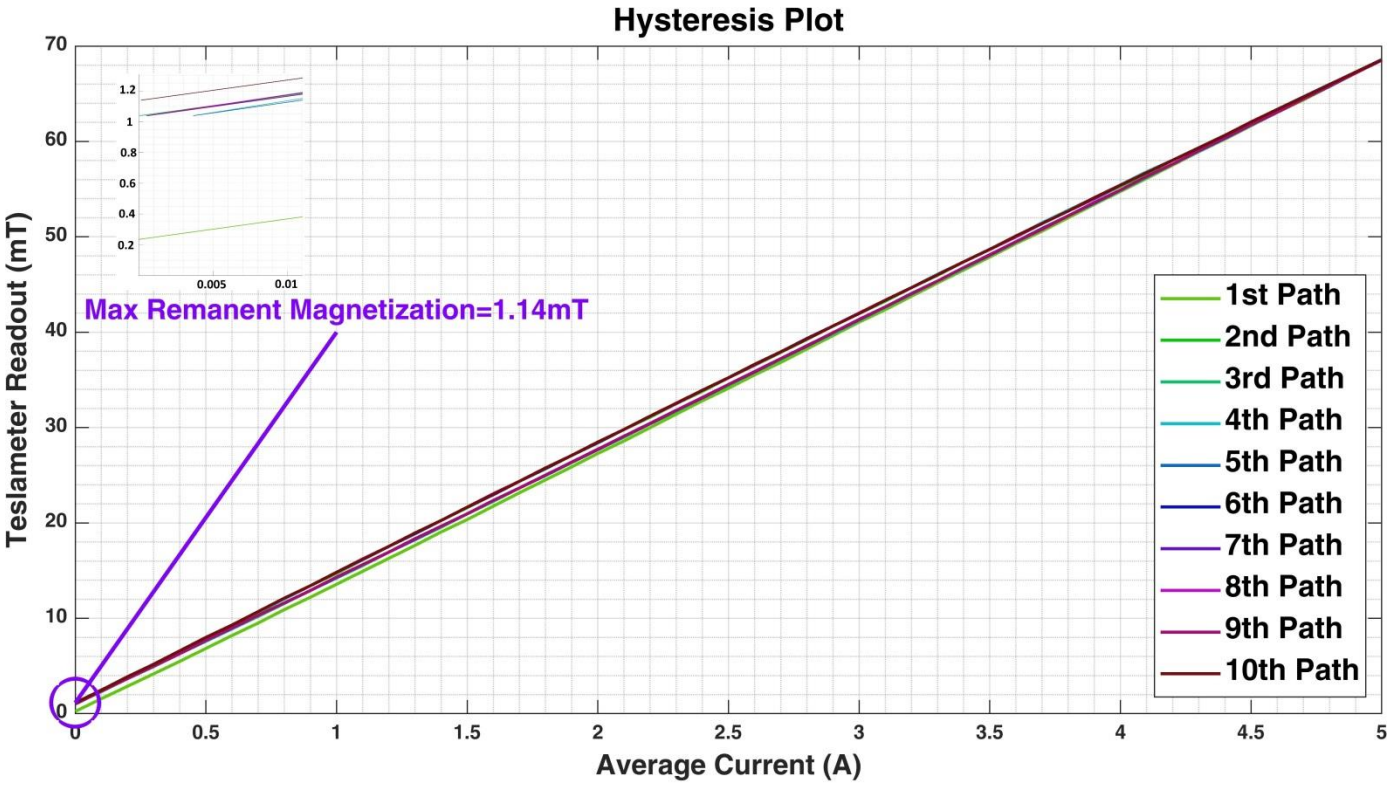

Figure 4.15 Magnetic hysteresis in the electromagnet under periodic current changing from 0 to 5A and back. Hysteresis manifests itself in the form of a small offset from the origin after a few loops. Note that the end field at maximum current changes insignificantly nevertheless.

4.2.5 Electromagnet's Temperature

Current running through cupper wires create heat due to resistance. Increase in temperature can melt the coating of the wires and short the circuit. Therefore, it is prudent to measure the heat production of the wires and find a solution accordingly. To test the heat response of the coils, each coil is set on 3A with constant current regime, and the temperature is monitored every 30 second for the duration of 45 minutes. The temperature is monitored continuously using a FLIR i7 Thermal Camera. Results are shown in **Figure 4.16**. The discrepancy in temperature of the two coils at the beginning of the test is due to the fact that the tests are taken prior to mounting the coils on the iron yoke. That is, the coils are measured separately and at different times of the day and at different placements. In addition, the measurement method introduces an uncertainty, as the camera needs to be pointed at a specific area, which may not be necessarily a heat node. **Figure 4.17** shows final measurement data of the two coils. The temperature of both coils, nevertheless, asymptotically reaches equilibrium after 45 minutes to roughly 45 °C.

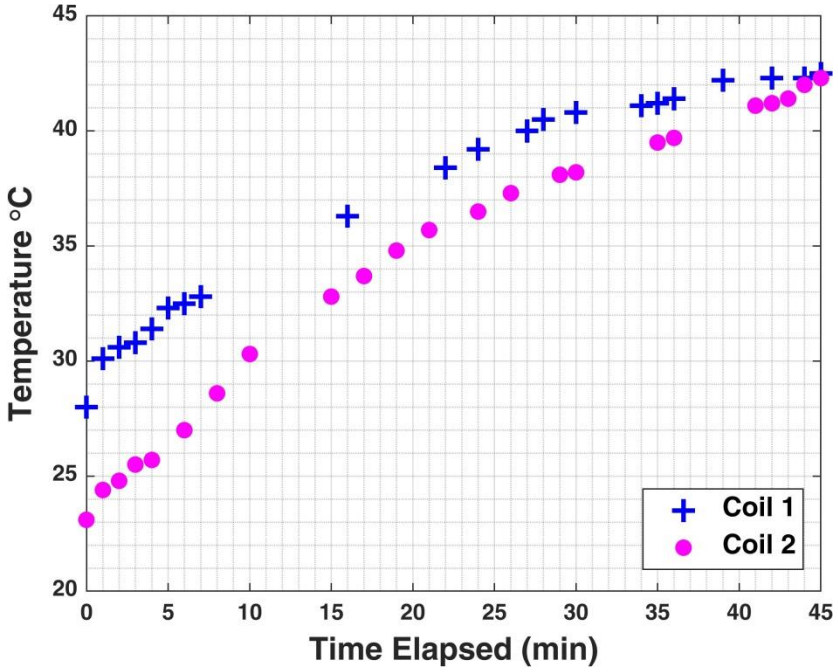

Figure 4.16 Temperature rise in the coils over time. Both coils reach roughly 45 °C after 45 minutes.

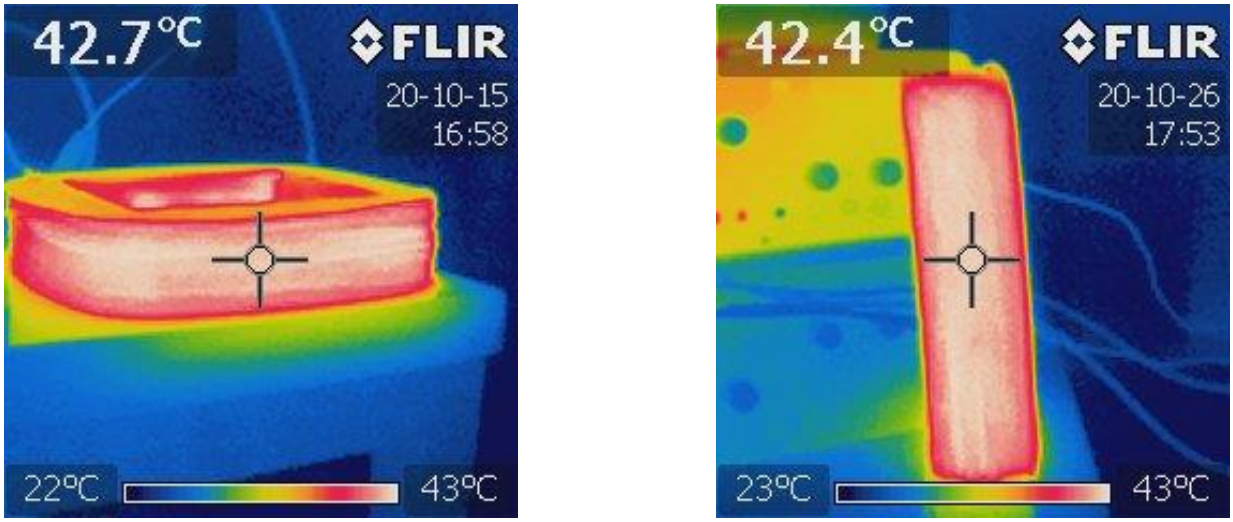

Figure 4.17 Final measurement of both coils with FLIR i7 Thermal Camera.

The measurements indicate that the coils do not reach critical temperatures even after prolonged use. However, it is imperative that the temperature of the magnet is monitored during the measurement. To that end, a PT100 temperature sensor is attached to the coils and is connected to a Keithley 2100 $6\frac{1}{2}-$ digit Resolution Digital Multimeter. The resistance of the connecting wires is measured (0.9 Ω) and subtracted from the signal of the multimeter to calculate accurate temperature. In addition, a 140mm Noctua NF-A14 industrialPPC-3000 PWM fan is mounted on the side of the electromagnet with a Noctua NA-FC1, 1-channel fan controller to adjust the speed of the fan based on its real-time temperature from the sensor. The fan facilitates heat dissipation and prevents the coils from overheating during prolonged use. The setup is shown in **Figure 4.18**.

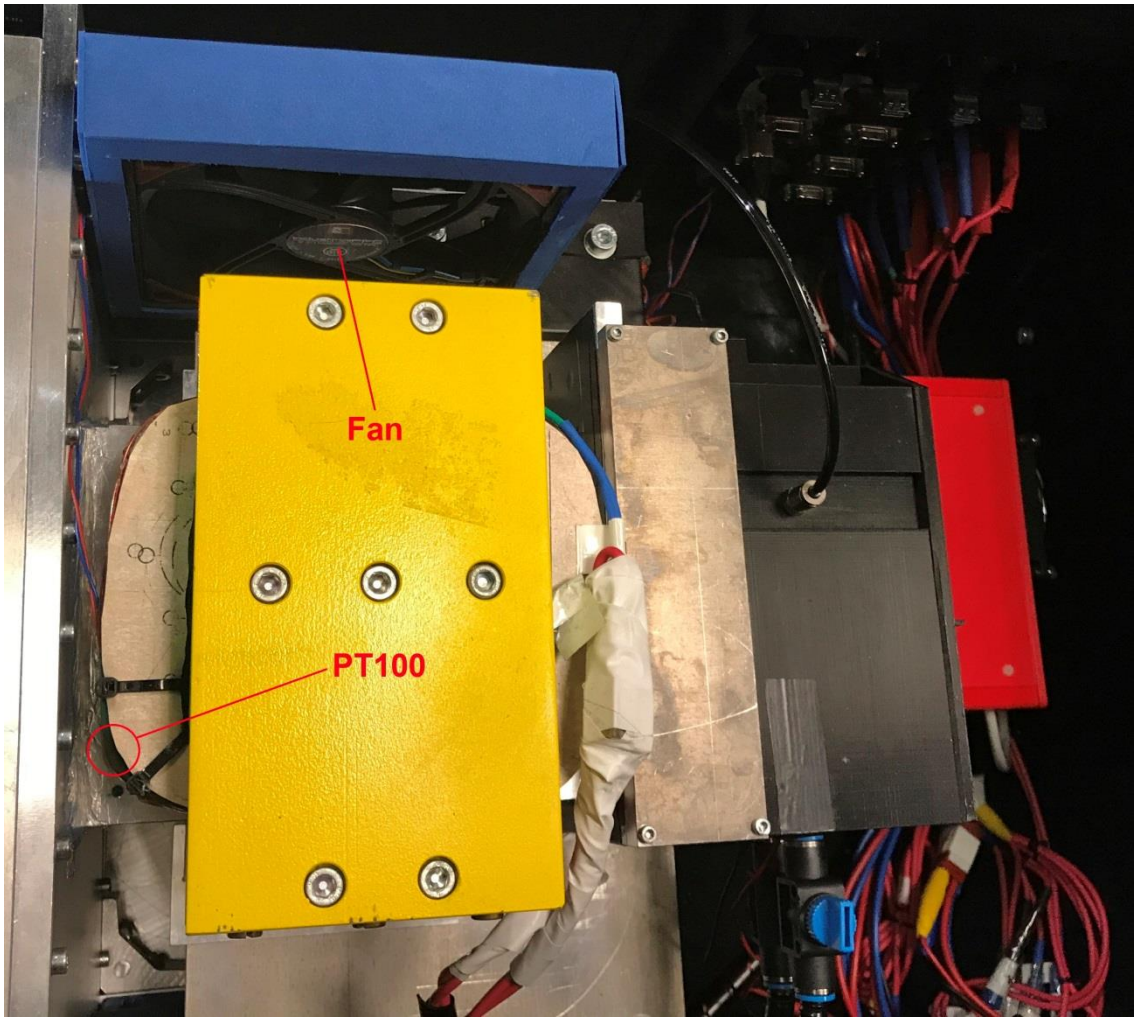

Figure 4.18 Heavy-duty fan (blue frame) with Pulse-Width Modulation controller allows adjusting the speed of the fan based on real-time temperature signal of PT100 temperature sensor attached to the coils.

4.3 Experimental Setup

With each component's specifications determined, we can move on to the entire experimental setup. The source itself is collimated (**Figure 4.19**) and positioned on a mechanism that changes location and angle depending on the intended energy. Exiting the source, electrons travel through a 165-millimeter mu-metal tube until they reach the magnet. After bending, the electrons are guided through another mu-metal with the length of 72 millemeter to the collimator before reaching the PMMA. The entire trajectory of the electrons outside magnetic exposure area is shielded by mu-metals to avoid stray unwanted magnetic fields.

The entire setup is housed inside three adjoining chambers made of non-magnetic Aluminum alloy with an average thickness of 10mm. the first Chamber (**Figure 4.19**) is larger than the rest and houses the positioning mechanism as well as the source. The vacuum pump hose is attached to the side of this chamber. The middle chamber (**Figure 4.19**) is a long corridor in which the electrons are exposed to the magnetic field. The end chamber houses the collimator, and PMMA and SiPM are mounted to it. All three

chambers are interconnected, creating a large sealed volume. **Figure 4.20** shows the entire experimental setup until SiPM.

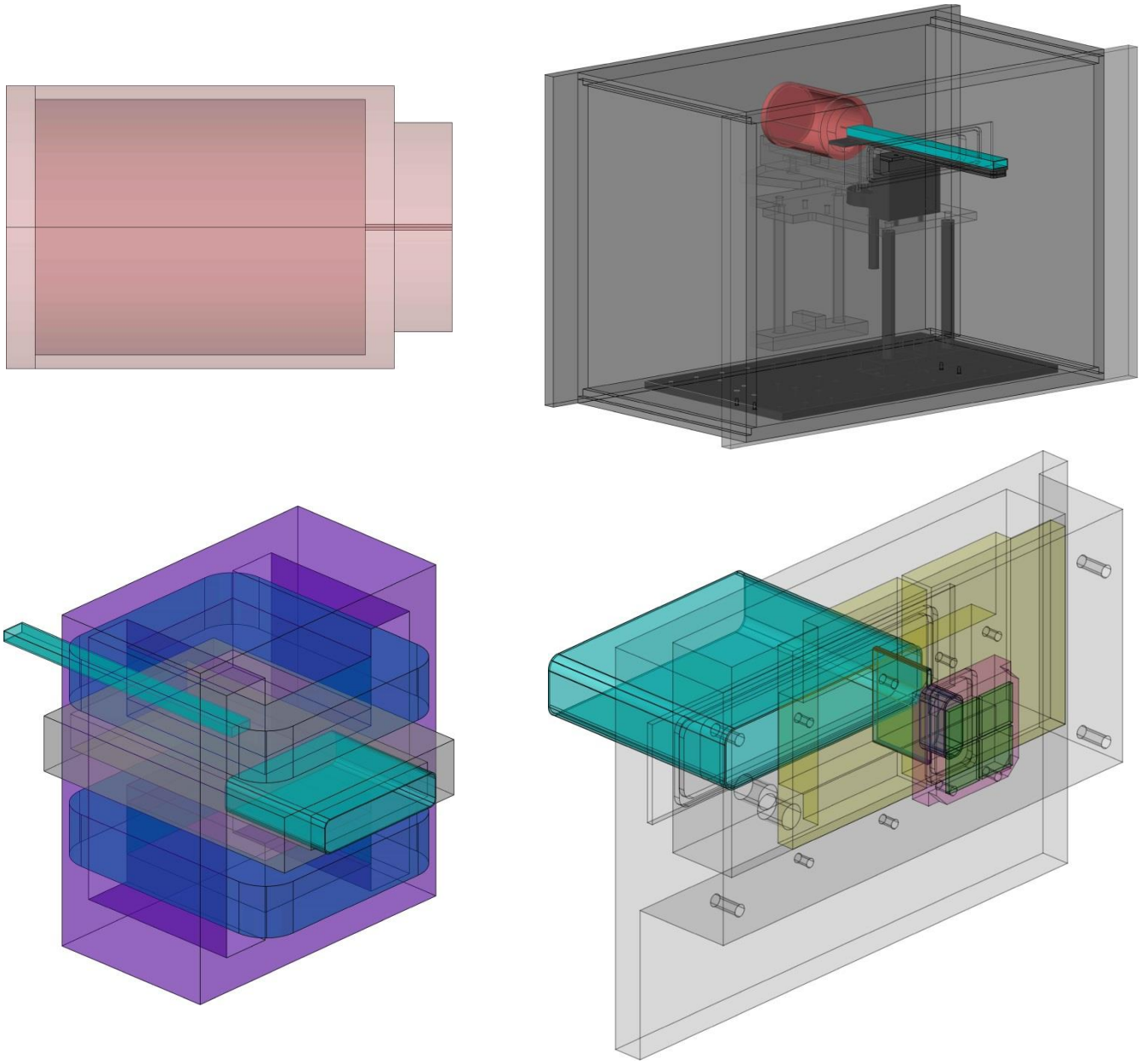

Figure 4.19 Top Left: Source housing. The end cap and the front end is composed of aluminum, and the main hollow, cylindrical chamber is made of lead. The source is collimated, and electrons can only exit the housing through a long narrow cylinder with the diameter of 0.5mm. Top Right: First vacuum chamber. The source (red) is mounted on the positioning mechanism (dark grey). The electrons exiting the source travel through a mu-metal (cyan) until they reach the magnet. Bottom Left: Middle chamber around which the electromagnet is positioned. After bending, the electrons are guided to the collimator through a wide mu-metal (cyan). Bottom Right: End Chamber, housing the collimator. Electrons travel through two separate mu-metals until they reach the PMMA (magenta). The SiPM (green) is attached to the PMMA.

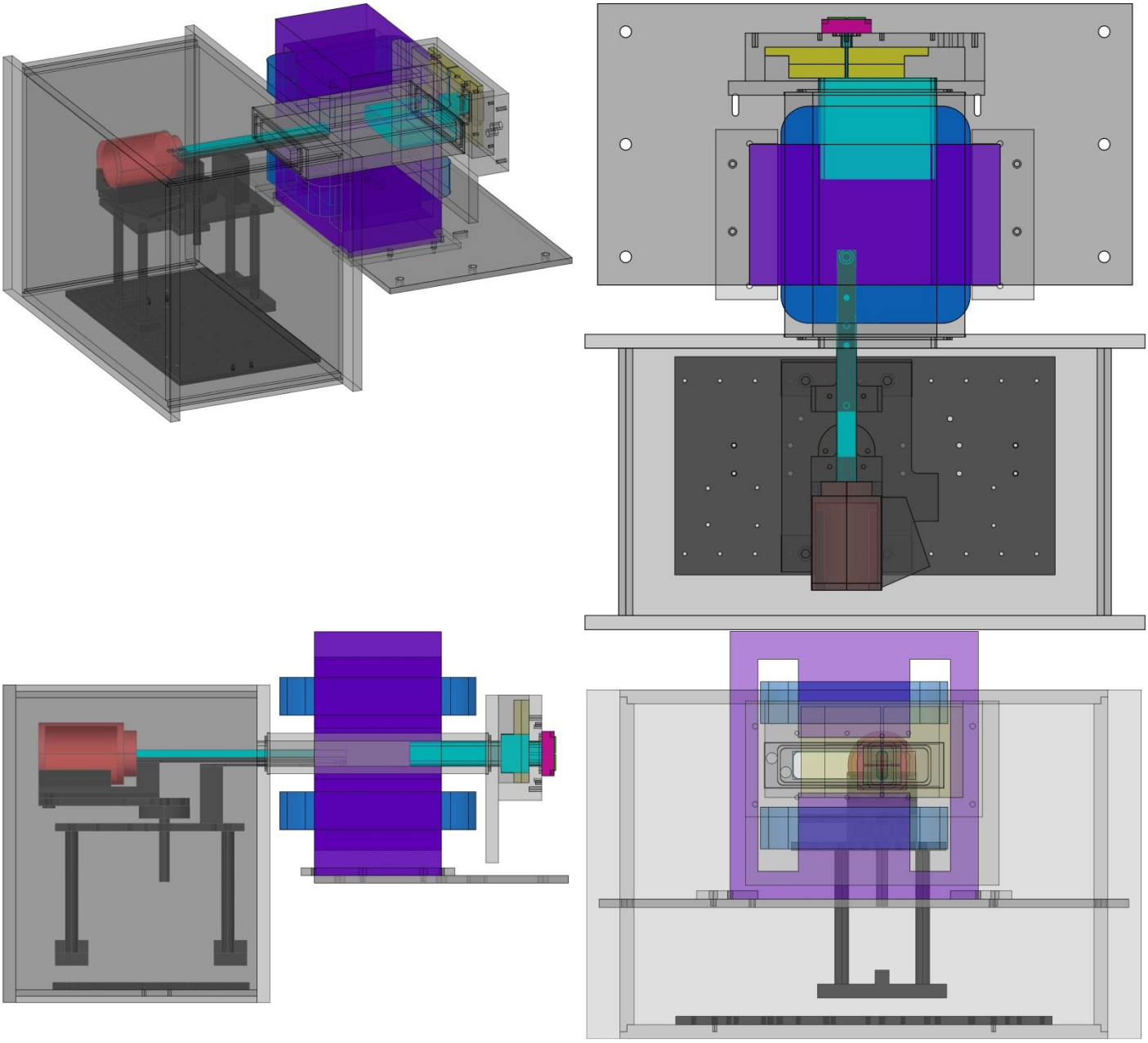

Figure 4.20 The entire setup in different views. For detailed description, see **Figure 4.19**.

4.4 Source Holder

A mechanical device is designed to adjust the source position and angle for different energies. **Figure 4.21** shows the device. The source is positioned at the back in an elevation that aligns the source collimator with the center of the SiPM. A long Mu-metal tube extends from the source until roughly 25 mm inside the magnet. The angle can be adjusted with an accuracy of 0.5 degrees; the rectilinear position accuracy is also roughly 0.5 mm. The entire mechanism is fixed inside the vacuum chamber with four screws.

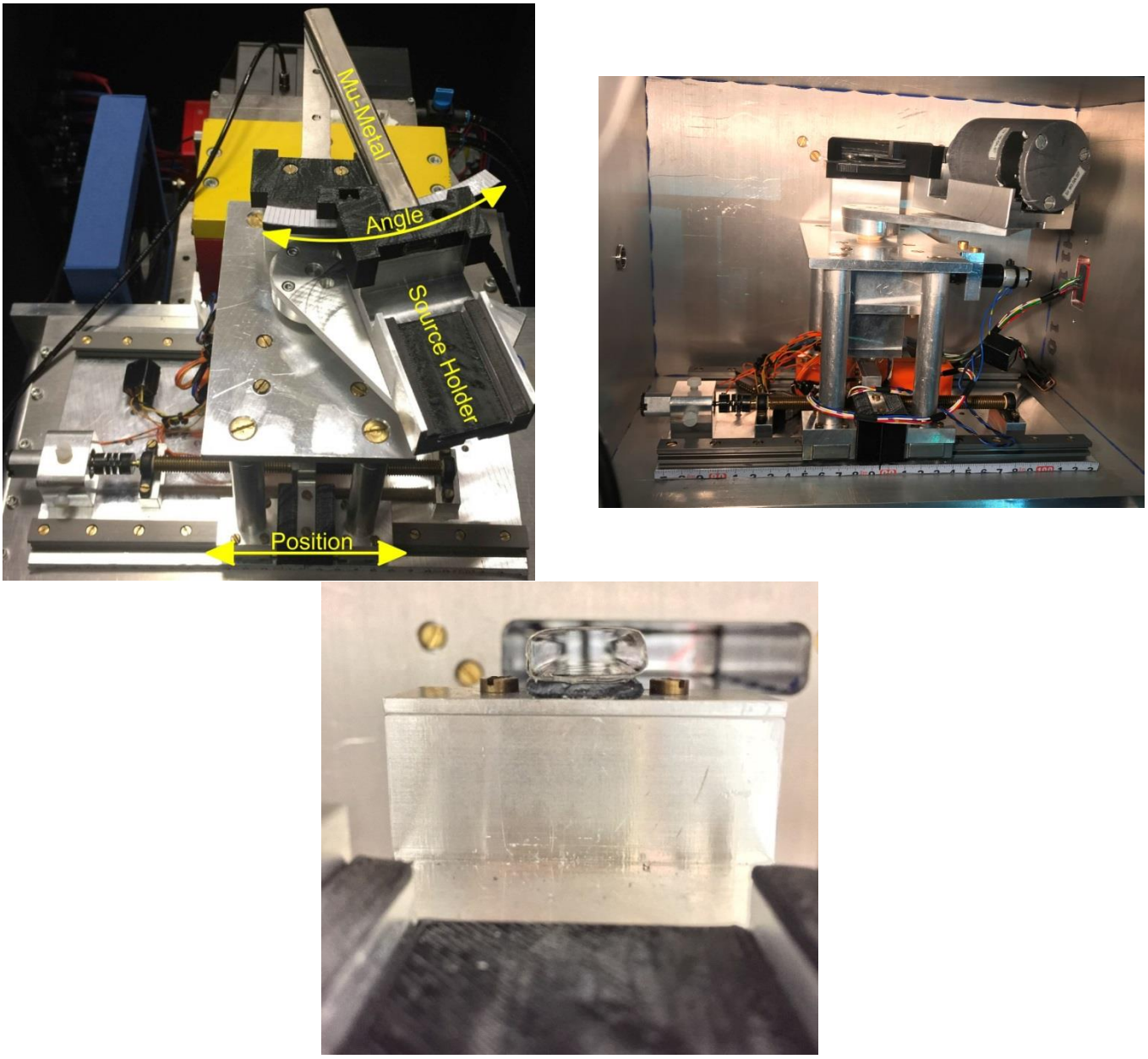

Figure 4.21 Top Left: The positioning device outside the vacuum chamber without the source. Top Right: The mechanism inside the vacuum chamber. Bottom: Close view of the source and the mu-metal when the mechanism is set to zero angle. The collimator is visible through the mu-metal.

4.5 Collimator

Electrons that are filtered through the magnetic field must travel through a collimator to further narrow down the energy band. The collimator in this experiment is comprised of three separate layers, ensuring that electrons that hit its wall are absorbed. **Figure 4.22** shows the front and back view of the collimator. The layers are made of PVC (10mm), Aluminum (6mm), and lead (6mm) respectively. The layers amount to a total length of 22 mm.

The three layers of material are chosen to effectively absorb electrons with energies up to 2.28 MeV. The amount of radiation that penetrates a material depends on the material's thickness, density, and atomic

number. PVC (Polyvinyl Chloride) is a relatively low-density material with a low atomic number. PVC is effective at stopping low-energy electrons and absorbing their energy through scattering and absorption processes. By doing so, the PVC layer can help to spread out the electron beam, making it less divergent.

Aluminum, on the other hand, has a higher density and atomic number than PVC. It can effectively stop electrons with higher energies than PVC by slowing them down through collisions with its dense atomic structure. It can further collimate the electrons by reducing the spread and divergence of the beam and making it more focused.

Finally, the lead layer, being the third and outermost layer of shielding, can help absorb any stray electrons that are not already collimated. This layer is particularly effective at absorbing high-energy electrons, which can be difficult to collimate using other materials. By absorbing these stray electrons, the lead layer can help further improve the collimation of the beam.

By combining these three materials in the order of PVC, aluminum, and lead, an effective collimation of electrons can be achieved. The opening gap can be adjusted between 0 and 5.5 mm using a custom 3D printed wrench.

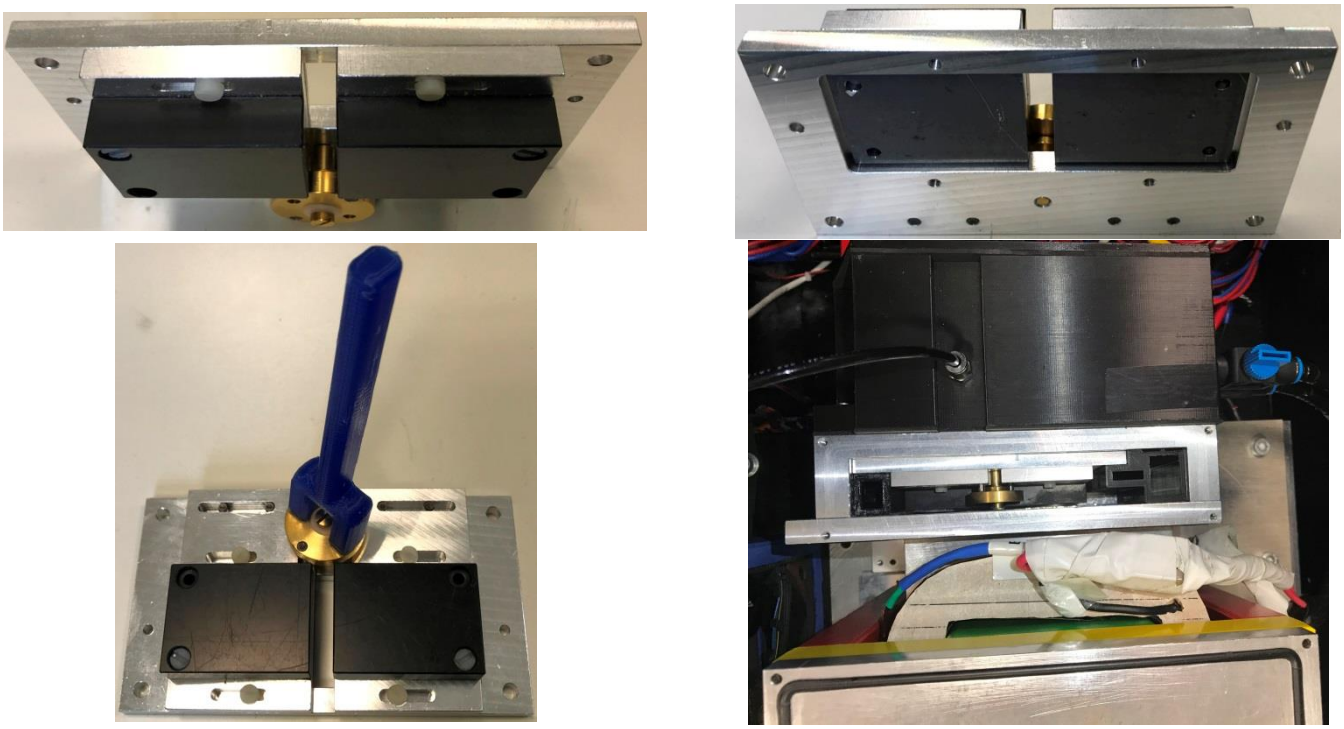

Figure 4.22 Top Left: Collimator's front view. The first two layers, PVC and Aluminum, are visible from this angle. Top Right: Collimator's back view. The last layer, lead (dark grey in the image), is visible from this angle. Bottom Left: Collimator's opening gap is adjusted via a custom-made wrench. Bottom Right: Top view of the collimator inside the last vacuum chamber. 3D printed parts in black are used to keep the collimator in the correct position.

4.6 SiPM Housing

The PMMA is mounted on the setup via a 3D printed housing which also aligns the SiPM modules at the center of the PMMA as shown in **Figure 4.23**. The SiPM modules are attached to the PMMA via optical grease BC630. The purpose of the grease is ensure firm contact while not obstructing light transmission. This silicone grease is chosen because its refractive index is very close to the PMMA itself $\left(n_{grease} = 1.465\right)$. Therefore it does not distort the Cherenkov light. The housing fully encompasses the PMMA, preventing any stray photon from reaching the glass from the sides.

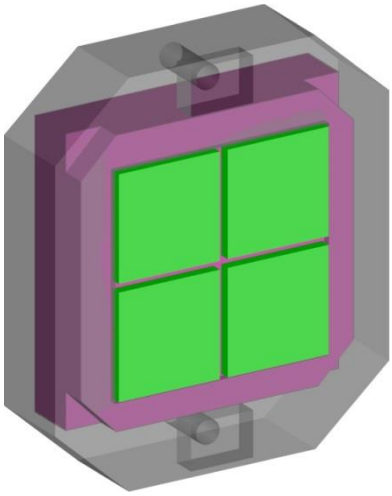

Figure 4.23 PMMA housing (grey) aligns the SiPM modules (green) at the center of PMMA (magenta).

The SiPM modules need to be cooled down to -18.5° C during operation to ensure minimum temperature-induced signal. The detectors are cooled via a Thermoelectric cooler (TEC). A TEC is a group of p-doped and n-doped semiconductors pairs, i.e., thermocouples, contained within two thermally conductive ceramic plates. Multiple p-n pairs are connected together in series electrically and in parallel thermally. A copper substrate at both ends of the semiconductors ensures electrical connection between all pairs in series. TEC module use in this work contains 127 p-n pairs and can draw 5A current (TEC12705). A 12V DC current via applied voltage through the p-n junction produces a temperature difference, creating a cold side and a hot side (**Figure 4.24**).

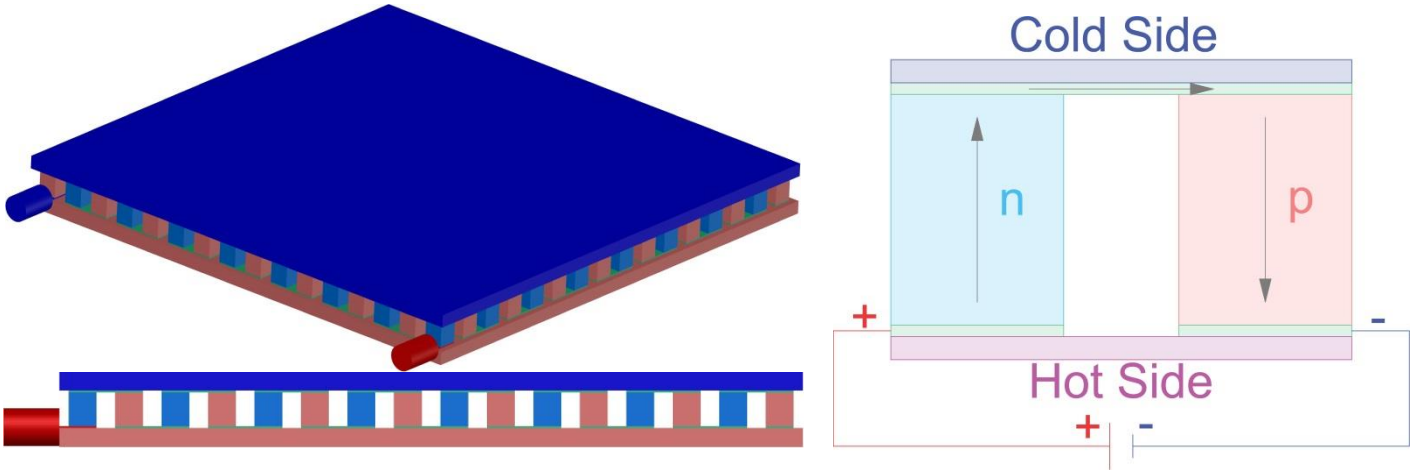

Figure 4.24 Left: Thermoelectric Cooler TEC12705. n-type (light blue) and p-type (light red) semiconductor pairs are connected in series via thin cupper layers (green). Right: Applied voltage creates a DC current that pumps heat from the cold side to the hot side.

The cold side of the peltier element (TEC 12705) is attached to a cupper heat sink, which is in direct contact with the back of the detector board, and the hot side is liquid-cooled via a cupper block to maximize heat transfer. The contact area between the detector PCB and the heat sink, heat sink and the TEC, and TEC and

the water block must be filled with a thermal compound to increase the contact area and facilitate heat transfer. The real area of contact between two surfaces is drastically different than the apparent area of contact is due mainly to microscopic imperfections in the surfaces. In extreme cases, it can be as low as 1% of the apparent area of contact **[59]**.

In case of contact between the heat sink and the SiPM PCB, we expect even lower contact area due to installed electronics components on the PCB and lack of Integrated Heat Spreader (IHS). The contact between TEC and water block and heat sink is covered with Thermal Grizzly Kryonaut thermal paste due to its desirable thermal conductivity at subzero temperatures. The contact between the SiPM PCB and the heat sink is covered with a mixture of Thermal Grizzly Kryonaut thermal paste and 0.5mm Gelid GP-Extreme thermal pad to improve the area of contact. To prevent damage to the SiPM PCB, a very thin layer of plastic is placed on top of the thermal compound. The role of the thermal paste is to fill the narrow clearance between SiPM and SiPM PCB and ensure light pressure on both boards so that both sides can be cooled. SiPM PCB is directly attached to the ASIC board, which will benefit from cooling. **Figure 4.25** demonstrates the cooling setup and all of its components. The approximate temperature of the SiPM is monitored via a PT100 temperature sensor, attached to the heat sink. The mounted setup is shown in **Figure 4.26**.

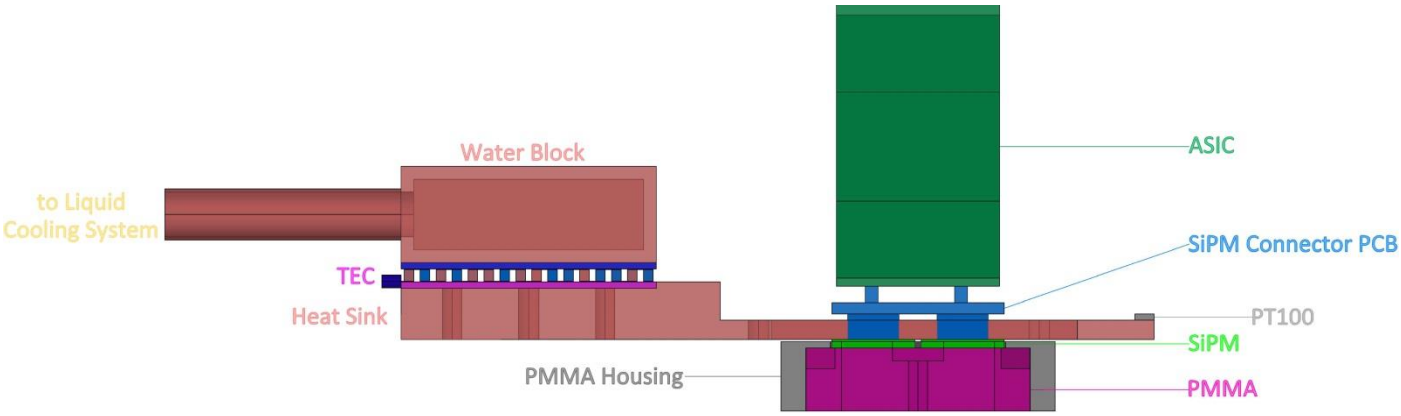

Figure 4.25 Cooling system for the SiPM. Contact areas are covered in thermal compounds to facilitate heat transfer.

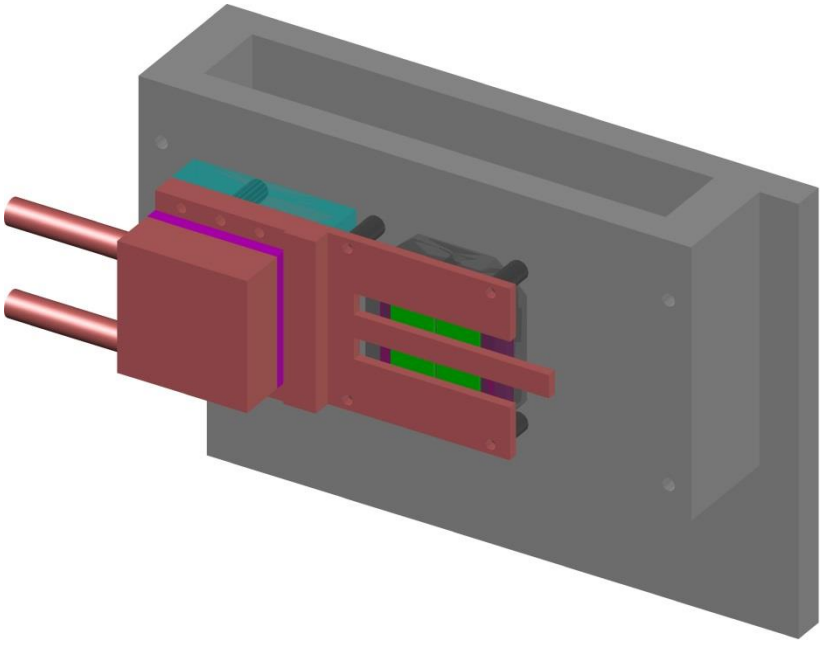

Figure 4.26 The detector and the cooling system mounted on the end vacuum chamber (Collimator housing).

Undesired but inevitable condensation and deposition of water and ice on the surface of the cold side of the thermocouple as well as the detector causes damage to the circuit board during operation. In order to counteract that, the entire cooling and measurement components are placed inside a 3D printed enclosure. A continuous flow of dry air, provided by an air pump, ensures positive dry air pressure and zero humidity inside the chamber. The air pump provides pressure slightly above 1 bar. The air is then directed into a non-reactive, non-toxic, dehumidifying silicon oil to prevent water vapor from entering the detector enclosure. The air pipe then travels through a photon absorbing medium to ensure that no light (photon) enters the detector chamber through the dry air tube (**Figure 4.27**). The alternative method is to create a fully sealed chamber and flood it with nitrogen to ensure no moisture reaches the system. However, due to ASIC cables, this option is impractical.

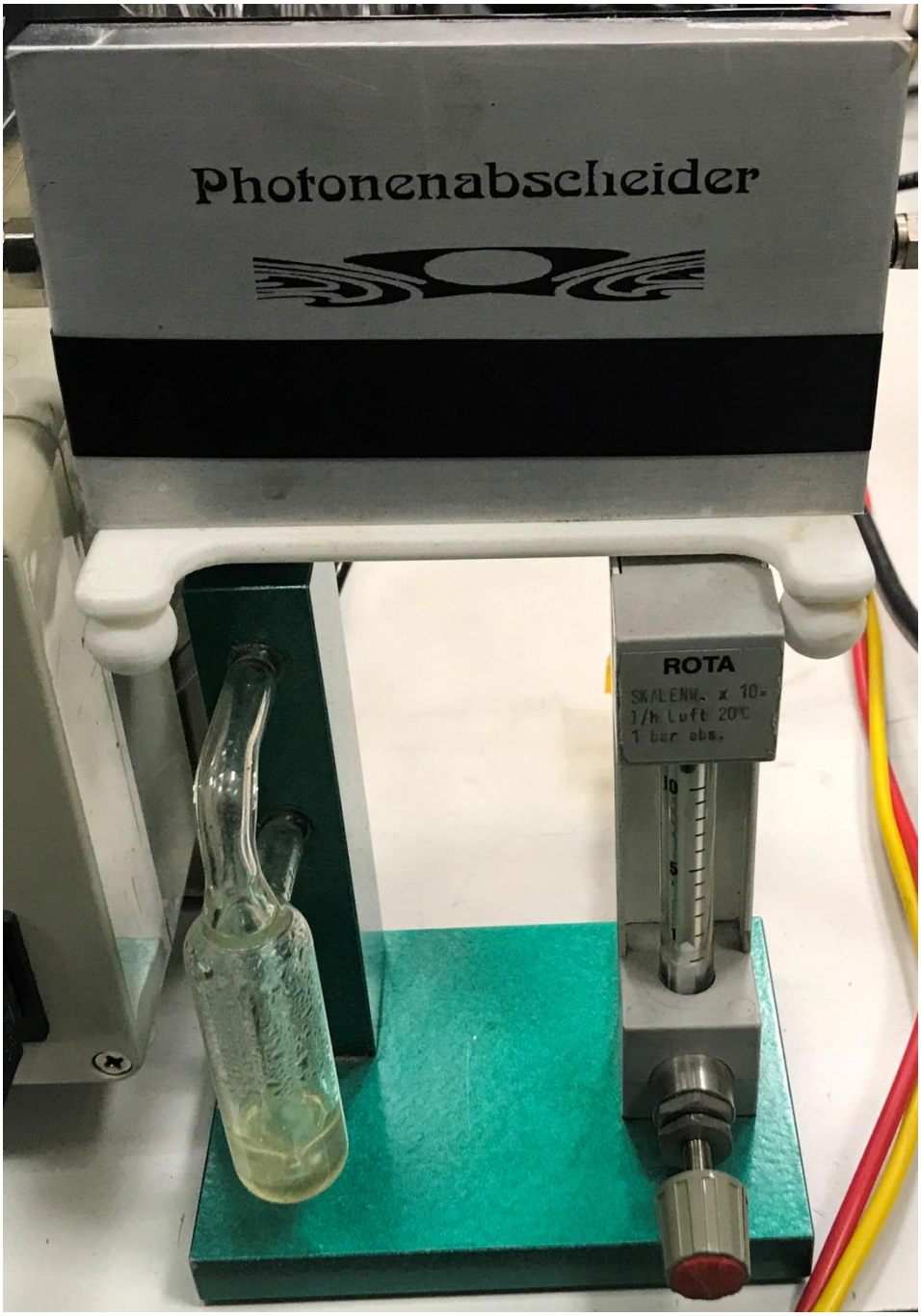

Figure 4.27 Air from the pump enters the dehumidifier and then travels through photon absorber before reaching the detector enclosure.

Figure 4.28 shows the detector enclosure design. The dry air enters from the top. The enclosure ensures a positive dry air pressure build up inside. The end product mounted on the setup is shown in **Figure 4.29**.

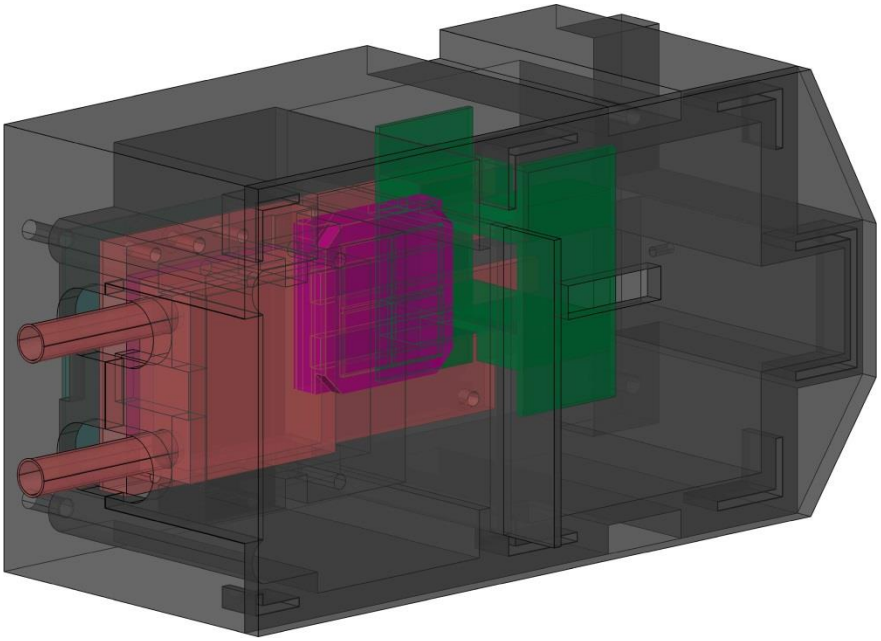

Figure 4.28 Detector enclosure.

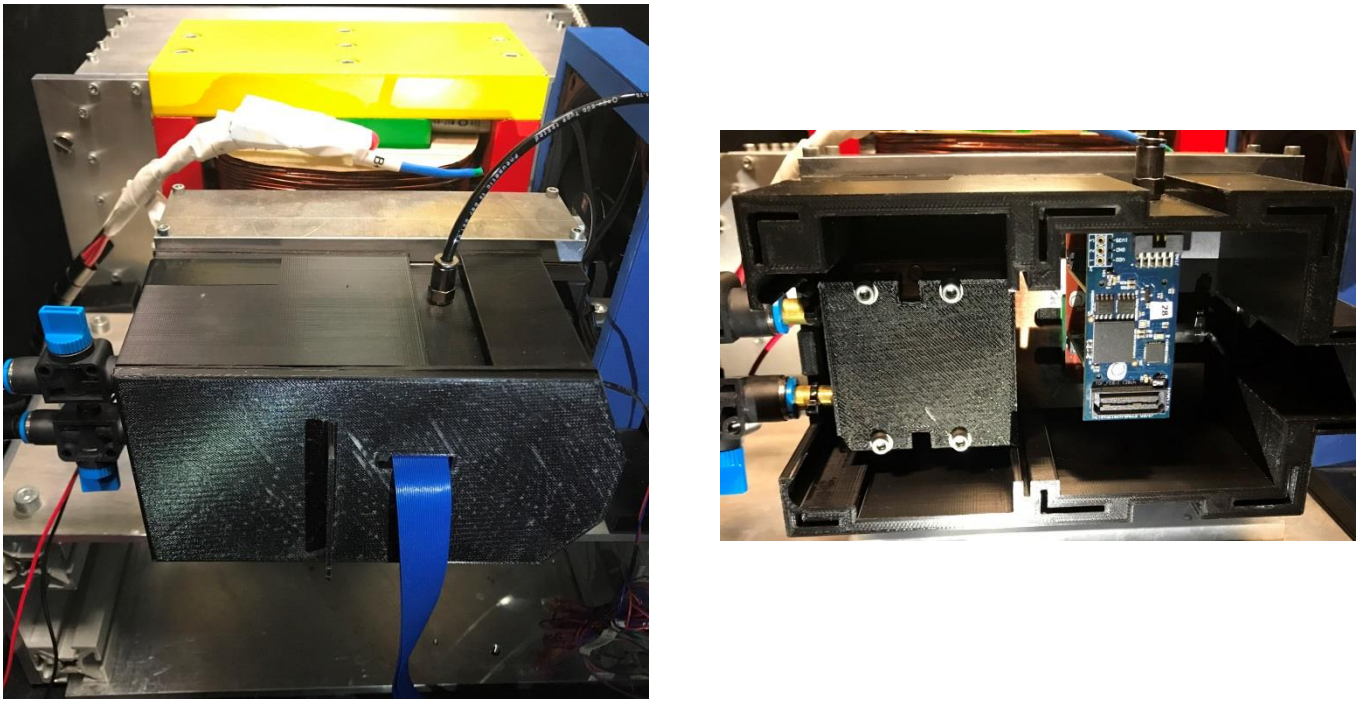

Figure 4.29 Left: Detector enclosure with ASIC cable attached The dry air is fed to the enclosure from the top. Right: Detector enclosure with the end cap removed. The TEC housing and the coolant tubes as well as the ASIC is visible.

4.7 Water Cooling System

The cold side of the TEC module is attached indirectly to the SiPM, and its hot side is cooled down via a liquid cooling system, which was available from previous research **[60]** and was made compatible with current work with certain modifications. **Figure 4.30** shows the components of the setup. The liquid

coolant which is comprised of deionized water, surfactant, and antifreeze, runs through a radiator attached to fans to dissipate heat in a closed circuit. The coolant mixture was adjusted experimentally multiple times to achieve the optimal outcome. After the radiator, the coolant enters a water reservoir followed by a DayPower WP-2507 DC water pump with 1.8 l/min maximum flow rate. The pump pushes the coolant to an array of TEC modules to precool the liquid before it reenters the water block. The TEC modules had to be rewired in parallel connections to become effective. Contact surfaces between the radiators and water blocks is filled with Thermal Grizzly Kryonaut thermal paste to improve heat transfer. The system is capable of maintaining -18.5 °C during operation. The entire water cooling setup was elevated so that the highest point in the system becomes the reservoir, not the main water block in order to avoid air formation in the water block. The reservoir had to be sealed with o-rings in order to decrease coolant loss when the system is not in operation. The SiPM model used in this work (Hamamatsu S13361-3075AS) has an operation temperature of -20 to 60 °C.

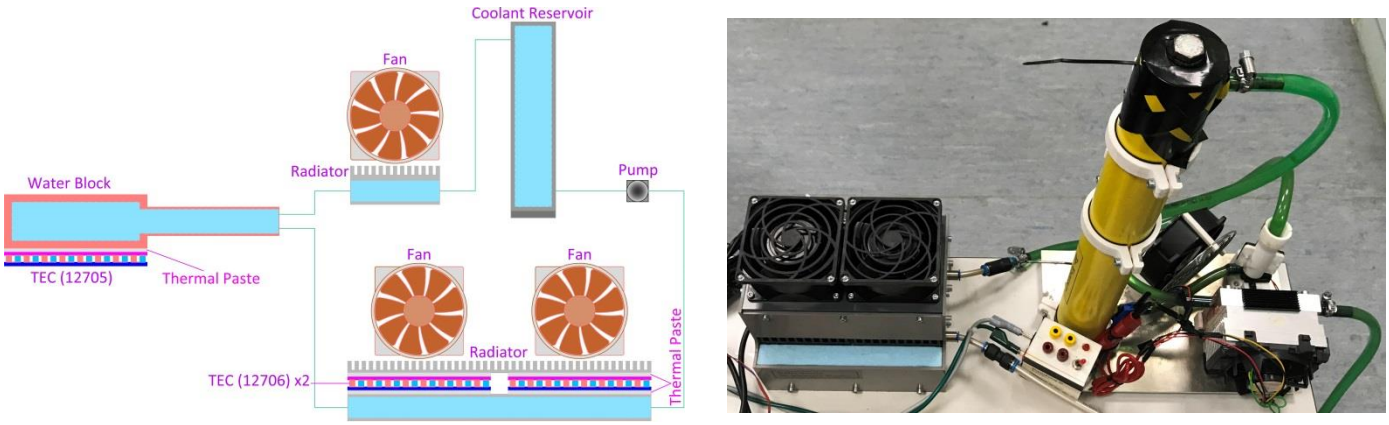

Figure 4.30 Left: Schematics of the water cooling system. Right: View of the radiator, reservoir, and the precooling setup.

4.8 Readout System:

The detector used in this experiment is an 8x8 S13361-3075AS SiPM array from Hamamatsu. It feeds data to the ASIC (Application-Specific Integrated Circuit) module from PETsys Electronics (**Figure 4.31**). The ASIC chip is installed on a Front-End-Module (FEM), which is comprised of one interface board called FEB/I for output, two FEB/A_v2 boards (one of which hosts a 64-channel ASIC), and one FEB/S board, capable of hosting two 8x8 SiPM arrays, making a set of 128 readable SiPM channels. The FEB/S also hosts two high-precision temperature sensors, each facing the back side of the SiPM array once inserted **[61]**.

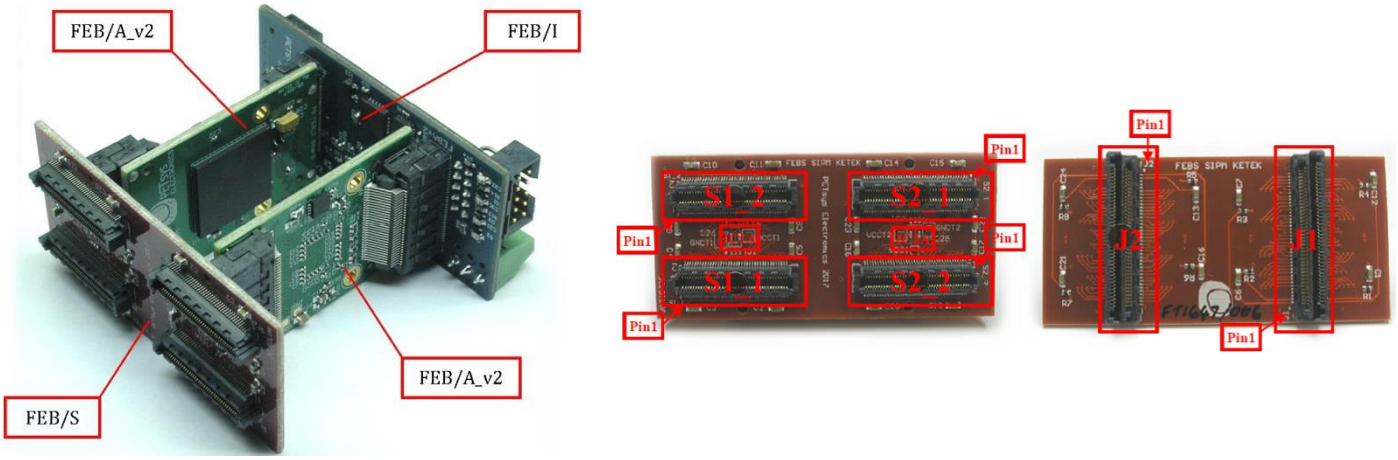

Figure 4.31 Left: Front-End-Module with an ASIC chip. Right: Front and back side of FEB/S board. Temperature sensors (IC1A and IC2A) are mounted at the center of the top side **[61]**.

The ASIC registers the signals which are above a specific threshold. Its intended application is the fast read-out of scintillator signals with sub-nanosecond time resolution for TOFPET systems (Time-Of-Flight measurement in Positron Emission Tomography) **[61].** The ASIC chip itself is able to process up to 64 channels, i.e., an 8x8 SiPM array, with a time to digital converter (TDC) module for every channel.

The ASIC is connected to an FPGA (Field-Programmable Gate Array) evaluation board from PETsys Electronics using an 14 Gbps HQCD series cable from SAMTEC. The FPGA provides communication between ASIC and the data taking device (measurement PC). It sets the parameters and performs tasks such as data taking, packaging/storing data into buffers to be written into file, supplying ultralow-ripple power supply for bias voltage of the SiPM, and providing power for the ASIC. The board provides 16 positive bias voltages that can be independently set within the range 0.75 V, and can supply 20 mA peak, or 2.5 mA on average per bias line (**Figure 4.32**) **[62]**. The computer is connected to the FPGA unit via 1Gbps Ethernet (RJ45), and the FPGA is powered by 12V, constant voltage power supply. FPGA is actively cooled by an 80mm fan 12V fan (**Figure 4.35**). Schematics of the readout system is shown in **Figure 4.33**.

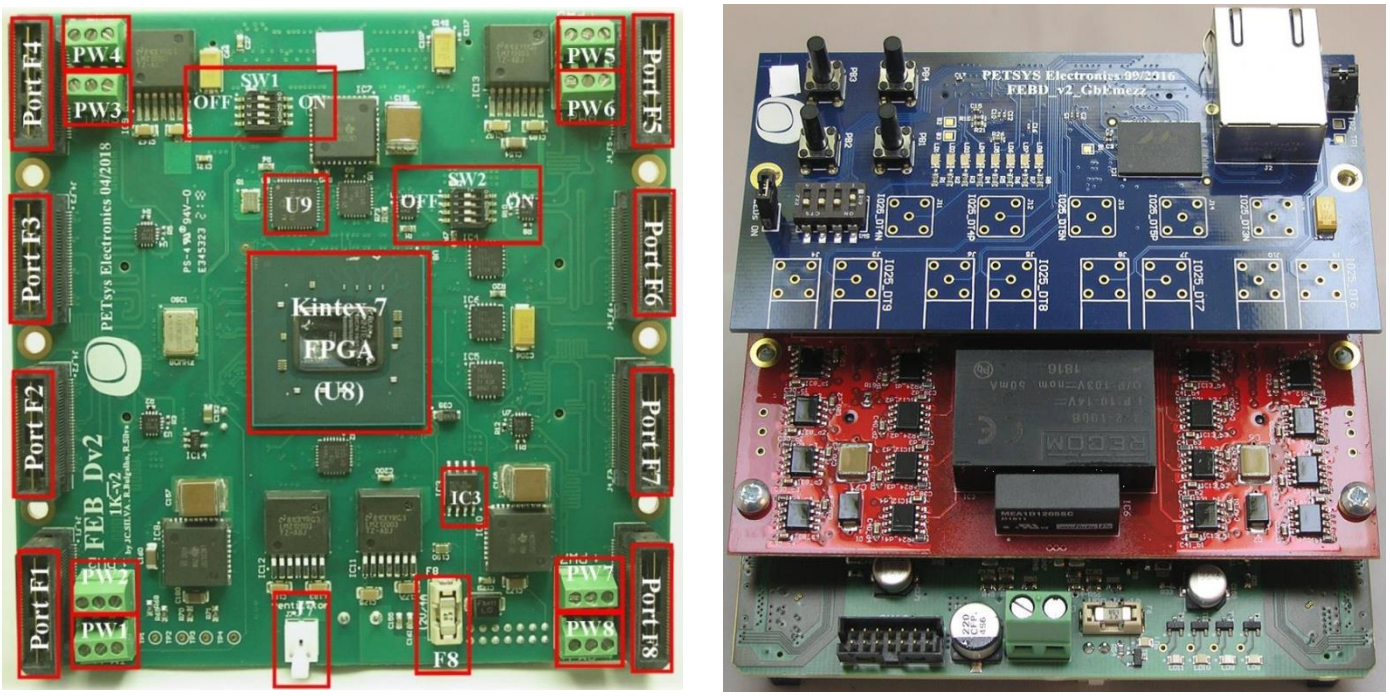

Figure 4.32 Left: Bottom side of the FPGA Board. Right: Top side of the FPGA board with positive bias mezzanine (red PCB) **[62]**.

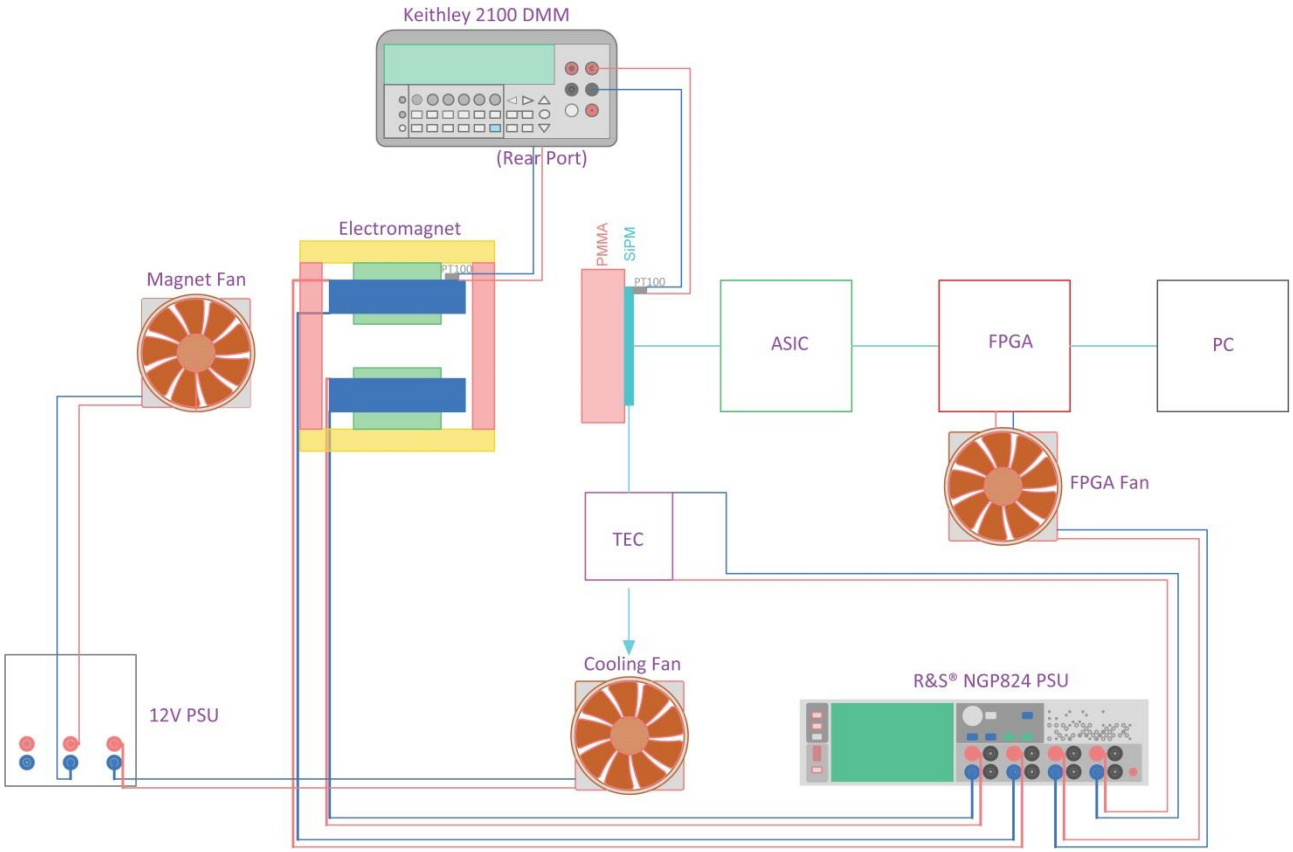

Figure 4.33 Readout system.

4.9 Dark Box

The experiment is extremely light sensitive, as the SiPM is a single photon detector. To achieve low background, the entire experiment is placed inside a dark box which was adapted from previous research with some modifications **[60]**. All the entries for power cables and coolant pipes are light sealed with 3D printed parts and rubber grommets. In order to ventilate the heat dissipated from the magnet, two 80mm 12V industrial fans were already mounted at one side of the box, and ventilation holes were drilled on the other. The entire ventilation system is light sealed. **Figure 4.34** shows the dark box.

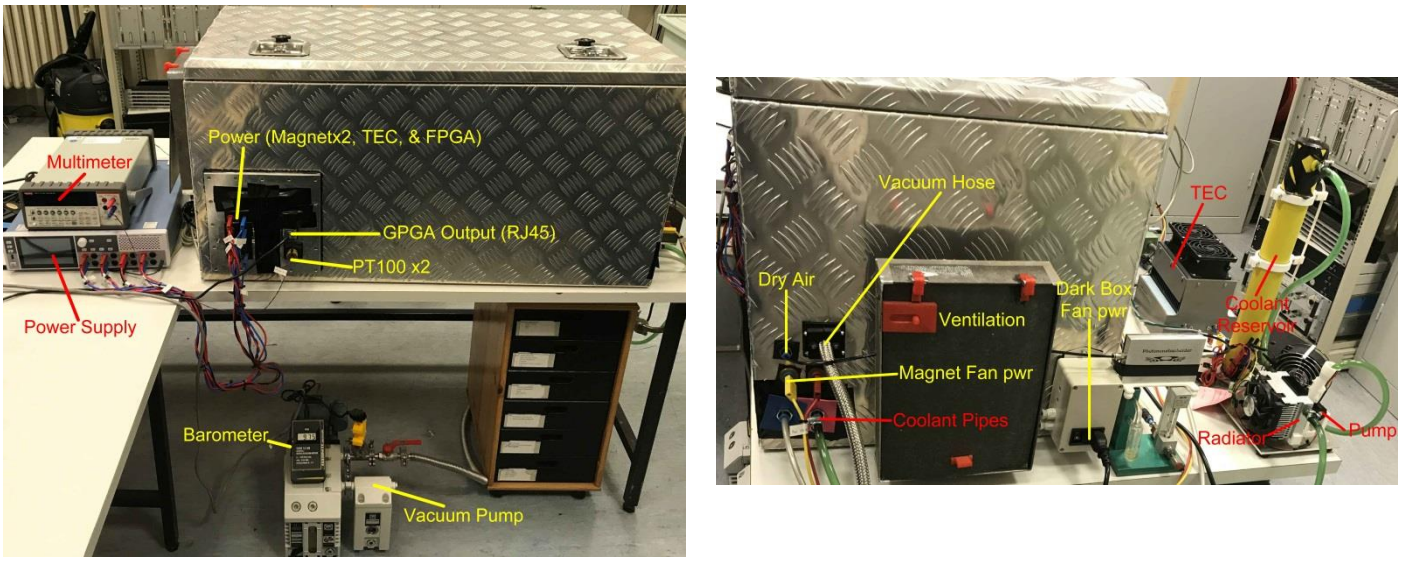

Figure 4.34 The dark box with periferals connected.

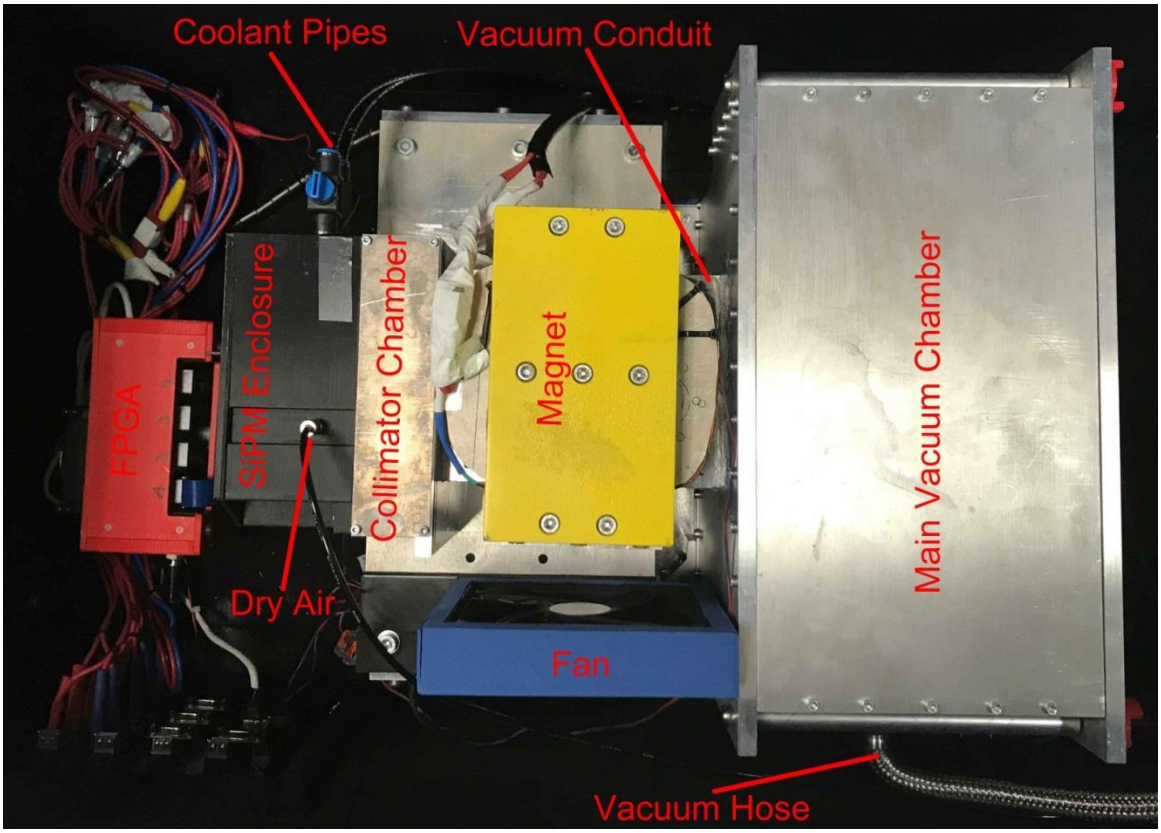

Figure 4.35 Experiment setup inside the dark box.

5. Electron Trajectory

5.1 Source Position/Angle Determination

Knowing the magnetic field profile, the electron trajectory for each intended energy can be determined. The procedure for calculating the electron trajectory is as follows: Assume the area at which the electrons are exposed to the magnetic field is Ω. We start with the right end of Ω, where the intended electron energy is supposed to enter the mu-metal at y-position corresponding to the center of the collimator. The magnetic field profile has a resolution of 0.3mm. Therefore, we gradually decrease x by a delta value smaller than magnetic profile resolution until we reach the beginning of the Ω. During each step, the electron is exposed to a magnetic field from the profile and bends accordingly. This process provides both the trajectory of the electron as well as its initial angle and position, which will be used to position the source for the experiment. A MATLAB script is written to calculate the trajectory according to the procedure described.

The source holder positions the source for each energy at correct location. **Figure 5.1** shows the trajectory of 1MeV electrons with 40mT magnetic profile and 5mm collimator opening. **Figure 5.2** shows the trajectories for 0.8-2.2 MeV electrons.

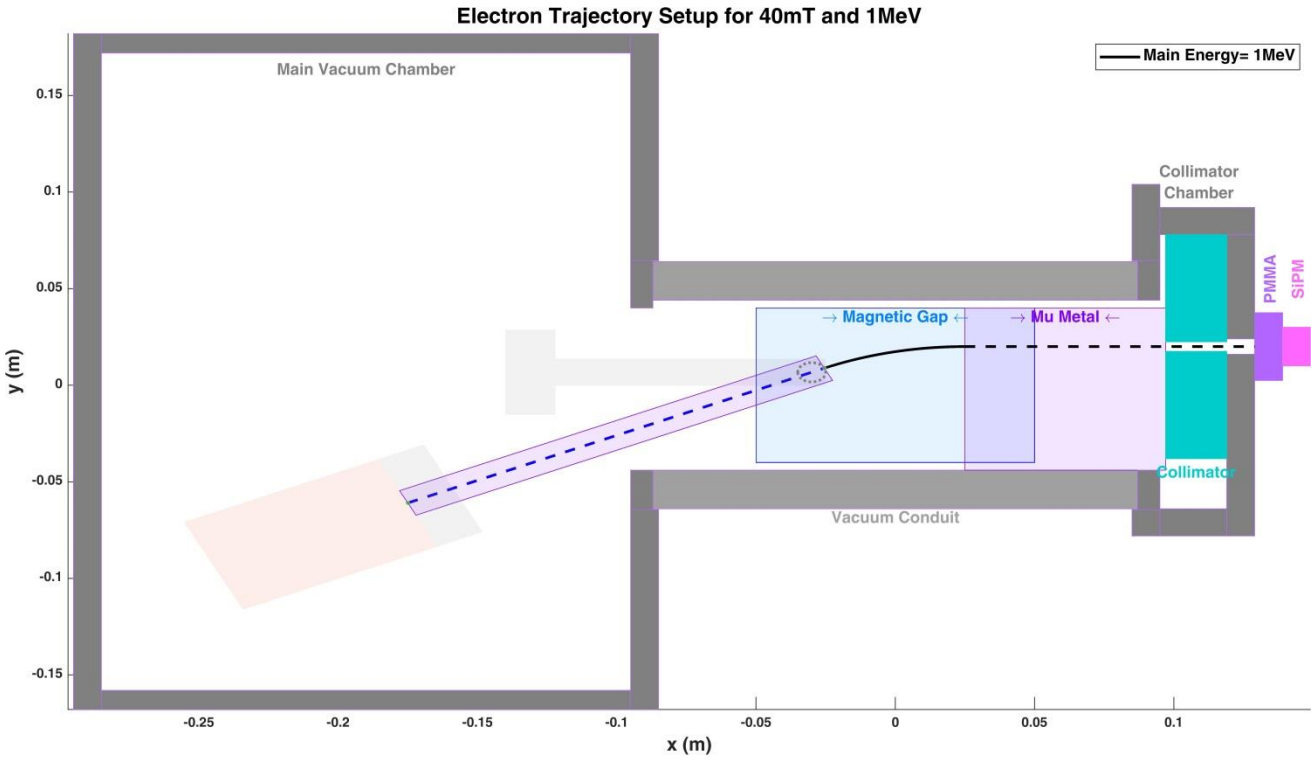

Figure 5.1 1MeV electron trajectory in the setup. Leaving the source, the electrons travel through a mu-metal tube until they reach the magent. They bend according to the magnetic field strength at each point until they reach the second mu-metal which extends until the collimator. The hammer shaped figure in the middle of the plot represents the set position on the device.

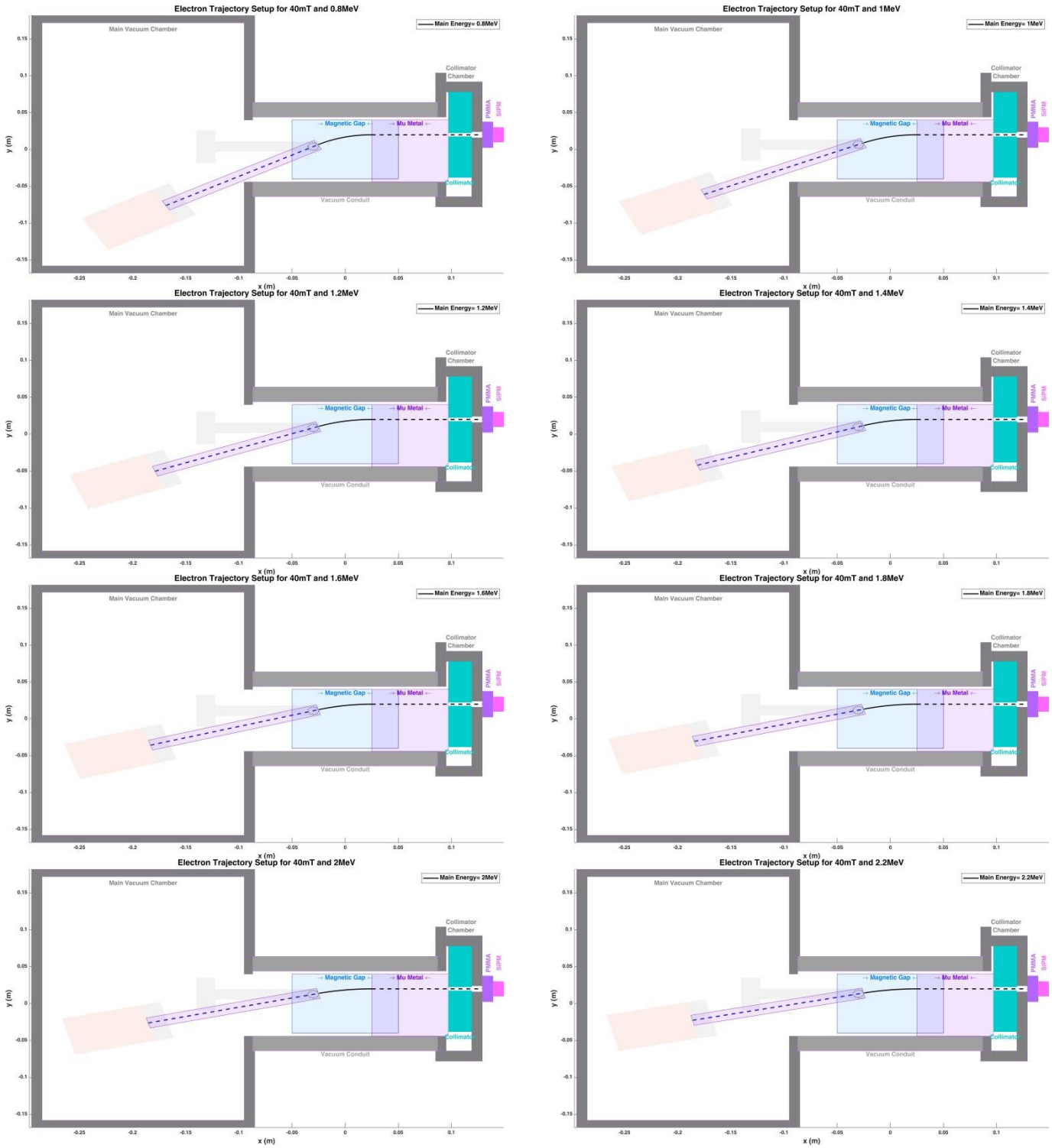

Figure 5.2 0.8 to 2.2 MeV electrons' trajetories. Lower energies require higher source angle and lower source position as they bend more in the magnetic field.

In current experiment, only 40 mT is examined, as it allows coverage of lower energies in the setup; the design of the first chamber prohibits use of energies below 1.2 MeV with 60 mT magnetic field. **Table 5.1** summarizes the source location and angle for electron energies between 0.8 and 2.2MeV.

Table 5.1: Source angle and position for different energies			
Magnetic Field (mT)	**Primary Energy (MeV)**	**Position to Set (mm)**	**Angle to Set (˚)**
40	0.8	-3.06	30.0
40	1	-0.28	25.0
40	1.2	1.60	21.5
40	1.4	2.99	18.9
40	1.6	4.06	16.9
40	1.8	4.92	15.3
40	2	5.62	14.0
40	2.2	6.20	12.9

Figure 5.3 show the magnetic field strength applied on the electron in its path for 0.8 to 2.2 MeV energies. The variations between the graphs are due to the fact that the electrons travel different paths for different energies and are exposed to different fields.

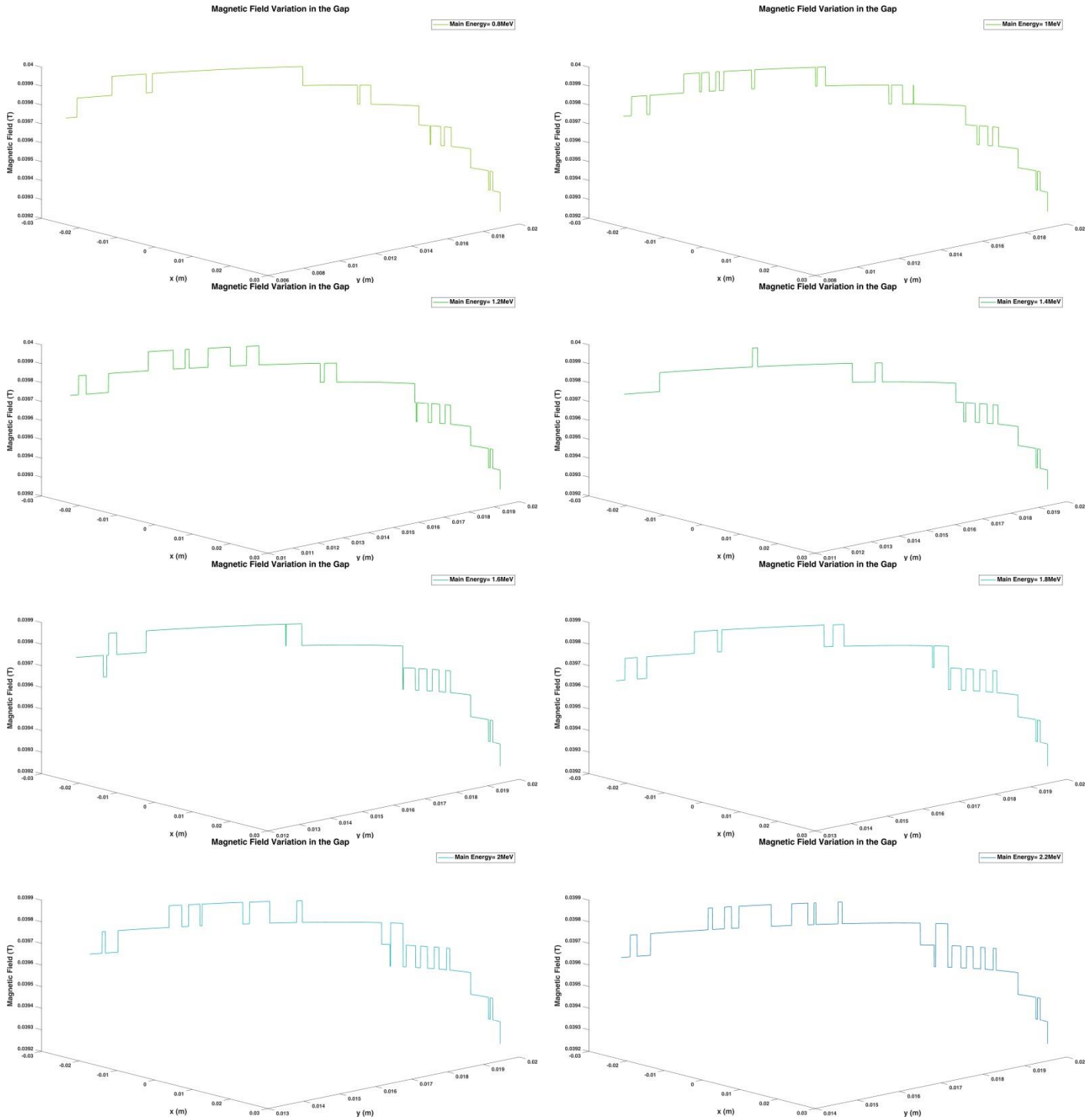

Figure 5.3 Magnetic field sensed by the electrons in their trajectory.

4.2 Energy Resolution

As discussed in Section 2.1.3, ^{90}Sr produces electrons through Beta decay in a spectrum. The detectors cannot identify electron energy based on the number of Cherenkov photons if they receive a large energy spectrum of electrons. One of the primary goals of this experimental setup is to refine the energy of the electron beam to a narrow spectrum before the Cherenkov Effect, i.e., to improve the energy resolution. In this context, the energy resolution is defined as:

$$\sigma_E = \frac{\Delta E}{E} \qquad \textbf{Eq. (5.1)}$$

where ΔE denotes the difference between the highest and lowest energies that enter the detector, and E is the intended energy which is to reach the detector. In order to improve the resolution, the magnetic field and collimator's length and opening gap need to be optimized. We discuss the effect of each on the resolution in this chapter.

A strong magnetic field bends the electrons more and brings about a better resolution due to better separation of energies. The only limitations are the size of the magnet and its capability to provide stable, homogeneous magnetic field without saturation. The magnet in this experiment has a gap dimensions of 100x80 mm, and can provide a stable field of up to 60 mT in a 50x40 mm section at its center (**Figure 1.5**).

Minimizing the opening gap of the collimator and extending its length both improve the energy resolution significantly. However, these measures also decrease the number of detected hits and are, hence, undesirable. For instance, for 2mm collimator opening, the measurement has to run for a longer duration to provide the same statistics as 4mm opening does. The collimator is set to 5mm opening to build sufficient statistics. Such large opening however comes at the expense of lower energy resolutions.

In order to determine the energy resolution when the experiment is adjusted for a specific energy, escape angle of each energy must be determined. That is, when the source is placed at a specific angle and position, the escaping angles of other energies need to be determined. If the intended energy is E, the escaping angles of a higher energy (E_1) and a lower energy (E_2) are α_1 and α_2 respectively (**Figure 5.4**). The trajectory function of the main energy becomes:

$$y_E = \sqrt{{r_E}^2 - (x_E - x_0)^2} + y_0 \qquad \textbf{Eq. (5.2)}$$

Where (x_0, y_0) is the coordinates of the center of a circle with radius equal to the bending radius r_E of the trajectory at any given (x_E, y_E). r_E is calculated from **Equation 2.58** for each (x_E, y_E).

To calculate the trajectory function of other energies, we start at angle and location determined in Section 5.2 for any given main energy. X-coordinate is incrementally increased until mu-metal and trajectory and angle are determined for each step. The final point's angle corresponds to α of that energy. Once the electrons enter the mu-metal, their movement is no longer influenced by the magnetic field, and they move in a straight line. Therefore, determination of escaped energies and their corresponding angles involves calculating their trajectory inside the magnetic field and in the mu-metal after the magnet.

$$y_{E_1/E_2} = \begin{cases} \sqrt{{r_{E_1/E_2}}^2 - \left(x_{r_{E_1/E_2}} - {x'}_0\right)^2} + {y'}_0 & inside\ the\ magnet \\ tan(\alpha_1/\alpha_2) \times x_{E_1/E_2} + c & outsidethe\ magnet \end{cases} \qquad \textbf{Eq. (5.3)}$$

$({x'}_0, {y'}_0)$ corresponds to the center of the circle for E_1/E_2 energies at any point in electrons' path. c is the constant offset from the origin easily calculable for last coordinate of the first trajectory function.

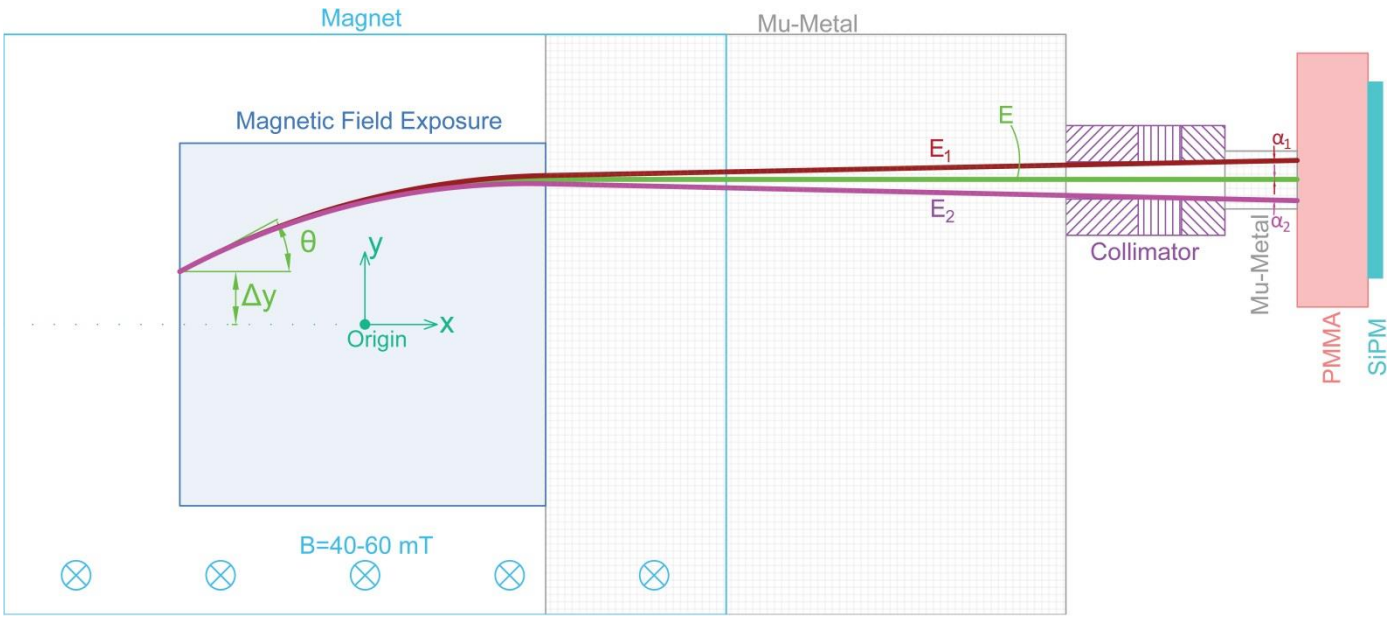

Figure 5.4 Determination of the escaping angle of highest and lowest energies.

Knowing α of each energy determines whether or not it escapes the collimator. Highest and lowest escaped energies are then used to determine the energy resolution for each main energy. A MATLAB code is written to calculate the angle of each escaping energy as well as their final location with regard to the PMMA surface. **Tables 5.2** summarizes the results.

Tables 5.2 Escaping energies and their angle/position.				
Primary Energy (MeV)	Collimator Opening (mm)	Energy Resolution (%)	Min Escaping Energy	Max Escaping Energy
0.8	5	10	0.76MeV at -1.09°	0.84MeV at 0.99°
1	5	12	0.94MeV at -1.15°	1.06MeV at 1.04°
1.2	5	14.17	1.12MeV at -1.15°	1.29MeV at 1.15°
1.4	5	15.71	1.3MeV at -1.12°	1.52MeV at 1.18°
1.6	5	17.5	1.47MeV at -1.18°	1.75MeV at 1.17°
1.8	5	18.33	1.65MeV at -1.12°	1.98MeV at 1.15°
2	5	20	1.82MeV at -1.13°	2.22MeV at 1.16°
2.2	5	13.18	1.98MeV at -1.19°	2.27MeV at 0.33°

Figure 5.5 shows the escaping electrons energy range for 0.8 to 2.2 MeV energies.

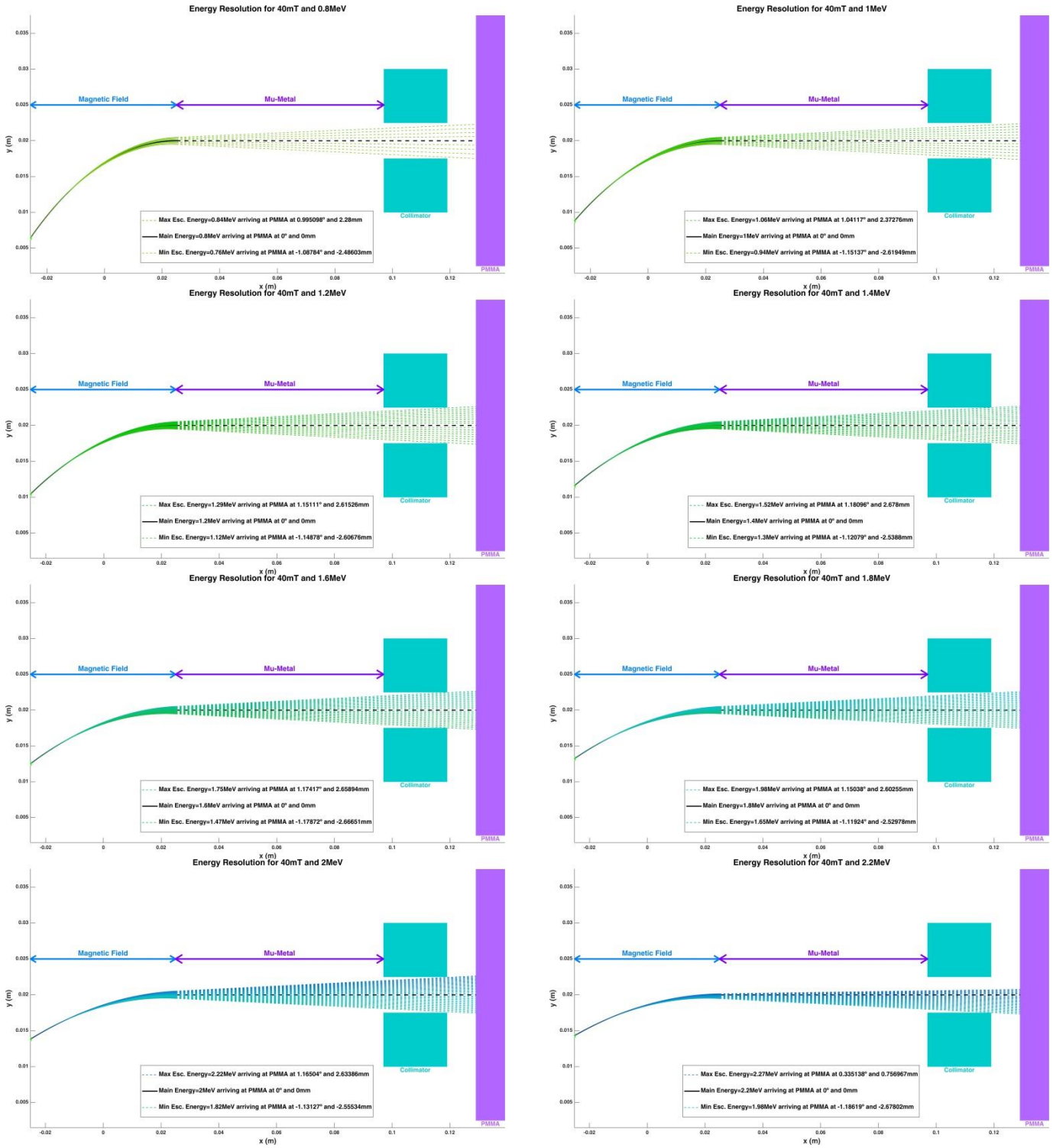

Figure 5.5 Results of energy resolution calculations for 0.8 to 2.2MeV trajectories.

At 40mT magnetic field, the best resolution is achieved for the lowest energy, i.e., 0.8MeV, for which the energy resolution is around 10%. The highest and the lowest escaping energies are 0.76 MeV and 0.84 MeV respectively. Higher energies have worse resolution, as they bend less in the same magnetic field (**Figure 5.6**). Therefore, the energy separation is less than that of lower energies are. The lowest energy resolution in the range is for 2.2 MeV. However, since ^{90}Sr's spectrum has a maximum energy of 2.276 MeV, its effect is not fully realized. That is, there are non-existing escaping energies higher than 2.276 MeV. For 2 MeV, resolution is around 20%, and energies from 1.82 to 2.22 MeV escape the collimator. The

experiment will run for 0.8 to 2 MeV electrons, as 2.2MeV electrons have such low statistics that requires measurement time beyond the capability of current setup. Overall, we expect a resolution of 10 to 20%.

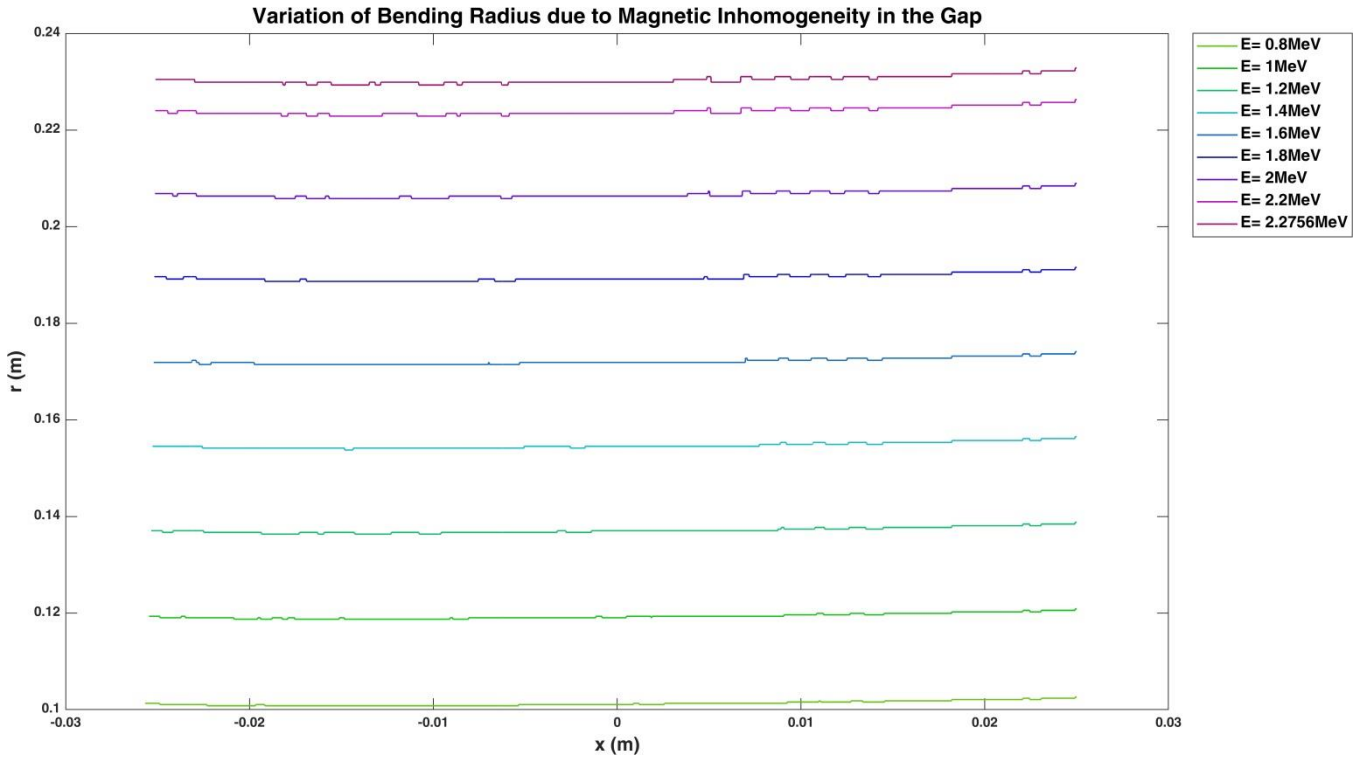

Figure 5.6 Average bending radius of each energy in 40mT magnetic field.

6. Calibration of Data Acquisition System

This chapter outlines procedures followed for preparation of the hardware for measurement. Prior to start of the procedure, the cooling system must provide a stable temperature for the ASICs and the SiPM. Large temperature shifts can affect the performance of certain modules of the ASIC. With the current cooling system, a temperature of -18.5 °C can be achieved at the tip of the cooling finger where the PT100 temperature sensor is located. The cooling system takes roughly 5 minutes to reach equilibrium. Before taking measurements, certain modules of the ASIC circuitry, namely trigger threshold of discriminators, Time-to-Digital Converter (TDC) and Charge-to-Digital Converter (QDC) need to be calibrated **[63]**. TDC has a time binning of 30ps **[60]** and is used extensively for the measurement, whereas QDC is not used for the type of measurement relevant to this experiment.

6.1 Discriminator Calibration

The TPFPET2 ASIC has 64 independent channels, each of which is equipped with two transimpedance post-amplifiers, optimized for time resolution and charge integration, three voltage mode discriminators, high performance Time-to-Digital converter (TDC), and Charge-to-Digital Converters (CDC) on a 110 nm CMOS technology **[64]**. The three discriminators T1, T2, and E are used alone or in combination to perform trigger logic for Time and Charge Integration or Time-over-Threshold (ToT) measurement modes using four available triggers T, E, Q, and B as shown in **Figure 6.1**. The discriminators' main functions are timing measurements, rejection of low amplitude pulses, start of the charge integration window, and trigger the event data readout. ToT mode requires triggers T and E to be validated by trigger B, whereas Charge Integration mode requires Triggers T, E, and Q to be validated by trigger B. Charge Integration mode is not sensitive enough to 1p.e. level. Charge Integration mode is usually used for PET applications where the energy of the incident photons produced by a scintillator is measured. In this work ToT method is used. Given that timing threshold and amplitude discrimination are identical and within dynamic range in the current work, discriminator T1 can be used alone in ToT. In this case, ToT is the time during which, the signal stays above the T1 discriminator threshold, measured directly by TDC.

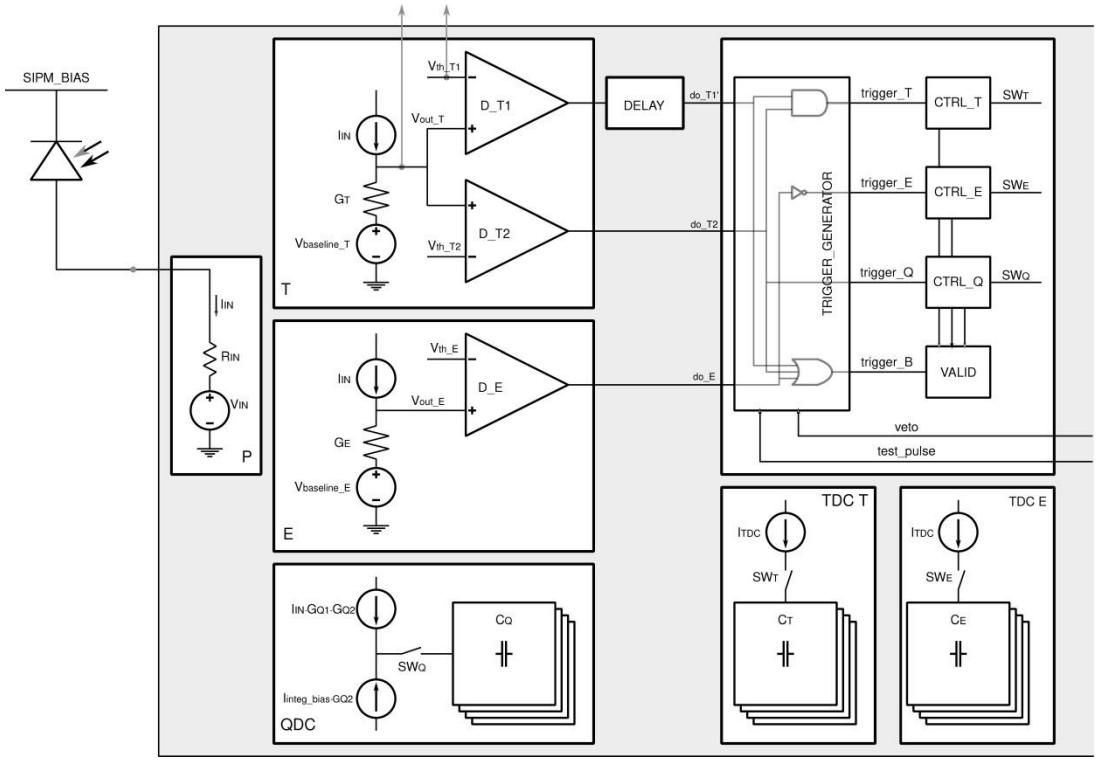

Figure 6.1 Simplified equivalent of a single TOFPET ASIC channel **[64]**.

Discriminator calibration involves scan of the T1 discriminator threshold at a bias voltage below breakdown to determine baseline and noise and a second identical scan at operational voltage to determine dark count. The procedure is carried out at -18.5 °C when the collimator is open by 5 mm and the source is removed. It is common to perform this task when the collimator is shut to reduce the effect of stray light creating signal and contributing to the dark signal. On the other hand, since the dark count will be subtracted from the signal in the measurement phase, the effect of stray light can be also removed from the signal if the collimator remains open during calibration. **Figure 6.2** demonstrates the result of discriminator calibration.

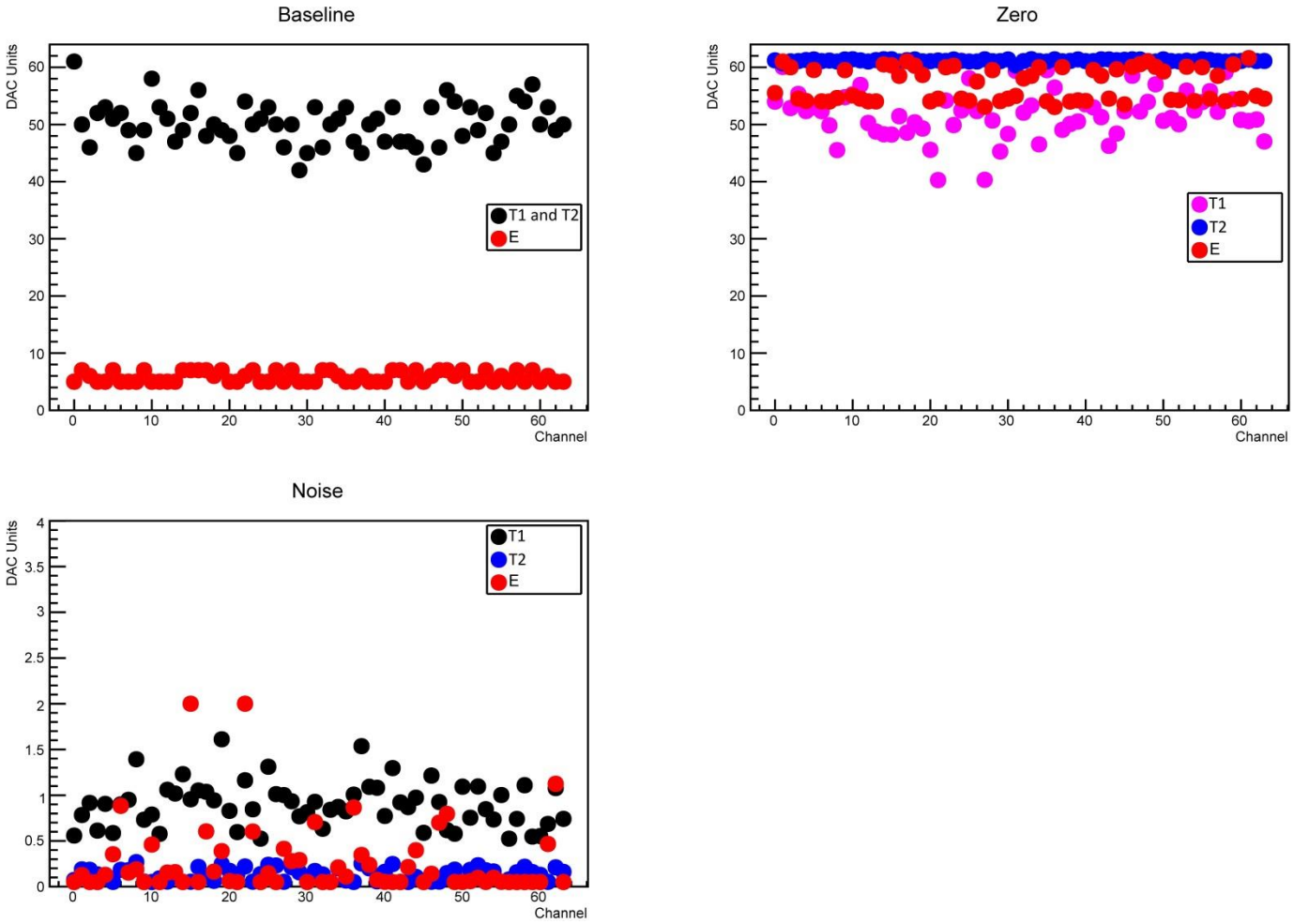

Figure 6.2 Discriminator calibration summary plots for each of the 64 channels. Baseline plot (Top Left) represents the value of amplifier's adjusted DAC value after convergence. Zero plot (Top right) corresponds to amplifier's baseline in DAC units. Bottom plot represents amplifier's noise level in DAC units. Each of the three discriminators are color coded.

6.2 TDC Calibration

As mentioned previously, each of the 64 channels of the ASIC houses its own quad-buffered analogue interpolation TDCs with time binning of 30 ps and charge integration ADCs with linear response up to 1500 pC input charge **[64]**. TDC calibration makes corrections to the very low level of non-linearity in the correspondence between TDC codes and reference clock phase. Using a test pulse signal which is synchronous to the clock with an adjustable phase delay, the trigger signal is scanned and a correction curve is obtained via a second order polynomial fit function. The results are shown in **Figure 6.3**.

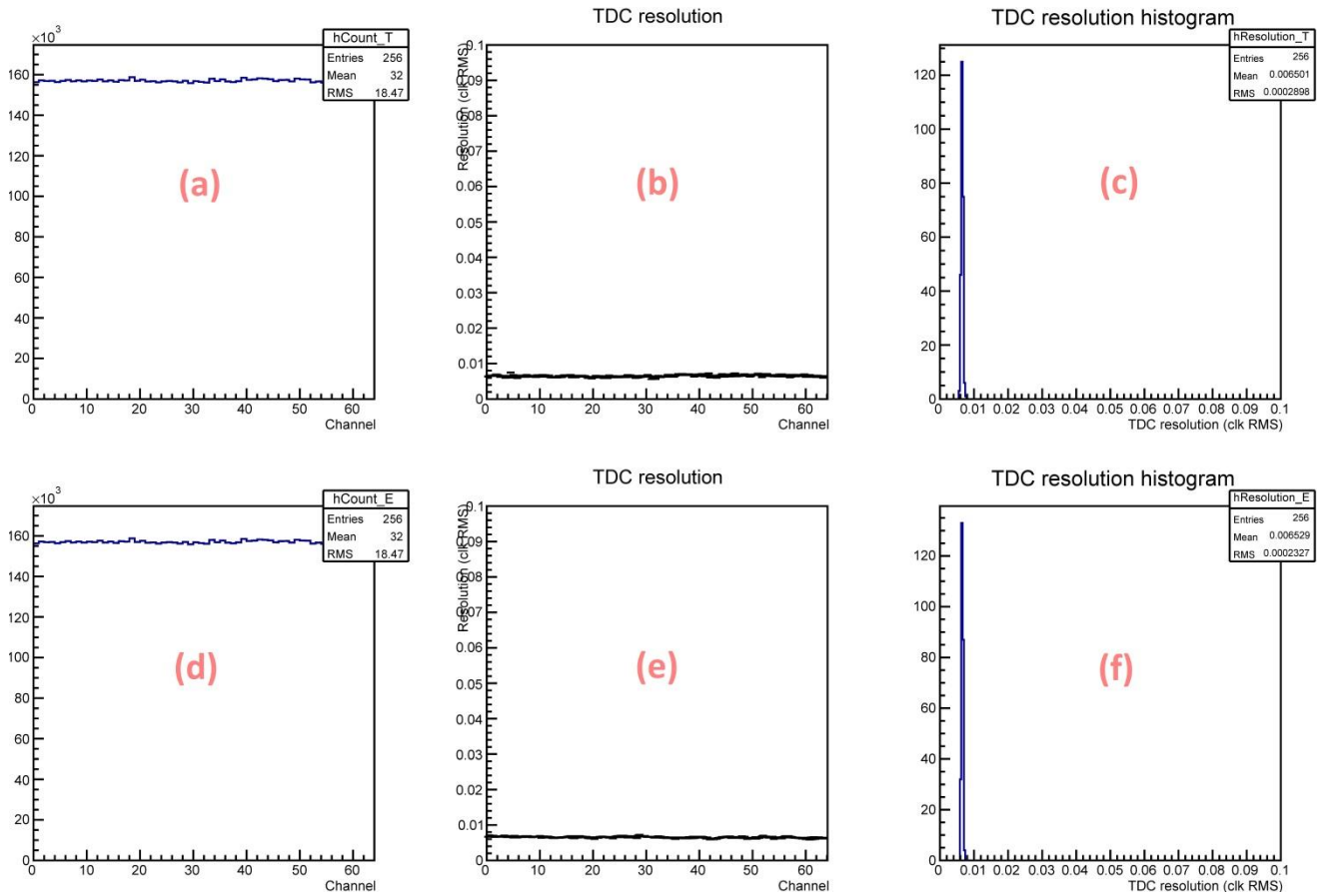

Figure 6.3 TDC calibration summary plots for each of the 64 channels. The upper plots show the number of test pulse events used for calibration (a), the distribution per channel of the obtained TDC resolution after calibration (b) and the overall distribution of resolutions obtained after calibration (c), for the first discriminator (T1 in default trigger mode). The plots on the bottom (d, e, and f) are the same but for the second discriminator (E in default trigger mode).

6.3 Discriminator Threshold Adjustment

The signals from the SiPM have distinct amplitudes. TOFPET application produces a series of staircase functions for dark count rate at all available threshold levels after calibrating the T1 discriminator (**Figure 6.4**). In order to identify the correct threshold value the location of steps must be identified for all channels. Based on the cooling provided to the SiPM, dark count rate can vary drastically and the trigger level has to be adjusted accordingly. Given the extreme cooling provided and the dark count rate, triggering the SiPM at 1 p.e. level is possible.

Triggering the SiPm at 1 p.e. requires setting the threshold somewhere in the flat region of the 1 p.e. level in DCR-versus-threshold graph. Ideally, the trigger must be set at a threshold lower than 1p.e. in order to capture 1 p.e. signal as well as 2 p.e. and larger. As shown in **Figure 6.5** (voltage signal), if we trigger at 1p.e., we can only capture 2p.e. or higher signals. 0.5p.e. corresponds to the middle of the flat area in 1p.e. level. If we trigger at the left corner of the 1p.e., we will lose 1p.e signals. That is the point where the Dark

Count Rate starts to drop. A C++/ROOT script was written to read the data points and calculate the derivative in a numerical fashion, i.e., it takes the slope between every two consecutive points. The script enables the program to recognize where noise level is and where each jump occurs. In order to set for 1p.e., ideally we choose a point after the last jump and before the noise level, e.g., 0.5p.e. level. This procedure is carried out for all 64 channels. **Figure 6.4** shows the output of calibration for Channel 18 with 1 p.e. levels identified using the script. The threshold values are stored and will be later used by the hardware to trigger the SiPM at 1 p.e. level during measurement.

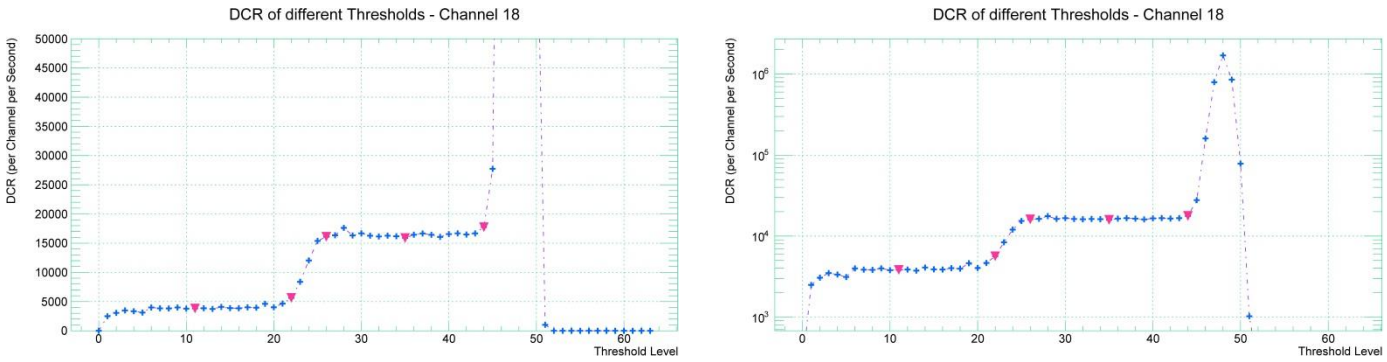

Figure 6.4 Dark count rate at different threshold levels for channel 18. Y-axis is shown in normal form in left plot and in log form in the right plot to show the noise level. The script identifies start and end of 1 p.e. level and sets the threshold to the middle, ensuring that the detector triggers at 1 p.e.

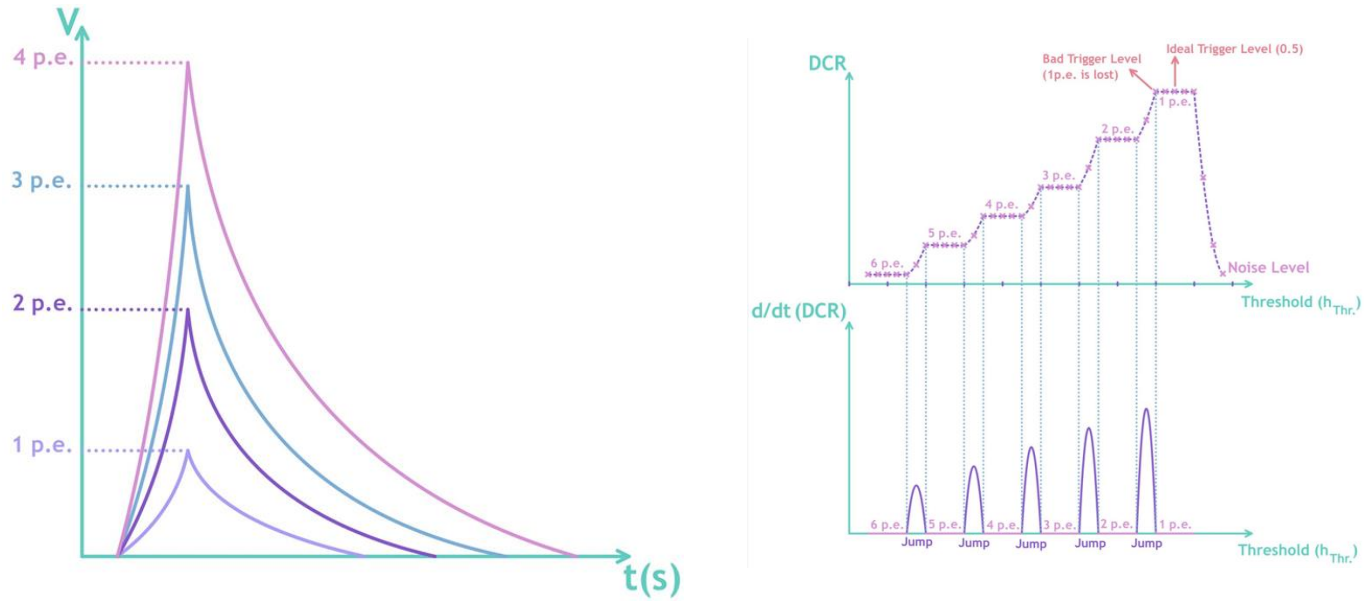

Figure 6.5 Left: Typical output signal of SiPM. Right: DCR-Vs.-Threshold graph with p.e. levels.

6.4 ToT to Number-of Photons Conversion

The discriminator T1 is responsible for measuring the ToT of a signal. TOFPET program provides a histogram of the ToT counts for every channel after each measurement. A typical voltage signal of an SiPM

is shown in **Figure 6.6-a**. The algorithm discussed in Section 6.3, determines and sets the threshold automatically. The objective is to convert the signal amplitude into number of photons. A mathematical model of the signal requires two assumptions.

First, t=0 corresponds to the time when signal rises beyond threshold $A_{Thr.}$. Therefore, time axis needs to be shifted forward. Second, discharge time τ_d is assumed to be negligible compared to recovery time $\tau_{recovery}$. As mentioned in Section 3.4, recovery time is an order of magnitude larger than discharge time is due to the difference between quenching resistor and serial resistor in SPADs **[65]**. Both discharge and recovery time are reduced proportionally by reducing net capacitance of SPADs according to **Equations 3.6** and **3.7**. Once threshold value is introduced, only a portion of the discharge time τ_d contributes to the ToT, as shown in **Figure 6.6-b**. Hence, the assumption is not unrealistic.

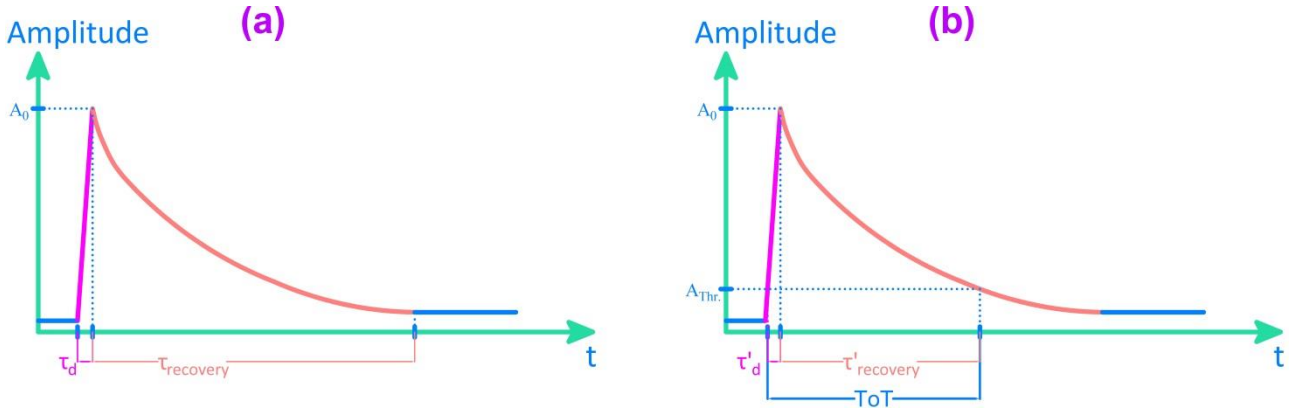

Figure 6.6 (a) Conceptual output pulse of an SiPM channel with discharge time and recovery time in the order of ~1ns and ~10ns respectively. (b) Introduction of the threshold value cuts part of the discharge and recovery times.

The rising and recovery curves of the amplitude signal follow exponential curves.

$$A_d(t) = A_0 \cdot (1 - e^{\left(\frac{-t}{\tau_d}\right)}) \qquad \textbf{Eq. (6.1)}$$

$$A_{recovery}(t) = A_0 \cdot e^{\left(\frac{-t}{\tau_{recovery}}\right)} \qquad \textbf{Eq. (6.2)}$$

where A_0 is the total amplitude of the signal. A_0 can be expressed in terms of the amplitude of a 1p.e signal:

$$A_0 = n \cdot A_{1p.e.} \qquad \textbf{Eq. (6.3)}$$

n stands for the number of photons corresponding to amplitude A_0. Note that with the first and second assumption, t=0 in the **Equation 6.2** refers to the peak of the signal. Solving **Equation 6.2** for time t=ToT yields the threshold value.

$$A_{recovery}(ToT) = n \cdot A_{1p.e.} \cdot e^{\left(\frac{-ToT}{\tau_{recovery}}\right)} = A_{Thr.} \qquad \textbf{Eq. (6.4)}$$

Rearranging **Equation 6.4** provides the relation between ToT and number of photons which is required to perform measurements.

$$ToT = \tau_{recovery} \cdot \left(ln(n) - ln\left(\frac{A_{Thr.}}{A_{1p.e.}}\right)\right) \qquad \textbf{Eq. (6.5)}$$

$$n = \frac{A_{Thr.}}{A_{1p.e.}} \cdot e^{\left(\frac{ToT}{\tau_{recovery}}\right)} \qquad \textbf{Eq. (6.6)}$$

Equation 6.6 can be used to determine the number of photons from the measurement, provided the parameters $\frac{A_{Thr.}}{A_{1p.e.}}$ and $\tau_{recovery}$ are known. The following procedure is used to determine the number of photons.

The radioactive source is positioned so that it is directed towards the center of the SiPM array (**Figure 6.7**), and a measurement is carried out for 18 minutes to accumulate enough statistics. PETsys program creates a ToT histogram for all 64 channels. A typical ToT histogram is shown in **Figure 6.8-a**. A peak finding algorithm **[60]** which finds peak values in ToT histograms and associates each peak with its corresponding p.e. signal was modified to match the parameters of the current work and used to create a ToT-vs.-n graph such as the one shown in **Figure 6.8-b** for each channel.

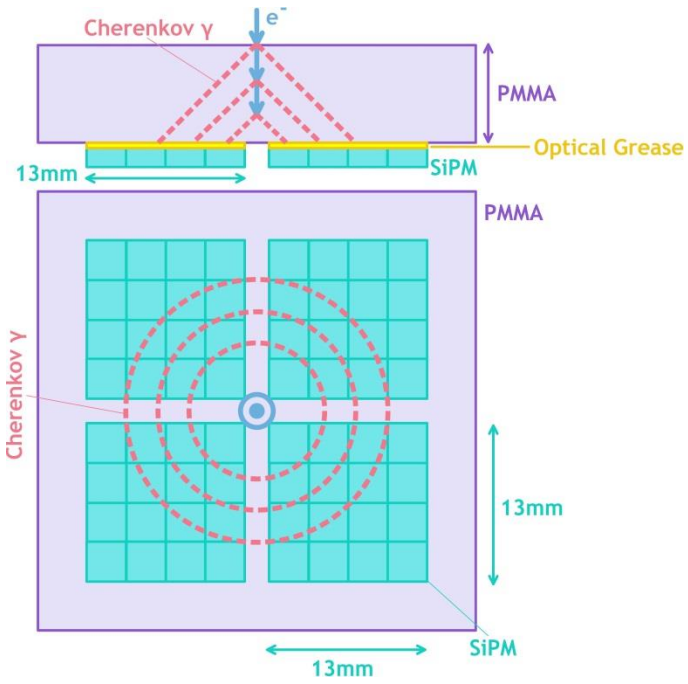

Figure 6.7 Schematics of the callibration setup to determine τ value

The peak finding algorithm searches through all the peaks in histograms and finds the ToT value corresponding to each peak. Given that the trigger is set to 1 p.e., the first peak corresponds to 1 photon, the second peak corresponds to 2 and so forth. All photon numbers are determined in this fashion and plotted against their corresponding ToT value in a graph such as the one shown in **Figure 6.7-b**. Then, the algorithm performs a fit to the discrete entries on n-vs.-ToT using **Equation 6.6** to determine $\frac{A_{Thr.}}{A_{1p.e.}}$ and $\tau_{recovery}$ parameters for each channel. These two values are stored for each channel and will later be used to calculate number of photons created in each channel during 100-ns events. **Figure 6.9** shows the result of the algorithm for channel 35.

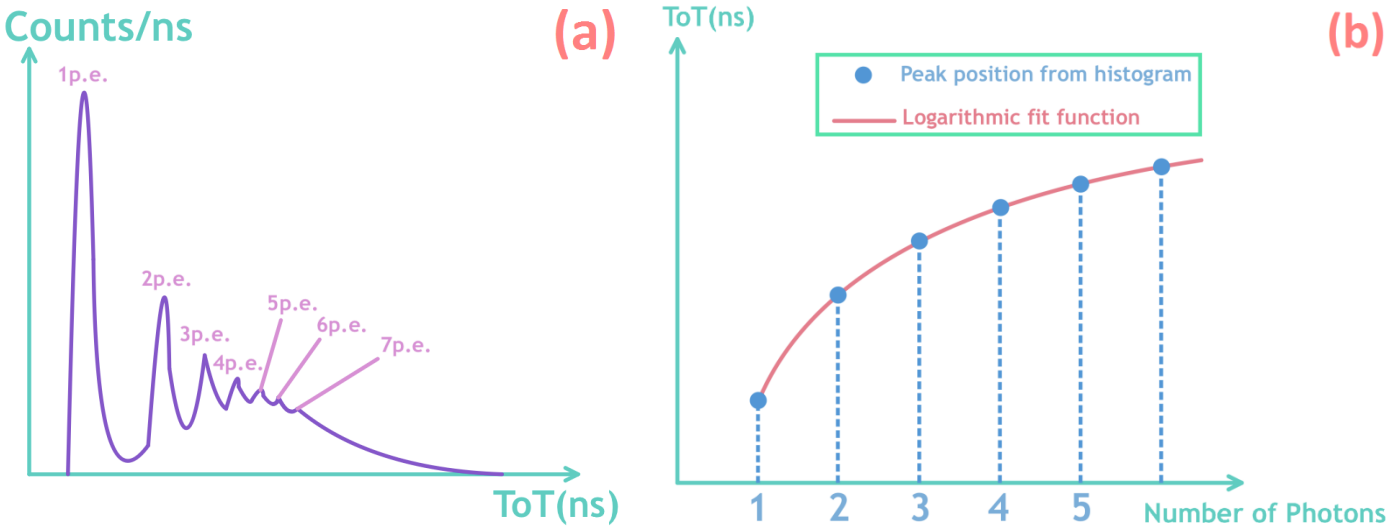

Figure 6.8 (a) Output ToT histogram of PETsys. (b) Number of Photons Vs. Tot graph and its fit based on **Equation 6.6**.

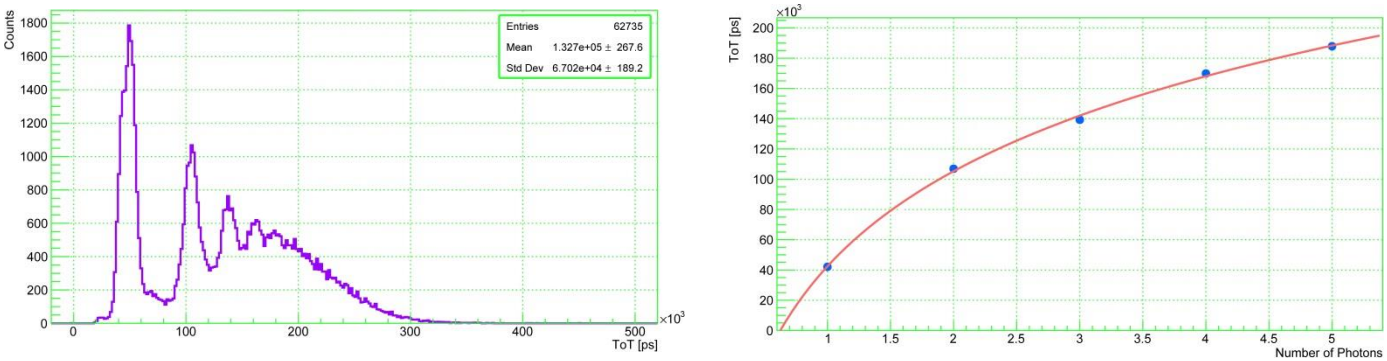

Figure 6.9 Output result of the algorithm for Channel 35. On the left side, the ToT distribution is shown.

The algorithm finds the peaks, associates them to photon numbers, and plots them against their corresponding ToT values (right side plot). Finally, a fit function using **Equation 6.6** is used to determine $\frac{A_{Thr.}}{A_{1p.e.}}$ and $\tau_{recovery}$ parameters for each channel.

This concludes the calibration procedure.

7. Measurement and analysis

In previous chapters, we discussed each equipment used in the experiment and the calibrations required to prepare different modules such as the electromagnet, ASIC, and the cooling system, etc. for the measurements. This chapter focuses on outlining the measurement procedure and examining the results.

7.1 Measurement Conditions

The measurements are performed with a 35x35x9.8mm PMMA at -18.5°C. The magnetic field is set to 40mT for all measurements. A high-power fan dissipates the heat from the magnet coils, and a PT100 temperature sensor constantly monitors the temperature of the coils. A stable, 6-mbar vacuum is provided by a rotary vane vacuum pump during the measurements. The ^{90}Sr source used for the experiment has a strength of 180 Mbq. The source is positioned in a way that primary energies entering the collimator are 0.8, 1, 1.2, 1.4, 1.6, 1.8, and 2MeV according to **Table 5.1**. For each energy, the duration of the measurement is selected based on spectrum of the $^{90}Sr/^{90}Y$ **[66]** as shown in **Figure 7.1**, so that all measured energies produce similar statistics. For that purpose, spectrum of ^{90}Sr and ^{90}Y are combined and renormalized. For instance, for 0.8MeV, the spectrum suggests the highest population; therefore, the minimum duration of 1080 seconds is assigned to it. On the other hand, 2MeV has the lowest population, and the duration is adjusted to 5526 seconds to match that population. The cooling system can provide a stable temperature for 6 to 7 minutes, after which the heat from the SiPM and water pump disturbs the quasi steady-state condition, and the system needs to be reinitialized. Therefore, all the measurements are divided into smaller durations of up to 400 seconds, and the data are collated at the end. **Table 7.1** outlines the conditions of each measurement. During each set of data taking, the laboratory is kept in dry and cool conditions via a HVAC unit. In addition to using the dark box, all measurements are carried out during night time and in complete darkness to ensure minimum stray light reaches the SiPM.

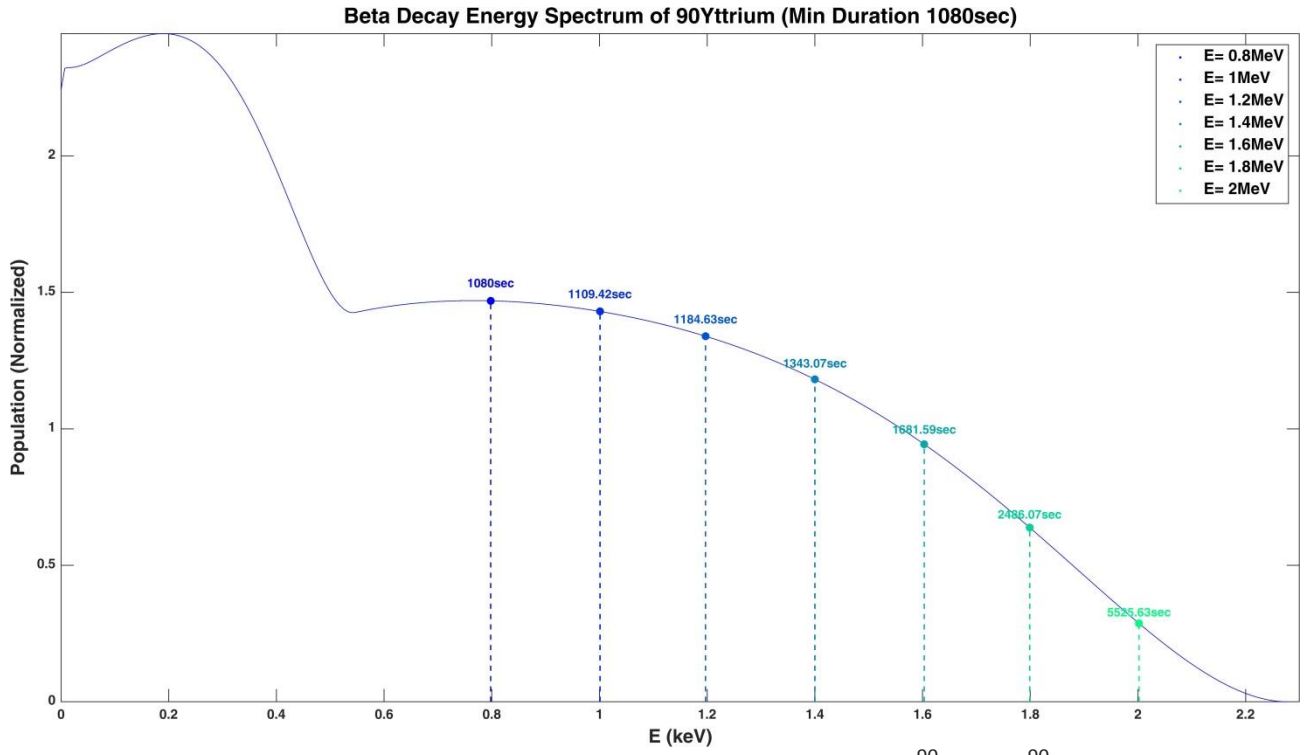

Figure 7.1 Combined and renormalized spectrum of ^{90}Sr and ^{90}Y.

Tables 7.1 Measurement Conditions for different Electron Energies					
Energy (MeV)	**Total Time (Sec)**	**Duration of each run (Sec)**	**# of Measurements**	**Time of Day**	**Temperature (Ohm/°C)**
0.8	1080	360	3	6 p.m.-9 p.m.	93Ω/-17.9°C
1	1110	370	3	9 p.m.-11 p.m.	93Ω/-17.9°C
1.2	1185	395	3	11 p.m.-1:40 a.m.	93Ω/-17.9°C
1.4	1344	336	4	2 a.m.-5 a.m.	93Ω/-17.9°C
1.6	1685	337	5	6 p.m.-10 p.m.	93Ω/-17.9°C
1.8	2492	356	7	11 p.m.-5 a.m.	93Ω/-17.9°C
2	5530	395	14	6 p.m.-5 a.m.	93Ω/-17.9°C

7.2 Data Taking

The temperature of the SiPM is monitored by a PT100 sensor attached to a Keithley 2100 $6\frac{1}{2}-$ digit Resolution Digital Multimeter. It takes roughly 5 minutes for the temperature to reach the vicinity of -18.5°C and about 45 seconds for the vacuum pump to reach 6 mbar. Therefore, the pump is turned on 4 minutes after cooling system so that once the temperature is stable, the measurement can commence immediately. For each energy, one set of dark measurement is taken without the source first, followed by source measurements. As mentioned before, after each measurement, the system needs to be reinitialized to ensure stable temperatures. A C++/Python code compiled by the previous research student [60] was already available. It was used with no modification to take data. The code uses the input data stored during calibration to calculate the number of photons. To ensure minimum dark count in the results, the

coincidence trigger of the SiPM is set to 10 channels, i.e., the SiPM only registers a signal when 10 or more channels register a signal during a coincidence time window of 10 nanoseconds.

7.3 Analysis

Once data taking for a specific energy is complete, the raw data is collated and analyzed. A C++/ROOT code is developed to extract necessary information, create histograms and data sets which will be discussed in the following. After the data taking is performed, each set of measurement is analyzed separately. The code produces the following data:

7.3.1. Time-over-Threshold Signal

ToT is the first data produced during analysis. The calibration parameters acquired in Chapter 6 are used to create ToT histograms. All subsequent data are created based on the ToT data. **Figure 7.2** demonstrates the ToT results of Channel 1 at different energies.

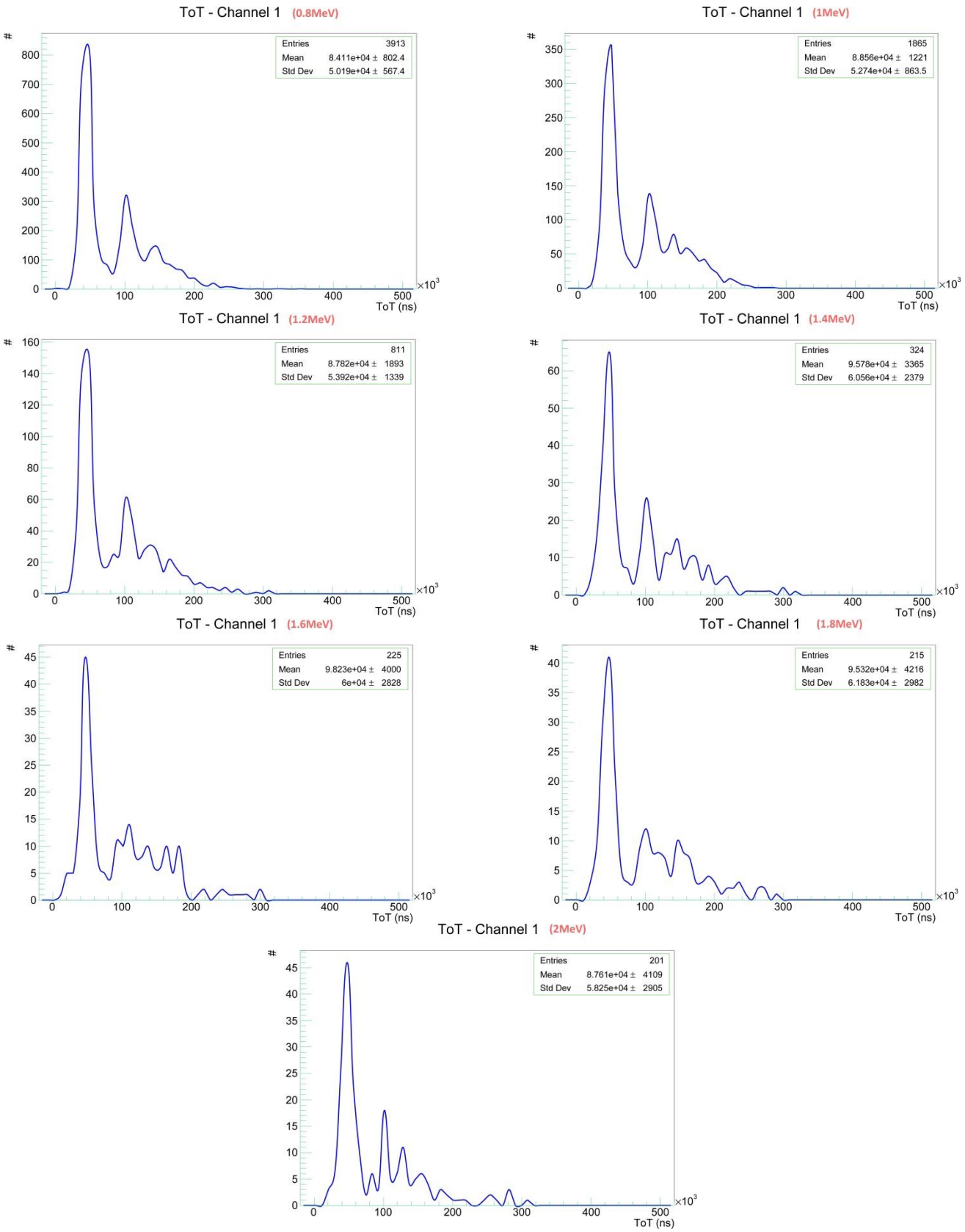

Figure 7.2 Time-over-Threshold Signal of the first channel for E=0.8, 1, 1.2, 1.4, 1.6, 1.8, and 2MeV energies. Afterpulse manifests itself in terms of small peaks mostly between 1p.e. and 2p.e. peaks. Roughly 10% afterpulse is expected with current SiPM.

7.3.2 Number of Coincidence-Triggered Channels

The program is set to trigger an event when more than 10 channels produce a signal within 10 ns. The number of events with different sets of triggered channels are tabulated in a histogram during the analysis phase. Each measurement set produces a histogram such as the one shown in **Figure 7.3**. Then, the histogram data of different sets are added together to create a single histogram for each energy. **Figure 7.3** represents the number of triggered channels when the experiment is set to allow 0.8 MeV electrons into the PMMA.

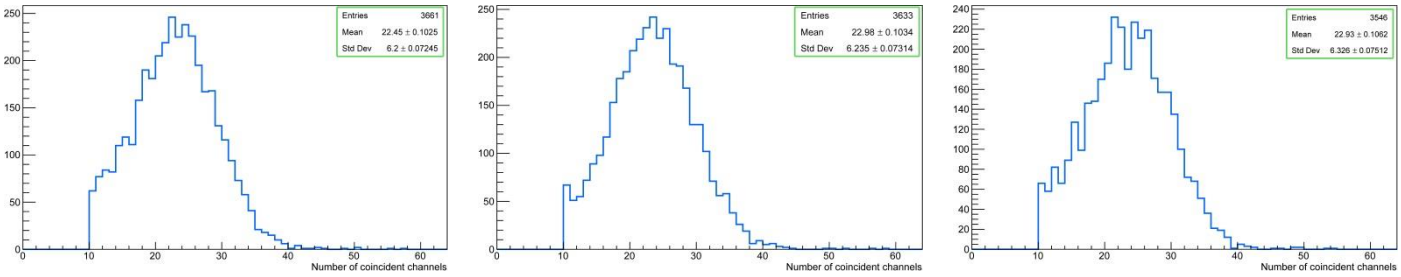

Figure 7.3 Number of Coincidence Channels histograms for E=0.8MeV energy. This energy entails three sets of measurements which are subsequently combined.

A similar procedure is performed on 1, 1.2, 1.4, 1.6, 1.8, and 2MeV energies. **Figures 7.4** and **7.5** show number of coincidence channel histograms for each energy individually and comparison of all energies respectively.

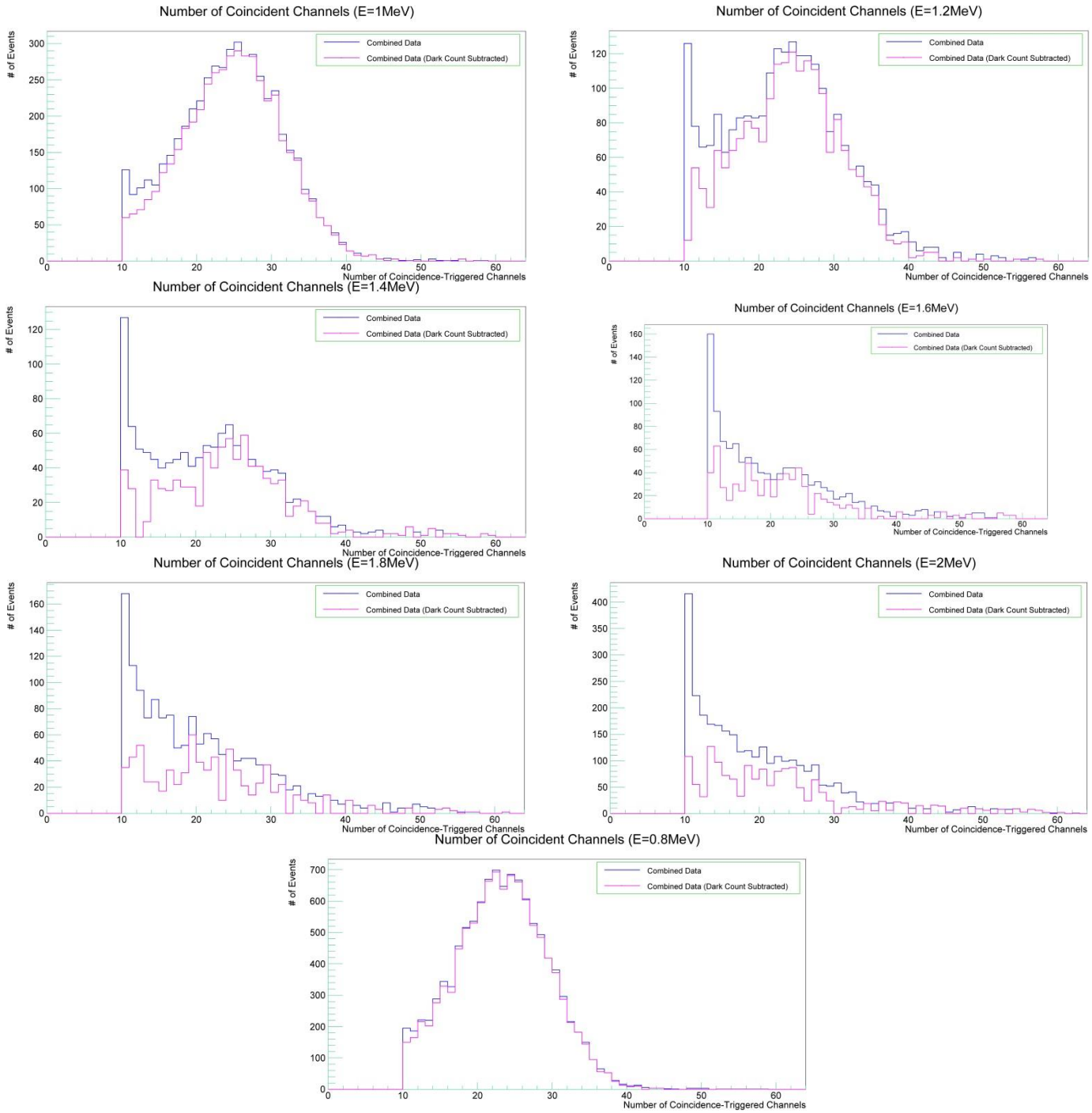

Figure 7.4 Number of Coincidence Channels histogram for E=0.8, 1, 1.2, 1.4, 1.6, 1.8, and 2MeV energies. Histograms are produced by combining measurement sets of each energy with error propagation taken into account. Subsequently, dark count measurement of equal duration is subtracted from the combined data.

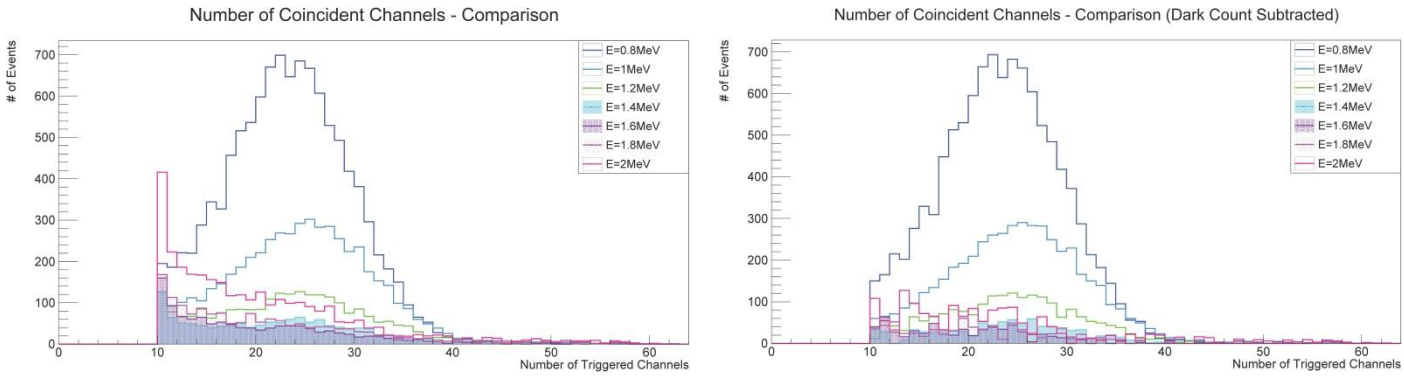

Figure 7.5 Left: Comparison of Number of Coincidence Channels histograms for E=0.8, 1, 1.2, 1.4, 1.6, 1.8, and 2MeV energies. Right: Same comparison for combined data with dark count subtracted.

7.3.3 Mean Number of Photons per Channel

When a channel is involved in an event (10ns time window), the number of photons registered by the channel is counted. Mean number of photons per channel refers to the number of photons detected by the channel during the entire measurement divided by the number of events in which the channels was involved. **Figure 7.6** shows the mean number of photons per channel for all examined energies.

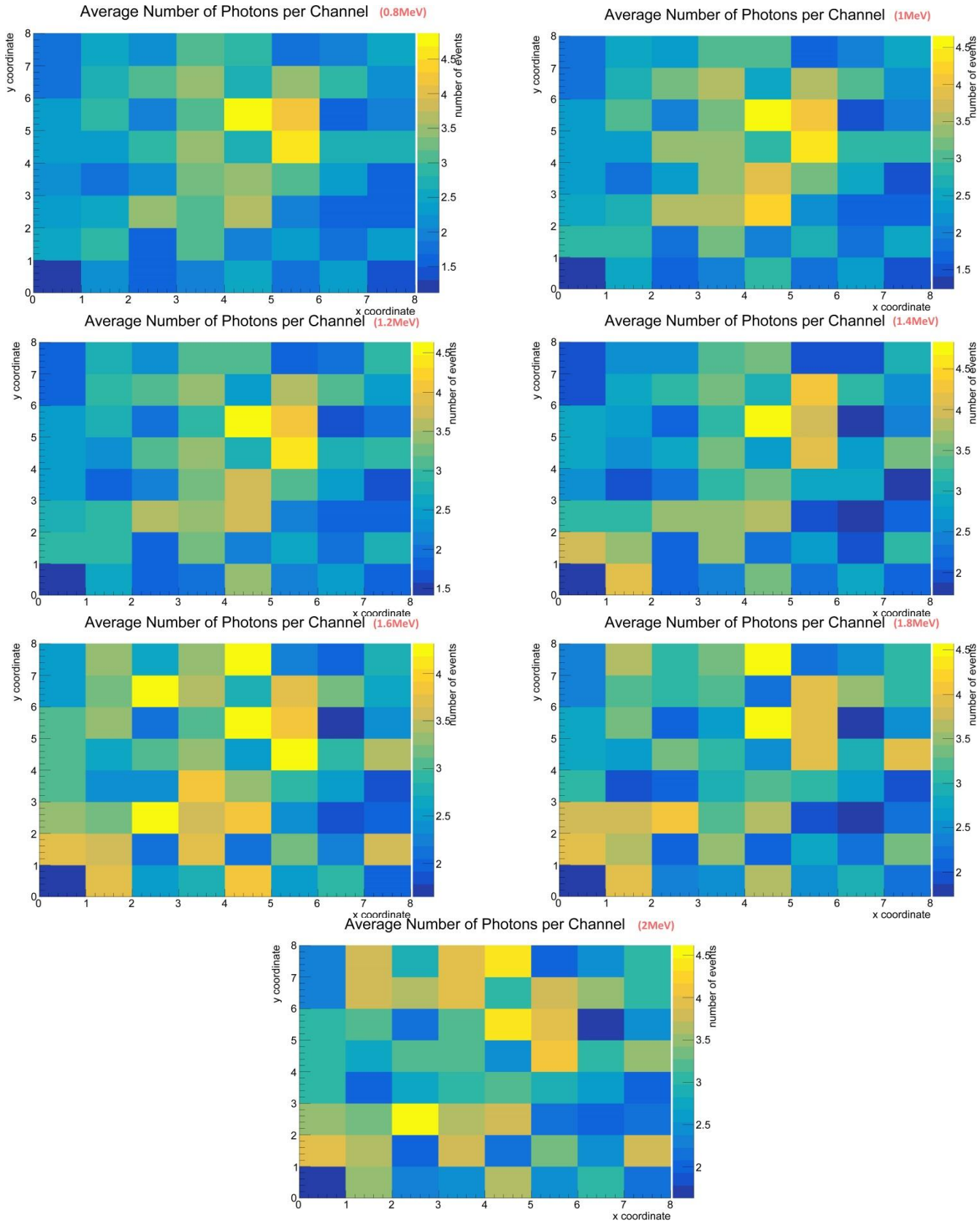

Figure 7.6 Mean number of photons per channel histograms for E=0.8, 1, 1.2, 1.4, 1.6, 1.8, and 2MeV energies. The frequency with which the channels are involved are not shown here. Only the average number of photons per channel when the channel was involved in 10-nanosecond events.

Mean number of photons per channel is not the average number of photons per channel per event, as not every channel is involved in every event. Therefore, the frequency with which a channel was involved

cannot be inferred from this data. For instance, in 2MeV, there is a concentration of photons at the bottom left edge. This can be from a single or only a handful isolated events caused by stray photons. Nevertheless, this type of data can reveal important information. First, when they are involved in an event, the central channels receive more photons than the peripheral channels do. For instance, in case of 1 MeV, the central channels produce roughly 4 photons, whereas, channels in the edge produce only 1 to 2 photons when they are involved in an event. Second, there is a tangible hollow shape in the middle of the central channels in most of the data, indicating existence of a Cherenkov cone in the middle (**Figure 7.7**). The spatial resolution of the SiPM is of course not fine enough to determine the radius, angle, and eccentricity of the cone, but the graphical demonstration confirms that the experiment was successful in guiding the electrons to the center of the PMMA for most of the energies.

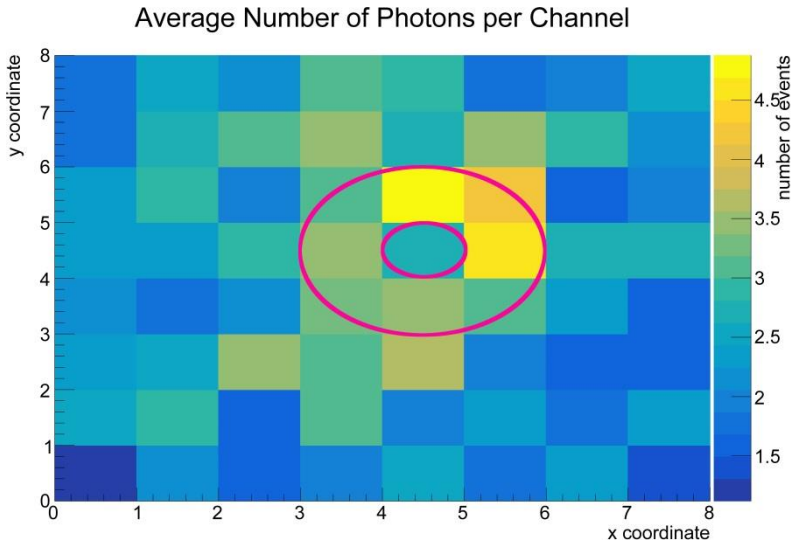

Figure 7.7 Mean number of photons per channel histograms for E=0.8MeV. The hollow shape is produced by Cherenkov cone.

7.3.4 Number of Photons per Event

The number of photons produced per event follows a statistical distribution. The mean value of such distribution can be associated with Cherenkov yield of a specific electron energy. Similar to previous sections, the histograms produced by individual measurement sets are combined in order to obtain number of photons per event histograms for each energy. **Figure 7.8** demonstrates the results for all examined energies.

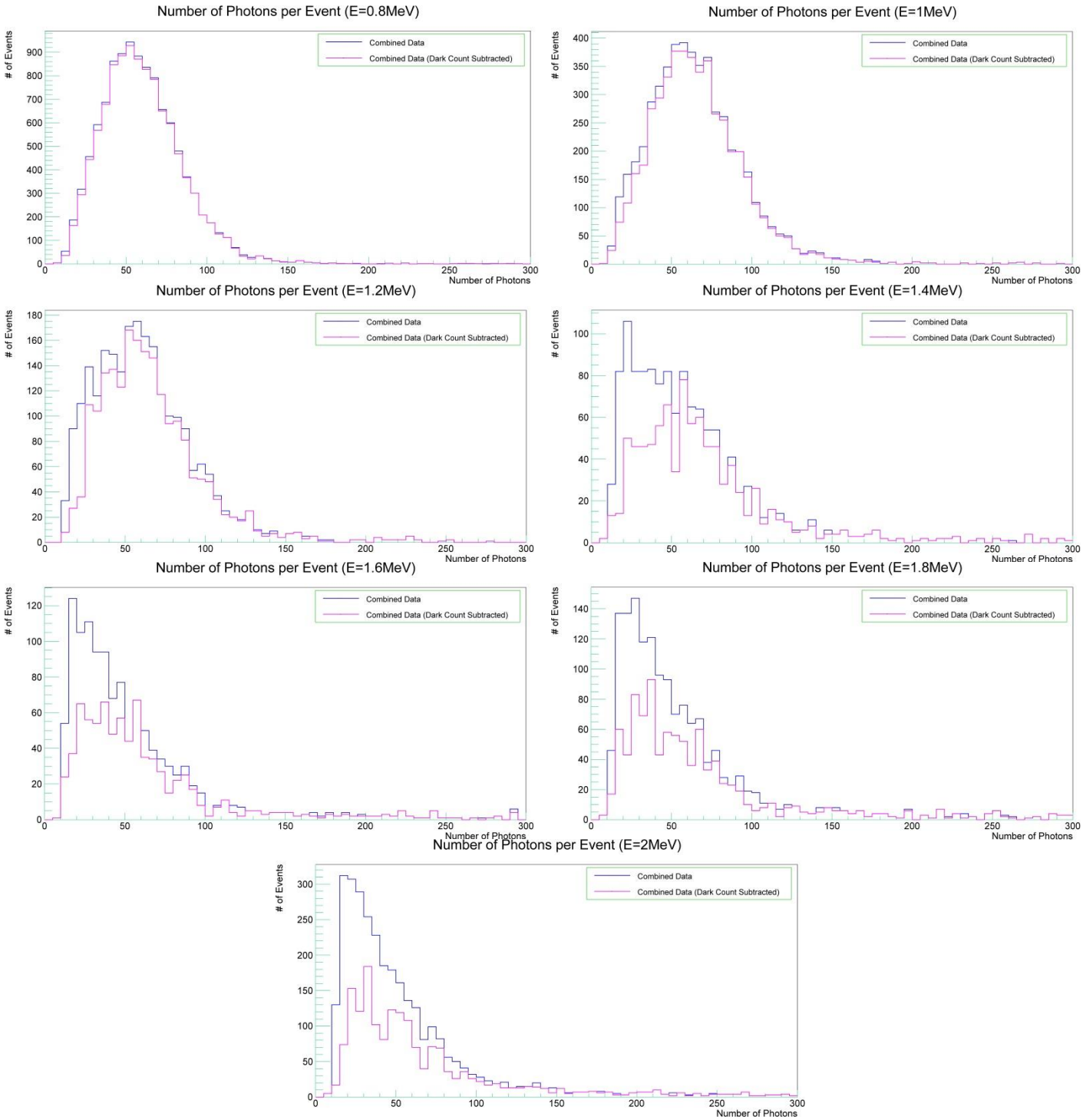

Figure 7.8 Number of photons per event histograms for E=0.8, 1, 1.2, 1.4, 1.6, 1.8, and 2MeV energies.

In addition, dark measurement sets with equal durations to measurements with ^{90}Sr source were taken so that they can be subtracted from measurement. For each energy, only a single dark measurement is performed. The final combined data is then subtracted by the dark measurement times the number of actual measurements carried out for that energy. For instance, 2MeV measurements are carried out 14 times, each with 395 sec duration. The measurement is followed by a 395 sec measurement without the source. At the end, all 14 data sets are combined and subtracted by 14 times dark data.

Finally, the error propagation on the final data is corrected using **Equation 7.1**.

$$Error_{Final} = \sqrt{n \times (Error_{dark})^2 + \sum_i Error_i{}^2} \qquad \textbf{Eq. (7.1)}$$

where n signifies the number of individual measurement sets to be combined, $\mathrm{Error_{dark}}$ is the error value of the dark count, and $\mathrm{Error_i}$ is the error value of ith measurement set. Dark count subtraction introduces significant increase in error values as shown in **Figure 7.9**. Nevertheless, given the accuracy it provides at lower coincidence channels, the error is inevitable.

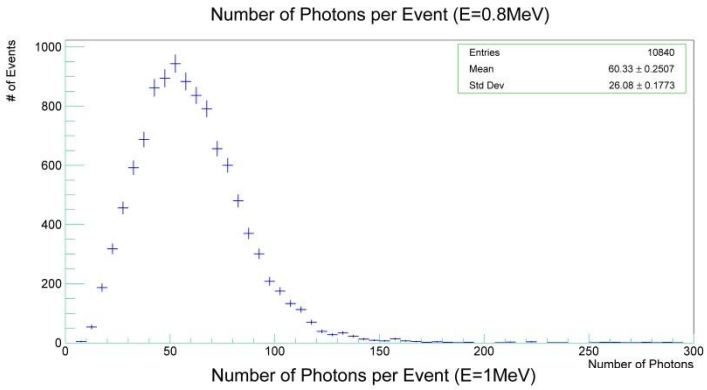
Number of Photons per Event (E=0.8MeV)
Entries 10840
Mean 60.33 ± 0.2507
Std Dev 26.08 ± 0.1773
# of Events
Number of Photons

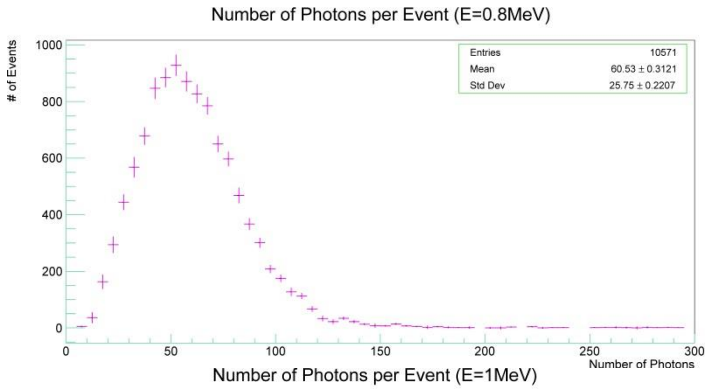
Number of Photons per Event (E=0.8MeV)
Entries 10571
Mean 60.53 ± 0.3121
Std Dev 25.75 ± 0.2207
# of Events
Number of Photons

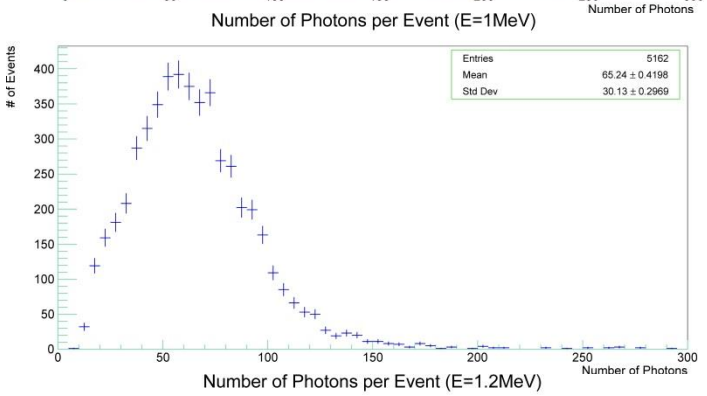
Number of Photons per Event (E=1MeV)
Entries 5162
Mean 65.24 ± 0.4198
Std Dev 30.13 ± 0.2969
# of Events
Number of Photons

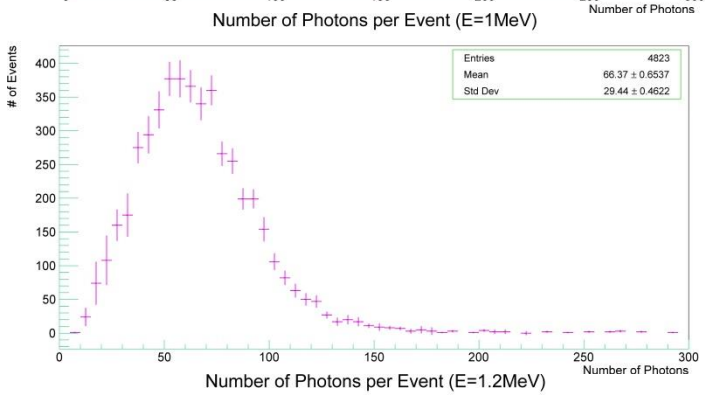
Number of Photons per Event (E=1MeV)
Entries 4823
Mean 66.37 ± 0.6537
Std Dev 29.44 ± 0.4622
# of Events
Number of Photons

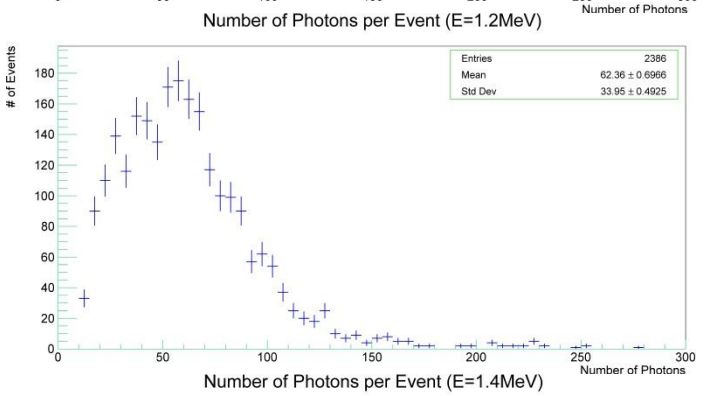
Number of Photons per Event (E=1.2MeV)
Entries 2386
Mean 62.36 ± 0.6966
Std Dev 33.95 ± 0.4925
# of Events
Number of Photons

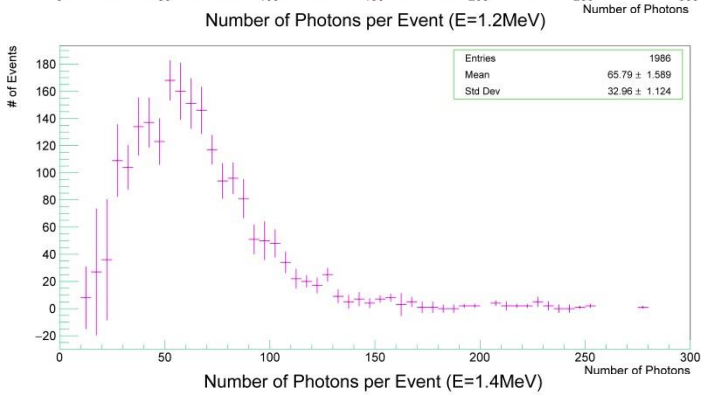
Number of Photons per Event (E=1.2MeV)
Entries 1986
Mean 65.79 ± 1.589
Std Dev 32.96 ± 1.124
# of Events
Number of Photons

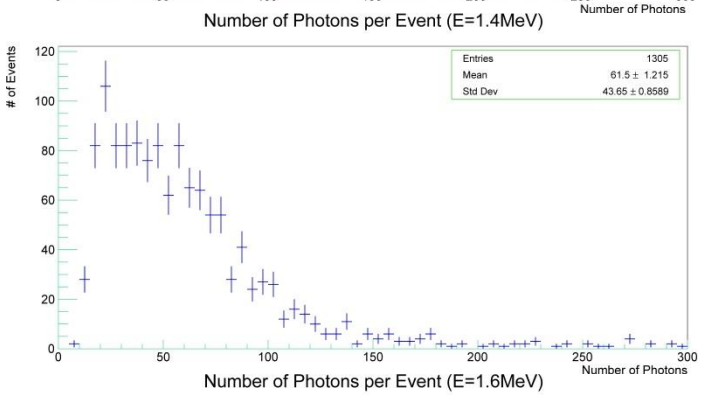
Number of Photons per Event (E=1.4MeV)
Entries 1305
Mean 61.5 ± 1.215
Std Dev 43.65 ± 0.8589
# of Events
Number of Photons

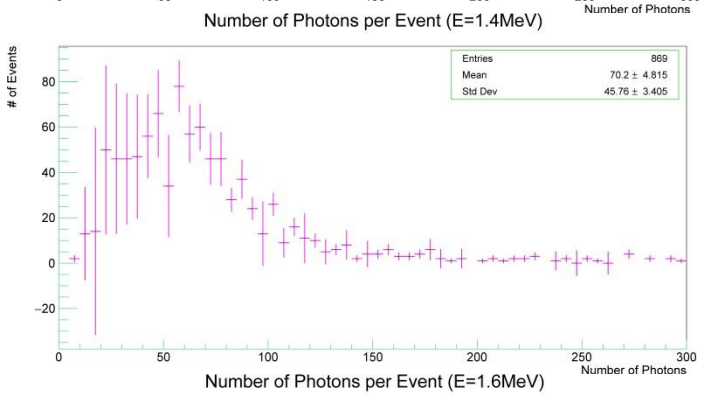
Number of Photons per Event (E=1.4MeV)
Entries 869
Mean 70.2 ± 4.815
Std Dev 45.76 ± 3.405
# of Events
Number of Photons

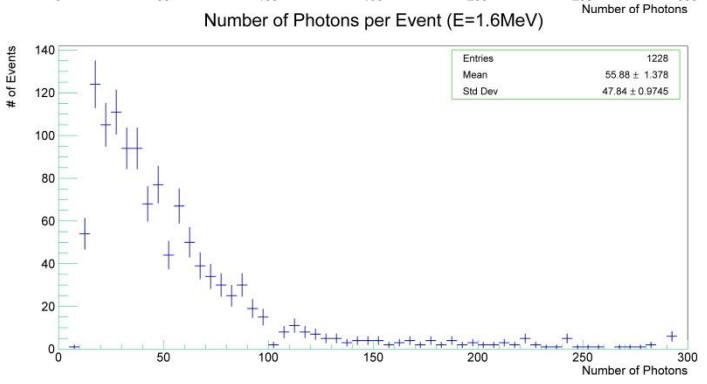
Number of Photons per Event (E=1.6MeV)
Entries 1228
Mean 55.88 ± 1.378
Std Dev 47.84 ± 0.9745
# of Events
Number of Photons

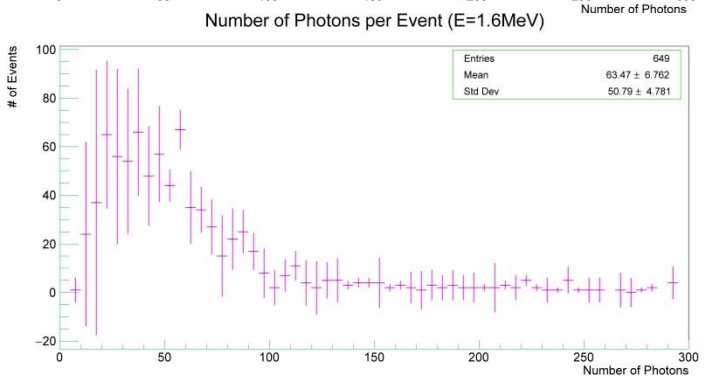
Number of Photons per Event (E=1.6MeV)
Entries 649
Mean 63.47 ± 6.762
Std Dev 50.79 ± 4.781
# of Events
Number of Photons

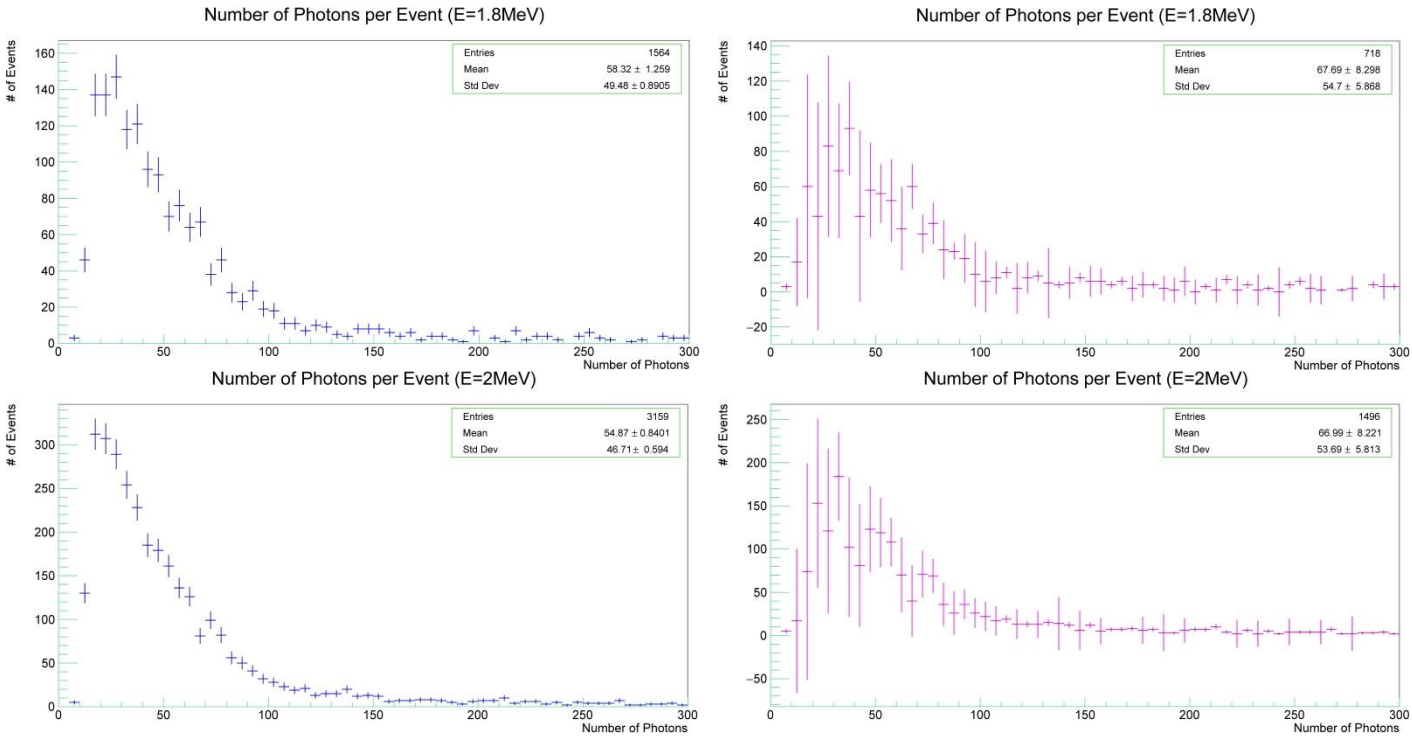

Figure 7.9 Number of photons per event histograms for E=0.8, 1, 1.2, 1.4, 1.6, 1.8, and 2MeV energies. Comparison between error values combined data (Left) and combined data with dark count subtraction (Right) are demonstrated.

This method has the potential to remove random signals from the histograms, provided the dark measurements are taken in the same ambient light and temperature as actual measurement. For instance, 0.8MeV measurements included 10840 entries which was reduced to 10571 entries after dark count subtraction. However, the very nature of the experiment and limitations of the current hardware casts doubts on the veracity of the dark count. As a case in point, 2MeV measurements include 14 sets, which takes more than 10 hours to complete. Dividing the measurement between different nights negates the possibility of getting consistent experiment condition and ambient temperature, while performing the measurement as we did all in one night has the disadvantage of different ambient lighting. Therefore, subtracting a single set of dark count at a specific time of day from all the data sets is bound to include some discrepancies. Upgrading the cooling system so that measurements can be performed continuously certainly diminishes this systematic error substantially. Despite the systematic error introduced by dark count subtraction, it is necessary to use the subtracted data for electron energy to photon yield correlation.

7.3.5 Photon Yield of each Energy

Figure 7.10 demonstrates total number of photons per event for all energies. Each energy follows a distribution which peaks at a certain number of photons. The number of photons corresponding to maximum number of events can be used as a representative of the photon yield for a given electron energy.

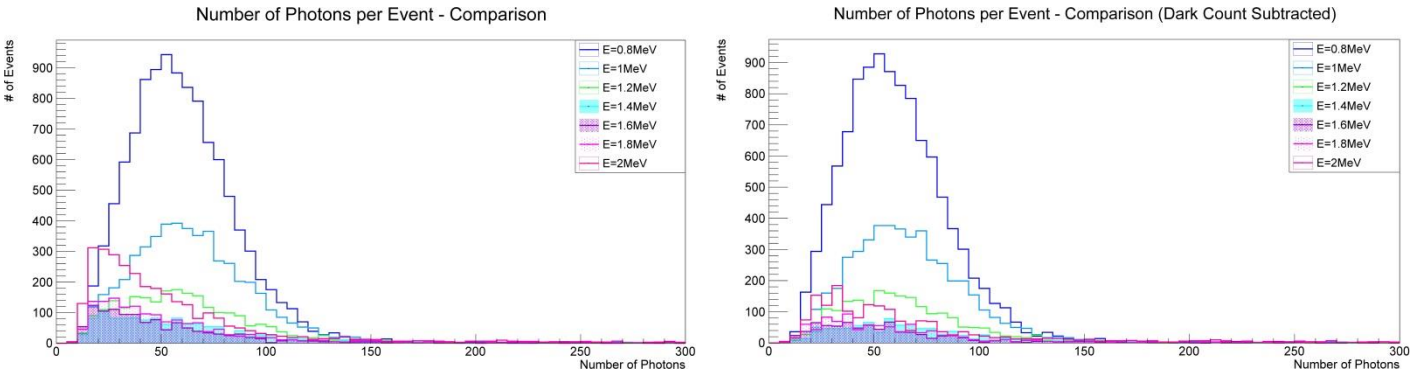

Figure 7.10 Number of photons per event histograms for E=0.8, 1, 1.2, 1.4, 1.6, 1.8, and 2MeV energies with (Right) and without (Left) dark count subtraction.

In order to find the peak of each histogram, a fit needs to be applied to each distribution. Most of the distributions resemble a Gaussian model at the peak with the long tail on the right side. Therefore, a Gaussian fit is applied to an interval around the peaks depending on the energy, and the long tail is excluded from the fit, as it bears no significance to the purpose of this study. **Table 7.2** summarizes the intervals for Gaussian fit for each energy.

Table 7.2 Parameters used for fitting the Number-of-Photons-per-Event Histograms

Electron Energy	Gaussian Distribution Interval	
	Lower Bound (X)	Upper Bound (X)
0.8 MeV	20	90
1 MeV	15	105
1.2 MeV	0	100
1.4 MeV	0	100
1.6 MeV	0	100
1.8 MeV	0	100
2 MeV	0	100

The values for the range of Gaussian distribution fit were found through trial and error in order to find the $\frac{\chi^2}{NDF}$ ratio closest to 1 while minimizing χ^2. **Figure 7.11** demonstrates the fit functions on number of photons per events histograms for all energies.

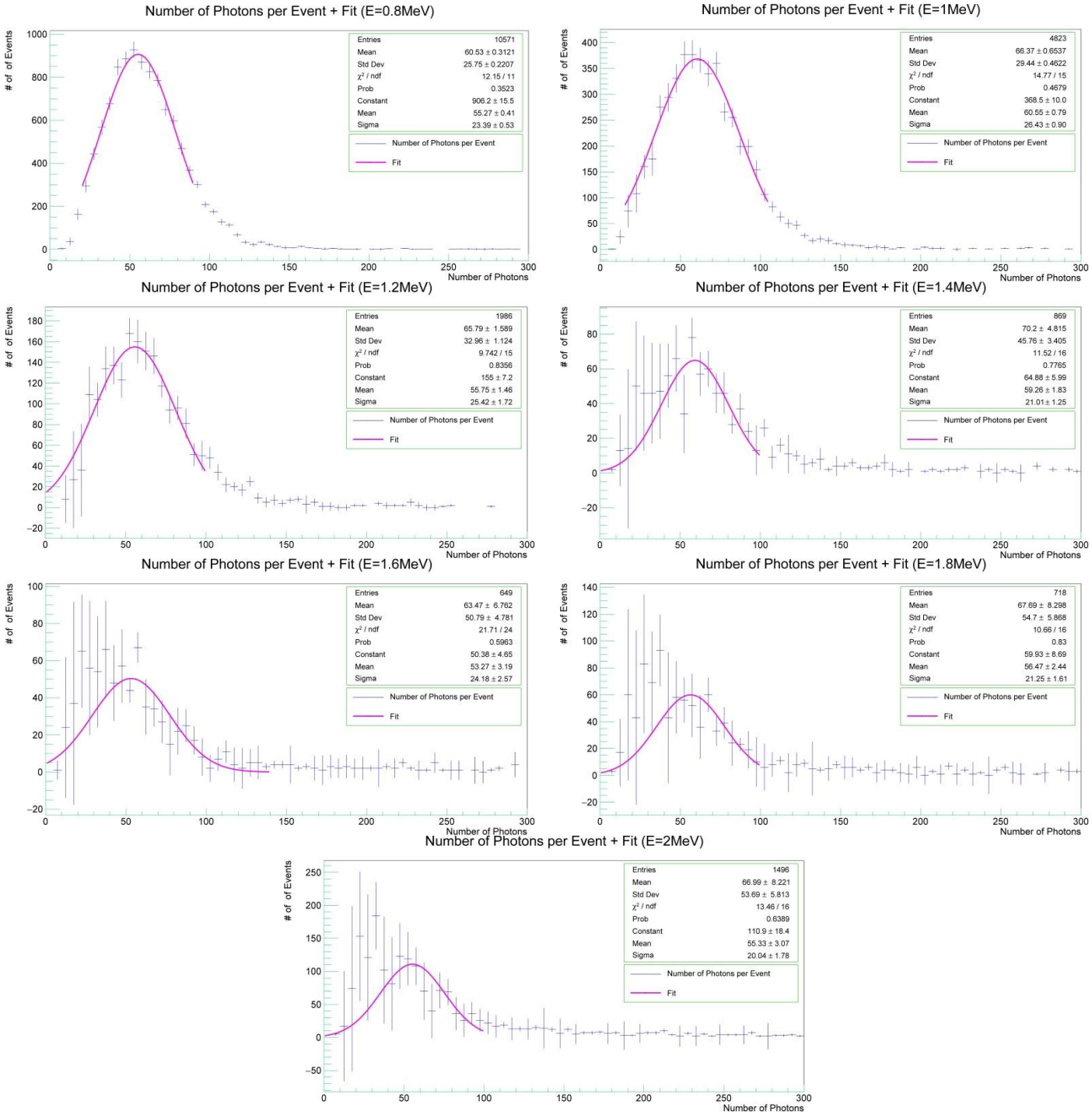

Figure 7.11 Number of photons per event histograms for E=0.8, 1, 1.2, 1.4, 1.6, 1.8, and 2MeV energies. The gaussian fit function combination are added to separate ranges of the distribution according to **Table 7.2**.

Having acquired the fit for the distributions, the peak of each distribution can be determined and tabulated. **Figure 7.12** shows a comparison of all the fit functions. **Figure 7.13** shows the results of the peak

finding analysis from fits and number-of-photons-per-event histograms. The maximum of the histograms does not necessarily represent the peak of the distribution. After all, finding the distribution of the peak as well as its associated error are primary purposes of the fit functions in the first place.

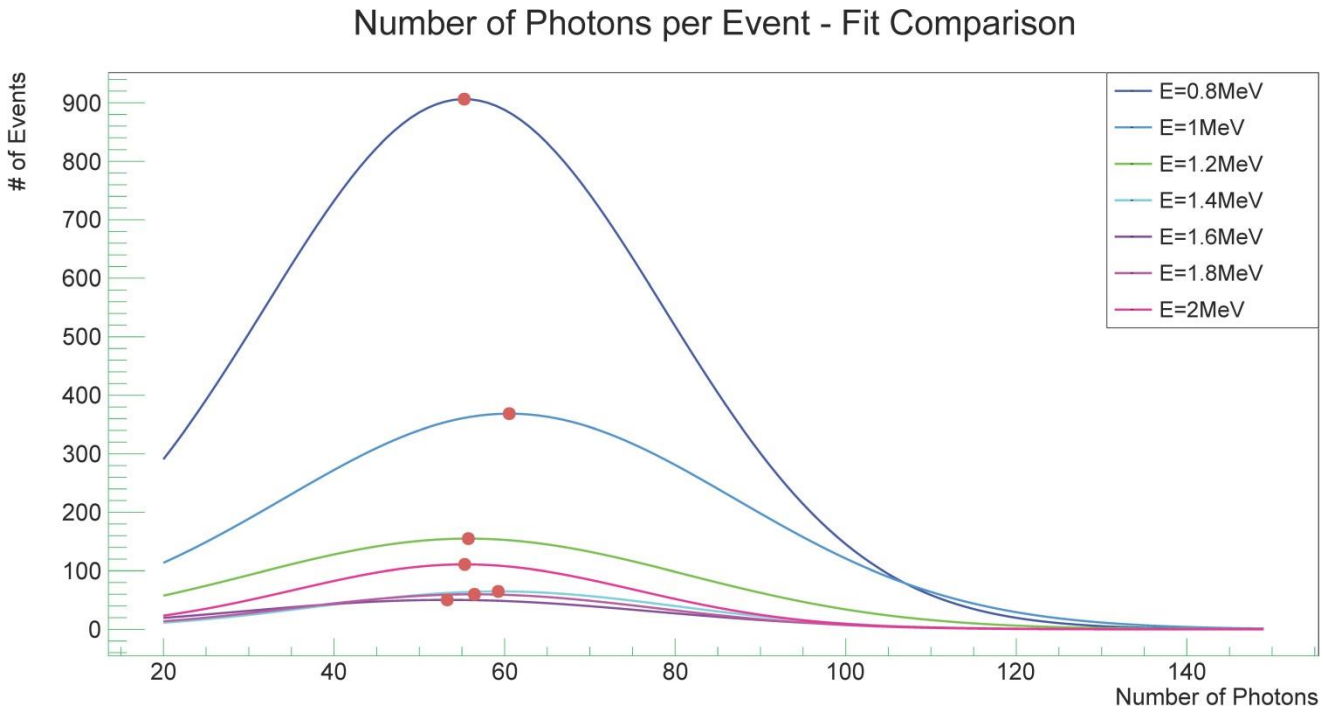

Figure 7.12 Fit functions for all energies.

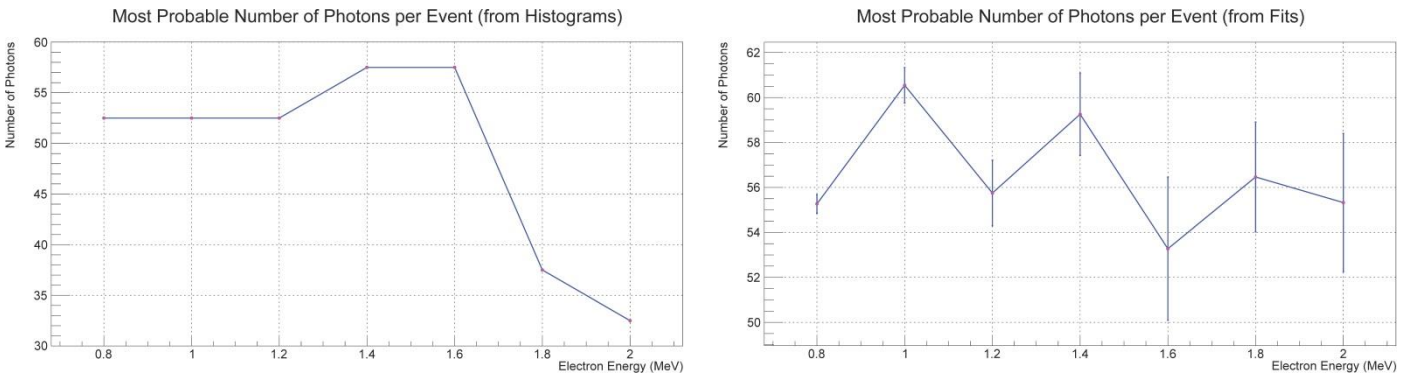

Figure 7.13 Photon yield of each electron energy from the experiment. Left: Most probable photon yield is the bin with maximum bin content from the number of photons per event histogram. Right: Most probable photon yield the bin with maximum content from the fit functions with the associated error of the peak.

Figure 7.14 shows the statistics associated with the histograms. Namely, mean, standard deviation, and entries for each electron energy.

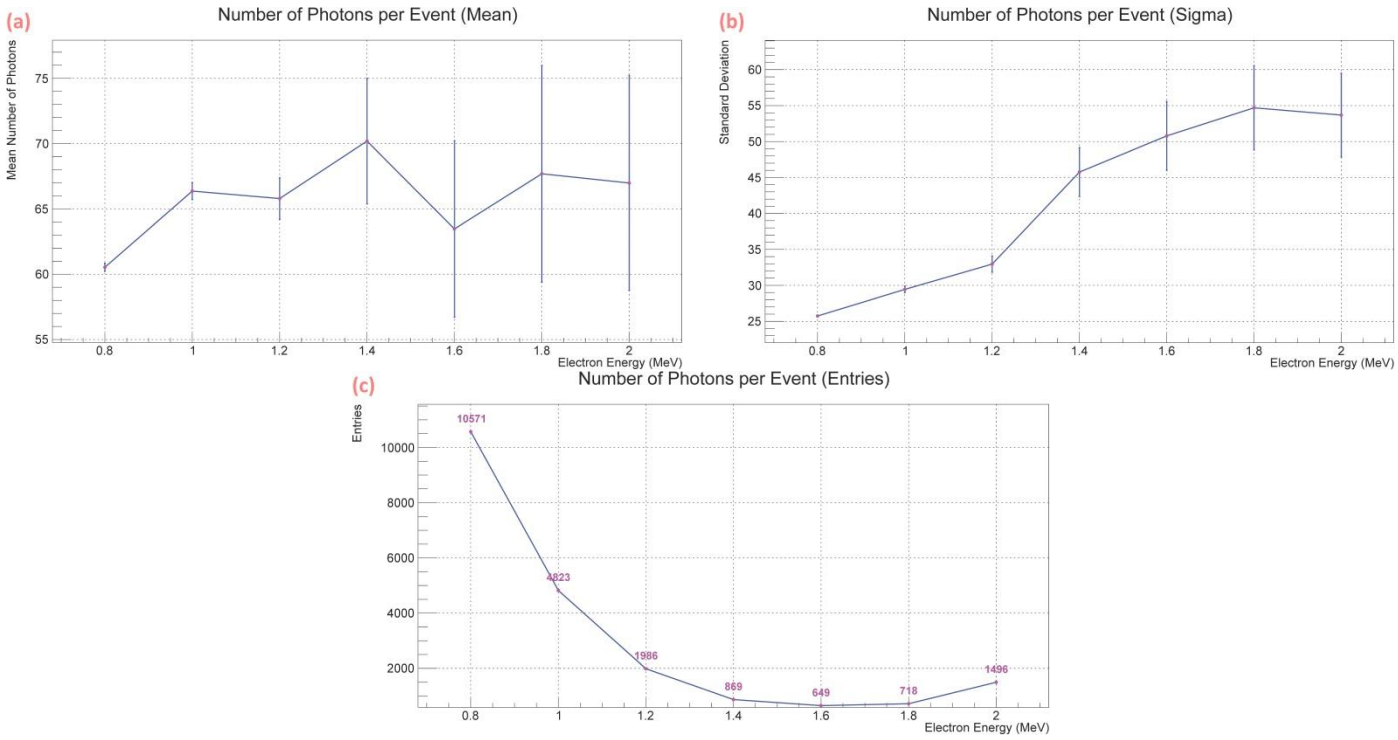

Figure 7.14 Mean number of photons (a) and their standard deviation (b) based on the distribution. The sample statistics of each energy are shown (c).

From theory, we know that photon yield of Cherenkov radiation increases with energy of the charged particle. However, the results for 1.6 MeV to 2 MeV from **Figure 7.13** suggest otherwise. The discrepancy can be explained when the mechanics of the experiment are taken into account. Electrons travel through multiple tubes in a relative vacuum of 6mbar before they reach the PMMA. Electrons with higher energies have higher probability of interacting with air atoms and lose their energy. Better vacuum conditions can improve the outcome and decrease interaction probability of electrons with air.

In addition, the electrons exit the ^{90}Sr source through a cylindrical collimator with r=0.5 mm, which contributes to less than 1% of the phase space of ^{90}Sr's radiation. Therefore, a percentage of the electrons do not meet the criteria of going in a straight line to reach the magnet and are lost.

Furthermore, **Figure 7.14-c** suggests that the time duration chosen based on ^{90}Sr's spectrum did not yield comparable statistics for all energies. Longer measurements are needed for higher energies to remedy the inconsistencies in statistics. As discussed before, the required time for separate measurement sets introduces another uncertainty to the outcome, as ambient light and measurement temperature inevitably change during a long measurement. Introducing a more robust cooling system can remedy this problem. Another source of systematic uncertainty is occurrence of afterpulse. If the afterpulse signal is released before recovery of the SPAD, the measured time-over-threshold can be affected as shown in **Figure 7.15**. Given the overvoltage of 4V used in the experiment, 10% afterpulse is expected in the signal. The recovery

time of the SiPM is in the order of 100ns **[60]**. Afterpulse signals that are released after the recovery time each increase number of photons by 1, which is another source of systematic error.

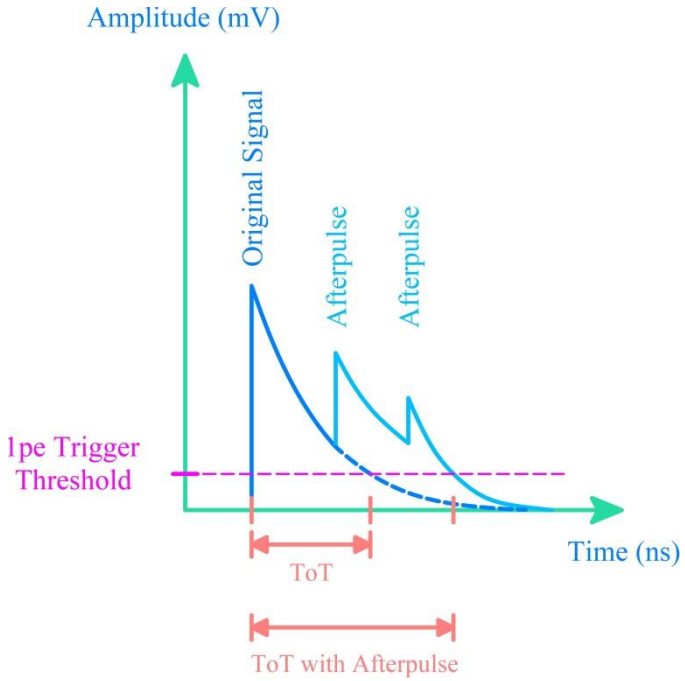

Figure 7.15 Afterpulse can artificially increase ToT if it is released within the recovery time of the SPAD.

7.4 Contribution of Random Signal

Random signal in this context refers to creation of 1pe or higher signal in the absence of a source and ambient light. As discussed in Section 3.6, random signal is purely related to phonon vibration and thermal excitation of the SiPM. In Chpater 6, the dark count rate of every channel was measured at all available threshold levels of the ASIC, which gives an indication of what rate of random signal is expected in every channel. The goal of this section is to determine the contribution of random signal to the total signal. The results are then compared with the measurement.

As mentioned in Chapter 3, the SiPM array is comprised of 64 channels, one of which is turned off due to malfunction. The probability of an individual channel firing a random signal during a 10 ns event follows a Poisson distribution. The probability of a single channel firing random signal "k" times is given by:

$$P_{poisson}(k,\lambda) = \frac{\lambda^k e^{-\lambda}}{k!} \qquad \textbf{Eq. (7.2)}$$

where λ is the expectation value. λ can be determined from the DCR of the channels acquired during calibration phase. **Figure 7.16** shows the dark count rate of every channel. The discrepancy between the channels is related to the temperature variance of different channels and construction variations of SPADs

in channels. The cooling block attached to the SiPM cannot provide a homogeneous temperature to all channels due to its geometry as shown in **Figure 4.26**. In addition, the production of SiPM channels itself at such microscopic scale is bound to produce differences in behavior which only increases as the device ages.

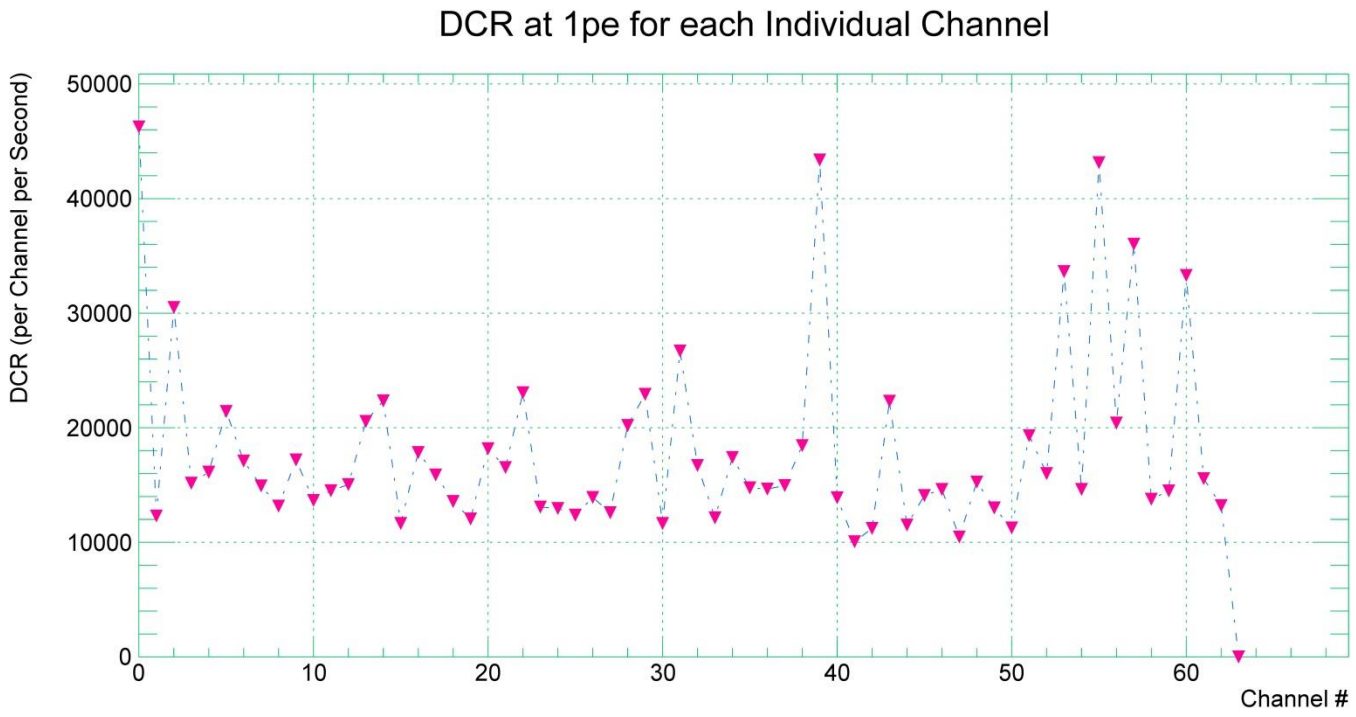

Figure 7.16 Dark Count Rate of individual channels. Channel numbering in the PETsys software starts at 0. Note that Channel 64 has been manually turned offline due to malfunction.

The difference in dark count rate requires finding an average value for all channels. **Figure 7.17** shows the distribution of DCR among channels.

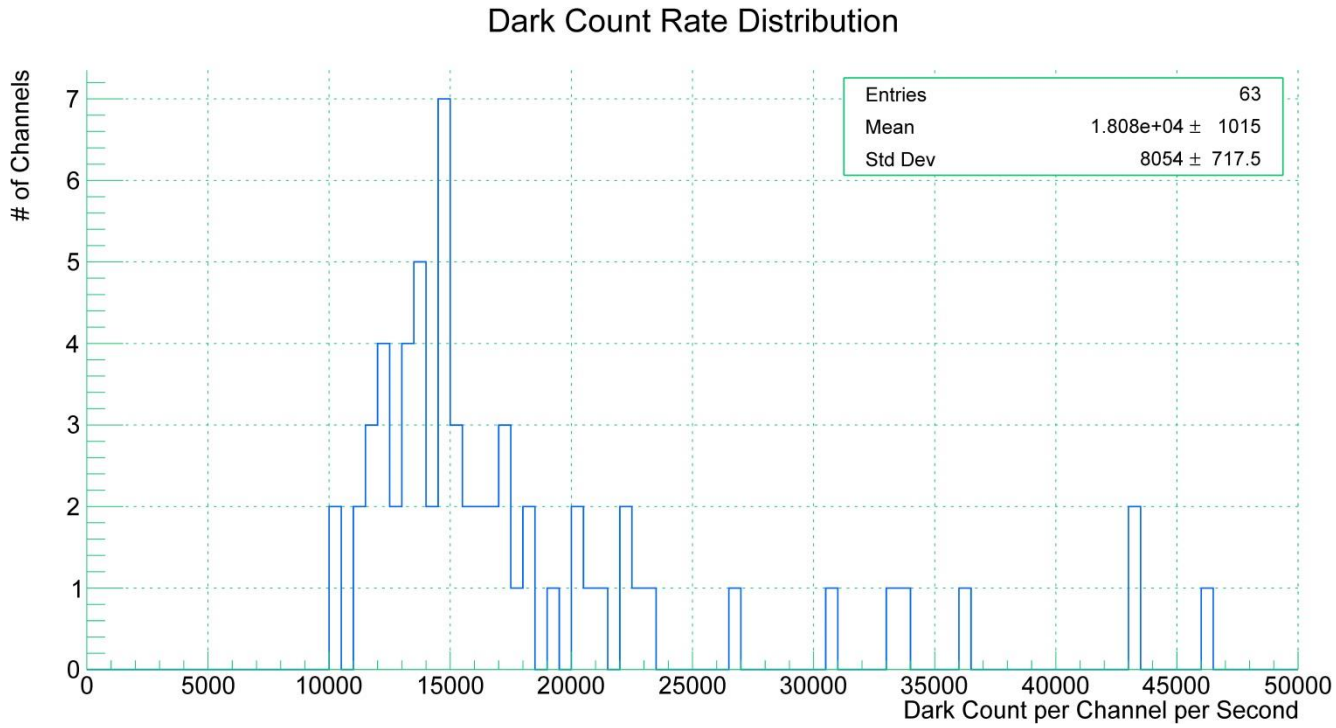

Figure 7.17 Dark Count Rate distribution of all channels. Channel 64 is excluded so that it does not affect the mean value.

From the distribution, a mean value of $18.1 \times 10^3 \pm 1015$ is chosen as the mean value, which will be used to determine λ in the **Equation 7.2**.

$$\lambda = DCR \times CTW \qquad \textbf{Eq. (7.3)}$$

where DCR is the mean value of dark count rate, and CTW is the coincidence time window (10ns). **Figure 7.18** shows the probability of a single channel firing 1, 2, and 3 random signals during a 10ns time window according to **Equation 7.2**.

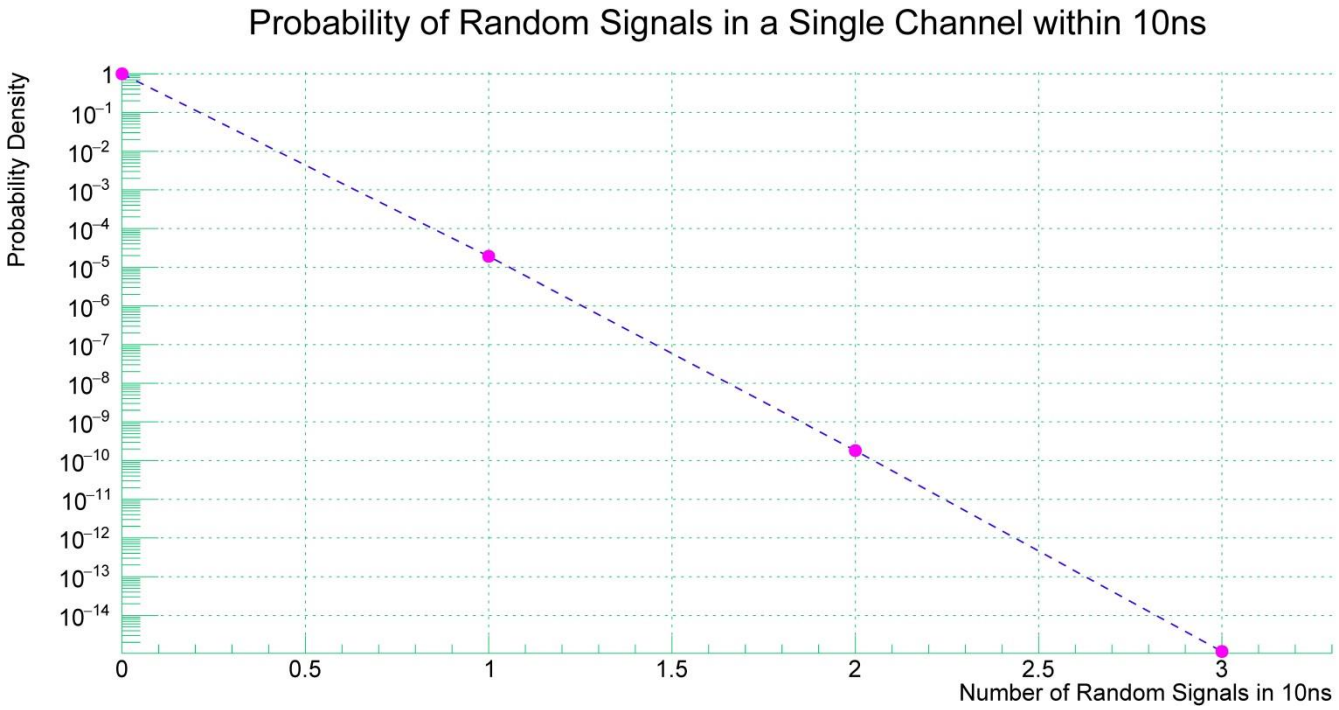

Figure 7.18 Probability of a single channel firing random signals during 10ns according to **Equation 7.2**.

The current SiPM houses 64 channels. Optical cross-talk may occur between neighboring SPADs within a single channel, but the probability of cross-talk between channels is rather low. Therefore, we can assume that the channels act independently as far as random signal is concerned. For the sake of theory, it is also assumed that no temperature difference exists between channels. Given, the probability of exactly n channels out of existing 63 firing a random signal follows the Binomial distribution.

$$P_{binom}(n, 63, p) = \binom{63}{n} \cdot p^n \cdot (1-p)^{63-n} \qquad \textbf{Eq. (7.4)}$$

where p is the probability of a single channel successfully firing once during 10ns, acquired from **Equation 7.2**. The first argument accounts for the number of ways we can select "n" channels out of the existing 63. The second and the third arguments account for probability of "n" channels creating signal and "63-n" channels not creating signal during 10ns time window respectively. Using the mean dark count rate from the experiment, the population of channels creating random signal rises with increase in the time window of single events, as shown in **Figure 7.19**.

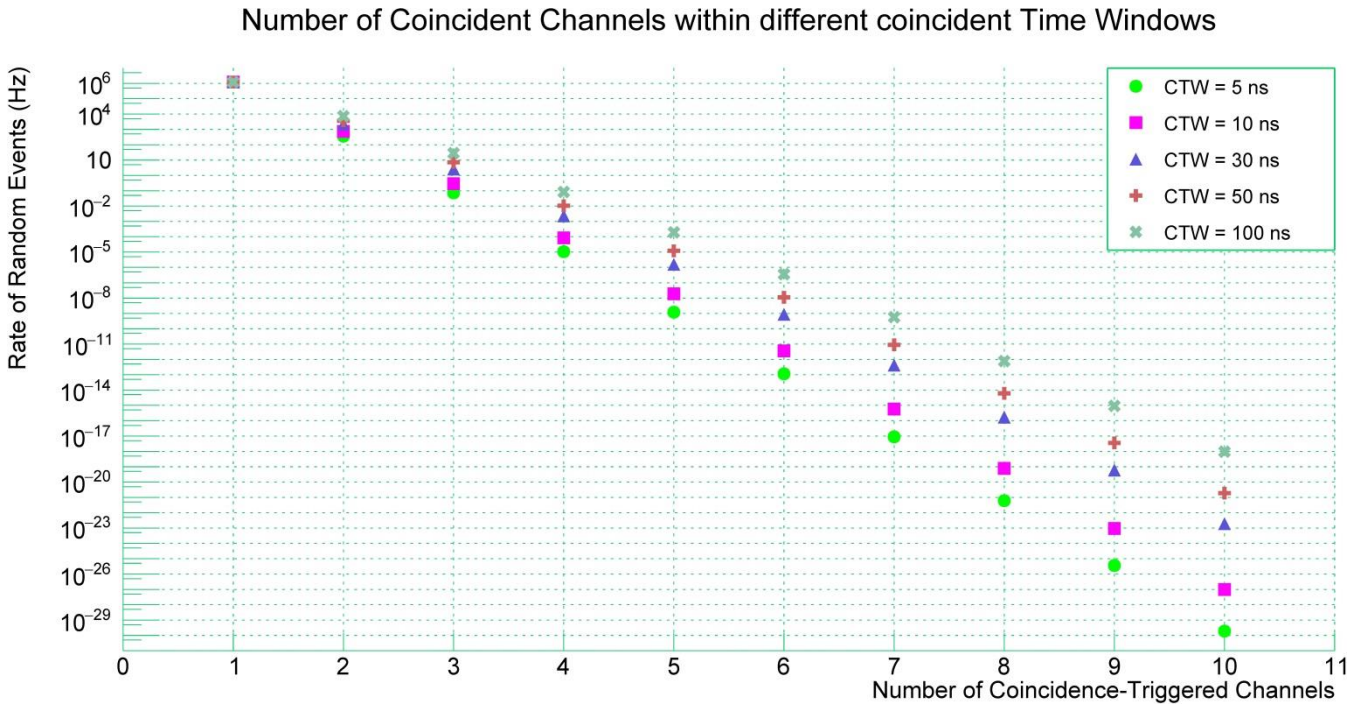

Figure 7.19 Population of channels creating random signal during 1 second with mean DCR of 18K.

Increasing the dark count rate (higher operating temperatures) also increases random signal population as shown in **Figure 7.20**.

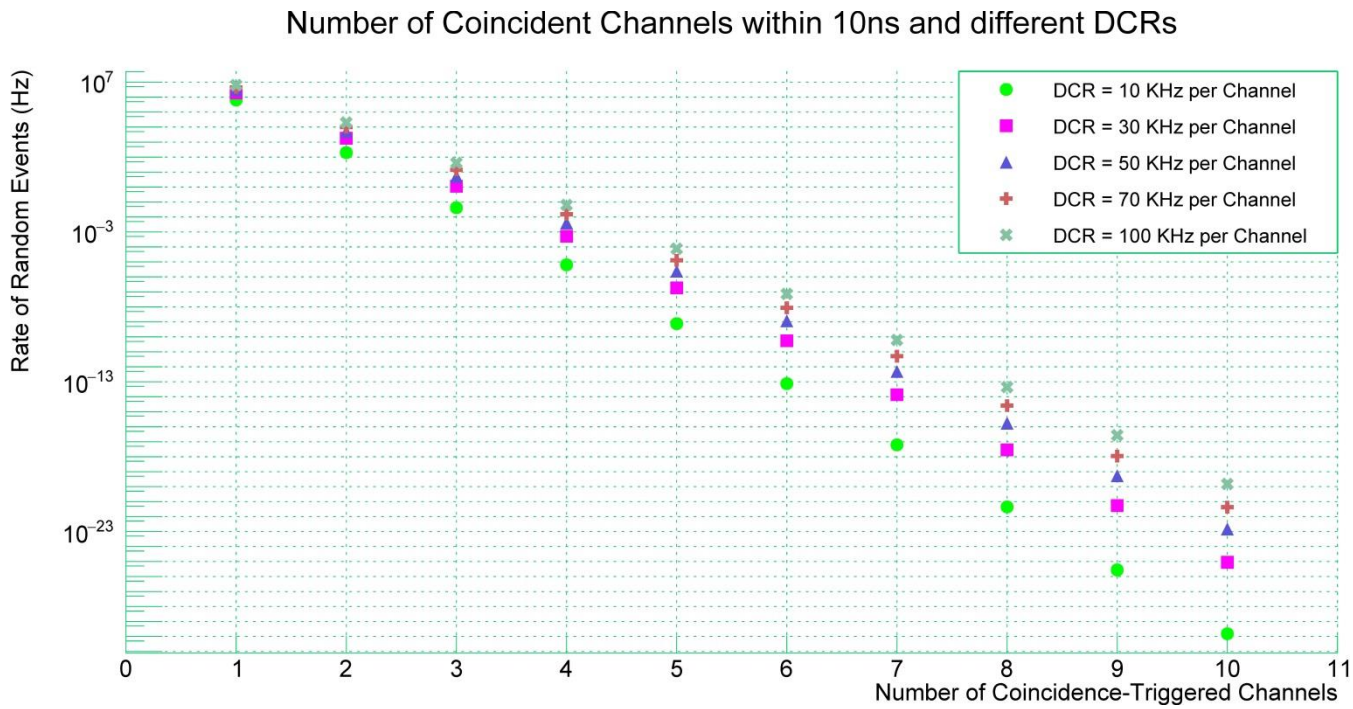

Figure 7.20 Population of channels creating random signal during 1 second with coincident time window of 10ns.

A 360 second dark measurement has been carried out in order to make a comparison with theory. The measurement values are adjusted to reflect only 1 second. **Figure 7.21** shows the comparison between theory and measurements. The discrepancy in results are primarily due to the following.

First, the assumption that each channel has a constant dark rate is inaccurate, and replacing it with a mean value introduces uncertainties to the result. In addition, the malfunctioning channel is still producing large amount of signal even though the channel has been set to extremely high threshold, as the bias voltage to individual channels cannot be cut off. Last, the theory only accounts for random signals, whereas the measurement cannot distinguish between stray photon and random signal. Even with a light-sealed environment, random stray photons can reach the PMMA and create signals. Also, cosmic muons created in the atmosphere can reach the PMMA and produce Cherenkov photons. Cosmic muons occur with the frequency of 1 per minute per square centimeter **[67]**. Given the size of the PMMA, between 12 to 13 muons in GeV energy range are expected to hit the PMMA every 60 seconds.

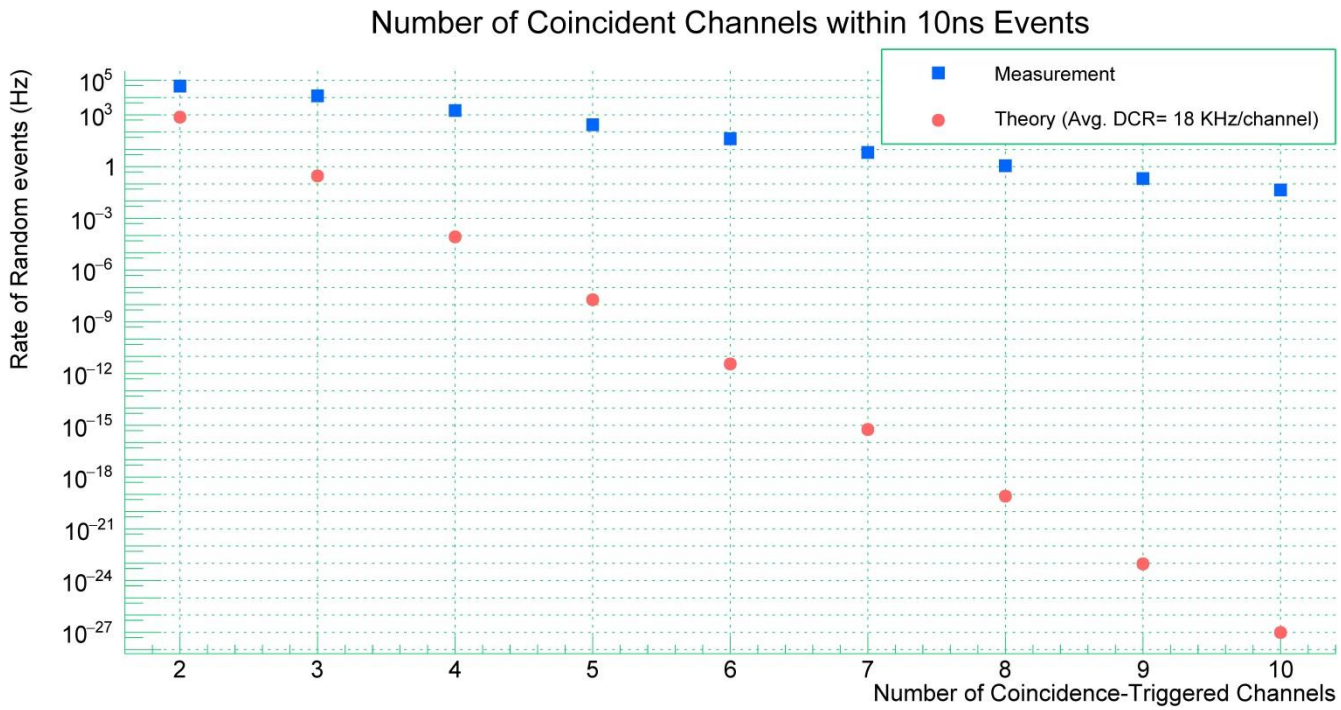

Figure 7.21 Population of channels creating random signal during 1 second with coincident time window of 10ns.

8. Conclusions and Suggestions for Further Work

8.1 Summary

A Compton Camera can be a great real-time imaging asset for Proton Beam Therapy cancer treatment and radio-immunotherapy in general. The main goal is imaging of gammas above 0.5 MeV, which cannot otherwise be resolved by conventional detectors such as SPECT with good efficiency. To that end, an experimental setup which reconstructs Compton electron's energy and direction using coincident detection of Cherenkov photons has been successfully designed and tested. In order to calibrate the energy reconstruction, a device has been built to separates electrons with energies up to 2.28 MeV from a $^{90}Sr/^{90}Y$ source to a very small spectrum using a magnetic field. The electrons subsequently undergo Cherenkov Effect in a PMMA radiator, in contact with an 8×8 SiPM array with $3 \times 3mm^2$ read-out channels. A resolution of 10 to 20% has been achieved for 7 different energies from 0.8 MeV to 2 MeV. The number of Cherenkov photons, collected within a time-window of 10 ns is used to reconstruct the electron energy. The results are compared with a mean value calculated from theory and energy loss databases. The analysis successfully established a correlation between electron energy and photon yield.

8.2 Outlook

The next step is to verify the reliability of the correlation between electron energy and photon yield. An experimental setup using ^{207}Bi is already on the way. ^{207}Bi has four distinct peaks in its spectrum which makes it a suitable candidate for verification of the experimental setup.

In addition, certain improvements to the cooling system as well as the SiPM detectors can potentially increase the accuracy of the results. A cooling system capable of maintaining a steady subzero temperature during long measurements eliminates uncertainties associated with temperature variations in SPADs. The SiPM itself can be replaced with a model fine-tuned to operate in near UV range at higher PDE (see **Figure 3.9**), as Cherenkov photons are primarily in UV range.

The magnetic setup can also be improved to allow use of higher magnetic field strength in order to improve electron separation. In the same vein, achieving a higher relative vacuum minimizes the electrons interaction before they reach the radiator.

Appendix A. Magnetic Field Calculations

Calculations for **Equation 2.71** are presented here. The sections 1 to 5 shown in **Figure 2.12** are analyzed separately for each coil, and the results are combined at the end. The parameters used are z_{15}, z_3, z_{Gap}, y_{24}, Δ, W, and L as shown in **Figure 2.12**.

A1. Sections 1 and 5

A1.1. Part a - Bottom Coil

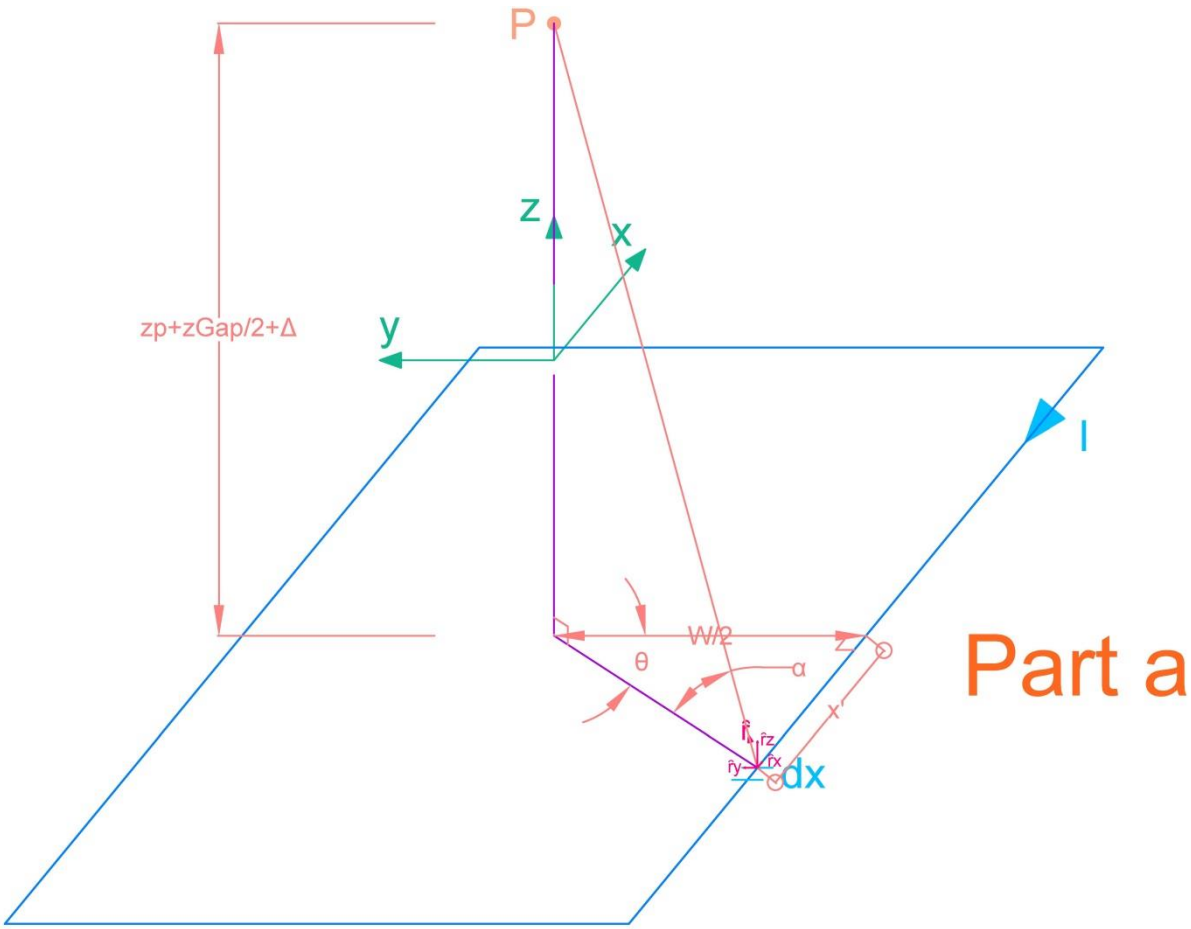

$$\vec{B}_{p,15,bottom,a} = \frac{\mu_0 I}{4\pi} \int \frac{d\vec{x} \times \hat{r}}{|\vec{r}|^2}$$

$$x = \frac{L}{2} - x' = \frac{L}{2} - \left(-\frac{W}{2} tan\theta\right) = \frac{L}{2} + \frac{W}{2} tan\theta$$

$$d\vec{x} = \frac{W}{2} \frac{d\theta}{cos^2\,\theta} (-\hat{\imath})$$

$$|\vec{r}| = \sqrt{\left(\frac{W}{2}tan\theta\right)^2 + \left(\frac{W}{2}\right)^2 + \left(z_p + \frac{z_{Gap}}{2} + \Delta\right)^2}$$

$$\hat{r} = \hat{r}_x + \hat{r}_y + \hat{r}_z$$

$$\left|\hat{r}_{xy}\right| = |\hat{r}|\, cos\,\alpha = cos\,\alpha$$

$$cos\alpha = \frac{\left|\vec{r}_{xy}\right|}{|\vec{r}|} = \frac{\left(\frac{W}{2}tan\theta\right)^2 + \left(\frac{W}{2}\right)^2}{\sqrt{\left(\frac{W}{2}tan\theta\right)^2 + \left(\frac{W}{2}\right)^2 + \left(z_p + \frac{z_{Gap}}{2} + \Delta\right)^2}}$$

$$= \frac{\frac{W}{2}}{cos\,\theta}\frac{1}{\sqrt{\left(\frac{W}{2}tan\theta\right)^2 + \left(\frac{W}{2}\right)^2 + \left(z_p + \frac{z_{Gap}}{2} + \Delta\right)^2}}$$

$$\Rightarrow \quad \left|\hat{r}_{xy}\right| = \frac{\frac{W}{2}}{cos\,\theta}\frac{1}{\sqrt{\left(\frac{W}{2}tan\theta\right)^2 + \left(\frac{W}{2}\right)^2 + \left(z_p + \frac{z_{Gap}}{2} + \Delta\right)^2}}$$

$$\hat{r}_x = \left|\hat{r}_{xy}\right| sin\,\theta\,(\hat{\imath}) = cos\,\alpha\, sin\,\theta\,(\hat{\imath}) = \frac{\frac{W}{2}tan\,\theta}{\sqrt{\left(\frac{W}{2}tan\theta\right)^2 + \left(\frac{W}{2}\right)^2 + \left(z_p + \frac{z_{Gap}}{2} + \Delta\right)^2}}(\hat{\imath})$$

$$\hat{r}_y = \left|\hat{r}_{xy}\right| cos\,\theta\,(\hat{\jmath}) = cos\,\alpha\, cos\,\theta\,(\hat{\jmath}) = \frac{\frac{W}{2}}{\sqrt{\left(\frac{W}{2}tan\theta\right)^2 + \left(\frac{W}{2}\right)^2 + \left(z_p + \frac{z_{Gap}}{2} + \Delta\right)^2}}(\hat{\jmath})$$

$$\hat{r}_z = |\hat{r}|\, sin\,\alpha\,(\hat{k}) = sin\,\alpha\,(\hat{k})$$

$$sin\,\alpha = \frac{\vec{r}_z}{|\vec{r}|} = \frac{z_p + \frac{z_{Gap}}{2} + \Delta}{\sqrt{\left(\frac{W}{2}tan\theta\right)^2 + \left(\frac{W}{2}\right)^2 + \left(z_p + \frac{z_{Gap}}{2} + \Delta\right)^2}}$$

$$\Rightarrow \quad \hat{r}_z = \frac{z_p + \frac{z_{Gap}}{2} + \Delta}{\sqrt{\left(\frac{W}{2}tan\theta\right)^2 + \left(\frac{W}{2}\right)^2 + \left(z_p + \frac{z_{Gap}}{2} + \Delta\right)^2}}(\hat{k})$$

$$\hat{r} = \left[\frac{\frac{W}{2}\tan\theta}{\sqrt{\left(\frac{W}{2}\tan\theta\right)^2 + \left(\frac{W}{2}\right)^2 + \left(z_p + \frac{z_{Gap}}{2} + \Delta\right)^2}} (\hat{\imath}) \right.$$

$$+ \frac{\frac{W}{2}}{\sqrt{\left(\frac{W}{2}\tan\theta\right)^2 + \left(\frac{W}{2}\right)^2 + \left(z_p + \frac{z_{Gap}}{2} + \Delta\right)^2}} (\hat{\jmath})$$

$$\left. + \frac{z_p + \frac{z_{Gap}}{2} + \Delta}{\sqrt{\left(\frac{W}{2}\tan\theta\right)^2 + \left(\frac{W}{2}\right)^2 + \left(z_p + \frac{z_{Gap}}{2} + \Delta\right)^2}} (\hat{k}) \right]$$

$$d\vec{x} \times \hat{r} = \frac{W}{2}\frac{d\theta}{\cos^2\theta}(-\hat{\imath}) \times$$

$$\left[\frac{\frac{W}{2}\tan\theta}{\sqrt{\left(\frac{W}{2}\tan\theta\right)^2 + \left(\frac{W}{2}\right)^2 + \left(z_p + \frac{z_{Gap}}{2} + \Delta\right)^2}} (\hat{\imath}) \right.$$

$$+ \frac{\frac{W}{2}}{\sqrt{\left(\frac{W}{2}\tan\theta\right)^2 + \left(\frac{W}{2}\right)^2 + \left(z_p + \frac{z_{Gap}}{2} + \Delta\right)^2}} (\hat{\jmath})$$

$$\left. + \frac{z_p + \frac{z_{Gap}}{2} + \Delta}{\sqrt{\left(\frac{W}{2}\tan\theta\right)^2 + \left(\frac{W}{2}\right)^2 + \left(z_p + \frac{z_{Gap}}{2} + \Delta\right)^2}} (\hat{k}) \right]$$

$$\Rightarrow \quad d\vec{x} \times \hat{r} = \frac{\left(\frac{W}{2}\right)^2}{\cos^2\theta} \frac{1}{\sqrt{\left(\frac{W}{2}\tan\theta\right)^2 + \left(\frac{W}{2}\right)^2 + \left(z_p + \frac{z_{Gap}}{2} + \Delta\right)^2}} d\theta(-\hat{k})$$

$$+ \frac{\left(\frac{W}{2}\right)}{\cos^2\theta} \frac{z_p + \frac{z_{Gap}}{2} + \Delta}{\sqrt{\left(\frac{W}{2}\tan\theta\right)^2 + \left(\frac{W}{2}\right)^2 + \left(z_p + \frac{z_{Gap}}{2} + \Delta\right)^2}} d\theta(\hat{\jmath})$$

$$\vec{B}_{p,15,bottom,a} = \frac{\mu_0 I}{4\pi} \int \frac{d\vec{x} \times \hat{r}}{|\vec{r}|^2}$$

$$\Rightarrow \quad \vec{B}_{p,15,bottom,a} = \frac{\mu_0 I}{4\pi} \int_{\theta_1}^{\theta_2} \frac{\frac{\left(\frac{W}{2}\right)^2}{\cos^2\theta} \frac{1}{\sqrt{\left(\frac{W}{2}\tan\theta\right)^2 + \left(\frac{W}{2}\right)^2 + \left(z_p + \frac{z_{Gap}}{2} + \Delta\right)^2}}}{\left(\frac{W}{2}\tan\theta\right)^2 + \left(\frac{W}{2}\right)^2 + \left(z_p + \frac{z_{Gap}}{2} + \Delta\right)^2} d\theta(-\hat{k})$$

$$+\frac{\mu_0 I}{4\pi}\int_{\theta_1}^{\theta_2}\frac{\frac{\left(\frac{W}{2}\right)}{\cos^2\theta}\frac{z_p+\frac{z_{Gap}}{2}+\Delta}{\sqrt{\left(\frac{W}{2}\tan\theta\right)^2+\left(\frac{W}{2}\right)^2+\left(z_p+\frac{z_{Gap}}{2}+\Delta\right)^2}}}{\left(\frac{W}{2}\tan\theta\right)^2+\left(\frac{W}{2}\right)^2+\left(z_p+\frac{z_{Gap}}{2}+\Delta\right)^2}d\theta(\hat{j})$$

$$\Rightarrow \quad \vec{B}_{p,15,bottom,a} = \qquad \textbf{Eq. (A.1)}$$

$$\frac{\mu_0 I\left(\frac{W}{2}\right)^2}{4\pi}\int_{\theta_1}^{\theta_2}\frac{1}{(\cos\theta)^2\left(\left(\frac{W}{2}\tan\theta\right)^2+\left(\frac{W}{2}\right)^2+\left(z_p+\frac{z_{Gap}}{2}+\Delta\right)^2\right)^{3/2}}d\theta(-\hat{k})$$

$$+\frac{\mu_0 I\left(\frac{W}{2}\right)\left(z_p+\frac{z_{Gap}}{2}+\Delta\right)}{4\pi}\int_{\theta_1}^{\theta_2}\frac{1}{(\cos\theta)^2\left(\left(\frac{W}{2}\tan\theta\right)^2+\left(\frac{W}{2}\right)^2+\left(z_p+\frac{z_{Gap}}{2}+\Delta\right)^2\right)^{3/2}}d\theta(\hat{j})$$

$$\theta_2 = \tan^{-1}\frac{L}{W} \quad , \quad \theta_1 = -\tan^{-1}\frac{L}{W}$$

A1.2. Part a - Top Coil

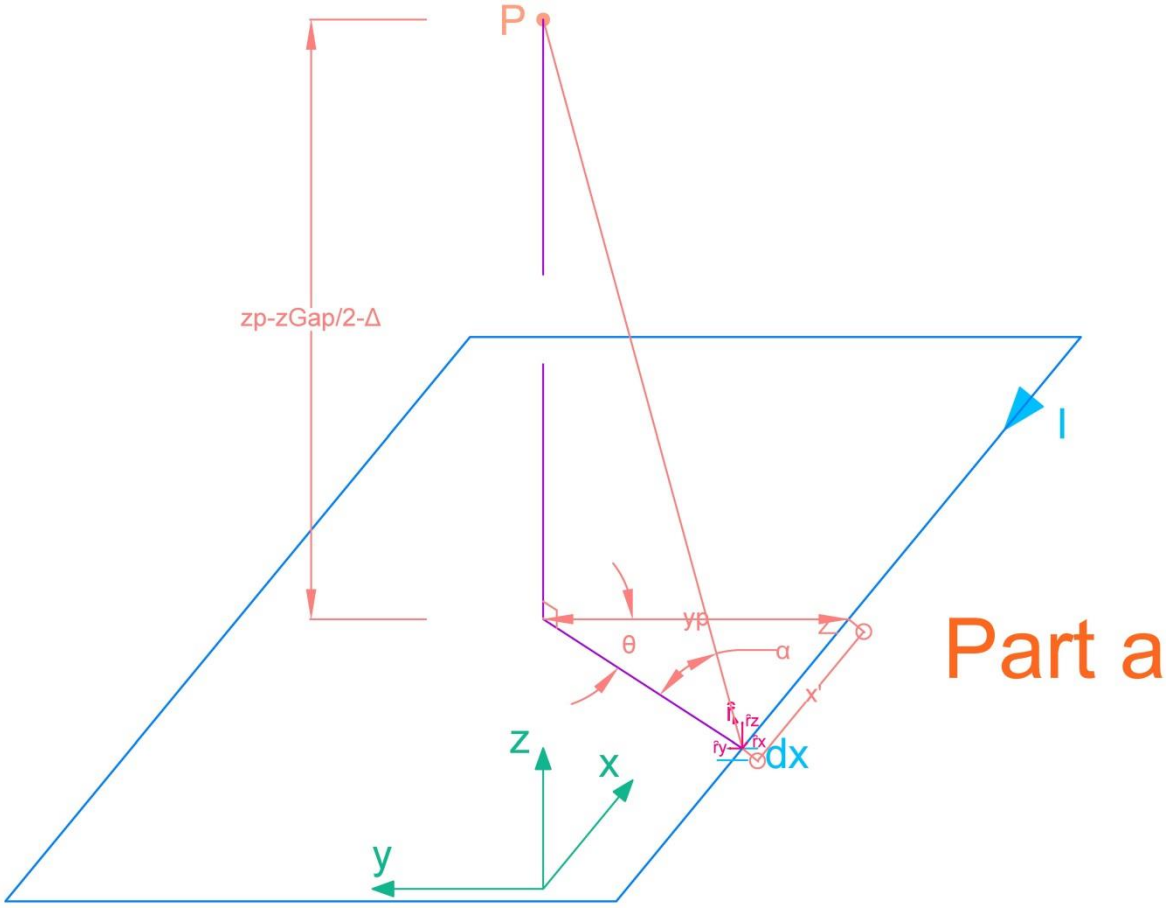

$$\vec{B}_{p,15,top,a} = \qquad \textbf{Eq. (A.2)}$$

$$\frac{\mu_0 I \left(\frac{W}{2}\right)^2}{4\pi} \int_{\theta_1}^{\theta_2} \frac{1}{(\cos\theta)^2 \left(\left(\frac{W}{2}\tan\theta\right)^2 + \left(\frac{W}{2}\right)^2 + \left(z_p - \frac{z_{Gap}}{2} - \Delta\right)^2\right)^{3/2}} d\theta(-\hat{k})$$

$$+\frac{\mu_0 I \left(\frac{W}{2}\right)\left(z_p - \frac{z_{Gap}}{2} - \Delta\right)}{4\pi} \int_{\theta_1}^{\theta_2} \frac{1}{(\cos\theta)^2 \left(\left(\frac{W}{2}\tan\theta\right)^2 + \left(\frac{W}{2}\right)^2 + \left(z_p - \frac{z_{Gap}}{2} - \Delta\right)^2\right)^{3/2}} d\theta(\hat{\jmath})$$

$$\theta_2 = \tan^{-1}\frac{L}{W} \quad , \quad \theta_1 = -\tan^{-1}\frac{L}{W}$$

A1.3. Part b - Bottom Coil

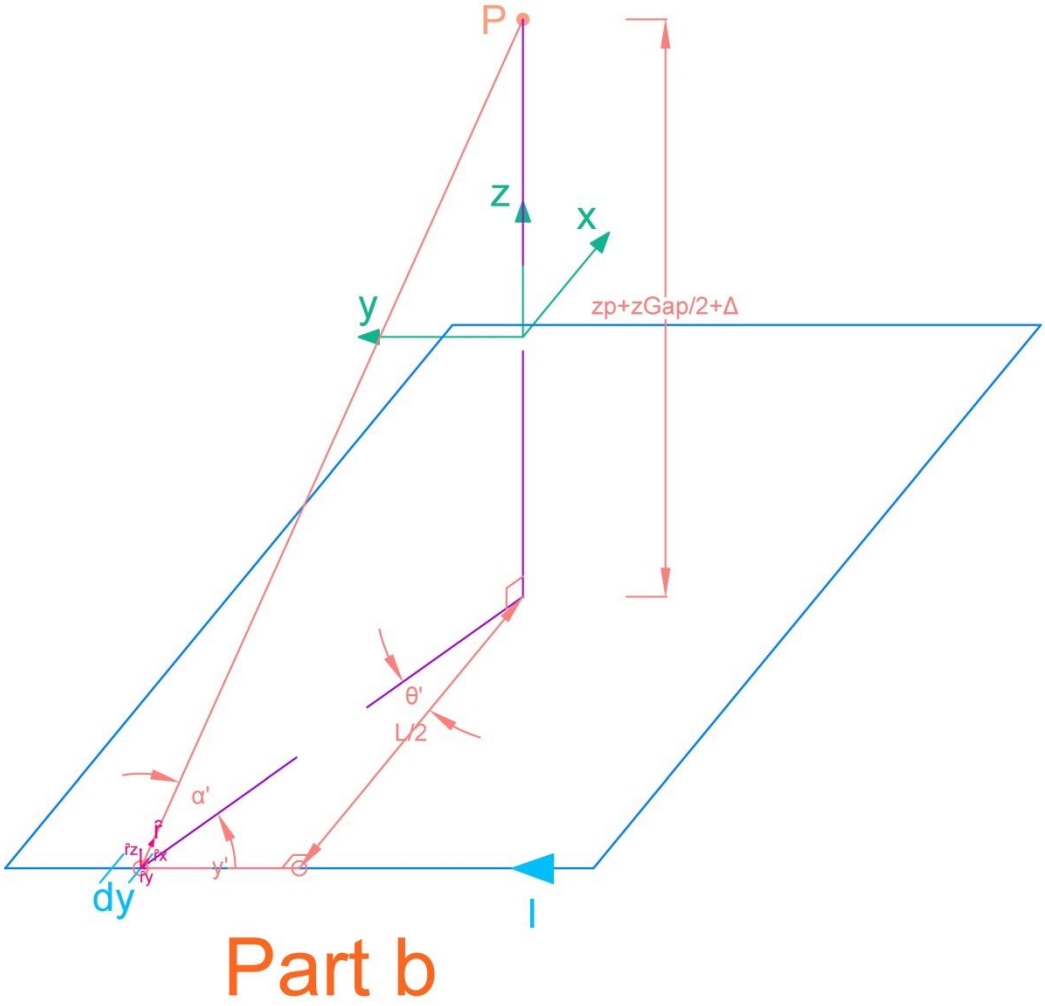

$$\vec{B}_{p,15,bottom,b} = \frac{\mu_{iron} I}{4\pi} \int \frac{d\vec{y} \times \hat{r}}{|\vec{r}|^2}$$

$$y = \frac{W}{2} + y' = \frac{W}{2} + \frac{L}{2} tan\theta'$$

$$d\vec{y} = \frac{L}{2} \frac{d\theta'}{cos^2 \theta'} (\hat{j})$$

$$|\vec{r}| = \sqrt{\left(\frac{L}{2}\right)^2 + \left(\frac{L}{2} tan\theta'\right)^2 + \left(z_p + \frac{z_{Gap}}{2} + \Delta\right)^2}$$

$$\hat{r} = \hat{r}_x + \hat{r}_y + \hat{r}_z$$

$$\left|\hat{r}_{xy}\right| = |\hat{r}| \, cos\, \alpha' = cos\, \alpha'$$

$$cos\alpha' = \frac{|\vec{r}_{xy}|}{|\vec{r}|} = \sqrt{\frac{\left(\frac{L}{2}\right)^2 + \left(\frac{L}{2}tan\theta'\right)^2}{\left(\frac{L}{2}\right)^2 + \left(\frac{L}{2}tan\theta'\right)^2 + \left(z_p + \frac{z_{Gap}}{2} + \Delta\right)^2}}$$

$$= \frac{\frac{L}{2}}{cos\,\theta'} \frac{1}{\sqrt{\left(\frac{L}{2}\right)^2 + \left(\frac{L}{2}tan\theta'\right)^2 + \left(z_p + \frac{z_{Gap}}{2} + \Delta\right)^2}}$$

$$\Rightarrow \quad |\hat{r}_{xy}| = \frac{\frac{L}{2}}{cos\,\theta'} \frac{1}{\sqrt{\left(\frac{L}{2}\right)^2 + \left(\frac{L}{2}tan\theta'\right)^2 + \left(z_p + \frac{z_{Gap}}{2} + \Delta\right)^2}}$$

$$\hat{r}_x = |\hat{r}_{xy}|\, cos\,\theta'\,(\hat{\imath}) = cos\,\alpha'\, cos\,\theta'\,(\hat{\imath}) = \frac{\frac{L}{2}}{\sqrt{\left(\frac{L}{2}\right)^2 + \left(\frac{L}{2}tan\theta'\right)^2 + \left(z_p + \frac{z_{Gap}}{2} + \Delta\right)^2}}(\hat{\imath})$$

$$\hat{r}_y = -|\hat{r}_{xy}|\, sin\,\theta'\,(\hat{\jmath}) = -\,cos\,\alpha'\, sin\,\theta'\,(\hat{\jmath}) = \frac{-\frac{L}{2}tan\,\theta'}{\sqrt{\left(\frac{L}{2}\right)^2 + \left(\frac{L}{2}tan\theta'\right)^2 + \left(z_p + \frac{z_{Gap}}{2} + \Delta\right)^2}}(\hat{\jmath})$$

$$\hat{r}_z = |\hat{r}|\, sin\,\alpha'\,(\hat{k}) = sin\,\alpha'\,(\hat{k})$$

$$sin\,\alpha' = \frac{\vec{r}_z}{|\vec{r}|} = \frac{z_p + z_{Gap} + \Delta}{\sqrt{\left(\frac{L}{2}\right)^2 + \left(\frac{L}{2}tan\theta'\right)^2 + \left(z_p + \frac{z_{Gap}}{2} + \Delta\right)^2}}$$

$$\Rightarrow \quad \hat{r}_z = \frac{z_p + \frac{z_{Gap}}{2} + \Delta}{\sqrt{\left(\frac{L}{2}\right)^2 + \left(\frac{L}{2}tan\theta'\right)^2 + \left(z_p + \frac{z_{Gap}}{2} + \Delta\right)^2}}(\hat{k})$$

$$\Rightarrow \quad \hat{r} = \left[\frac{\frac{L}{2}}{\sqrt{\left(\frac{L}{2}\right)^2 + \left(\frac{L}{2}tan\theta'\right)^2 + \left(z_p + \frac{z_{Gap}}{2} + \Delta\right)^2}}(\hat{\imath})\right.$$

$$+ \frac{\frac{L}{2}tan\,\theta'}{\sqrt{\left(\frac{L}{2}\right)^2 + \left(\frac{L}{2}tan\theta'\right)^2 + \left(z_p + \frac{z_{Gap}}{2} + \Delta\right)^2}}(-\hat{\jmath})$$

$$+ \frac{z_p + \frac{z_{Gap}}{2} + \Delta}{\sqrt{\left(\frac{L}{2}\right)^2 + \left(\frac{L}{2}tan\theta'\right)^2 + \left(z_p + \frac{z_{Gap}}{2} + \Delta\right)^2}}(\hat{k})$$

$$d\vec{y} \times \hat{r} = \frac{L}{2}\frac{d\theta'}{cos^2\,\theta'}(\hat{\jmath}) \times$$

$$\left[\frac{\frac{L}{2}}{\sqrt{\left(\frac{L}{2}\right)^2+\left(\frac{L}{2}tan\theta'\right)^2+\left(z_p+\frac{z_{Gap}}{2}+\Delta\right)^2}}(\hat{\imath})\right.$$

$$+\frac{\frac{L}{2}tan\,\theta'}{\sqrt{\left(\frac{L}{2}\right)^2+\left(\frac{L}{2}tan\theta'\right)^2+\left(z_p+\frac{z_{Gap}}{2}+\Delta\right)^2}}(-\hat{\jmath})$$

$$+\frac{z_p+\frac{z_{Gap}}{2}+\Delta}{\sqrt{\left(\frac{L}{2}\right)^2+\left(\frac{L}{2}tan\theta'\right)^2+\left(z_p+\frac{z_{Gap}}{2}+\Delta\right)^2}}(\hat{k})$$

$$\Rightarrow\quad d\vec{y}\times\hat{r}=\frac{\left(\frac{L}{2}\right)^2}{cos^2\,\theta'}\frac{1}{\sqrt{\left(\frac{L}{2}\right)^2+\left(\frac{L}{2}tan\theta'\right)^2+\left(z_p+\frac{z_{Gap}}{2}+\Delta\right)^2}}d\theta(-\hat{k})$$

$$+\frac{\left(\frac{L}{2}\right)}{cos^2\,\theta'}\frac{z_p+\frac{z_{Gap}}{2}+\Delta}{\sqrt{\left(\frac{L}{2}\right)^2+\left(\frac{L}{2}tan\theta'\right)^2+\left(z_p+\frac{z_{Gap}}{2}+\Delta\right)^2}}d\theta'(\hat{\imath})$$

$$\vec{B}_{p,15,bottom,b}=\frac{\mu_{iron}I}{4\pi}\int\frac{d\vec{y}\times\hat{r}}{|\vec{r}|^2}$$

$$\Rightarrow\quad \vec{B}_{p,15,bottom,b}=\frac{\mu_{iron}I}{4\pi}\int_{\theta'_1}^{\theta'_2}\frac{\frac{\left(\frac{L}{2}\right)^2}{cos^2\,\theta'}\frac{1}{\sqrt{\left(\frac{L}{2}\right)^2+\left(\frac{L}{2}tan\theta'\right)^2+\left(z_p+\frac{z_{Gap}}{2}+\Delta\right)^2}}}{\left(\frac{L}{2}\right)^2+\left(\frac{L}{2}tan\theta'\right)^2+\left(z_p+\frac{z_{Gap}}{2}+\Delta\right)^2}d\theta'(-\hat{k})$$

$$+\frac{\mu_{iron}I}{4\pi}\int_{\theta'_1}^{\theta'_2}\frac{\frac{\left(\frac{L}{2}\right)}{cos^2\,\theta'}\frac{z_p+\frac{z_{Gap}}{2}+\Delta}{\sqrt{\left(\frac{L}{2}\right)^2+\left(\frac{L}{2}tan\theta'\right)^2+\left(z_p+\frac{z_{Gap}}{2}+\Delta\right)^2}}}{\left(\frac{L}{2}\right)^2+\left(\frac{L}{2}tan\theta'\right)^2+\left(z_p+\frac{z_{Gap}}{2}+\Delta\right)^2}d\theta'(\hat{\imath})$$

$$\Rightarrow \quad \vec{B}_{p,15,bottom,b} = \qquad \textbf{Eq. (A.3)}$$

$$\frac{\mu_{iron} I \left(\frac{L}{2}\right)^2}{4\pi} \int_{\theta'_1}^{\theta'_2} \frac{1}{(\cos\theta')^2 \left(\left(\frac{L}{2}\right)^2 + \left(\frac{L}{2}\tan\theta'\right)^2 + \left(z_p + \frac{z_{Gap}}{2} + \Delta\right)^2\right)^{3/2}} d\theta' (-\hat{k})$$

$$+ \frac{\mu_{iron} I \left(\frac{L}{2}\right) \left(z_p + \frac{z_{Gap}}{2} + \Delta\right)}{4\pi} \int_{\theta'_1}^{\theta'_2} \frac{1}{(\cos\theta')^2 \left(\left(\frac{L}{2}\right)^2 + \left(\frac{L}{2}\tan\theta'\right)^2 + \left(z_p + \frac{z_{Gap}}{2} + \Delta\right)^2\right)^{3/2}} d\theta' (\hat{\imath})$$

$$\theta'_2 = \tan^{-1}\frac{W}{L} \quad , \quad \theta'_1 = -\tan^{-1}\frac{W}{L}$$

A1.4. Part b - Top Coil

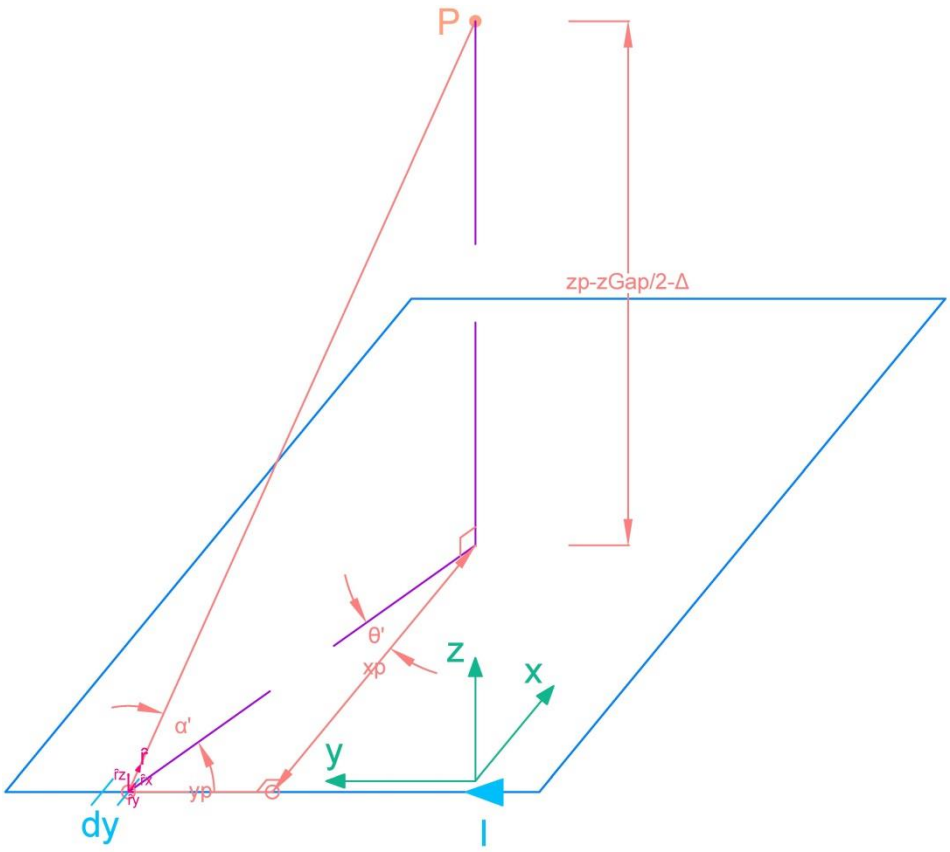

Part b

$$\vec{B}_{p,15,top,b} = \qquad \textbf{Eq. (A.4)}$$

$$\frac{\mu_{iron} I \left(\frac{L}{2}\right)^2}{4\pi} \int_{\theta'_1}^{\theta'_2} \frac{1}{(\cos\theta')^2 \left(\left(\frac{L}{2}\right)^2 + \left(\frac{L}{2}\tan\theta'\right)^2 + \left(z_p - \frac{z_{Gap}}{2} - \Delta\right)^2\right)^{3/2}} d\theta' \left(-\hat{k}\right)$$

$$+ \frac{\mu_{iron} I \left(\frac{L}{2}\right) \left(z_p - \frac{z_{Gap}}{2} - \Delta\right)}{4\pi} \int_{\theta'_1}^{\theta'_2} \frac{1}{(\cos\theta')^2 \left(\left(\frac{L}{2}\right)^2 + \left(\frac{L}{2}\tan\theta'\right)^2 + \left(z_p - \frac{z_{Gap}}{2} - \Delta\right)^2\right)^{3/2}} d\theta' (\hat{\imath})$$

$$\theta'_2 = \tan^{-1}\frac{W}{L} \quad , \quad \theta'_1 = -\tan^{-1}\frac{W}{L}$$

A1.5 Part c - Bottom Coil

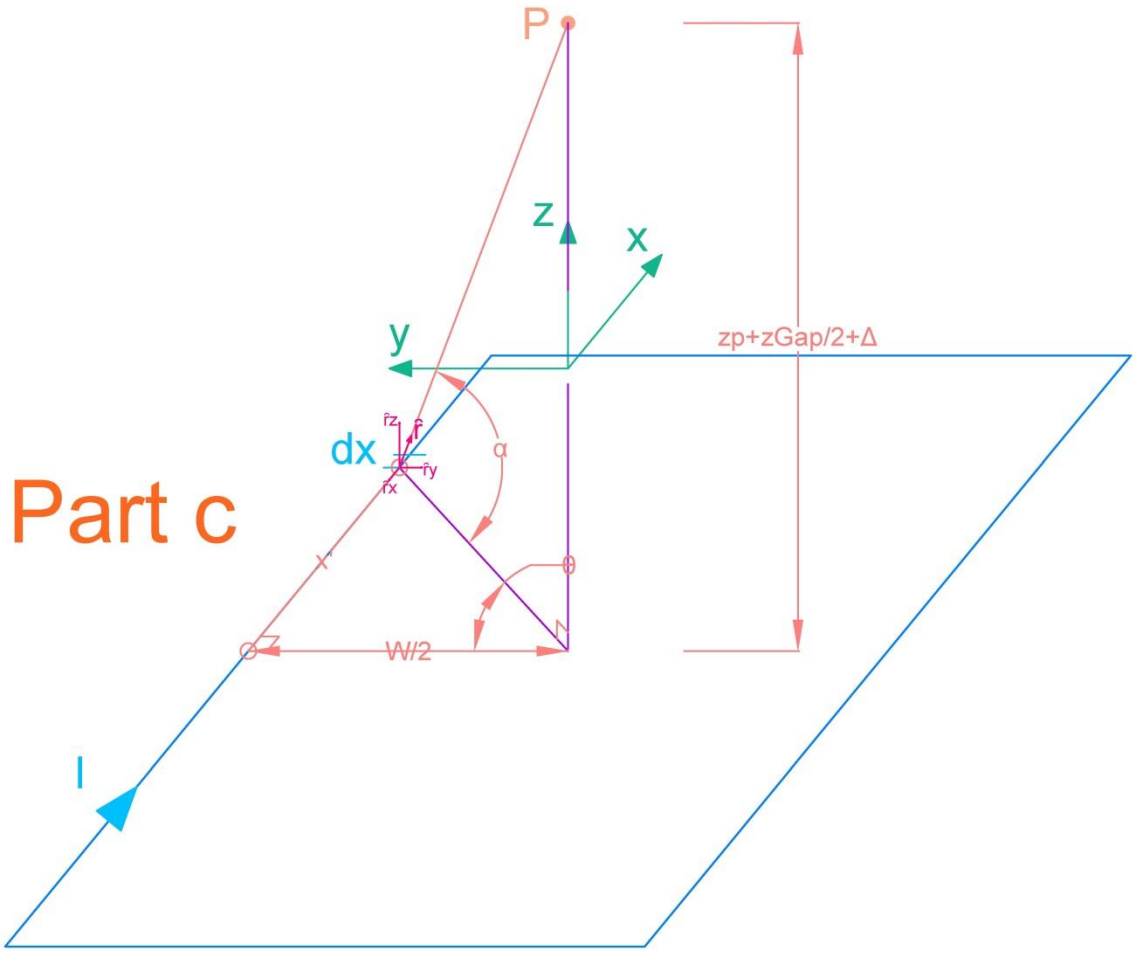

$$\vec{B}_{p,15,bottom,c} = \frac{\mu_{iron} I}{4\pi} \int \frac{d\vec{x} \times \hat{r}}{|\vec{r}|^2}$$

$$x = \frac{L}{2} + x' = \frac{L}{2} + \frac{W}{2} tan\theta$$

$$d\vec{x} = \frac{W}{2} \frac{d\theta}{cos^2\,\theta} (\hat{\imath})$$

$$|\vec{r}| = \sqrt{\left(\frac{W}{2} tan\theta\right)^2 + \left(\frac{W}{2}\right)^2 + \left(z_p + \frac{z_{Gap}}{2} + \Delta\right)^2}$$

$$\hat{r} = \hat{r}_x + \hat{r}_y + \hat{r}_z$$

$$\left|\hat{r}_{xy}\right| = |\hat{r}|\, cos\,\alpha = cos\,\alpha$$

$$cos\alpha = \frac{|\vec{r}_{xy}|}{|\vec{r}|} = \sqrt{\frac{\left(\frac{W}{2}tan\theta\right)^2 + \left(\frac{W}{2}\right)^2}{\left(\frac{W}{2}tan\theta\right)^2 + \left(\frac{W}{2}\right)^2 + \left(z_p + \frac{z_{Gap}}{2} + \Delta\right)^2}}$$

$$= \frac{\frac{W}{2}}{cos\,\theta} \frac{1}{\sqrt{\left(\frac{W}{2}tan\theta\right)^2 + \left(\frac{W}{2}\right)^2 + \left(z_p + \frac{z_{Gap}}{2} + \Delta\right)^2}}$$

$$\Rightarrow \quad |\hat{r}_{xy}| = \frac{\frac{W}{2}}{cos\,\theta} \frac{1}{\sqrt{\left(\frac{W}{2}tan\theta\right)^2 + \left(\frac{W}{2}\right)^2 + \left(z_p + \frac{z_{Gap}}{2} + \Delta\right)^2}}$$

$$\hat{r}_x = -|\hat{r}_{xy}|\,sin\,\theta\,(\hat{\imath}) = -\,cos\,\alpha\,sin\,\theta\,(\hat{\imath}) = \frac{-\frac{W}{2}tan\,\theta}{\sqrt{\left(\frac{W}{2}tan\theta\right)^2 + \left(\frac{W}{2}\right)^2 + \left(z_p + \frac{z_{Gap}}{2} + \Delta\right)^2}}(\hat{\imath})$$

$$\hat{r}_y = -|\hat{r}_{xy}|\,cos\,\theta\,(\hat{\jmath}) = -\,cos\,\alpha\,cos\,\theta\,(\hat{\jmath}) = \frac{-\frac{W}{2}}{\sqrt{\left(\frac{W}{2}tan\theta\right)^2 + \left(\frac{W}{2}\right)^2 + \left(z_p + \frac{z_{Gap}}{2} + \Delta\right)^2}}(\hat{\jmath})$$

$$\hat{r}_z = |\hat{r}|\,sin\,\alpha\,(\hat{k}) = sin\,\alpha\,(\hat{k})$$

$$sin\,\alpha = \frac{\vec{r}_z}{|\vec{r}|} = \frac{z_p + \frac{z_{Gap}}{2} + \Delta}{\sqrt{\left(\frac{W}{2}tan\theta\right)^2 + \left(\frac{W}{2}\right)^2 + \left(z_p + \frac{z_{Gap}}{2} + \Delta\right)^2}}$$

$$\Rightarrow \quad \hat{r}_z = \frac{z_p + \frac{z_{Gap}}{2} + \Delta}{\sqrt{\left(\frac{W}{2}tan\theta\right)^2 + \left(\frac{W}{2}\right)^2 + \left(z_p + \frac{z_{Gap}}{2} + \Delta\right)^2}}(\hat{k})$$

$$\hat{r} = \left[\frac{\frac{W}{2}tan\,\theta}{\sqrt{\left(\frac{W}{2}tan\theta\right)^2 + \left(\frac{W}{2}\right)^2 + \left(z_p + \frac{z_{Gap}}{2} + \Delta\right)^2}}(-\hat{\imath})\right.$$

$$+ \frac{\frac{W}{2}}{\sqrt{\left(\frac{W}{2}tan\theta\right)^2 + \left(\frac{W}{2}\right)^2 + \left(z_p + \frac{z_{Gap}}{2} + \Delta\right)^2}}(-\hat{\jmath})$$

$$\left. + \frac{z_p + \frac{z_{Gap}}{2} + \Delta}{\sqrt{\left(\frac{W}{2}tan\theta\right)^2 + \left(\frac{W}{2}\right)^2 + \left(z_p + \frac{z_{Gap}}{2} + \Delta\right)^2}}(\hat{k})\right]$$

$$d\vec{x} \times \hat{r} = \frac{W}{2}\frac{d\theta}{cos^2\,\theta}(\hat{\imath}) \times$$

$$\left[\frac{\frac{W}{2}tan\,\theta}{\sqrt{\left(\frac{W}{2}tan\theta\right)^2 + \left(\frac{W}{2}\right)^2 + \left(z_p + \frac{z_{Gap}}{2} + \Delta\right)^2}}(-\hat{\imath})\right.$$

$$+\frac{\frac{W}{2}}{\sqrt{\left(\frac{W}{2}tan\theta\right)^2 + \left(\frac{W}{2}\right)^2 + \left(z_p + \frac{z_{Gap}}{2} + \Delta\right)^2}}(-\hat{\jmath})$$

$$\left.+\frac{z_p + \frac{z_{Gap}}{2} + \Delta}{\sqrt{\left(\frac{W}{2}tan\theta\right)^2 + \left(\frac{W}{2}\right)^2 + \left(z_p + \frac{z_{Gap}}{2} + \Delta\right)^2}}(\hat{k})\right]$$

$$\Rightarrow \quad d\vec{x} \times \hat{r} = \frac{\left(\frac{W}{2}\right)^2}{cos^2\,\theta}\frac{1}{\sqrt{\left(\frac{W}{2}tan\theta\right)^2 + \left(\frac{W}{2}\right)^2 + \left(z_p + \frac{z_{Gap}}{2} + \Delta\right)^2}}d\theta(-\hat{k})$$

$$+\frac{\left(\frac{W}{2}\right)}{cos^2\,\theta}\frac{z_p + \frac{z_{Gap}}{2} + \Delta}{\sqrt{\left(\frac{W}{2}tan\theta\right)^2 + \left(\frac{W}{2}\right)^2 + \left(z_p + \frac{z_{Gap}}{2} + \Delta\right)^2}}d\theta(-\hat{\jmath})$$

$$\vec{B}_{p,15,bottom,c} = \frac{\mu_{iron}I}{4\pi}\int \frac{d\vec{x} \times \hat{r}}{|\vec{r}|^2}$$

$$\Rightarrow \quad \vec{B}_{p,15,bottom,c} = \frac{\mu_{iron}I}{4\pi}\int_{\theta_1}^{\theta_2} \frac{\frac{\left(\frac{W}{2}\right)^2}{cos^2\,\theta}\frac{1}{\sqrt{\left(\frac{W}{2}tan\theta\right)^2 + \left(\frac{W}{2}\right)^2 + \left(z_p + \frac{z_{Gap}}{2} + \Delta\right)^2}}}{\left(\frac{W}{2}tan\theta\right)^2 + \left(\frac{W}{2}\right)^2 + \left(z_p + \frac{z_{Gap}}{2} + \Delta\right)^2}d\theta(-\hat{k})$$

$$+\frac{\mu_{iron}I}{4\pi}\int_{\theta_1}^{\theta_2} \frac{\frac{\left(\frac{W}{2}\right)^2}{cos^2\,\theta}\frac{z_p + \frac{z_{Gap}}{2} + \Delta}{\sqrt{\left(\frac{W}{2}tan\theta\right)^2 + \left(\frac{W}{2}\right)^2 + \left(z_p + \frac{z_{Gap}}{2} + \Delta\right)^2}}}{\left(\frac{W}{2}tan\theta\right)^2 + \left(\frac{W}{2}\right)^2 + \left(z_p + \frac{z_{Gap}}{2} + \Delta\right)^2}d\theta(-\hat{\jmath})$$

$$\Rightarrow \quad \vec{B}_{p,15,bottom,c} = \qquad \textbf{Eq. (A.5)}$$

$$\frac{\mu_{iron} I \left(\frac{W}{2}\right)^2}{4\pi} \int_{\theta_1}^{\theta_2} \frac{1}{(cos\,\theta)^2 \left(\left(\frac{W}{2} tan\theta\right)^2 + \left(\frac{W}{2}\right)^2 + \left(z_p + \frac{z_{Gap}}{2} + \Delta\right)^2\right)^{3/2}} d\theta(-\hat{k})$$

$$+ \frac{\mu_{iron} I \left(\frac{W}{2}\right)(z_p + \frac{z_{Gap}}{2} + \Delta)}{4\pi} \int_{\theta_1}^{\theta_2} \frac{1}{(cos\,\theta)^2 \left(\left(\frac{W}{2} tan\theta\right)^2 + \left(\frac{W}{2}\right)^2 + \left(z_p + \frac{z_{Gap}}{2} + \Delta\right)^2\right)^{3/2}} d\theta(-\hat{j})$$

$$\theta_2 = tan^{-1}\frac{L}{W} \quad , \quad \theta_1 = -\,tan^{-1}\frac{L}{W}$$

A1.6. Part c - Top Coil

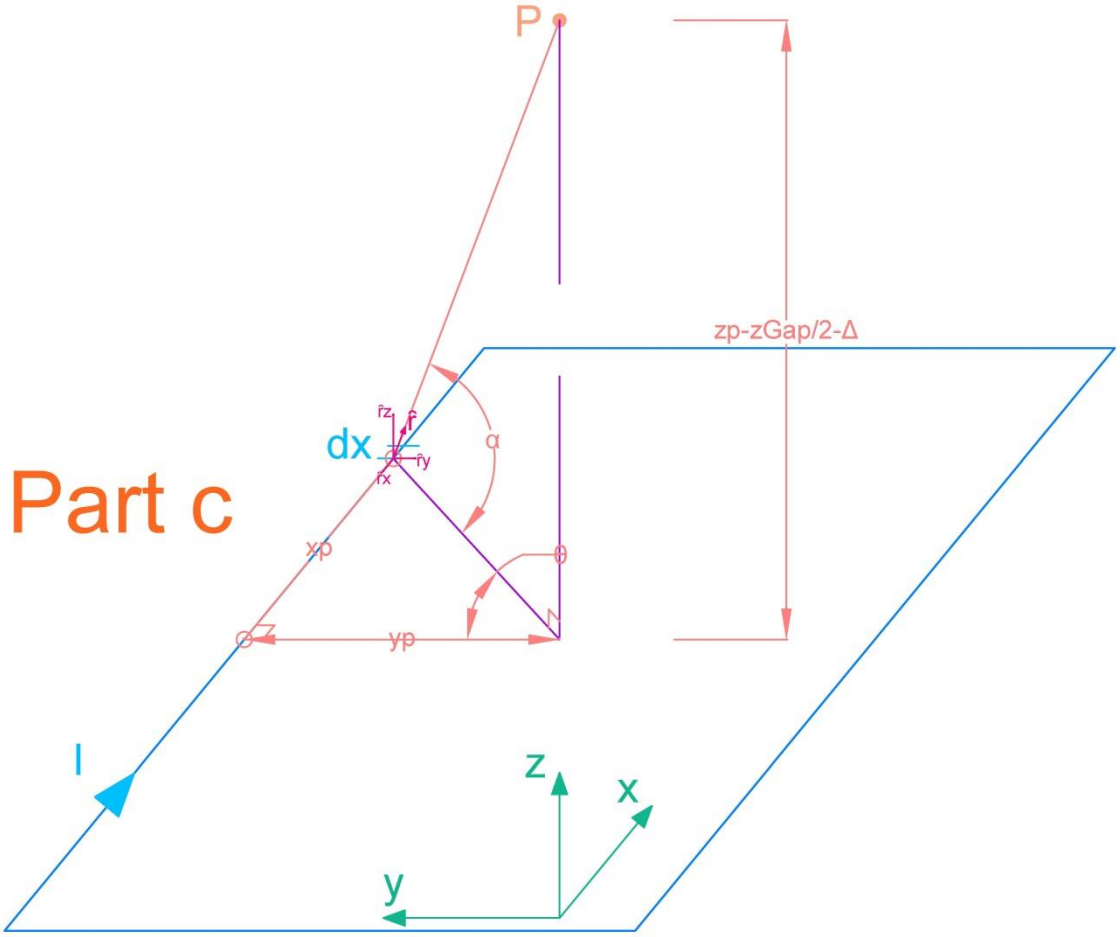

$$\vec{B}_{p,15,top,c} = \qquad \textbf{Eq. (A.6)}$$

$$\frac{\mu_0 I \left(\frac{W}{2}\right)^2}{4\pi} \int_{\theta_1}^{\theta_2} \frac{1}{(\cos\theta)^2 \left(\left(\frac{W}{2}\tan\theta\right)^2 + \left(\frac{W}{2}\right)^2 + \left(z_p - \frac{z_{Gap}}{2} - \Delta\right)^2\right)^{3/2}} d\theta(-\hat{k})$$

$$+\frac{\mu_0 I \left(\frac{W}{2}\right)\left(z_p - \frac{z_{Gap}}{2} - \Delta\right)}{4\pi} \int_{\theta_1}^{\theta_2} \frac{1}{(\cos\theta)^2 \left(\left(\frac{W}{2}\tan\theta\right)^2 + \left(\frac{W}{2}\right)^2 + \left(z_p - \frac{z_{Gap}}{2} - \Delta\right)^2\right)^{3/2}} d\theta(-\hat{j})$$

$$\theta_2 = \tan^{-1}\frac{L}{W} \quad , \quad \theta_1 = -\tan^{-1}\frac{L}{W}$$

A1.7. Part d - Bottom Coil

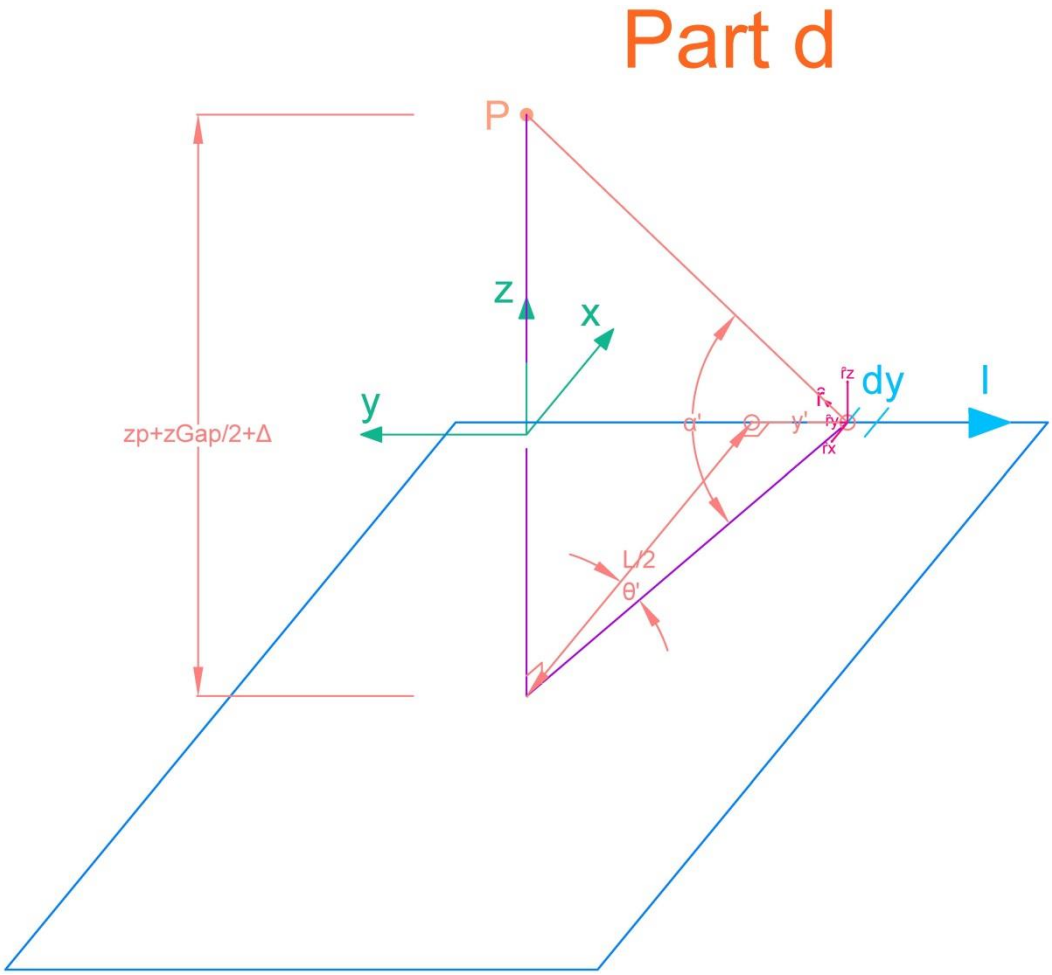

$$\vec{B}_{p,15,bottom,d} = \frac{\mu_{iron} I}{4\pi} \int \frac{d\vec{y} \times \hat{r}}{|\vec{r}|^2}$$

$$y = \frac{W}{2} - y' = \frac{W}{2} - \left(-\frac{L}{2} tan\theta'\right) = \frac{W}{2} + \frac{L}{2} tan\theta'$$

$$d\vec{y} = \frac{L}{2} \frac{d\theta'}{cos^2\,\theta'} (-\hat{j})$$

$$|\vec{r}| = \sqrt{\left(\frac{L}{2}\right)^2 + \left(\frac{L}{2} tan\theta'\right)^2 + \left(z_p + \frac{z_{Gap}}{2} + \Delta\right)^2}$$

$$\hat{r} = \hat{r}_x + \hat{r}_y + \hat{r}_z$$

$$\left|\hat{r}_{xy}\right| = |\hat{r}|\, cos\,\alpha' = cos\,\alpha'$$

$$cos\alpha' = \frac{|\vec{r}_{xy}|}{|\vec{r}|} = \sqrt{\frac{\left(\frac{L}{2}\right)^2 + \left(\frac{L}{2}tan\theta'\right)^2}{\left(\frac{L}{2}\right)^2 + \left(\frac{L}{2}tan\theta'\right)^2 + \left(z_p + \frac{z_{Gap}}{2} + \Delta\right)^2}}$$

$$= \frac{\frac{L}{2}}{cos\,\theta'} \frac{1}{\sqrt{\left(\frac{L}{2}\right)^2 + \left(\frac{L}{2}tan\theta'\right)^2 + \left(z_p + \frac{z_{Gap}}{2} + \Delta\right)^2}}$$

$$\Rightarrow \quad |\hat{r}_{xy}| = \frac{\frac{L}{2}}{cos\,\theta'} \frac{1}{\sqrt{\left(\frac{L}{2}\right)^2 + \left(\frac{L}{2}tan\theta'\right)^2 + \left(z_p + \frac{z_{Gap}}{2} + \Delta\right)^2}}$$

$$\hat{r}_x = |\hat{r}_{xy}|\, cos\,\theta'\,(-\hat{\imath}) = cos\,\alpha'\, cos\,\theta'\,(-\hat{\imath}) = \frac{\frac{L}{2}}{\sqrt{\left(\frac{L}{2}\right)^2 + \left(\frac{L}{2}tan\theta'\right)^2 + \left(z_p + \frac{z_{Gap}}{2} + \Delta\right)^2}}(-\hat{\imath})$$

$$\hat{r}_y = |\hat{r}_{xy}|\, sin\,\theta'\,(\hat{\jmath}) = cos\,\alpha'\, sin\,\theta'\,(\hat{\jmath}) = \frac{\frac{L}{2}tan\,\theta'}{\sqrt{\left(\frac{L}{2}\right)^2 + \left(\frac{L}{2}tan\theta'\right)^2 + \left(z_p + \frac{z_{Gap}}{2} + \Delta\right)^2}}(\hat{\jmath})$$

$$\hat{r}_z = |\hat{r}|\, sin\,\alpha'\,(\hat{k}) = sin\,\alpha'\,(\hat{k})$$

$$sin\,\alpha' = \frac{\vec{r}_z}{|\vec{r}|} = \frac{z_p + z_{Gap} + \Delta}{\sqrt{\left(\frac{L}{2}\right)^2 + \left(\frac{L}{2}tan\theta'\right)^2 + \left(z_p + \frac{z_{Gap}}{2} + \Delta\right)^2}}$$

$$\Rightarrow \quad \hat{r}_z = \frac{z_p + \frac{z_{Gap}}{2} + \Delta}{\sqrt{\left(\frac{L}{2}\right)^2 + \left(\frac{L}{2}tan\theta'\right)^2 + \left(z_p + \frac{z_{Gap}}{2} + \Delta\right)^2}}(\hat{k})$$

$$\Rightarrow \quad \hat{r} = \left[\frac{\frac{L}{2}}{\sqrt{\left(\frac{L}{2}\right)^2 + \left(\frac{L}{2}tan\theta'\right)^2 + \left(z_p + \frac{z_{Gap}}{2} + \Delta\right)^2}}(-\hat{\imath})\right.$$

$$+ \frac{\frac{L}{2}tan\,\theta'}{\sqrt{\left(\frac{L}{2}\right)^2 + \left(\frac{L}{2}tan\theta'\right)^2 + \left(z_p + \frac{z_{Gap}}{2} + \Delta\right)^2}}(\hat{\jmath})$$

$$+ \frac{z_p + \frac{z_{Gap}}{2} + \Delta}{\sqrt{\left(\frac{L}{2}\right)^2 + \left(\frac{L}{2}tan\theta'\right)^2 + \left(z_p + \frac{z_{Gap}}{2} + \Delta\right)^2}}(\hat{k})$$

$$d\vec{y} \times \hat{r} = \frac{L}{2}\frac{d\theta'}{cos^2\,\theta'}(-\hat{\jmath}) \times$$

$$\left[\frac{\frac{L}{2}}{\sqrt{\left(\frac{L}{2}\right)^2+\left(\frac{L}{2}tan\theta'\right)^2+\left(z_p+\frac{z_{Gap}}{2}+\Delta\right)^2}}(-\hat{\imath})\right.$$

$$+\frac{\frac{L}{2}tan\,\theta'}{\sqrt{\left(\frac{L}{2}\right)^2+\left(\frac{L}{2}tan\theta'\right)^2+\left(z_p+\frac{z_{Gap}}{2}+\Delta\right)^2}}(\hat{\jmath})$$

$$+\frac{z_p+\frac{z_{Gap}}{2}+\Delta}{\sqrt{\left(\frac{L}{2}\right)^2+\left(\frac{L}{2}tan\theta'\right)^2+\left(z_p+\frac{z_{Gap}}{2}+\Delta\right)^2}}(\hat{k})$$

$$\Rightarrow\quad d\vec{y}\times\hat{r}=\frac{\left(\frac{L}{2}\right)^2}{cos^2\,\theta'}\frac{1}{\sqrt{\left(\frac{L}{2}\right)^2+\left(\frac{L}{2}tan\theta'\right)^2+\left(z_p+\frac{z_{Gap}}{2}+\Delta\right)^2}}d\theta(-\hat{k})$$

$$+\frac{\left(\frac{L}{2}\right)}{cos^2\,\theta'}\frac{z_p+\frac{z_{Gap}}{2}+\Delta}{\sqrt{\left(\frac{L}{2}\right)^2+\left(\frac{L}{2}tan\theta'\right)^2+\left(z_p+\frac{z_{Gap}}{2}+\Delta\right)^2}}d\theta'(-\hat{\imath})$$

$$\vec{B}_{p,15,bottom,d}=\frac{\mu_{iron}I}{4\pi}\int\frac{d\vec{y}\times\hat{r}}{|\vec{r}|^2}$$

$$\Rightarrow\quad \vec{B}_{p,15,bottom,d}=\frac{\mu_{iron}I}{4\pi}\int_{\theta'_1}^{\theta'_2}\frac{\frac{\left(\frac{L}{2}\right)^2}{cos^2\,\theta'}\frac{1}{\sqrt{\left(\frac{L}{2}\right)^2+\left(\frac{L}{2}tan\theta'\right)^2+\left(z_p+\frac{z_{Gap}}{2}+\Delta\right)^2}}}{\left(\frac{L}{2}\right)^2+\left(\frac{L}{2}tan\theta'\right)^2+\left(z_p+\frac{z_{Gap}}{2}+\Delta\right)^2}d\theta'(-\hat{k})$$

$$+\frac{\mu_{iron}I}{4\pi}\int_{\theta'_1}^{\theta'_2}\frac{\frac{\left(\frac{L}{2}\right)}{cos^2\,\theta'}\frac{z_p+\frac{z_{Gap}}{2}+\Delta}{\sqrt{\left(\frac{L}{2}\right)^2+\left(\frac{L}{2}tan\theta'\right)^2+\left(z_p+\frac{z_{Gap}}{2}+\Delta\right)^2}}}{\left(\frac{L}{2}\right)^2+\left(\frac{L}{2}tan\theta'\right)^2+\left(z_p+\frac{z_{Gap}}{2}+\Delta\right)^2}d\theta'(-\hat{\imath})$$

$$\Rightarrow \quad \vec{B}_{p,15,bottom,d} = \qquad \textbf{Eq. (A.7)}$$

$$\frac{\mu_{iron} I \left(\frac{L}{2}\right)^2}{4\pi} \int_{\theta'_1}^{\theta'_2} \frac{1}{(\cos\theta')^2 \left(\left(\frac{L}{2}\right)^2 + \left(\frac{L}{2}\tan\theta'\right)^2 + \left(z_p + \frac{z_{Gap}}{2} + \Delta\right)^2\right)^{3/2}} d\theta'(-\hat{k})$$

$$+ \frac{\mu_{iron} I \left(\frac{L}{2}\right)\left(z_p + \frac{z_{Gap}}{2} + \Delta\right)}{4\pi} \int_{\theta'_1}^{\theta'_2} \frac{1}{(\cos\theta')^2 \left(\left(\frac{L}{2}\right)^2 + \left(\frac{L}{2}\tan\theta'\right)^2 + \left(z_p + \frac{z_{Gap}}{2} + \Delta\right)^2\right)^{3/2}} d\theta'(-\hat{\imath})$$

$$\theta'_2 = \tan^{-1}\frac{W}{L} \quad , \quad \theta'_1 = -\tan^{-1}\frac{W}{L}$$

A1.8. Part d - Top Coil

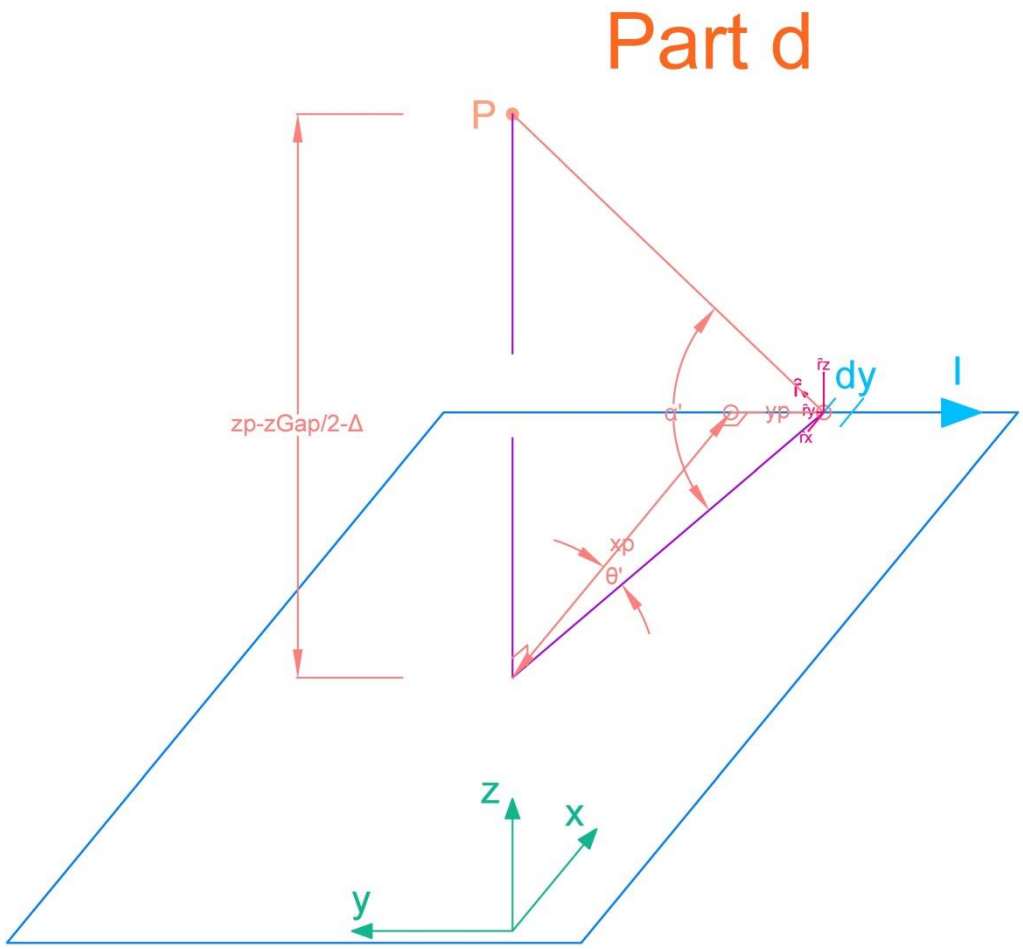

$$\vec{B}_{p,15,top,d} =$$ **Eq. (A.8)**

$$\frac{\mu_{iron} I \left(\frac{L}{2}\right)^2}{4\pi} \int_{\theta'_1}^{\theta'_2} \frac{1}{(\cos\theta')^2 \left(\left(\frac{L}{2}\right)^2 + \left(\frac{L}{2}\tan\theta'\right)^2 + \left(z_p - \frac{z_{Gap}}{2} - \Delta\right)^2\right)^{3/2}} d\theta' (-\hat{k})$$

$$+ \frac{\mu_{iron} I \left(\frac{L}{2}\right) \left(z_p - \frac{z_{Gap}}{2} - \Delta\right)}{4\pi} \int_{\theta'_1}^{\theta'_2} \frac{1}{(\cos\theta')^2 \left(\left(\frac{L}{2}\right)^2 + \left(\frac{L}{2}\tan\theta'\right)^2 + \left(z_p - \frac{z_{Gap}}{2} - \Delta\right)^2\right)^{3/2}} d\theta' (-\hat{\imath})$$

$$\theta'_2 = \tan^{-1}\frac{W}{L} \quad , \quad \theta'_1 = -\tan^{-1}\frac{W}{L}$$

A2. Sections 2 and 4

A2.1. Part a - Bottom Coil

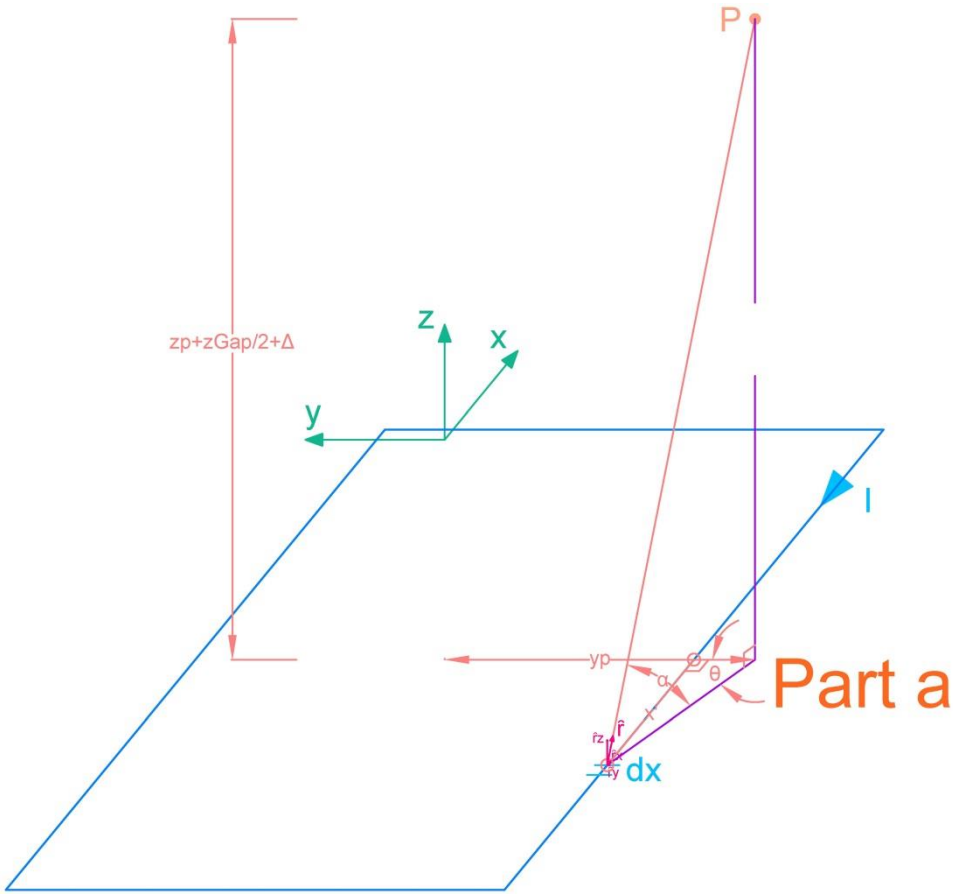

$$\vec{B}_{p,24,bottom,a} = \frac{\mu_0 I}{4\pi}\int \frac{d\vec{x}\times\hat{r}}{|\vec{r}|^2}$$

$$x = \frac{L}{2} - x' = \frac{L}{2} - \left(-\left|\frac{W}{2}+y_p\right| tan\theta\right) = \frac{L}{2} + \left|\frac{W}{2}+y_p\right| tan\theta$$

$$d\vec{x} = \left|\frac{W}{2}+y_p\right| \frac{d\theta}{cos^2\theta}(-\hat{\imath})$$

$$|\vec{r}| = \sqrt{\left(\left|\frac{W}{2}+y_p\right| tan\theta\right)^2 + \left(\frac{W}{2}+y_p\right)^2 + \left(z_p + \frac{z_{Gap}}{2} + \Delta\right)^2}$$

$$\hat{r} = \hat{r}_x + \hat{r}_y + \hat{r}_z$$

$$\left|\hat{r}_{xy}\right| = |\hat{r}|\, cos\,\alpha = cos\,\alpha$$

$$cos\alpha = \frac{|\vec{r}_{xy}|}{|\vec{r}|} = \sqrt{\frac{\left(\left|\frac{W}{2}+y_p\right| tan\theta\right)^2 + \left(\frac{W}{2}+y_p\right)^2}{\left(\left|\frac{W}{2}+y_p\right| tan\theta\right)^2 + \left(\frac{W}{2}+y_p\right)^2 + \left(z_p + \frac{z_{Gap}}{2} + \Delta\right)^2}}$$

$$= \frac{\left|\frac{W}{2} + y_p\right|}{\cos\theta} \frac{1}{\sqrt{\left(\left|\frac{W}{2} + y_p\right| tan\theta\right)^2 + \left(\frac{W}{2} + y_p\right)^2 + \left(z_p + \frac{z_{Gap}}{2} + \Delta\right)^2}}$$

$$\Rightarrow \quad |\hat{r}_{xy}| = \frac{\left|\frac{W}{2} + y_p\right|}{\cos\theta} \frac{1}{\sqrt{\left(\left|\frac{W}{2} + y_p\right| tan\theta\right)^2 + \left(\frac{W}{2} + y_p\right)^2 + \left(z_p + \frac{z_{Gap}}{2} + \Delta\right)^2}}$$

$$\hat{r}_x = |\hat{r}_{xy}| \sin\theta\,(\hat{\imath}) = \cos\alpha \sin\theta\,(\hat{\imath})$$

$$= \frac{\left|\frac{W}{2} + y_p\right| \tan\theta}{\sqrt{\left(\left|\frac{W}{2} + y_p\right| tan\theta\right)^2 + \left(\frac{W}{2} + y_p\right)^2 + \left(z_p + \frac{z_{Gap}}{2} + \Delta\right)^2}} (\hat{\imath})$$

$$\hat{r}_y = |\hat{r}_{xy}| \cos\theta\,(\hat{\jmath}) = \cos\alpha \cos\theta\,(\hat{\jmath})$$

$$= \frac{\left(\frac{W}{2} + y_p\right)}{\sqrt{\left(\left|\frac{W}{2} + y_p\right| tan\theta\right)^2 + \left(\frac{W}{2} + y_p\right)^2 + \left(z_p + \frac{z_{Gap}}{2} + \Delta\right)^2}} (\hat{\jmath})$$

$$\hat{r}_z = |\hat{r}| \sin\alpha\,(\hat{k}) = \sin\alpha\,(\hat{k})$$

$$\sin\alpha = \frac{\vec{r}_z}{|\vec{r}|} = \frac{z_p + \frac{z_{Gap}}{2} + \Delta}{\sqrt{\left(\left|\frac{W}{2} + y_p\right| tan\theta\right)^2 + \left(\frac{W}{2} + y_p\right)^2 + \left(z_p + \frac{z_{Gap}}{2} + \Delta\right)^2}}$$

$$\Rightarrow \quad \hat{r}_z = \frac{z_p + \frac{z_{Gap}}{2} + \Delta}{\sqrt{\left(\left|\frac{W}{2} + y_p\right| tan\theta\right)^2 + \left(\frac{W}{2} + y_p\right)^2 + \left(z_p + \frac{z_{Gap}}{2} + \Delta\right)^2}} (\hat{k})$$

$$\hat{r} = \left[\frac{\left|\frac{W}{2} + y_p\right| \tan\theta}{\sqrt{\left(\left|\frac{W}{2} + y_p\right| tan\theta\right)^2 + \left(\frac{W}{2} + y_p\right)^2 + \left(z_p + \frac{z_{Gap}}{2} + \Delta\right)^2}} (\hat{\imath})\right.$$

$$+ \frac{\left(\frac{W}{2} + y_p\right)}{\sqrt{\left(\left|\frac{W}{2} + y_p\right| tan\theta\right)^2 + \left(\frac{W}{2} + y_p\right)^2 + \left(z_p + \frac{z_{Gap}}{2} + \Delta\right)^2}} (\hat{\jmath})$$

$$\left. + \frac{z_p + \frac{z_{Gap}}{2} + \Delta}{\sqrt{\left(\left|\frac{W}{2} + y_p\right| tan\theta\right)^2 + \left(\frac{W}{2} + y_p\right)^2 + \left(z_p + \frac{z_{Gap}}{2} + \Delta\right)^2}} (\hat{k})\right]$$

$$d\vec{x} \times \hat{r} = \left|\frac{W}{2} + y_p\right| \frac{d\theta}{\cos^2\theta} (-\hat{\imath}) \times$$

$$\left[\frac{\left|\frac{W}{2}+y_p\right|\tan\theta}{\sqrt{\left(\left|\frac{W}{2}+y_p\right|\tan\theta\right)^2+\left(\frac{W}{2}+y_p\right)^2+\left(z_p+\frac{z_{Gap}}{2}+\Delta\right)^2}}(\hat{\imath})\right.$$

$$+\frac{\left(\frac{W}{2}+y_p\right)}{\sqrt{\left(\left|\frac{W}{2}+y_p\right|\tan\theta\right)^2+\left(\frac{W}{2}+y_p\right)^2+\left(z_p+\frac{z_{Gap}}{2}+\Delta\right)^2}}(\hat{\jmath})$$

$$\left.+\frac{z_p+\frac{z_{Gap}}{2}+\Delta}{\sqrt{\left(\left|\frac{W}{2}+y_p\right|\tan\theta\right)^2+\left(\frac{W}{2}+y_p\right)^2+\left(z_p+\frac{z_{Gap}}{2}+\Delta\right)^2}}(\hat{k})\right]$$

$$\Rightarrow \quad d\vec{x}\times\hat{r}=$$

$$\frac{\left|\frac{W}{2}+y_p\right|\left(\frac{W}{2}+y_p\right)}{\cos^2\theta}\frac{1}{\sqrt{\left(\left|\frac{W}{2}+y_p\right|\tan\theta\right)^2+\left(\frac{W}{2}+y_p\right)^2+\left(z_p+\frac{z_{Gap}}{2}+\Delta\right)^2}}d\theta(-\hat{k})$$

$$+\frac{\left|\frac{W}{2}+y_p\right|}{\cos^2\theta}\frac{z_p+\frac{z_{Gap}}{2}+\Delta}{\sqrt{\left(\left|\frac{W}{2}+y_p\right|\tan\theta\right)^2+\left(\frac{W}{2}+y_p\right)^2+\left(z_p+\frac{z_{Gap}}{2}+\Delta\right)^2}}d\theta(\hat{\jmath})$$

$$\vec{B}_{p,24,bottom,a}=\frac{\mu_0 I}{4\pi}\int\frac{d\vec{x}\times\hat{r}}{|\vec{r}|^2}$$

$$\Rightarrow \quad \vec{B}_{p,24,bottom,a}=$$

$$\frac{\mu_0 I}{4\pi}\int_{\theta_1}^{\theta_2}\frac{\frac{\left|\frac{W}{2}+y_p\right|\left(\frac{W}{2}+y_p\right)}{\cos^2\theta}}{\left(\left(\left|\frac{W}{2}+y_p\right|\tan\theta\right)^2+\left(\frac{W}{2}+y_p\right)^2+\left(z_p+\frac{z_{Gap}}{2}+\Delta\right)^2\right)^{3/2}}d\theta(-\hat{k})$$

$$+\frac{\mu_0 I}{4\pi}\int_{\theta_1}^{\theta_2}\frac{\frac{\left|\frac{W}{2}+y_p\right|}{\cos^2\theta}\left(z_p+\frac{z_{Gap}}{2}+\Delta\right)}{\left(\left(\left|\frac{W}{2}+y_p\right|\tan\theta\right)^2+\left(\frac{W}{2}+y_p\right)^2+\left(z_p+\frac{z_{Gap}}{2}+\Delta\right)^2\right)^{3/2}}d\theta(\hat{\jmath})$$

Eq. (A.9)

$$\Rightarrow \quad \vec{B}_{p,24,bottom,a} = \frac{\mu_0 I \left|\frac{W}{2} + y_p\right| \left(\frac{W}{2} + y_p\right)}{4\pi}$$

$$\times \int_{\theta_1}^{\theta_2} \frac{1}{cos^2\theta \left(\left(\left|\frac{W}{2} + y_p\right| tan\theta\right)^2 + \left(\frac{W}{2} + y_p\right)^2 + \left(z_p + \frac{z_{Gap}}{2} + \Delta\right)^2\right)^{3/2}} d\theta(-\hat{k})$$

$$+ \frac{\mu_0 I \left|\frac{W}{2} + y_p\right| \left(z_p + \frac{z_{Gap}}{2} + \Delta\right)}{4\pi}$$

$$\times \int_{\theta_1}^{\theta_2} \frac{1}{cos^2\theta \left(\left(\left|\frac{W}{2} + y_p\right| tan\theta\right)^2 + \left(\frac{W}{2} + y_p\right)^2 + \left(z_p + \frac{z_{Gap}}{2} + \Delta\right)^2\right)^{3/2}} d\theta(\hat{j})$$

$$\theta_2 = tan^{-1} \frac{L}{2\left|\frac{W}{2} + y_p\right|} \quad , \quad \theta_1 = -tan^{-1} \frac{L}{2\left|\frac{W}{2} + y_p\right|}$$

A2.2. Part a - Top Coil

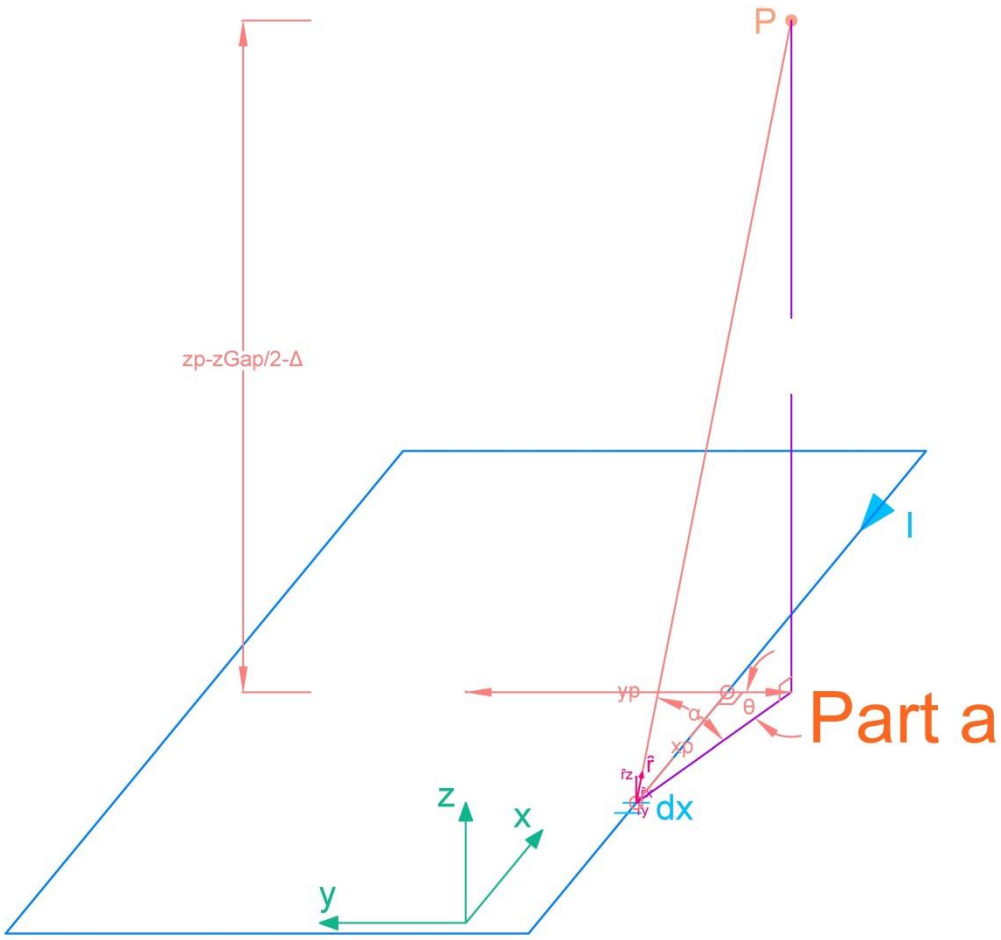

$$\Rightarrow \quad \vec{B}_{p,24,top,a} = \frac{\mu_0 I \left|\frac{W}{2}+y_p\right|\left(\frac{W}{2}+y_p\right)}{4\pi} \times \int_{\theta_1}^{\theta_2} \frac{1}{cos^2\theta\left(\left(\left|\frac{W}{2}+y_p\right| tan\theta\right)^2+\left(\frac{W}{2}+y_p\right)^2+\left(z_p-\frac{z_{Gap}}{2}-\Delta\right)^2\right)^{3/2}} d\theta(-\hat{k})$$

Eq. (A.10)

$$+\frac{\mu_0 I \left|\frac{W}{2}+y_p\right|\left(z_p-\frac{z_{Gap}}{2}-\Delta\right)}{4\pi} \times \int_{\theta_1}^{\theta_2} \frac{1}{cos^2\theta\left(\left(\left|\frac{W}{2}+y_p\right| tan\theta\right)^2+\left(\frac{W}{2}+y_p\right)^2+\left(z_p-\frac{z_{Gap}}{2}-\Delta\right)^2\right)^{3/2}} d\theta(\hat{\jmath})$$

$$\theta_2 = tan^{-1}\frac{L}{2\left|\frac{W}{2}+y_p\right|} \quad , \quad \theta_1 = -tan^{-1}\frac{L}{2\left|\frac{W}{2}+y_p\right|}$$

A2.3. Part c - Bottom Coil

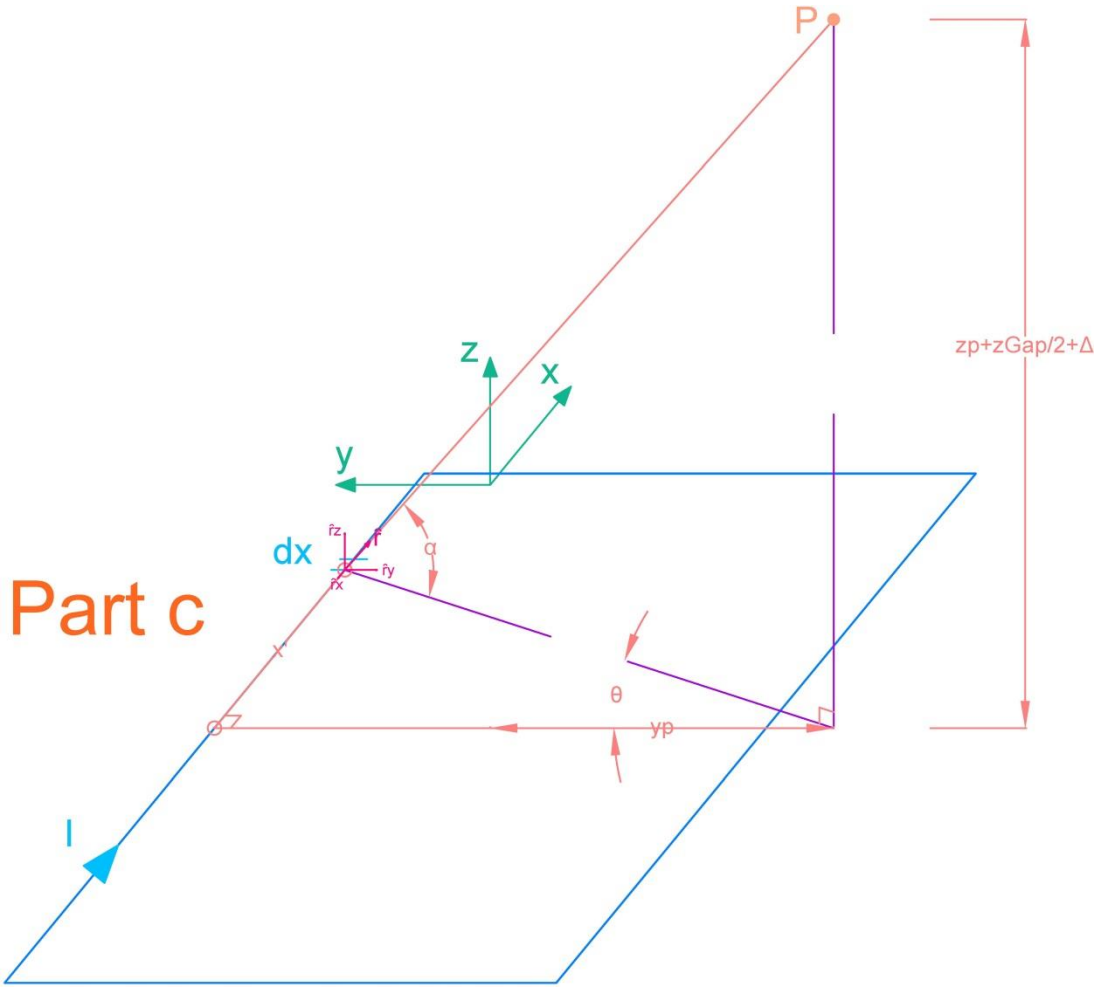

$$\vec{B}_{p,24,bottom,c} = \frac{\mu_0 I}{4\pi}\int \frac{d\vec{x}\times\hat{r}}{|\vec{r}|^2}$$

$$x = \frac{L}{2} + x' = \frac{L}{2} + \left|\frac{W}{2} - y_p\right| tan\theta$$

$$d\vec{x} = \left|\frac{W}{2} - y_p\right| \frac{d\theta}{cos^2\,\theta}(\hat{\imath})$$

$$|\vec{r}| = \sqrt{\left(\left|\frac{W}{2} - y_p\right| tan\theta\right)^2 + \left(\frac{W}{2} - y_p\right)^2 + \left(z_p + \frac{z_{Gap}}{2} + \Delta\right)^2}$$

$$\hat{r} = \hat{r}_x + \hat{r}_y + \hat{r}_z$$

$$\left|\hat{r}_{xy}\right| = |\hat{r}|\,cos\,\alpha = cos\,\alpha$$

$$cos\alpha = \frac{|\vec{r}_{xy}|}{|\vec{r}|} = \sqrt{\frac{\left(\left|\frac{W}{2} - y_p\right| tan\theta\right)^2 + \left(\frac{W}{2} - y_p\right)^2}{\left(\left|\frac{W}{2} - y_p\right| tan\theta\right)^2 + \left(\frac{W}{2} - y_p\right)^2 + \left(z_p + \frac{z_{Gap}}{2} + \Delta\right)^2}}$$

$$= \frac{\left|\frac{W}{2} - y_p\right|}{\cos\theta} \frac{1}{\sqrt{\left(\left|\frac{W}{2} - y_p\right| tan\theta\right)^2 + \left(\frac{W}{2} - y_p\right)^2 + \left(z_p + \frac{z_{Gap}}{2} + \Delta\right)^2}}$$

$$\Rightarrow \quad |\hat{r}_{xy}| = \frac{\left|\frac{W}{2} - y_p\right|}{\cos\theta} \frac{1}{\sqrt{\left(\left|\frac{W}{2} - y_p\right| tan\theta\right)^2 + \left(\frac{W}{2} - y_p\right)^2 + \left(z_p + \frac{z_{Gap}}{2} + \Delta\right)^2}}$$

$$\hat{r}_x = |\hat{r}_{xy}| \sin\theta\,(-\hat{\imath}) = \cos\alpha \sin\theta\,(-\hat{\imath})$$

$$= \frac{\left|\frac{W}{2} - y_p\right| \tan\theta}{\sqrt{\left(\left|\frac{W}{2} - y_p\right| tan\theta\right)^2 + \left(\frac{W}{2} - y_p\right)^2 + \left(z_p + \frac{z_{Gap}}{2} + \Delta\right)^2}}(-\hat{\imath})$$

$$\hat{r}_y = |\hat{r}_{xy}| \cos\theta\,(\hat{\jmath}) = \cos\alpha \cos\theta\,(-\hat{\jmath})$$

$$= \frac{\left|\frac{W}{2} - y_p\right|}{\sqrt{\left(\left|\frac{W}{2} - y_p\right| tan\theta\right)^2 + \left(\frac{W}{2} - y_p\right)^2 + \left(z_p + \frac{z_{Gap}}{2} + \Delta\right)^2}}(-\hat{\jmath})$$

$$\hat{r}_z = |\hat{r}| \sin\alpha\,(\hat{k}) = \sin\alpha\,(\hat{k})$$

$$\sin\alpha = \frac{\vec{r}_z}{|\vec{r}|} = \frac{z_p + \frac{z_{Gap}}{2} + \Delta}{\sqrt{\left(\left|\frac{W}{2} - y_p\right| tan\theta\right)^2 + \left(\frac{W}{2} - y_p\right)^2 + \left(z_p + \frac{z_{Gap}}{2} + \Delta\right)^2}}$$

$$\Rightarrow \quad \hat{r}_z = \frac{z_{Yoke} + \frac{z_{Gap}}{2} + \Delta}{\sqrt{\left(\left|\frac{W}{2} - y_p\right| tan\theta\right)^2 + \left(\frac{W}{2} - y_p\right)^2 + \left(z_p + \frac{z_{Gap}}{2} + \Delta\right)^2}}(\hat{k})$$

$$\hat{r} = \left[\frac{\left|\frac{W}{2} - y_p\right| \tan\theta}{\sqrt{\left(\left|\frac{W}{2} - y_p\right| tan\theta\right)^2 + \left(\frac{W}{2} - y_p\right)^2 + \left(z_p + \frac{z_{Gap}}{2} + \Delta\right)^2}}(-\hat{\imath})\right.$$

$$+ \frac{\left|\frac{W}{2} - y_p\right|}{\sqrt{\left(\left|\frac{W}{2} - y_p\right| tan\theta\right)^2 + \left(\frac{W}{2} - y_p\right)^2 + \left(z_p + \frac{z_{Gap}}{2} + \Delta\right)^2}}(-\hat{\jmath})$$

$$\left. + \frac{z_p + \frac{z_{Gap}}{2} + \Delta}{\sqrt{\left(\left|\frac{W}{2} - y_p\right| tan\theta\right)^2 + \left(\frac{W}{2} - y_p\right)^2 + \left(z_p + \frac{z_{Gap}}{2} + \Delta\right)^2}}(\hat{k})\right]$$

$$d\vec{x} \times \hat{r} = \left|\frac{W}{2} - y_p\right| \frac{d\theta}{\cos^2\theta}(\hat{\imath}) \times$$

$$\left[\frac{\left|\frac{W}{2}-y_p\right|\tan\theta}{\sqrt{\left(\left|\frac{W}{2}-y_p\right|\tan\theta\right)^2+\left(\frac{W}{2}-y_p\right)^2+\left(z_p+\frac{z_{Gap}}{2}+\Delta\right)^2}}(-\hat{\imath})\right.$$

$$+\frac{\left|\frac{W}{2}-y_p\right|}{\sqrt{\left(\left|\frac{W}{2}-y_p\right|\tan\theta\right)^2+\left(\frac{W}{2}-y_p\right)^2+\left(z_p+\frac{z_{Gap}}{2}+\Delta\right)^2}}(-\hat{\jmath})$$

$$\left.+\frac{z_{Yoke}+\frac{z_{Gap}}{2}+\Delta}{\sqrt{\left(\left|\frac{W}{2}-y_p\right|\tan\theta\right)^2+\left(\frac{W}{2}-y_p\right)^2+\left(z_p+\frac{z_{Gap}}{2}+\Delta\right)^2}}(\hat{k})\right]$$

$$\Rightarrow \quad d\vec{x}\times\hat{r}=$$

$$\frac{\left(\frac{W}{2}-y_p\right)^2}{\cos^2\theta}\frac{1}{\sqrt{\left(\left|\frac{W}{2}-y_p\right|\tan\theta\right)^2+\left(\frac{W}{2}-y_p\right)^2+\left(z_p+\frac{z_{Gap}}{2}+\Delta\right)^2}}d\theta(-\hat{k})$$

$$+\frac{\left|\frac{W}{2}-y_p\right|}{\cos^2\theta}\frac{z_p+\frac{z_{Gap}}{2}+\Delta}{\sqrt{\left(\left|\frac{W}{2}-y_p\right|\tan\theta\right)^2+\left(\frac{W}{2}-y_p\right)^2+\left(z_p+\frac{z_{Gap}}{2}+\Delta\right)^2}}d\theta(-\hat{\jmath})$$

$$\vec{B}_{p,24,bottom,c}=\frac{\mu_0 I}{4\pi}\int\frac{d\vec{x}\times\hat{r}}{|\vec{r}|^2}$$

$$\Rightarrow \quad \vec{B}_{p,24,bottom,c}=$$

$$\frac{\mu_0 I}{4\pi}\int_{\theta_1}^{\theta_2}\frac{\frac{\left(\frac{W}{2}-y_p\right)^2}{\cos^2\theta}}{\left(\left(\left|\frac{W}{2}-y_p\right|\tan\theta\right)^2+\left(\frac{W}{2}-y_p\right)^2+\left(z_p+\frac{z_{Gap}}{2}+\Delta\right)^2\right)^{3/2}}d\theta(-\hat{k})$$

$$+\frac{\mu_0 I}{4\pi}\int_{\theta_1}^{\theta_2}\frac{\frac{\left|\frac{W}{2}-y_p\right|}{\cos^2\theta}\left(z_p+\frac{z_{Gap}}{2}+\Delta\right)}{\left(\left(\left|\frac{W}{2}-y_p\right|\tan\theta\right)^2+\left(\frac{W}{2}-y_p\right)^2+\left(z_p+\frac{z_{Gap}}{2}+\Delta\right)^2\right)^{3/2}}d\theta(-\hat{\jmath})$$

Eq. (A.11)

$$\Rightarrow \quad \vec{B}_{p,24,bottom,c} = \frac{\mu_0 I \left(\frac{W}{2} - y_p\right)^2}{4\pi}$$

$$\times \int_{\theta_1}^{\theta_2} \frac{1}{cos^2\theta \left(\left(\left|\frac{W}{2} - y_p\right| tan\theta\right)^2 + \left(\frac{W}{2} - y_p\right)^2 + \left(z_p + \frac{z_{Gap}}{2} + \Delta\right)^2\right)^{3/2}} d\theta(-\hat{k})$$

$$+ \frac{\mu_0 I \left|\frac{W}{2} - y_p\right| \left(z_p + \frac{z_{Gap}}{2} + \Delta\right)}{4\pi}$$

$$\times \int_{\theta_1}^{\theta_2} \frac{1}{cos^2\theta \left(\left(\left|\frac{W}{2} - y_p\right| tan\theta\right)^2 + \left(\frac{W}{2} - y_p\right)^2 + \left(z_p + \frac{z_{Gap}}{2} + \Delta\right)^2\right)^{3/2}} d\theta(-\hat{j})$$

$$\theta_2 = tan^{-1} \frac{L}{2\left|\frac{W}{2} - y_p\right|} \quad , \quad \theta_1 = -tan^{-1} \frac{L}{2\left|\frac{W}{2} - y_p\right|}$$

A2.4. Part c - Top Coil

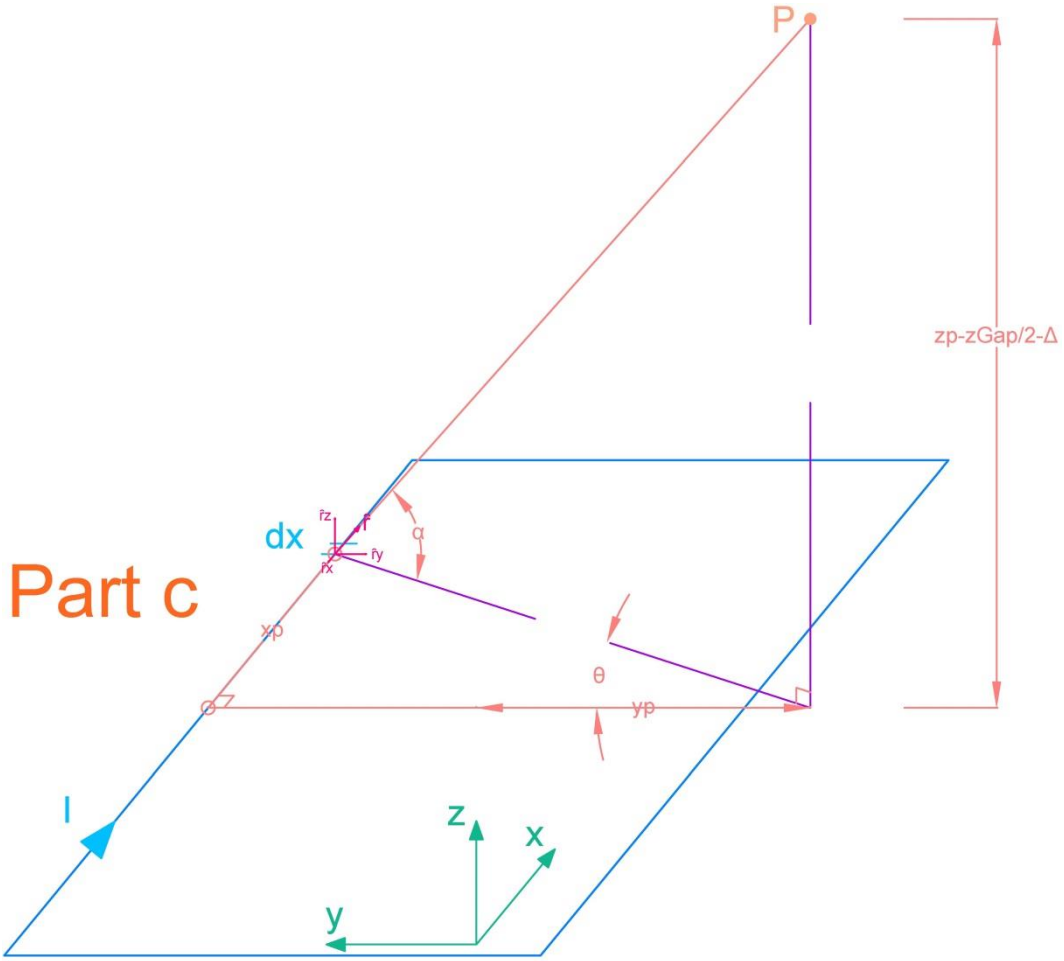

$$\Rightarrow \quad \vec{B}_{p,24,top,c} = \frac{\mu_0 I \left(\frac{W}{2} - y_p\right)^2}{4\pi} \times \int_{\theta_1}^{\theta_2} \frac{1}{cos^2\theta \left(\left(\left|\frac{W}{2} - y_p\right| tan\theta\right)^2 + \left(\frac{W}{2} - y_p\right)^2 + \left(z_p - \frac{z_{Gap}}{2} - \Delta\right)^2\right)^{3/2}} d\theta(-\hat{k})$$

Eq. (A.12)

$$+ \frac{\mu_0 I \left|\frac{W}{2} - y_p\right| \left(z_p - \frac{z_{Gap}}{2} - \Delta\right)}{4\pi} \times \int_{\theta_1}^{\theta_2} \frac{1}{cos^2\theta \left(\left(\left|\frac{W}{2} - y_p\right| tan\theta\right)^2 + \left(\frac{W}{2} - y_p\right)^2 + \left(z_p - \frac{z_{Gap}}{2} - \Delta\right)^2\right)^{3/2}} d\theta(-\hat{j})$$

$$\theta_2 = tan^{-1} \frac{L}{2\left|\frac{W}{2} - y_p\right|} \quad , \quad \theta_1 = -tan^{-1} \frac{L}{2\left|\frac{W}{2} - y_p\right|}$$

A3. Section 3

A3.1. Part a - Bottom Coil

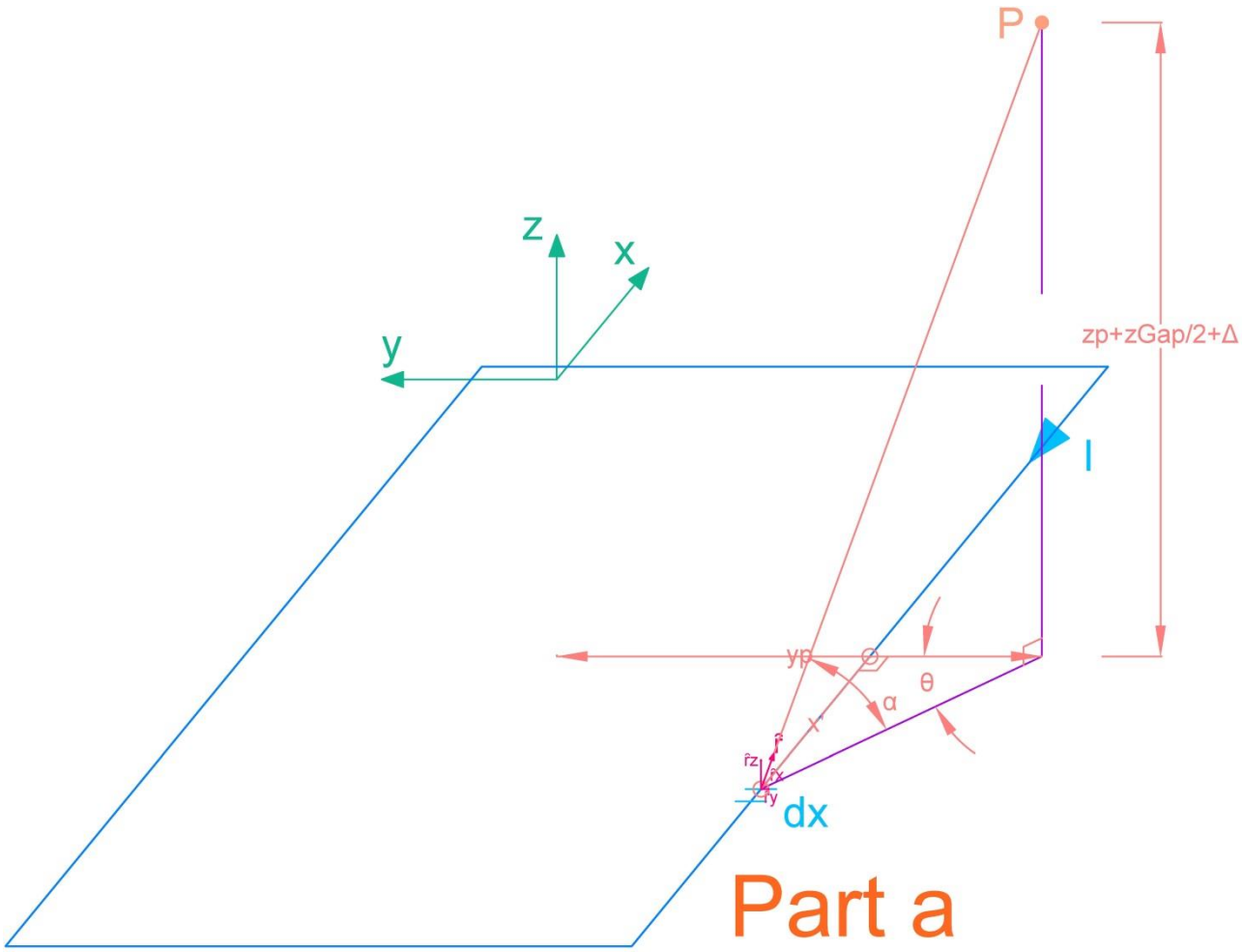

$$\vec{B}_{p,3,bottom,a} = \frac{\mu_0 I}{4\pi} \int \frac{d\vec{x} \times \hat{r}}{|\vec{r}|^2}$$

$$x = \frac{L}{2} - x' = \frac{L}{2} - \left(-\left|\frac{W}{2} + y_p\right| tan\theta\right) = \frac{L}{2} + \left|\frac{W}{2} + y_p\right| tan\theta$$

$$d\vec{x} = \left|\frac{W}{2} + y_p\right| \frac{d\theta}{cos^2\,\theta} (-\hat{\imath})$$

$$|\vec{r}| = \sqrt{\left(\left|\frac{W}{2} + y_p\right| tan\theta\right)^2 + \left(\frac{W}{2} + y_p\right)^2 + \left(z_p + \frac{z_{Gap}}{2} + \Delta\right)^2}$$

$$\hat{r} = \hat{r}_x + \hat{r}_y + \hat{r}_z$$

$$\left|\hat{r}_{xy}\right| = |\hat{r}|\, cos\,\alpha = cos\,\alpha$$

$$cos\alpha = \frac{|\vec{r}_{xy}|}{|\vec{r}|} = \sqrt{\frac{\left(\left|\frac{W}{2} + y_p\right| tan\theta\right)^2 + \left(\frac{W}{2} + y_p\right)^2}{\left(\left|\frac{W}{2} + y_p\right| tan\theta\right)^2 + \left(\frac{W}{2} + y_p\right)^2 + \left(z_p + \frac{z_{Gap}}{2} + \Delta\right)^2}}$$

$$= \frac{\left|\frac{W}{2} + y_p\right|}{\cos\theta} \frac{1}{\sqrt{\left(\left|\frac{W}{2} + y_p\right| tan\theta\right)^2 + \left(\frac{W}{2} + y_p\right)^2 + \left(z_p + \frac{z_{Gap}}{2} + \Delta\right)^2}}$$

$$\Rightarrow \quad |\hat{r}_{xy}| = \frac{\left|\frac{W}{2} + y_p\right|}{\cos\theta} \frac{1}{\sqrt{\left(\left|\frac{W}{2} + y_p\right| tan\theta\right)^2 + \left(\frac{W}{2} + y_p\right)^2 + \left(z_p + \frac{z_{Gap}}{2} + \Delta\right)^2}}$$

$$\hat{r}_x = |\hat{r}_{xy}| \sin\theta\,(\hat{\imath}) = \cos\alpha \sin\theta\,(\hat{\imath})$$

$$= \frac{\left|\frac{W}{2} + y_p\right| \tan\theta}{\sqrt{\left(\left|\frac{W}{2} + y_p\right| tan\theta\right)^2 + \left(\frac{W}{2} + y_p\right)^2 + \left(z_p + \frac{z_{Gap}}{2} + \Delta\right)^2}} (\hat{\imath})$$

$$\hat{r}_y = |\hat{r}_{xy}| \cos\theta\,(\hat{\jmath}) = \cos\alpha \cos\theta\,(\hat{\jmath})$$

$$= \frac{\left|\frac{W}{2} + y_p\right|}{\sqrt{\left(\left|\frac{W}{2} + y_p\right| tan\theta\right)^2 + \left(\frac{W}{2} + y_p\right)^2 + \left(z_p + \frac{z_{Gap}}{2} + \Delta\right)^2}} (-\hat{\jmath})$$

$$\hat{r}_z = |\hat{r}| \sin\alpha\,(\hat{k}) = \sin\alpha\,(\hat{k})$$

$$\sin\alpha = \frac{\vec{r}_z}{|\vec{r}|} = \frac{z_p + \frac{z_{Gap}}{2} + \Delta}{\sqrt{\left(\left|\frac{W}{2} + y_p\right| tan\theta\right)^2 + \left(\frac{W}{2} + y_p\right)^2 + \left(z_p + \frac{z_{Gap}}{2} + \Delta\right)^2}}$$

$$\Rightarrow \quad \hat{r}_z = \frac{z_p + \frac{z_{Gap}}{2} + \Delta}{\sqrt{\left(\left|\frac{W}{2} + y_p\right| tan\theta\right)^2 + \left(\frac{W}{2} + y_p\right)^2 + \left(z_p + \frac{z_{Gap}}{2} + \Delta\right)^2}} (\hat{k})$$

$$\hat{r} = \left[\frac{\left|\frac{W}{2} + y_p\right| \tan\theta}{\sqrt{\left(\left|\frac{W}{2} + y_p\right| tan\theta\right)^2 + \left(\frac{W}{2} + y_p\right)^2 + \left(z_p + \frac{z_{Gap}}{2} + \Delta\right)^2}} (\hat{\imath})\right.$$

$$+ \frac{\left|\frac{W}{2} + y_p\right|}{\sqrt{\left(\left|\frac{W}{2} + y_p\right| tan\theta\right)^2 + \left(\frac{W}{2} + y_p\right)^2 + \left(z_p + \frac{z_{Gap}}{2} + \Delta\right)^2}} (-\hat{\jmath})$$

$$\left. + \frac{z_p + \frac{z_{Gap}}{2} + \Delta}{\sqrt{\left(\left|\frac{W}{2} + y_p\right| tan\theta\right)^2 + \left(\frac{W}{2} + y_p\right)^2 + \left(z_p + \frac{z_{Gap}}{2} + \Delta\right)^2}} (\hat{k})\right]$$

$$d\vec{x} \times \hat{r} = \left|\frac{W}{2} + y_p\right| \frac{d\theta}{\cos^2\theta} (-\hat{\imath}) \times$$

$$\left[\frac{\left|\frac{W}{2}+y_p\right|\tan\theta}{\sqrt{\left(\left|\frac{W}{2}+y_p\right|\tan\theta\right)^2+\left(\frac{W}{2}+y_p\right)^2+\left(z_p+\frac{z_{Gap}}{2}+\Delta\right)^2}}(\hat{\imath})\right.$$

$$+\frac{\left|\frac{W}{2}+y_p\right|}{\sqrt{\left(\left|\frac{W}{2}+y_p\right|\tan\theta\right)^2+\left(\frac{W}{2}+y_p\right)^2+\left(z_p+\frac{z_{Gap}}{2}+\Delta\right)^2}}(-\hat{\jmath})$$

$$\left.+\frac{z_p+\frac{z_{Gap}}{2}+\Delta}{\sqrt{\left(\left|\frac{W}{2}+y_p\right|\tan\theta\right)^2+\left(\frac{W}{2}+y_p\right)^2+\left(z_p+\frac{z_{Gap}}{2}+\Delta\right)^2}}(\hat{k})\right]$$

$$\Rightarrow \quad d\vec{x}\times\hat{r}=$$

$$\frac{\left(\frac{W}{2}+y_p\right)^2}{\cos^2\theta}\frac{1}{\sqrt{\left(\left|\frac{W}{2}+y_p\right|\tan\theta\right)^2+\left(\frac{W}{2}+y_p\right)^2+\left(z_p+\frac{z_{Gap}}{2}+\Delta\right)^2}}d\theta(\hat{k})$$

$$+\frac{\left|\frac{W}{2}+y_p\right|}{\cos^2\theta}\frac{z_p+\frac{z_{Gap}}{2}+\Delta}{\sqrt{\left(\left|\frac{W}{2}+y_p\right|\tan\theta\right)^2+\left(\frac{W}{2}+y_p\right)^2+\left(z_p+\frac{z_{Gap}}{2}+\Delta\right)^2}}d\theta(\hat{\jmath})$$

$$\vec{B}_{p,3,bottom,a}=\frac{\mu_0 I}{4\pi}\int\frac{d\vec{x}\times\hat{r}}{|\vec{r}|^2}$$

$$\Rightarrow \quad \vec{B}_{p,3,bottom,a}=$$

$$\frac{\mu_0 I}{4\pi}\int_{\theta_1}^{\theta_2}\frac{\frac{\left(\frac{W}{2}+y_p\right)^2}{\cos^2\theta}}{\left(\left(\left|\frac{W}{2}+y_p\right|\tan\theta\right)^2+\left(\frac{W}{2}+y_p\right)^2+\left(z_p+\frac{z_{Gap}}{2}+\Delta\right)^2\right)^{3/2}}d\theta(\hat{k})$$

$$+\frac{\mu_0 I}{4\pi}\int_{\theta_1}^{\theta_2}\frac{\frac{\left|\frac{W}{2}+y_p\right|}{\cos^2\theta}\left(z_p+\frac{z_{Gap}}{2}+\Delta\right)}{\left(\left(\left|\frac{W}{2}+y_p\right|\tan\theta\right)^2+\left(\frac{W}{2}+y_p\right)^2+\left(z_p+\frac{z_{Gap}}{2}+\Delta\right)^2\right)^{3/2}}d\theta(\hat{\jmath})$$

Eq. (A.13)

$$\Rightarrow \quad \vec{B}_{p,3,bottom,a} = \frac{\mu_0 I \left(\frac{W}{2} + y_p\right)^2}{4\pi}$$

$$\times \int_{\theta_1}^{\theta_2} \frac{1}{cos^2\theta \left(\left(\left|\frac{W}{2} + y_p\right| tan\theta\right)^2 + \left(\frac{W}{2} + y_p\right)^2 + \left(z_p + \frac{z_{Gap}}{2} + \Delta\right)^2\right)^{3/2}} d\theta(\hat{k})$$

$$+ \frac{\mu_0 I \left|\frac{W}{2} + y_p\right| \left(z_p + \frac{z_{Gap}}{2} + \Delta\right)}{4\pi}$$

$$\times \int_{\theta_1}^{\theta_2} \frac{1}{cos^2\theta \left(\left(\left|\frac{W}{2} + y_p\right| tan\theta\right)^2 + \left(\frac{W}{2} + y_p\right)^2 + \left(z_p + \frac{z_{Gap}}{2} + \Delta\right)^2\right)^{3/2}} d\theta(\hat{j})$$

$$\theta_2 = tan^{-1} \frac{L}{2\left|\frac{W}{2} + y_p\right|} \quad , \quad \theta_1 = -tan^{-1} \frac{L}{2\left|\frac{W}{2} + y_p\right|}$$

A3.2. Part a - Top Coil

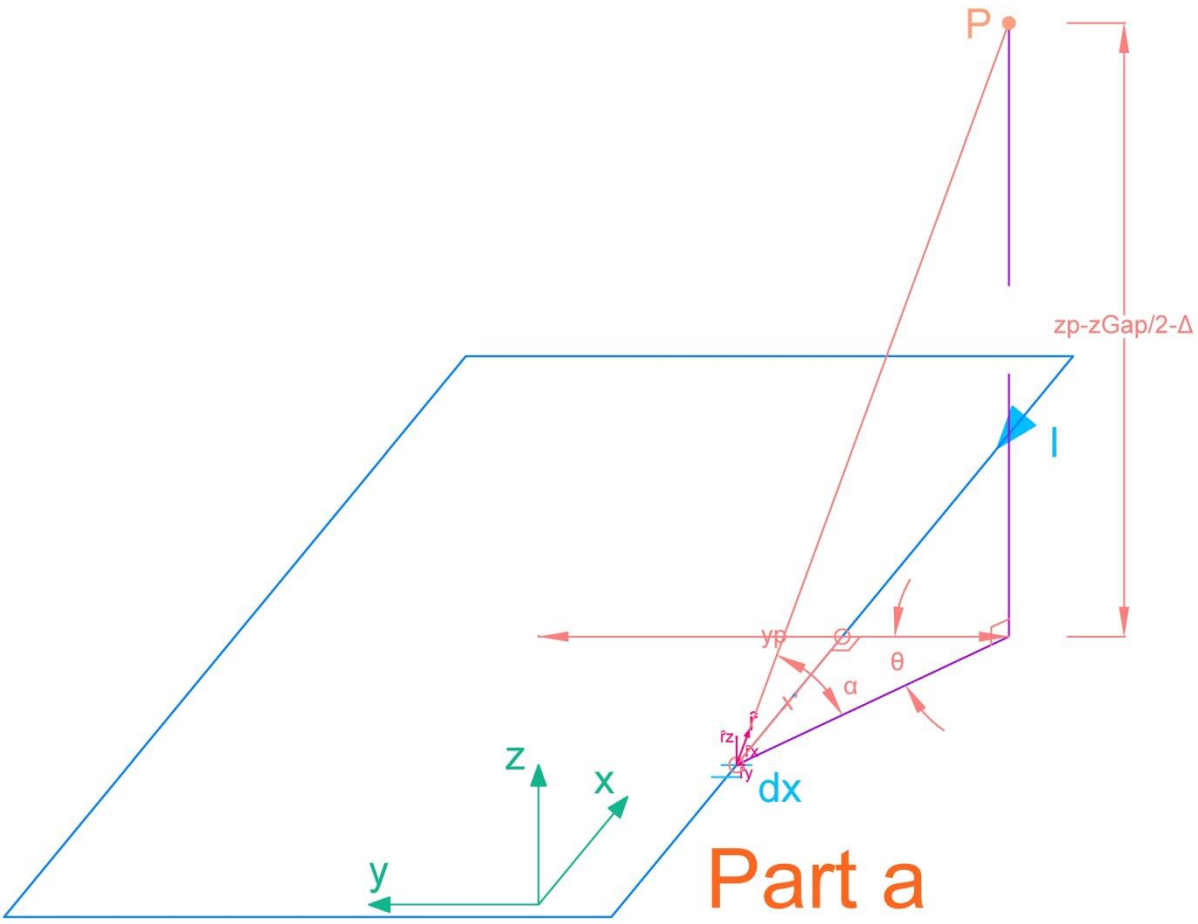

Eq. (A.14)

$$\Rightarrow \quad \vec{B}_{p,3,top,a} = \frac{\mu_0 I \left(\frac{W}{2} + y_p\right)^2}{4\pi}$$

$$\times \int_{\theta_1}^{\theta_2} \frac{1}{cos^2\theta \left(\left(\left|\frac{W}{2} + y_p\right| tan\theta\right)^2 + \left(\frac{W}{2} + y_p\right)^2 + \left(z_p - \frac{z_{Gap}}{2} - \Delta\right)^2\right)^{3/2}} d\theta(\hat{k})$$

$$+ \frac{\mu_0 I \left|\frac{W}{2} + y_p\right| \left(z_p - \frac{z_{Gap}}{2} - \Delta\right)}{4\pi}$$

$$\times \int_{\theta_1}^{\theta_2} \frac{1}{cos^2\theta \left(\left(\left|\frac{W}{2} + y_p\right| tan\theta\right)^2 + \left(\frac{W}{2} + y_p\right)^2 + \left(z_p - \frac{z_{Gap}}{2} - \Delta\right)^2\right)^{3/2}} d\theta(\hat{j})$$

$$\theta_2 = tan^{-1} \frac{L}{2\left|\frac{W}{2} + y_p\right|} \quad , \quad \theta_1 = -tan^{-1} \frac{L}{2\left|\frac{W}{2} + y_p\right|}$$

A3.3. Part b - Bottom Coil

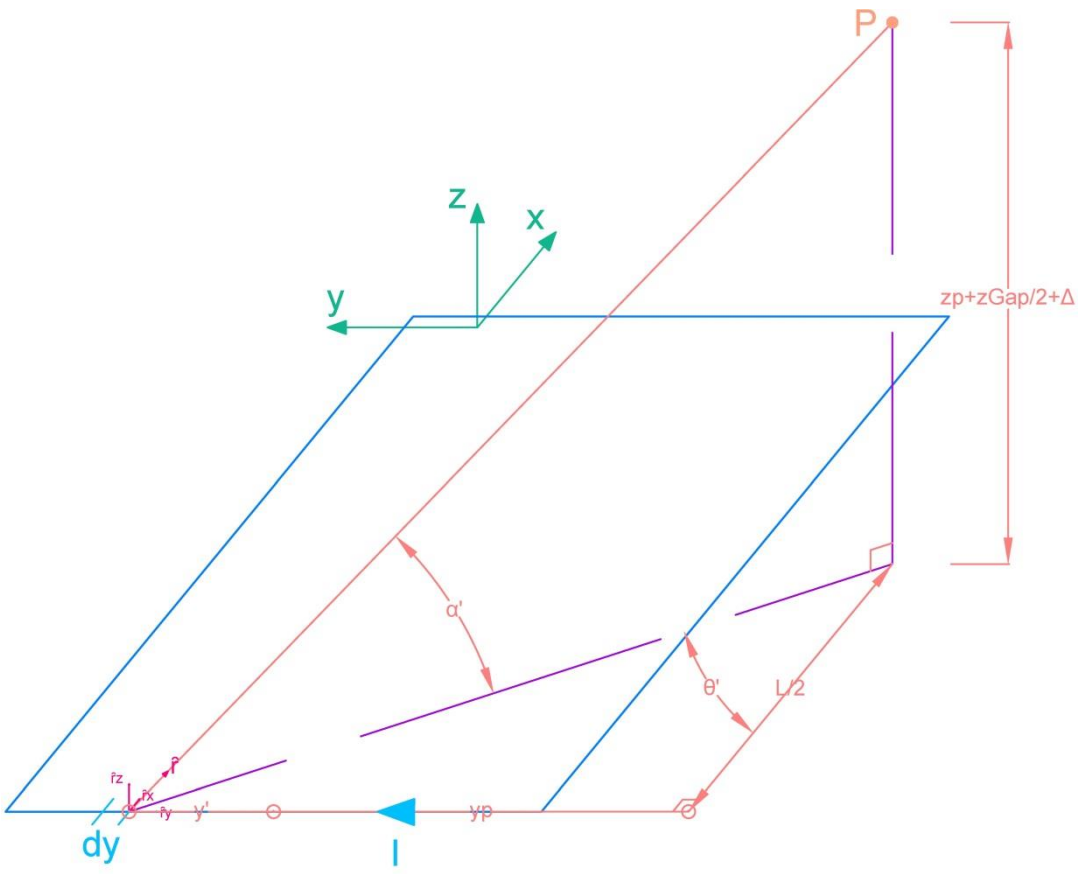

Part b

$$d\vec{B}_{p,3,bottom,b} = \frac{\mu_0 I}{4\pi}\int \frac{d\vec{y}\times\hat{r}}{|\vec{r}|^2}$$

$$y = \frac{W}{2} + y' = \frac{W}{2} + \left(\frac{L}{2}tan\theta' - |y_p|\right)$$

$$d\vec{y} = \frac{L}{2}\frac{d\theta'}{cos^2\,\theta'}(\hat{j})$$

$$|\vec{r}| = \sqrt{\left(\frac{L}{2}\right)^2 + \left(\frac{L}{2}tan\theta'\right)^2 + \left(z_p + \frac{z_{Gap}}{2} + \Delta\right)^2}$$

$$\hat{r} = \hat{r}_x + \hat{r}_y + \hat{r}_z$$

$$|\hat{r}_{xy}| = |\hat{r}|\,cos\,\alpha' = cos\,\alpha'$$

$$cos\alpha' = \frac{|\vec{r}_{xy}|}{|\vec{r}|} = \sqrt{\frac{\left(\frac{L}{2}\right)^2 + \left(\frac{L}{2}tan\theta'\right)^2}{\left(\frac{L}{2}\right)^2 + \left(\frac{L}{2}tan\theta'\right)^2 + \left(z_p + \frac{z_{Gap}}{2} + \Delta\right)^2}}$$

$$= \frac{\frac{L}{2}}{\cos\theta'} \frac{1}{\sqrt{\left(\frac{L}{2}\right)^2 + \left(\frac{L}{2}\tan\theta'\right)^2 + \left(z_p + \frac{z_{Gap}}{2} + \Delta\right)^2}}$$

$$\Rightarrow \quad |\hat{r}_{xy}| = \frac{\frac{L}{2}}{\cos\theta'} \frac{1}{\sqrt{\left(\frac{L}{2}\right)^2 + \left(\frac{L}{2}\tan\theta'\right)^2 + \left(z_p + \frac{z_{Gap}}{2} + \Delta\right)^2}}$$

$$\hat{r}_x = |\hat{r}_{xy}| \cos\theta' (\hat{\imath}) = \cos\alpha' \cos\theta' (\hat{\imath}) = \frac{\frac{L}{2}}{\sqrt{\left(\frac{L}{2}\right)^2 + \left(\frac{L}{2}\tan\theta'\right)^2 + \left(z_p + \frac{z_{Gap}}{2} + \Delta\right)^2}} (\hat{\imath})$$

$$\hat{r}_y = -|\hat{r}_{xy}| \sin\theta' (\hat{\jmath}) = -\cos\alpha' \sin\theta' (\hat{\jmath}) = \frac{\frac{L}{2}\tan\theta'}{\sqrt{\left(\frac{L}{2}\right)^2 + \left(\frac{L}{2}\tan\theta'\right)^2 + \left(z_p + \frac{z_{Gap}}{2} + \Delta\right)^2}} (-\hat{\jmath})$$

$$\hat{r}_z = |\hat{r}| \sin\alpha' (\hat{k}) = \sin\alpha' (\hat{k})$$

$$\sin\alpha = \frac{\vec{r}_z}{|\vec{r}|} = \frac{z_p + z_{Gap} + \Delta}{\sqrt{\left(\frac{L}{2}\right)^2 + \left(\frac{L}{2}\tan\theta'\right)^2 + \left(z_p + \frac{z_{Gap}}{2} + \Delta\right)^2}}$$

$$\Rightarrow \quad \hat{r}_z = \frac{z_p + \frac{z_{Gap}}{2} + \Delta}{\sqrt{\left(\frac{L}{2}\right)^2 + \left(\frac{L}{2}\tan\theta'\right)^2 + \left(z_p + \frac{z_{Gap}}{2} + \Delta\right)^2}} (\hat{k})$$

$$\Rightarrow \quad \hat{r} = \left[\frac{\frac{L}{2}}{\sqrt{\left(\frac{L}{2}\right)^2 + \left(\frac{L}{2}\tan\theta'\right)^2 + \left(z_p + \frac{z_{Gap}}{2} + \Delta\right)^2}} (\hat{\imath}) \right.$$

$$+ \frac{\frac{L}{2}\tan\theta'}{\sqrt{\left(\frac{L}{2}\right)^2 + \left(\frac{L}{2}\tan\theta'\right)^2 + \left(z_p + \frac{z_{Gap}}{2} + \Delta\right)^2}} (-\hat{\jmath})$$

$$\left. + \frac{z_p + \frac{z_{Gap}}{2} + \Delta}{\sqrt{\left(\frac{L}{2}\right)^2 + \left(\frac{L}{2}\tan\theta'\right)^2 + \left(z_p + \frac{z_{Gap}}{2} + \Delta\right)^2}} (\hat{k}) \right]$$

$$d\vec{y} \times \hat{r} = \frac{L}{2} \frac{d\theta'}{\cos^2\theta'} (\hat{\jmath}) \times$$

$$\left[\frac{\frac{L}{2}}{\sqrt{\left(\frac{L}{2}\right)^2 + \left(\frac{L}{2}\tan\theta'\right)^2 + \left(z_p + \frac{z_{Gap}}{2} + \Delta\right)^2}} (\hat{\imath}) \right.$$

$$+\frac{\frac{L}{2}\tan\theta'}{\sqrt{\left(\frac{L}{2}\right)^2+\left(\frac{L}{2}\tan\theta'\right)^2+\left(z_p+\frac{z_{Gap}}{2}+\Delta\right)^2}}(-\hat{j})$$

$$+\frac{z_p+\frac{z_{Gap}}{2}+\Delta}{\sqrt{\left(\frac{L}{2}\right)^2+\left(\frac{L}{2}\tan\theta'\right)^2+\left(z_p+\frac{z_{Gap}}{2}+\Delta\right)^2}}(\hat{k})\Bigg]$$

$$\Rightarrow \quad d\vec{y}\times\hat{r}=\frac{\left(\frac{L}{2}\right)^2}{\cos^2\theta'}\frac{1}{\sqrt{\left(\frac{L}{2}\right)^2+\left(\frac{L}{2}\tan\theta'\right)^2+\left(z_p+\frac{z_{Gap}}{2}+\Delta\right)^2}}d\theta(-\hat{k})$$

$$+\frac{\left(\frac{L}{2}\right)}{\cos^2\theta'}\frac{z_p+\frac{z_{Gap}}{2}+\Delta}{\sqrt{\left(\frac{L}{2}\right)^2+\left(\frac{L}{2}\tan\theta'\right)^2+\left(z_p+\frac{z_{Gap}}{2}+\Delta\right)^2}}d\theta'(\hat{\imath})$$

$$\vec{B}_{p,3,bottom,b}=\frac{\mu_0 I}{4\pi}\int\frac{d\vec{y}\times\hat{r}}{|\vec{r}|^2}$$

$$\Rightarrow \quad d\vec{B}_{p,15,bottom,b}=\frac{\mu_0 I}{4\pi}\int_{\theta'_1}^{\theta'_2}\frac{\frac{\left(\frac{L}{2}\right)^2}{\cos^2\theta'}\frac{1}{\sqrt{\left(\frac{L}{2}\right)^2+\left(\frac{L}{2}\tan\theta'\right)^2+\left(z_p+\frac{z_{Gap}}{2}+\Delta\right)^2}}}{\left(\frac{L}{2}\right)^2+\left(\frac{L}{2}\tan\theta'\right)^2+\left(z_p+\frac{z_{Gap}}{2}+\Delta\right)^2}d\theta'(-\hat{k})$$

$$+\frac{\mu_0 I}{4\pi}\int_{\theta'_1}^{\theta'_2}\frac{\frac{\left(\frac{L}{2}\right)}{\cos^2\theta'}\frac{z_p+\frac{z_{Gap}}{2}+\Delta}{\sqrt{\left(\frac{L}{2}\right)^2+\left(\frac{L}{2}\tan\theta'\right)^2+\left(z_p+\frac{z_{Gap}}{2}+\Delta\right)^2}}}{\left(\frac{L}{2}\right)^2+\left(\frac{L}{2}\tan\theta'\right)^2+\left(z_p+\frac{z_{Gap}}{2}+\Delta\right)^2}d\theta'(\hat{\imath})$$

$$\Rightarrow \quad d\vec{B}_{p,3,bottom,b} = \qquad \textbf{Eq. (A.15)}$$

$$\frac{\mu_0 I \left(\frac{L}{2}\right)^2}{4\pi} \int_{\theta'_1}^{\theta'_2} \frac{1}{(\cos\theta')^2 \left(\left(\frac{L}{2}\right)^2 + \left(\frac{L}{2}\tan\theta'\right)^2 + \left(z_p + \frac{z_{Gap}}{2} + \Delta\right)^2\right)^{3/2}} d\theta'(-\hat{k})$$

$$+ \frac{\mu_0 I \left(\frac{L}{2}\right)(z_p + \frac{z_{Gap}}{2} + \Delta)}{4\pi} \int_{\theta'_1}^{\theta'_2} \frac{1}{(\cos\theta')^2 \left(\left(\frac{L}{2}\right)^2 + \left(\frac{L}{2}\tan\theta'\right)^2 + \left(z_p + \frac{z_{Gap}}{2} + \Delta\right)^2\right)^{3/2}} d\theta'(\hat{\imath})$$

$$\theta'_2 = \tan^{-1}\frac{|y_p| + \frac{W}{2}}{\frac{L}{2}} \quad , \quad \theta'_1 = \tan^{-1}\frac{|y_p| - \frac{W}{2}}{\frac{L}{2}}$$

A3.4. Part b - Top Coil

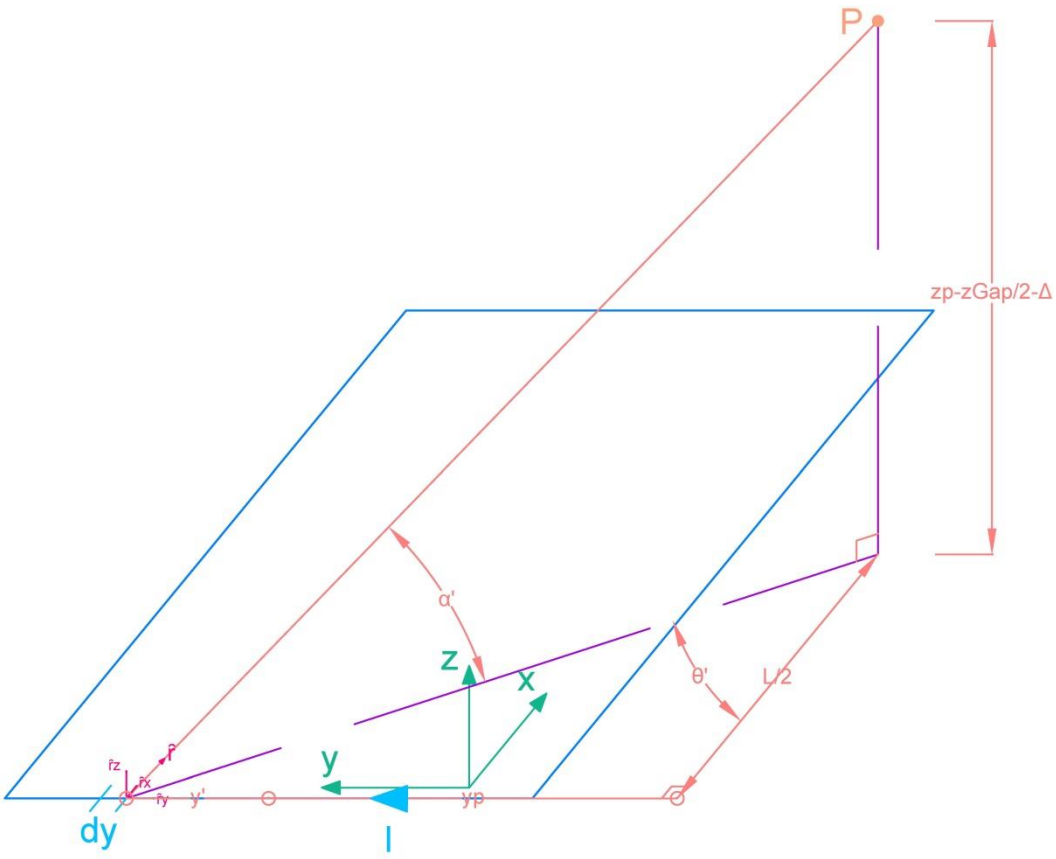

Part b

$$\Rightarrow \quad d\vec{B}_{p,3,top,b} = \qquad \textbf{Eq. (A.16)}$$

$$\frac{\mu_0 I \left(\frac{L}{2}\right)^2}{4\pi} \int_{\theta'_1}^{\theta'_2} \frac{1}{(\cos\theta')^2 \left(\left(\frac{L}{2}\right)^2 + \left(\frac{L}{2}\tan\theta'\right)^2 + \left(z_p - \frac{z_{Gap}}{2} - \Delta\right)^2\right)^{3/2}} d\theta'(-\hat{k})$$

$$+\frac{\mu_0 I \left(\frac{L}{2}\right)(z_p - \frac{z_{Gap}}{2} - \Delta)}{4\pi} \int_{\theta'_1}^{\theta'_2} \frac{1}{(\cos\theta')^2 \left(\left(\frac{L}{2}\right)^2 + \left(\frac{L}{2}\tan\theta'\right)^2 + \left(z_p - \frac{z_{Gap}}{2} - \Delta\right)^2\right)^{3/2}} d\theta'(\hat{\imath})$$

$$\theta'_2 = \tan^{-1}\frac{|y_p| + \frac{W}{2}}{\frac{L}{2}} \quad , \quad \theta'_1 = \tan^{-1}\frac{|y_p| - \frac{W}{2}}{\frac{L}{2}}$$

A3.5. Part c - Bottom Coil

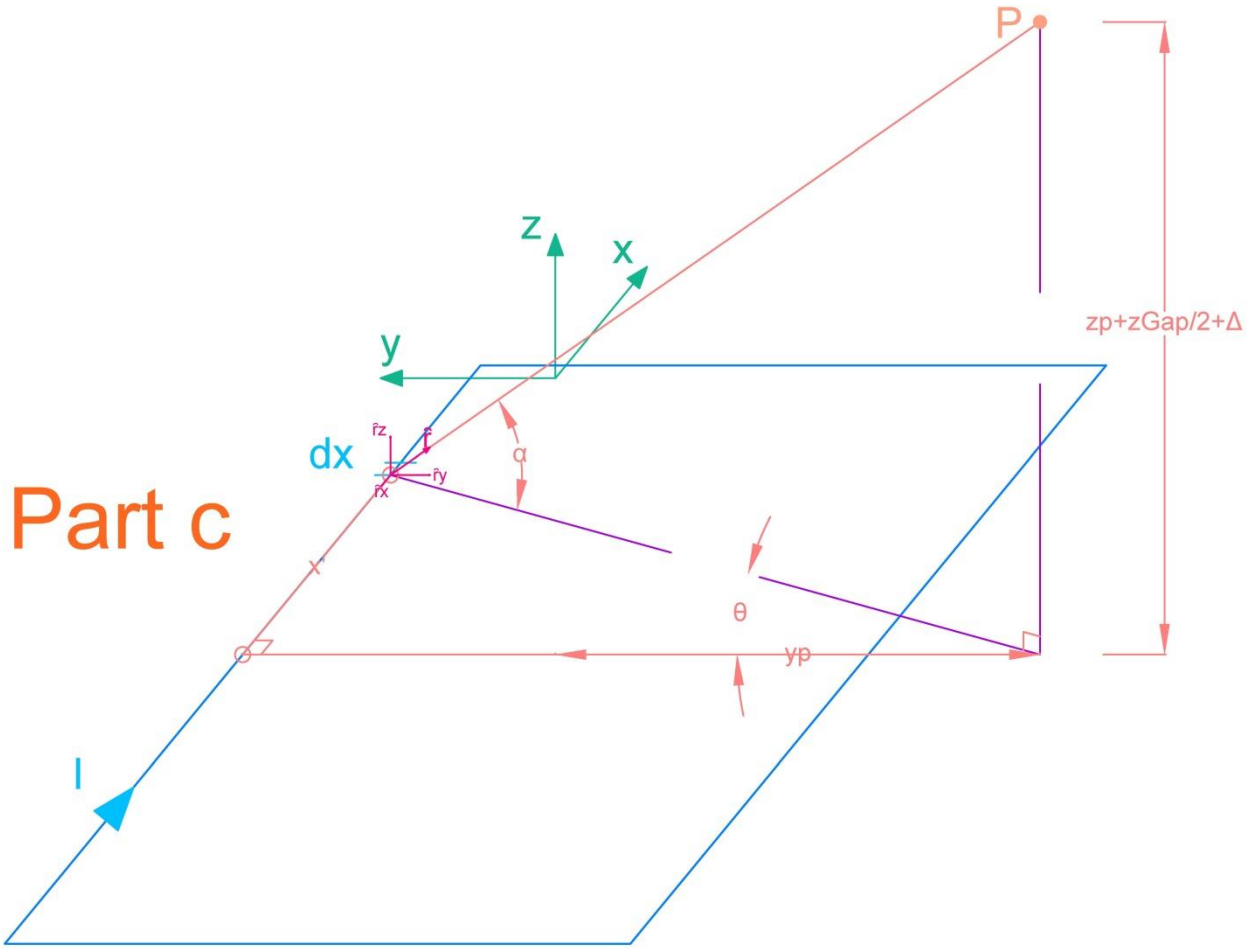

$$\vec{B}_{p,3,bottom,c} = \frac{\mu_0 I}{4\pi}\int \frac{d\vec{x}\times\hat{r}}{|\vec{r}|^2}$$

$$x = \frac{L}{2} + x' = \frac{L}{2} + \left|\frac{W}{2} - y_p\right| tan\theta$$

$$d\vec{x} = \left|\frac{W}{2} - y_p\right| \frac{d\theta}{cos^2\,\theta}(\hat{\imath})$$

$$|\vec{r}| = \sqrt{\left(\left|\frac{W}{2} - y_p\right| tan\theta\right)^2 + \left(\frac{W}{2} - y_p\right)^2 + \left(z_p + \frac{z_{Gap}}{2} + \Delta\right)^2}$$

$$\hat{r} = \hat{r}_x + \hat{r}_y + \hat{r}_z$$

$$\left|\hat{r}_{xy}\right| = |\hat{r}|\,cos\,\alpha = cos\,\alpha$$

$$cos\alpha = \frac{|\vec{r}_{xy}|}{|\vec{r}|} = \sqrt{\frac{\left(\left|\frac{W}{2} - y_p\right| tan\theta\right)^2 + \left(\frac{W}{2} - y_p\right)^2}{\left(\left|\frac{W}{2} - y_p\right| tan\theta\right)^2 + \left(\frac{W}{2} - y_p\right)^2 + \left(z_p + \frac{z_{Gap}}{2} + \Delta\right)^2}}$$

$$= \frac{\left|\frac{W}{2} - y_p\right|}{\cos\theta} \frac{1}{\sqrt{\left(\left|\frac{W}{2} - y_p\right| tan\theta\right)^2 + \left(\frac{W}{2} - y_p\right)^2 + \left(z_p + \frac{z_{Gap}}{2} + \Delta\right)^2}}$$

$$\Rightarrow \quad |\hat{r}_{xy}| = \frac{\left|\frac{W}{2} - y_p\right|}{\cos\theta} \frac{1}{\sqrt{\left(\left|\frac{W}{2} - y_p\right| tan\theta\right)^2 + \left(\frac{W}{2} - y_p\right)^2 + \left(z_p + \frac{z_{Gap}}{2} + \Delta\right)^2}}$$

$$\hat{r}_x = |\hat{r}_{xy}| \sin\theta\,(-\hat{\imath}) = \cos\alpha \sin\theta\,(-\hat{\imath})$$

$$= \frac{\left|\frac{W}{2} - y_p\right| \tan\theta}{\sqrt{\left(\left|\frac{W}{2} - y_p\right| tan\theta\right)^2 + \left(\frac{W}{2} - y_p\right)^2 + \left(z_p + \frac{z_{Gap}}{2} + \Delta\right)^2}}(-\hat{\imath})$$

$$\hat{r}_y = |\hat{r}_{xy}| \cos\theta\,(\hat{\jmath}) = \cos\alpha \cos\theta\,(-\hat{\jmath})$$

$$= \frac{\left|\frac{W}{2} - y_p\right|}{\sqrt{\left(\left|\frac{W}{2} - y_p\right| tan\theta\right)^2 + \left(\frac{W}{2} - y_p\right)^2 + \left(z_p + \frac{z_{Gap}}{2} + \Delta\right)^2}}(-\hat{\jmath})$$

$$\hat{r}_z = |\hat{r}| \sin\alpha\,(\hat{k}) = \sin\alpha\,(\hat{k})$$

$$\sin\alpha = \frac{\vec{r}_z}{|\vec{r}|} = \frac{z_p + \frac{z_{Gap}}{2} + \Delta}{\sqrt{\left(\left|\frac{W}{2} - y_p\right| tan\theta\right)^2 + \left(\frac{W}{2} - y_p\right)^2 + \left(z_p + \frac{z_{Gap}}{2} + \Delta\right)^2}}$$

$$\Rightarrow \quad \hat{r}_z = \frac{z_{Yoke} + \frac{z_{Gap}}{2} + \Delta}{\sqrt{\left(\left|\frac{W}{2} - y_p\right| tan\theta\right)^2 + \left(\frac{W}{2} - y_p\right)^2 + \left(z_p + \frac{z_{Gap}}{2} + \Delta\right)^2}}(\hat{k})$$

$$\hat{r} = \left[\frac{\left|\frac{W}{2} - y_p\right| \tan\theta}{\sqrt{\left(\left|\frac{W}{2} - y_p\right| tan\theta\right)^2 + \left(\frac{W}{2} - y_p\right)^2 + \left(z_p + \frac{z_{Gap}}{2} + \Delta\right)^2}}(-\hat{\imath})\right.$$

$$+ \frac{\left|\frac{W}{2} - y_p\right|}{\sqrt{\left(\left|\frac{W}{2} - y_p\right| tan\theta\right)^2 + \left(\frac{W}{2} - y_p\right)^2 + \left(z_p + \frac{z_{Gap}}{2} + \Delta\right)^2}}(-\hat{\jmath})$$

$$\left. + \frac{z_p + \frac{z_{Gap}}{2} + \Delta}{\sqrt{\left(\left|\frac{W}{2} - y_p\right| tan\theta\right)^2 + \left(\frac{W}{2} - y_p\right)^2 + \left(z_p + \frac{z_{Gap}}{2} + \Delta\right)^2}}(\hat{k})\right]$$

$$d\vec{x} \times \hat{r} = \left|\frac{W}{2} - y_p\right| \frac{d\theta}{\cos^2\theta}(\hat{\imath}) \times$$

$$\left[\frac{\left|\frac{W}{2}-y_p\right|\tan\theta}{\sqrt{\left(\left|\frac{W}{2}-y_p\right|\tan\theta\right)^2+\left(\frac{W}{2}-y_p\right)^2+\left(z_p+\frac{z_{Gap}}{2}+\Delta\right)^2}}(-\hat{\imath})\right.$$

$$+\frac{\left|\frac{W}{2}-y_p\right|}{\sqrt{\left(\left|\frac{W}{2}-y_p\right|\tan\theta\right)^2+\left(\frac{W}{2}-y_p\right)^2+\left(z_p+\frac{z_{Gap}}{2}+\Delta\right)^2}}(-\hat{\jmath})$$

$$\left.+\frac{z_{Yoke}+\frac{z_{Gap}}{2}+\Delta}{\sqrt{\left(\left|\frac{W}{2}-y_p\right|\tan\theta\right)^2+\left(\frac{W}{2}-y_p\right)^2+\left(z_p+\frac{z_{Gap}}{2}+\Delta\right)^2}}(\hat{k})\right]$$

$$\Rightarrow \quad d\vec{x}\times\hat{r}=$$

$$\frac{\left(\frac{W}{2}-y_p\right)^2}{\cos^2\theta}\frac{1}{\sqrt{\left(\left|\frac{W}{2}-y_p\right|\tan\theta\right)^2+\left(\frac{W}{2}-y_p\right)^2+\left(z_p+\frac{z_{Gap}}{2}+\Delta\right)^2}}d\theta(-\hat{k})$$

$$+\frac{\left|\frac{W}{2}-y_p\right|}{\cos^2\theta}\frac{z_p+\frac{z_{Gap}}{2}+\Delta}{\sqrt{\left(\left|\frac{W}{2}-y_p\right|\tan\theta\right)^2+\left(\frac{W}{2}-y_p\right)^2+\left(z_p+\frac{z_{Gap}}{2}+\Delta\right)^2}}d\theta(-\hat{\jmath})$$

$$\vec{B}_{p,3,bottom,c}=\frac{\mu_0 I}{4\pi}\int\frac{d\vec{x}\times\hat{r}}{|\vec{r}|^2}$$

$$\Rightarrow \quad \vec{B}_{p,3,bottom,c}=$$

$$\frac{\mu_0 I}{4\pi}\int_{\theta_1}^{\theta_2}\frac{\frac{\left(\frac{W}{2}-y_p\right)^2}{\cos^2\theta}}{\left(\left(\left|\frac{W}{2}-y_p\right|\tan\theta\right)^2+\left(\frac{W}{2}-y_p\right)^2+\left(z_p+\frac{z_{Gap}}{2}+\Delta\right)^2\right)^{3/2}}d\theta(-\hat{k})$$

$$+\frac{\mu_0 I}{4\pi}\int_{\theta_1}^{\theta_2}\frac{\frac{\left|\frac{W}{2}-y_p\right|}{\cos^2\theta}\left(z_p+\frac{z_{Gap}}{2}+\Delta\right)}{\left(\left(\left|\frac{W}{2}-y_p\right|\tan\theta\right)^2+\left(\frac{W}{2}-y_p\right)^2+\left(z_p+\frac{z_{Gap}}{2}+\Delta\right)^2\right)^{3/2}}d\theta(-\hat{\jmath})$$

Eq. (A.17)

$$\Rightarrow \quad \vec{B}_{p,3,bottom,c} = \frac{\mu_0 I \left(\frac{W}{2} - y_p\right)^2}{4\pi}$$

$$\times \int_{\theta_1}^{\theta_2} \frac{1}{cos^2\theta \left(\left(\left|\frac{W}{2} - y_p\right| tan\theta\right)^2 + \left(\frac{W}{2} - y_p\right)^2 + \left(z_p + \frac{z_{Gap}}{2} + \Delta\right)^2\right)^{3/2}} d\theta(-\hat{k})$$

$$+ \frac{\mu_0 I \left|\frac{W}{2} - y_p\right| \left(z_p + \frac{z_{Gap}}{2} + \Delta\right)}{4\pi}$$

$$\times \int_{\theta_1}^{\theta_2} \frac{1}{cos^2\theta \left(\left(\left|\frac{W}{2} - y_p\right| tan\theta\right)^2 + \left(\frac{W}{2} - y_p\right)^2 + \left(z_p + \frac{z_{Gap}}{2} + \Delta\right)^2\right)^{3/2}} d\theta(-\hat{j})$$

$$\theta_2 = tan^{-1} \frac{L}{2\left|\frac{W}{2} - y_p\right|} \quad , \quad \theta_1 = -tan^{-1} \frac{L}{2\left|\frac{W}{2} - y_p\right|}$$

A3.6. Part c - Top Coil

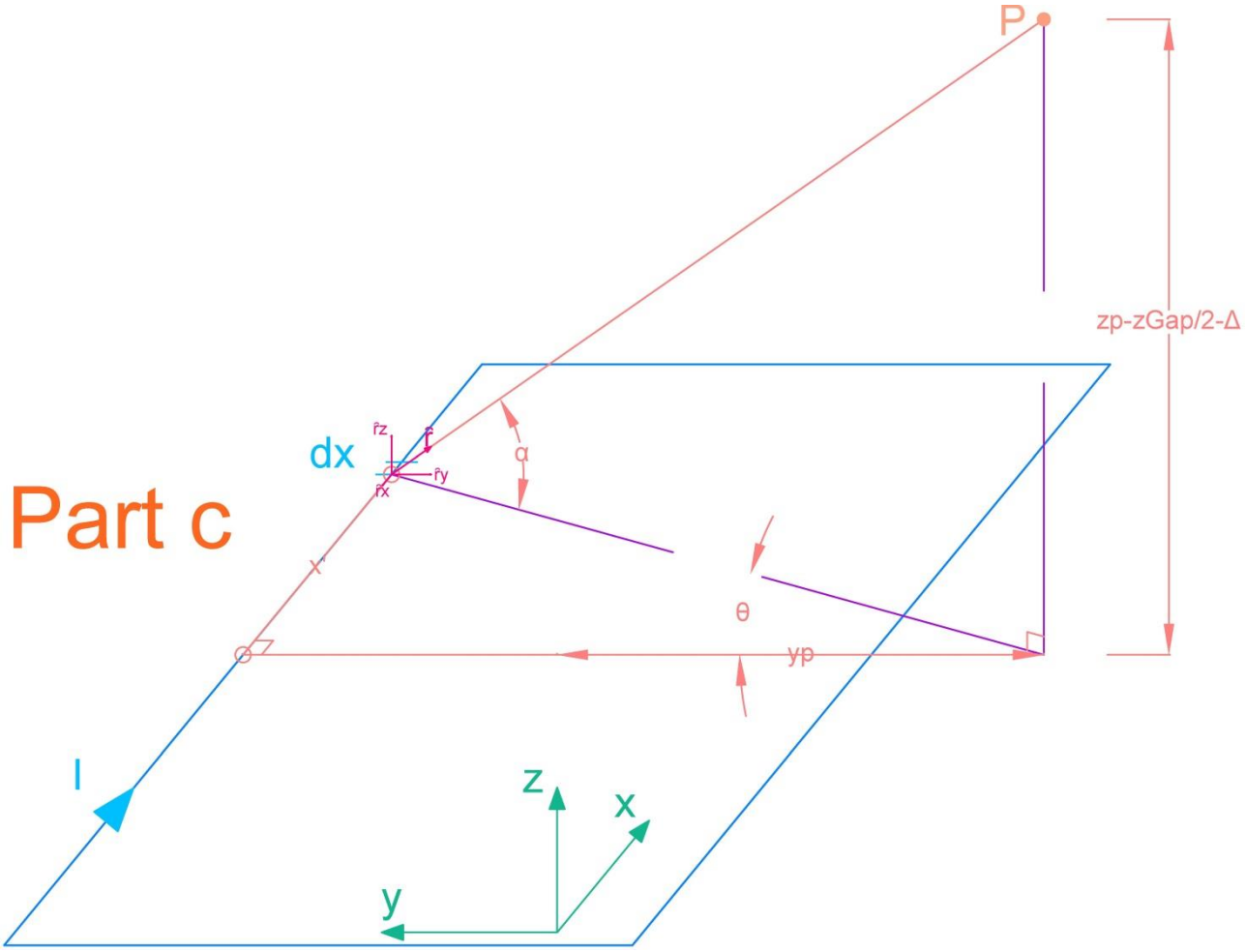

$$\Rightarrow \quad \vec{B}_{p,3,top,c} = \frac{\mu_0 I \left(\frac{W}{2} - y_p\right)^2}{4\pi}$$ **Eq. (A.18)**

$$\times \int_{\theta_1}^{\theta_2} \frac{1}{cos^2\theta \left(\left(\left|\frac{W}{2} - y_p\right| tan\theta\right)^2 + \left(\frac{W}{2} - y_p\right)^2 + \left(z_p - \frac{z_{Gap}}{2} - \Delta\right)^2\right)^{3/2}} d\theta(-\hat{k})$$

$$+ \frac{\mu_0 I \left|\frac{W}{2} - y_p\right| \left(z_p - \frac{z_{Gap}}{2} - \Delta\right)}{4\pi}$$

$$\times \int_{\theta_1}^{\theta_2} \frac{1}{cos^2\theta \left(\left(\left|\frac{W}{2} - y_p\right| tan\theta\right)^2 + \left(\frac{W}{2} - y_p\right)^2 + \left(z_p - \frac{z_{Gap}}{2} - \Delta\right)^2\right)^{3/2}} d\theta(-\hat{\jmath})$$

$$\theta_2 = tan^{-1} \frac{L}{2\left|\frac{W}{2} - y_p\right|} \quad , \quad \theta_1 = -tan^{-1} \frac{L}{2\left|\frac{W}{2} - y_p\right|}$$

A3.7. Part d - Bottom Coil

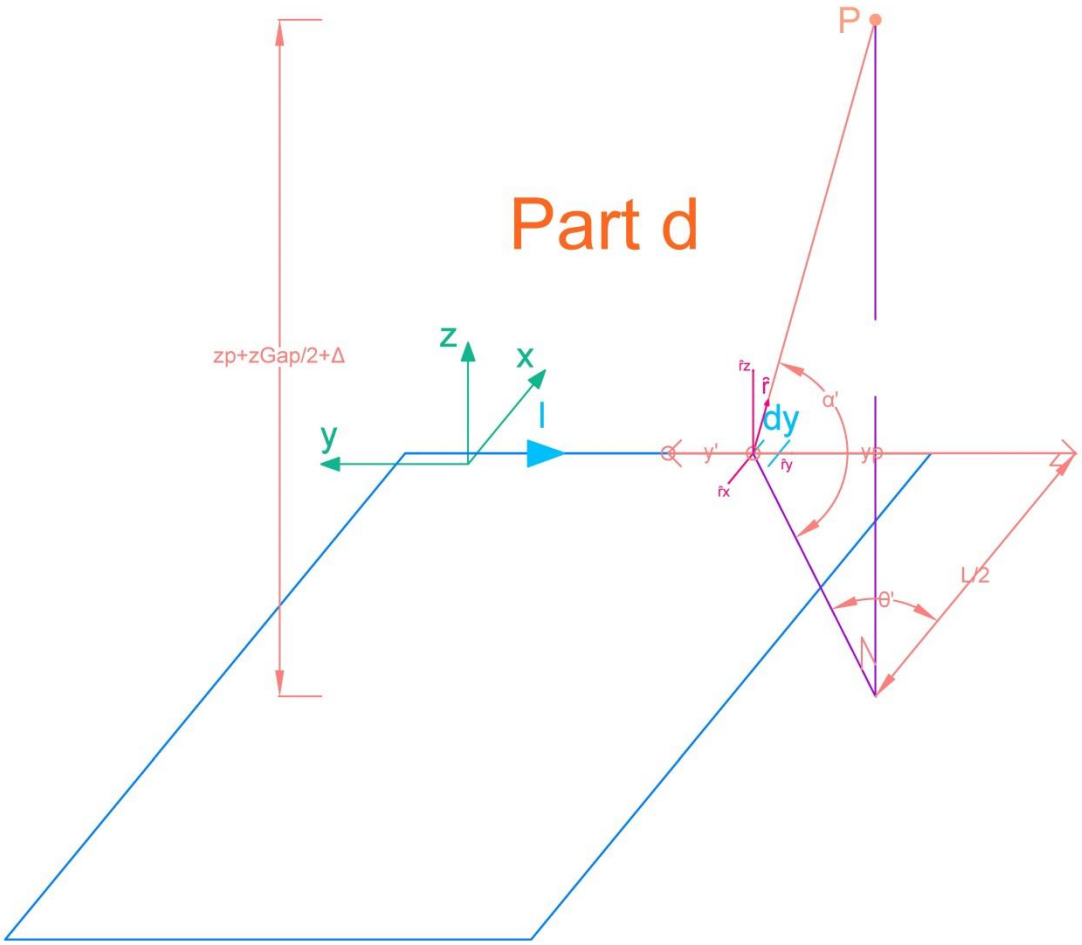

$$\vec{B}_{p,3,bottom,d} = \frac{\mu_0 I}{4\pi}\int \frac{d\vec{y}\times\hat{r}}{|\vec{r}|^2}$$

$$y = \frac{W}{2} - y' = \frac{W}{2} - \left(\frac{L}{2}tan\theta' - |y_p|\right)$$

$$d\vec{y} = \frac{L}{2}\frac{d\theta'}{cos^2\,\theta'}(-\hat{j})$$

$$|\vec{r}| = \sqrt{\left(\frac{L}{2}\right)^2 + \left(\frac{L}{2}tan\theta'\right)^2 + \left(z_p + \frac{z_{Gap}}{2} + \Delta\right)^2}$$

$$\hat{r} = \hat{r}_x + \hat{r}_y + \hat{r}_z$$

$$|\hat{r}_{xy}| = |\hat{r}|\,cos\,\alpha' = cos\,\alpha'$$

$$cos\alpha' = \frac{|\vec{r}_{xy}|}{|\vec{r}|} = \sqrt{\frac{\left(\frac{L}{2}\right)^2 + \left(\frac{L}{2}tan\theta'\right)^2}{\left(\frac{L}{2}\right)^2 + \left(\frac{L}{2}tan\theta'\right)^2 + \left(z_p + \frac{z_{Gap}}{2} + \Delta\right)^2}}$$

$$= \frac{\frac{L}{2}}{\cos\theta'} \frac{1}{\sqrt{\left(\frac{L}{2}\right)^2 + \left(\frac{L}{2}\tan\theta'\right)^2 + \left(z_p + \frac{z_{Gap}}{2} + \Delta\right)^2}}$$

$$\Rightarrow \quad |\hat{r}_{xy}| = \frac{\frac{L}{2}}{\cos\theta'} \frac{1}{\sqrt{\left(\frac{L}{2}\right)^2 + \left(\frac{L}{2}\tan\theta'\right)^2 + \left(z_p + \frac{z_{Gap}}{2} + \Delta\right)^2}}$$

$$\hat{r}_x = -|\hat{r}_{xy}| \cos\theta' (\hat{\imath}) = -\cos\alpha' \cos\theta' (\hat{\imath}) = \frac{\frac{L}{2}}{\sqrt{\left(\frac{L}{2}\right)^2 + \left(\frac{L}{2}\tan\theta'\right)^2 + \left(z_p + \frac{z_{Gap}}{2} + \Delta\right)^2}} (-\hat{\imath})$$

$$\hat{r}_y = -|\hat{r}_{xy}| \sin\theta' (\hat{\jmath}) = -\cos\alpha' \sin\theta' (\hat{\jmath}) = \frac{\frac{L}{2}\tan\theta'}{\sqrt{\left(\frac{L}{2}\right)^2 + \left(\frac{L}{2}\tan\theta'\right)^2 + \left(z_p + \frac{z_{Gap}}{2} + \Delta\right)^2}} (-\hat{\jmath})$$

$$\hat{r}_z = |\hat{r}| \sin\alpha' (\hat{k}) = \sin\alpha' (\hat{k})$$

$$\sin\alpha = \frac{\vec{r}_z}{|\vec{r}|} = \frac{z_p + z_{Gap} + \Delta}{\sqrt{\left(\frac{L}{2}\right)^2 + \left(\frac{L}{2}\tan\theta'\right)^2 + \left(z_p + \frac{z_{Gap}}{2} + \Delta\right)^2}}$$

$$\Rightarrow \quad \hat{r}_z = \frac{z_p + \frac{z_{Gap}}{2} + \Delta}{\sqrt{\left(\frac{L}{2}\right)^2 + \left(\frac{L}{2}\tan\theta'\right)^2 + \left(z_p + \frac{z_{Gap}}{2} + \Delta\right)^2}} (\hat{k})$$

$$\Rightarrow \quad \hat{r} = \left[\frac{\frac{L}{2}}{\sqrt{\left(\frac{L}{2}\right)^2 + \left(\frac{L}{2}\tan\theta'\right)^2 + \left(z_p + \frac{z_{Gap}}{2} + \Delta\right)^2}} (-\hat{\imath}) \right.$$

$$+ \frac{\frac{L}{2}\tan\theta'}{\sqrt{\left(\frac{L}{2}\right)^2 + \left(\frac{L}{2}\tan\theta'\right)^2 + \left(z_p + \frac{z_{Gap}}{2} + \Delta\right)^2}} (-\hat{\jmath})$$

$$\left. + \frac{z_p + \frac{z_{Gap}}{2} + \Delta}{\sqrt{\left(\frac{L}{2}\right)^2 + \left(\frac{L}{2}\tan\theta'\right)^2 + \left(z_p + \frac{z_{Gap}}{2} + \Delta\right)^2}} (\hat{k}) \right]$$

$$d\vec{y} \times \hat{r} = \frac{L}{2} \frac{d\theta'}{\cos^2\theta'} (-\hat{\jmath}) \times$$

$$\left[\frac{\frac{L}{2}}{\sqrt{\left(\frac{L}{2}\right)^2 + \left(\frac{L}{2}\tan\theta'\right)^2 + \left(z_p + \frac{z_{Gap}}{2} + \Delta\right)^2}} (-\hat{\imath}) \right.$$

$$+\frac{\frac{L}{2}\tan\theta'}{\sqrt{\left(\frac{L}{2}\right)^2+\left(\frac{L}{2}\tan\theta'\right)^2+\left(z_p+\frac{z_{Gap}}{2}+\Delta\right)^2}}(-\hat{j})$$

$$+\frac{z_p+\frac{z_{Gap}}{2}+\Delta}{\sqrt{\left(\frac{L}{2}\right)^2+\left(\frac{L}{2}\tan\theta'\right)^2+\left(z_p+\frac{z_{Gap}}{2}+\Delta\right)^2}}(\hat{k})\Bigg]$$

$$\Rightarrow \quad d\vec{y}\times\hat{r}=\frac{\left(\frac{L}{2}\right)^2}{\cos^2\theta'}\frac{1}{\sqrt{\left(\frac{L}{2}\right)^2+\left(\frac{L}{2}\tan\theta'\right)^2+\left(z_p+\frac{z_{Gap}}{2}+\Delta\right)^2}}d\theta(-\hat{k})$$

$$+\frac{\left(\frac{L}{2}\right)}{\cos^2\theta'}\frac{z_p+\frac{z_{Gap}}{2}+\Delta}{\sqrt{\left(\frac{L}{2}\right)^2+\left(\frac{L}{2}\tan\theta'\right)^2+\left(z_p+\frac{z_{Gap}}{2}+\Delta\right)^2}}d\theta'(-\hat{\imath})$$

$$\vec{B}_{p,3,bottom,d}=\frac{\mu_0 I}{4\pi}\int\frac{d\vec{y}\times\hat{r}}{|\vec{r}|^2}$$

$$\Rightarrow \quad d\vec{B}_{p,3,bottom,d}=\frac{\mu_0 I}{4\pi}\int_{\theta'_1}^{\theta'_2}\frac{\frac{\left(\frac{L}{2}\right)^2}{\cos^2\theta'}\frac{1}{\sqrt{\left(\frac{L}{2}\right)^2+\left(\frac{L}{2}\tan\theta'\right)^2+\left(z_p+\frac{z_{Gap}}{2}+\Delta\right)^2}}}{\left(\frac{L}{2}\right)^2+\left(\frac{L}{2}\tan\theta'\right)^2+\left(z_p+\frac{z_{Gap}}{2}+\Delta\right)^2}d\theta'(-\hat{k})$$

$$+\frac{\mu_0 I}{4\pi}\int_{\theta'_1}^{\theta'_2}\frac{\frac{\left(\frac{L}{2}\right)}{\cos^2\theta'}\frac{z_p+\frac{z_{Gap}}{2}+\Delta}{\sqrt{\left(\frac{L}{2}\right)^2+\left(\frac{L}{2}\tan\theta'\right)^2+\left(z_p+\frac{z_{Gap}}{2}+\Delta\right)^2}}}{\left(\frac{L}{2}\right)^2+\left(\frac{L}{2}\tan\theta'\right)^2+\left(z_p+\frac{z_{Gap}}{2}+\Delta\right)^2}d\theta'(-\hat{\imath})$$

$$\Rightarrow \quad d\vec{B}_{p,3,bottom,b}= \qquad \textbf{Eq. (A.19)}$$

$$\frac{\mu_0 I\left(\frac{L}{2}\right)^2}{4\pi}\int_{\theta'_1}^{\theta'_2}\frac{1}{(\cos\theta')^2\left(\left(\frac{L}{2}\right)^2+\left(\frac{L}{2}\tan\theta'\right)^2+\left(z_p+\frac{z_{Gap}}{2}+\Delta\right)^2\right)^{3/2}}d\theta'(-\hat{k})$$

$$+\frac{\mu_0 I\left(\frac{L}{2}\right)(z_p+\frac{z_{Gap}}{2}+\Delta)}{4\pi}\int_{\theta'_1}^{\theta'_2}\frac{1}{(\cos\theta')^2\left(\left(\frac{L}{2}\right)^2+\left(\frac{L}{2}\tan\theta'\right)^2+\left(z_p+\frac{z_{Gap}}{2}+\Delta\right)^2\right)^{3/2}}d\theta'(-\hat{\imath})$$

$$\theta'_2=\tan^{-1}\frac{|y_p|-\frac{W}{2}}{\frac{L}{2}} \quad , \quad \theta'_1=\tan^{-1}\frac{|y_p|+\frac{W}{2}}{\frac{L}{2}}$$

A3.8. Part d - Top Coil

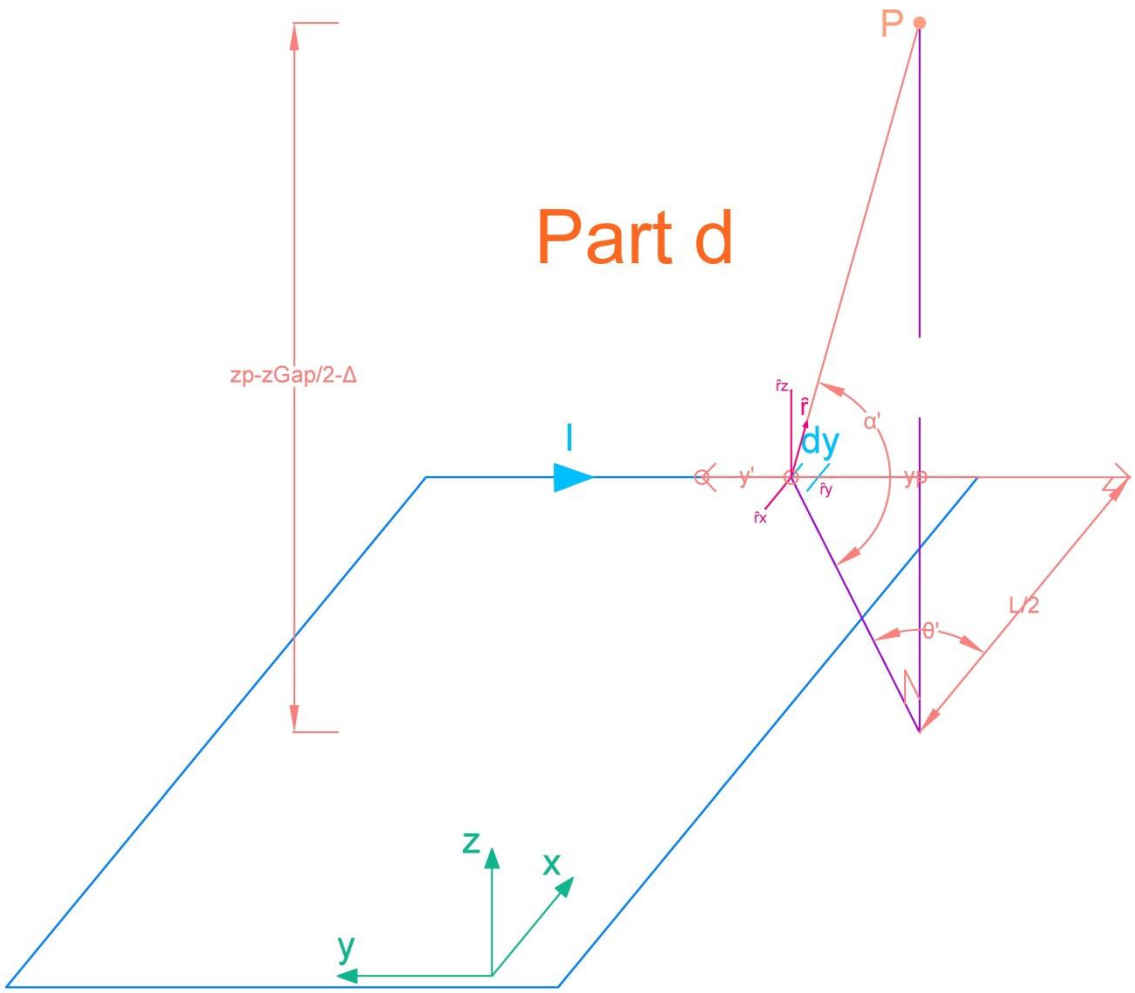

$$\Rightarrow \quad d\vec{B}_{p,3,top,d} = \qquad \textbf{Eq. (A.20)}$$

$$\frac{\mu_0 I \left(\frac{L}{2}\right)^2}{4\pi} \int_{\theta'_1}^{\theta'_2} \frac{1}{(\cos\theta')^2 \left(\left(\frac{L}{2}\right)^2 + \left(\frac{L}{2}\tan\theta'\right)^2 + \left(z_p - \frac{z_{Gap}}{2} - \Delta\right)^2\right)^{3/2}} d\theta' \left(-\hat{k}\right)$$

$$+ \frac{\mu_0 I \left(\frac{L}{2}\right)\left(z_p - \frac{z_{Gap}}{2} - \Delta\right)}{4\pi} \int_{\theta'_1}^{\theta'_2} \frac{1}{(\cos\theta')^2 \left(\left(\frac{L}{2}\right)^2 + \left(\frac{L}{2}\tan\theta'\right)^2 + \left(z_p - \frac{z_{Gap}}{2} - \Delta\right)^2\right)^{3/2}} d\theta' \left(-\hat{\imath}\right)$$

$$\theta'_2 = \tan^{-1} \frac{|y_p| - \frac{W}{2}}{\frac{L}{2}} \quad , \quad \theta'_1 = \tan^{-1} \frac{|y_p| + \frac{W}{2}}{\frac{L}{2}}$$

A4. Combining the Fields

A4.1. Sections 1 and 5

For Sections 1 and 5, magnetic fields in z direction contribute to the Amperian loop; components in other directions are ignored.

$$\vec{\mathbf{B}}_{\mathbf{p,15}} = \vec{\mathbf{B}}_{\mathbf{p,15,bottom,a}} + \vec{\mathbf{B}}_{\mathbf{p,15,top,a}} + \vec{\mathbf{B}}_{\mathbf{p,15,bottom,b}} + \vec{\mathbf{B}}_{\mathbf{p,15,top,b}} + \vec{\mathbf{B}}_{\mathbf{p,15,bottom,c}} + \vec{\mathbf{B}}_{\mathbf{p,15,top,c}} + \vec{\mathbf{B}}_{\mathbf{p,15,bottom,d}} + \vec{\mathbf{B}}_{\mathbf{p,15,top,d}}$$

$$\vec{B}_{p,15,a,c} = \vec{B}_{p,15,bottom,a} + \vec{B}_{p,15,top,a} + \vec{B}_{p,15,bottom,c} + \vec{B}_{p,15,top,c} =$$

$$\frac{\mu_0 I \left(\frac{W}{2}\right)^2}{4\pi} \int_{-\tan^{-1}\frac{L}{W}}^{\tan^{-1}\frac{L}{W}} \frac{1}{(\cos\theta)^2 \left(\left(\frac{W}{2}\tan\theta\right)^2 + \left(\frac{W}{2}\right)^2 + \left(z_p + \frac{z_{Gap}}{2} + \Delta\right)^2\right)^{3/2}} d\theta(-\hat{k})$$

$$\frac{\mu_0 I \left(\frac{W}{2}\right)^2}{4\pi} \int_{-\tan^{-1}\frac{L}{W}}^{\tan^{-1}\frac{L}{W}} \frac{1}{(\cos\theta)^2 \left(\left(\frac{W}{2}\tan\theta\right)^2 + \left(\frac{W}{2}\right)^2 + \left(z_p - \frac{z_{Gap}}{2} - \Delta\right)^2\right)^{3/2}} d\theta(-\hat{k})$$

$$+\frac{\mu_0 I \left(\frac{W}{2}\right)^2}{4\pi} \int_{-\tan^{-1}\frac{L}{W}}^{\tan^{-1}\frac{L}{W}} \frac{1}{(\cos\theta)^2 \left(\left(\frac{W}{2}\tan\theta\right)^2 + \left(\frac{W}{2}\right)^2 + \left(z_p + \frac{z_{Gap}}{2} + \Delta\right)^2\right)^{3/2}} d\theta(-\hat{k})$$

$$\frac{\mu_0 I \left(\frac{W}{2}\right)^2}{4\pi} \int_{-\tan^{-1}\frac{L}{W}}^{\tan^{-1}\frac{L}{W}} \frac{1}{(\cos\theta)^2 \left(\left(\frac{W}{2}\tan\theta\right)^2 + \left(\frac{W}{2}\right)^2 + \left(z_p - \frac{z_{Gap}}{2} - \Delta\right)^2\right)^{3/2}} d\theta(-\hat{k})$$

$$\Rightarrow \quad \vec{B}_{p,15,a,c} =$$

$$2 \times \frac{\mu_0 I \left(\frac{W}{2}\right)^2}{4\pi} \int_{-\tan^{-1}\frac{L}{W}}^{\tan^{-1}\frac{L}{W}} \frac{1}{(\cos\theta)^2 \left(\left(\frac{W}{2}\tan\theta\right)^2 + \left(\frac{W}{2}\right)^2 + \left(z_p + \frac{z_{Gap}}{2} + \Delta\right)^2\right)^{3/2}} d\theta(-\hat{k})$$

$$+2 \times \frac{\mu_0 I \left(\frac{W}{2}\right)^2}{4\pi} \int_{-\tan^{-1}\frac{L}{W}}^{\tan^{-1}\frac{L}{W}} \frac{1}{(\cos\theta)^2 \left(\left(\frac{W}{2}\tan\theta\right)^2 + \left(\frac{W}{2}\right)^2 + \left(z_p - \frac{z_{Gap}}{2} - \Delta\right)^2\right)^{3/2}} d\theta(-\hat{k})$$

$$\vec{B}_{p,15,b,d} = \vec{B}_{p,15,bottom,b} + \vec{B}_{p,15,top,b} + \vec{B}_{p,15,bottom,d} + \vec{B}_{p,15,top,d} =$$

$$\frac{\mu_0 I\left(\frac{L}{2}\right)^2}{4\pi}\int_{-\tan^{-1}\frac{W}{L}}^{\tan^{-1}\frac{W}{L}}\frac{1}{(\cos\theta')^2\left(\left(\frac{L}{2}\right)^2+\left(\frac{L}{2}\tan\theta'\right)^2+\left(z_p+\frac{z_{Gap}}{2}+\Delta\right)^2\right)^{3/2}}d\theta'(-\hat{k})$$

$$\frac{\mu_0 I\left(\frac{L}{2}\right)^2}{4\pi}\int_{-\tan^{-1}\frac{W}{L}}^{\tan^{-1}\frac{W}{L}}\frac{1}{(\cos\theta')^2\left(\left(\frac{L}{2}\right)^2+\left(\frac{L}{2}\tan\theta'\right)^2+\left(z_p-\frac{z_{Gap}}{2}-\Delta\right)^2\right)^{3/2}}d\theta'(-\hat{k})$$

$$\frac{\mu_0 I\left(\frac{L}{2}\right)^2}{4\pi}\int_{-\tan^{-1}\frac{W}{L}}^{\tan^{-1}\frac{W}{L}}\frac{1}{(\cos\theta')^2\left(\left(\frac{L}{2}\right)^2+\left(\frac{L}{2}\tan\theta'\right)^2+\left(z_p+\frac{z_{Gap}}{2}+\Delta\right)^2\right)^{3/2}}d\theta'(-\hat{k})$$

$$\frac{\mu_0 I\left(\frac{L}{2}\right)^2}{4\pi}\int_{-\tan^{-1}\frac{W}{L}}^{\tan^{-1}\frac{W}{L}}\frac{1}{(\cos\theta')^2\left(\left(\frac{L}{2}\right)^2+\left(\frac{L}{2}\tan\theta'\right)^2+\left(z_p-\frac{z_{Gap}}{2}-\Delta\right)^2\right)^{3/2}}d\theta'(-\hat{k})$$

$$\Rightarrow \quad \vec{B}_{p,15,b,d} =$$

$$2\times\frac{\mu_0 I\left(\frac{L}{2}\right)^2}{4\pi}\int_{-\tan^{-1}\frac{W}{L}}^{\tan^{-1}\frac{W}{L}}\frac{1}{(\cos\theta')^2\left(\left(\frac{L}{2}\right)^2+\left(\frac{L}{2}\tan\theta'\right)^2+\left(z_p+\frac{z_{Gap}}{2}+\Delta\right)^2\right)^{3/2}}d\theta'(-\hat{k})$$

$$+2\times\frac{\mu_0 I\left(\frac{L}{2}\right)^2}{4\pi}\int_{-\tan^{-1}\frac{W}{L}}^{\tan^{-1}\frac{W}{L}}\frac{1}{(\cos\theta')^2\left(\left(\frac{L}{2}\right)^2+\left(\frac{L}{2}\tan\theta'\right)^2+\left(z_p-\frac{z_{Gap}}{2}-\Delta\right)^2\right)^{3/2}}d\theta'(-\hat{k})$$

$$\Rightarrow \quad \vec{B}_{p,15} = \vec{B}_{p,15,a,c} + \vec{B}_{p,15,b,d} = \qquad \textbf{Eq. (A.21)}$$

$$2 \times \frac{\mu_0 I \left(\frac{W}{2}\right)^2}{4\pi} \int_{-\tan^{-1}\frac{L}{W}}^{\tan^{-1}\frac{L}{W}} \frac{1}{(\cos\theta)^2 \left(\left(\frac{W}{2}\tan\theta\right)^2 + \left(\frac{W}{2}\right)^2 + \left(z_p + \frac{z_{Gap}}{2} + \Delta\right)^2\right)^{3/2}} d\theta\left(-\hat{k}\right)$$

$$+2 \times \frac{\mu_0 I \left(\frac{W}{2}\right)^2}{4\pi} \int_{-\tan^{-1}\frac{L}{W}}^{\tan^{-1}\frac{L}{W}} \frac{1}{(\cos\theta)^2 \left(\left(\frac{W}{2}\tan\theta\right)^2 + \left(\frac{W}{2}\right)^2 + \left(z_p - \frac{z_{Gap}}{2} - \Delta\right)^2\right)^{3/2}} d\theta\left(-\hat{k}\right)$$

$$+2 \times \frac{\mu_0 I \left(\frac{L}{2}\right)^2}{4\pi} \int_{-\tan^{-1}\frac{W}{L}}^{\tan^{-1}\frac{W}{L}} \frac{1}{(\cos\theta')^2 \left(\left(\frac{L}{2}\right)^2 + \left(\frac{L}{2}\tan\theta'\right)^2 + \left(z_p + \frac{z_{Gap}}{2} + \Delta\right)^2\right)^{3/2}} d\theta'\left(-\hat{k}\right)$$

$$+2 \times \frac{\mu_0 I \left(\frac{L}{2}\right)^2}{4\pi} \int_{-\tan^{-1}\frac{W}{L}}^{\tan^{-1}\frac{W}{L}} \frac{1}{(\cos\theta')^2 \left(\left(\frac{L}{2}\right)^2 + \left(\frac{L}{2}\tan\theta'\right)^2 + \left(z_p - \frac{z_{Gap}}{2} - \Delta\right)^2\right)^{3/2}} d\theta'\left(-\hat{k}\right)$$

A4.2. Sections 2 and 4

For sections 2 and 4, magnetic fields in y direction contribute to the Amperian loop. Therefore, components in other directions are ignored. Note that parts b and d do not produce fields in y direction and are also ignored.

$$\vec{\mathbf{B}}_{\mathbf{p,24}} = \vec{\mathbf{B}}_{\mathbf{p,24,bottom,a}} + \vec{\mathbf{B}}_{\mathbf{p,24,top,a}} + \vec{\mathbf{B}}_{\mathbf{p,24,bottom,c}} + \vec{\mathbf{B}}_{\mathbf{p,24,top,c}}$$

$$\vec{B}_{p,24,a,c} = \vec{B}_{p,24,bottom,a} + \vec{B}_{p,24,top,a} + \vec{B}_{p,24,bottom,c} + \vec{B}_{p,24,top,c} =$$

$$+\frac{\mu_0 I \left|\frac{W}{2}+y_p\right| \left(z_p + \frac{z_{Gap}}{2} + \Delta\right)}{4\pi}$$

$$\times \int_{-\tan^{-1}\frac{L}{2\left|\frac{W}{2}+y_p\right|}}^{\tan^{-1}\frac{L}{2\left|\frac{W}{2}+y_p\right|}} \frac{1}{\cos^2\theta \left(\left(\left|\frac{W}{2}+y_p\right| \tan\theta\right)^2 + \left(\frac{W}{2}+y_p\right)^2 + \left(z_p + \frac{z_{Gap}}{2} + \Delta\right)^2\right)^{3/2}} d\theta(\hat{j})$$

$$+\frac{\mu_0 I \left|\frac{W}{2}+y_p\right| \left(z_p - \frac{z_{Gap}}{2} - \Delta\right)}{4\pi}$$

$$\times \int_{-\tan^{-1}\frac{L}{2\left|\frac{W}{2}+y_p\right|}}^{\tan^{-1}\frac{L}{2\left|\frac{W}{2}+y_p\right|}} \frac{1}{\cos^2\theta \left(\left(\left|\frac{W}{2}+y_p\right| \tan\theta\right)^2 + \left(\frac{W}{2}+y_p\right)^2 + \left(z_p - \frac{z_{Gap}}{2} - \Delta\right)^2\right)^{3/2}} d\theta(\hat{j})$$

$$+\frac{\mu_0 I \left|\frac{W}{2}-y_p\right| \left(z_p + \frac{z_{Gap}}{2} + \Delta\right)}{4\pi}$$

$$\times \int_{-\tan^{-1}\frac{L}{2\left|\frac{W}{2}-y_p\right|}}^{\tan^{-1}\frac{L}{2\left|\frac{W}{2}-y_p\right|}} \frac{1}{\cos^2\theta \left(\left(\left|\frac{W}{2}-y_p\right| \tan\theta\right)^2 + \left(\frac{W}{2}-y_p\right)^2 + \left(z_p + \frac{z_{Gap}}{2} + \Delta\right)^2\right)^{3/2}} d\theta(-\hat{j})$$

$$+\frac{\mu_0 I \left|\frac{W}{2}-y_p\right| \left(z_p - \frac{z_{Gap}}{2} - \Delta\right)}{4\pi}$$

$$\times \int_{-\tan^{-1}\frac{L}{2\left|\frac{W}{2}-y_p\right|}}^{\tan^{-1}\frac{L}{2\left|\frac{W}{2}-y_p\right|}} \frac{1}{\cos^2\theta \left(\left(\left|\frac{W}{2}-y_p\right| \tan\theta\right)^2 + \left(\frac{W}{2}-y_p\right)^2 + \left(z_p - \frac{z_{Gap}}{2} - \Delta\right)^2\right)^{3/2}} d\theta(-\hat{j})$$

$$\Rightarrow \quad \vec{B}_{p,24,a,c} = \frac{\mu_0 I \left|\frac{W}{2} + y_p\right| \left(z_p + \frac{z_{Gap}}{2} + \Delta\right)}{4\pi}$$

$$\times \int_{-\tan^{-1}\frac{L}{2\left|\frac{W}{2}+y_p\right|}}^{\tan^{-1}\frac{L}{2\left|\frac{W}{2}+y_p\right|}} \frac{1}{\cos^2\theta \left(\left(\left|\frac{W}{2} + y_p\right| \tan\theta\right)^2 + \left(\frac{W}{2} + y_p\right)^2 + \left(z_p + \frac{z_{Gap}}{2} + \Delta\right)^2\right)^{3/2}} d\theta(\hat{j})$$

$$+ \frac{\mu_0 I \left|\frac{W}{2} + y_p\right| \left(z_p - \frac{z_{Gap}}{2} - \Delta\right)}{4\pi}$$

$$\times \int_{-\tan^{-1}\frac{L}{2\left|\frac{W}{2}+y_p\right|}}^{\tan^{-1}\frac{L}{2\left|\frac{W}{2}+y_p\right|}} \frac{1}{\cos^2\theta \left(\left(\left|\frac{W}{2} + y_p\right| \tan\theta\right)^2 + \left(\frac{W}{2} + y_p\right)^2 + \left(z_p - \frac{z_{Gap}}{2} - \Delta\right)^2\right)^{3/2}} d\theta(\hat{j})$$

$$+ \frac{\mu_0 I \left|\frac{W}{2} - y_p\right| \left(z_p + \frac{z_{Gap}}{2} + \Delta\right)}{4\pi}$$

$$\times \int_{-\tan^{-1}\frac{L}{2\left|\frac{W}{2}-y_p\right|}}^{\tan^{-1}\frac{L}{2\left|\frac{W}{2}-y_p\right|}} \frac{1}{\cos^2\theta \left(\left(\left|\frac{W}{2} - y_p\right| \tan\theta\right)^2 + \left(\frac{W}{2} - y_p\right)^2 + \left(z_p + \frac{z_{Gap}}{2} + \Delta\right)^2\right)^{3/2}} d\theta(-\hat{j})$$

$$+ \frac{\mu_0 I \left|\frac{W}{2} - y_p\right| \left(z_p - \frac{z_{Gap}}{2} - \Delta\right)}{4\pi}$$

$$\times \int_{-\tan^{-1}\frac{L}{2\left|\frac{W}{2}-y_p\right|}}^{\tan^{-1}\frac{L}{2\left|\frac{W}{2}-y_p\right|}} \frac{1}{\cos^2\theta \left(\left(\left|\frac{W}{2} - y_p\right| \tan\theta\right)^2 + \left(\frac{W}{2} - y_p\right)^2 + \left(z_p - \frac{z_{Gap}}{2} - \Delta\right)^2\right)^{3/2}} d\theta(-\hat{j})$$

$$\Rightarrow \quad \vec{B}_{p,24} = \qquad \textbf{Eq. (A.22)}$$

$$\frac{\mu_0 I \left|\frac{W}{2}+y_p\right| \left(z_p+\frac{z_{Gap}}{2}+\Delta\right)}{4\pi}$$

$$\times \int_{-\tan^{-1}\frac{L}{2\left|\frac{W}{2}+y_p\right|}}^{\tan^{-1}\frac{L}{2\left|\frac{W}{2}+y_p\right|}} \frac{1}{\cos^2\theta \left(\left(\left|\frac{W}{2}+y_p\right| tan\theta\right)^2+\left(\frac{W}{2}+y_p\right)^2+\left(z_p+\frac{z_{Gap}}{2}+\Delta\right)^2\right)^{3/2}} d\theta(\hat{j})$$

$$+\frac{\mu_0 I \left|\frac{W}{2}+y_p\right| \left(z_p-\frac{z_{Gap}}{2}-\Delta\right)}{4\pi}$$

$$\times \int_{-\tan^{-1}\frac{L}{2\left|\frac{W}{2}+y_p\right|}}^{\tan^{-1}\frac{L}{2\left|\frac{W}{2}+y_p\right|}} \frac{1}{\cos^2\theta \left(\left(\left|\frac{W}{2}+y_p\right| tan\theta\right)^2+\left(\frac{W}{2}+y_p\right)^2+\left(z_p-\frac{z_{Gap}}{2}-\Delta\right)^2\right)^{3/2}} d\theta(\hat{j})$$

$$+\frac{\mu_0 I \left|\frac{W}{2}-y_p\right| \left(z_p+\frac{z_{Gap}}{2}+\Delta\right)}{4\pi}$$

$$\times \int_{-\tan^{-1}\frac{L}{2\left|\frac{W}{2}-y_p\right|}}^{\tan^{-1}\frac{L}{2\left|\frac{W}{2}-y_p\right|}} \frac{1}{\cos^2\theta \left(\left(\left|\frac{W}{2}-y_p\right| tan\theta\right)^2+\left(\frac{W}{2}-y_p\right)^2+\left(z_p+\frac{z_{Gap}}{2}+\Delta\right)^2\right)^{3/2}} d\theta(-\hat{j})$$

$$+\frac{\mu_0 I \left|\frac{W}{2}-y_p\right| \left(z_p-\frac{z_{Gap}}{2}-\Delta\right)}{4\pi}$$

$$\times \int_{-\tan^{-1}\frac{L}{2\left|\frac{W}{2}-y_p\right|}}^{\tan^{-1}\frac{L}{2\left|\frac{W}{2}-y_p\right|}} \frac{1}{\cos^2\theta \left(\left(\left|\frac{W}{2}-y_p\right| tan\theta\right)^2+\left(\frac{W}{2}-y_p\right)^2+\left(z_p-\frac{z_{Gap}}{2}-\Delta\right)^2\right)^{3/2}} d\theta(-\hat{j})$$

A4.3. Section 3

For Section 3, fields in z direction contribute to the Amperian loop. However, contribution of parts b, c, and d are negative, whereas part a produces fields in the positive direction.

$$\vec{\mathbf{B}}_{\mathbf{p,3}} = \vec{\mathbf{B}}_{\mathbf{p,3,bottom,a}} + \vec{\mathbf{B}}_{\mathbf{p,3,top,a}} + \vec{\mathbf{B}}_{\mathbf{p,3,bottom,b}} + \vec{\mathbf{B}}_{\mathbf{p,3,top,b}} + \vec{\mathbf{B}}_{\mathbf{p,3,bottom,c}} + \vec{\mathbf{B}}_{\mathbf{p,3,top,c}} + \vec{\mathbf{B}}_{\mathbf{p,15,bottom,d}} + \vec{\mathbf{B}}_{\mathbf{p,3,top,d}}$$

$$\vec{B}_{p,3,a,c} = \vec{B}_{p,3,bottom,a} + \vec{B}_{p,3,top,a} + \vec{B}_{p,3,bottom,c} + \vec{B}_{p,3,top,c} =$$

$$\frac{\mu_0 I \left(\frac{W}{2} + y_p\right)^2}{4\pi}$$

$$\times \int_{-\tan^{-1}\frac{L}{2\left|\frac{W}{2}+y_p\right|}}^{\tan^{-1}\frac{L}{2\left|\frac{W}{2}+y_p\right|}} \frac{1}{\cos^2\theta \left(\left(\left|\frac{W}{2} + y_p\right| \tan\theta\right)^2 + \left(\frac{W}{2} + y_p\right)^2 + \left(z_p + \frac{z_{Gap}}{2} + \Delta\right)^2\right)^{3/2}} d\theta(\hat{k})$$

$$+ \frac{\mu_0 I \left(\frac{W}{2} + y_p\right)^2}{4\pi}$$

$$\times \int_{-\tan^{-1}\frac{L}{2\left|\frac{W}{2}+y_p\right|}}^{\tan^{-1}\frac{L}{2\left|\frac{W}{2}+y_p\right|}} \frac{1}{\cos^2\theta \left(\left(\left|\frac{W}{2} + y_p\right| \tan\theta\right)^2 + \left(\frac{W}{2} + y_p\right)^2 + \left(z_p - \frac{z_{Gap}}{2} - \Delta\right)^2\right)^{3/2}} d\theta(\hat{k})$$

$$+ \frac{\mu_0 I \left(\frac{W}{2} - y_p\right)^2}{4\pi}$$

$$\times \int_{-\tan^{-1}\frac{L}{2\left|\frac{W}{2}-y_p\right|}}^{\tan^{-1}\frac{L}{2\left|\frac{W}{2}-y_p\right|}} \frac{1}{\cos^2\theta \left(\left(\left|\frac{W}{2} - y_p\right| \tan\theta\right)^2 + \left(\frac{W}{2} - y_p\right)^2 + \left(z_p + \frac{z_{Gap}}{2} + \Delta\right)^2\right)^{3/2}} d\theta(-\hat{k})$$

$$+ \frac{\mu_0 I \left(\frac{W}{2} - y_p\right)^2}{4\pi}$$

$$\times \int_{-\tan^{-1}\frac{L}{2\left|\frac{W}{2}-y_p\right|}}^{\tan^{-1}\frac{L}{2\left|\frac{W}{2}-y_p\right|}} \frac{1}{\cos^2\theta \left(\left(\left|\frac{W}{2} - y_p\right| \tan\theta\right)^2 + \left(\frac{W}{2} - y_p\right)^2 + \left(z_p - \frac{z_{Gap}}{2} - \Delta\right)^2\right)^{3/2}} d\theta(-\hat{k})$$

$$\Rightarrow \quad \vec{B}_{p,3,a,c} =$$

$$\frac{\mu_0 I \left(\frac{W}{2} + y_p\right)^2}{4\pi}$$

$$\times \int_{-\tan^{-1}\frac{L}{2\left|\frac{W}{2}+y_p\right|}}^{\tan^{-1}\frac{L}{2\left|\frac{W}{2}+y_p\right|}} \frac{1}{\cos^2\theta\left(\left(\left|\frac{W}{2}+y_p\right|\tan\theta\right)^2+\left(\frac{W}{2}+y_p\right)^2+\left(z_p+\frac{z_{Gap}}{2}+\Delta\right)^2\right)^{3/2}} d\theta(\hat{k})$$

$$+\frac{\mu_0 I\left(\frac{W}{2}+y_p\right)^2}{4\pi}$$

$$\times \int_{-\tan^{-1}\frac{L}{2\left|\frac{W}{2}+y_p\right|}}^{\tan^{-1}\frac{L}{2\left|\frac{W}{2}+y_p\right|}} \frac{1}{\cos^2\theta\left(\left(\left|\frac{W}{2}+y_p\right|\tan\theta\right)^2+\left(\frac{W}{2}+y_p\right)^2+\left(z_p-\frac{z_{Gap}}{2}-\Delta\right)^2\right)^{3/2}} d\theta(\hat{k})$$

$$+\frac{\mu_0 I\left(\frac{W}{2}-y_p\right)^2}{4\pi}$$

$$\times \int_{-\tan^{-1}\frac{L}{2\left|\frac{W}{2}-y_p\right|}}^{\tan^{-1}\frac{L}{2\left|\frac{W}{2}-y_p\right|}} \frac{1}{\cos^2\theta\left(\left(\left|\frac{W}{2}-y_p\right|\tan\theta\right)^2+\left(\frac{W}{2}-y_p\right)^2+\left(z_p+\frac{z_{Gap}}{2}+\Delta\right)^2\right)^{3/2}} d\theta(-\hat{k})$$

$$+\frac{\mu_0 I\left(\frac{W}{2}-y_p\right)^2}{4\pi}$$

$$\times \int_{-\tan^{-1}\frac{L}{2\left|\frac{W}{2}-y_p\right|}}^{\tan^{-1}\frac{L}{2\left|\frac{W}{2}-y_p\right|}} \frac{1}{\cos^2\theta\left(\left(\left|\frac{W}{2}-y_p\right|\tan\theta\right)^2+\left(\frac{W}{2}-y_p\right)^2+\left(z_p-\frac{z_{Gap}}{2}-\Delta\right)^2\right)^{3/2}} d\theta(-\hat{k})$$

$$\vec{B}_{p,3,b,d}=\vec{B}_{p,3,bottom,b}+\vec{B}_{p,3,top,b}+\vec{B}_{p,3,bottom,d}+\vec{B}_{p,3,top,d}=$$

$$\frac{\mu_0 I\left(\frac{L}{2}\right)^2}{4\pi} \int_{\tan^{-1}\frac{|y_p|-\frac{W}{2}}{\frac{L}{2}}}^{\tan^{-1}\frac{|y_p|+\frac{W}{2}}{\frac{L}{2}}} \frac{1}{(\cos\theta')^2\left(\left(\frac{L}{2}\right)^2+\left(\frac{L}{2}\tan\theta'\right)^2+\left(z_p+\frac{z_{Gap}}{2}+\Delta\right)^2\right)^{3/2}} d\theta'(-\hat{k})$$

$$+\frac{\mu_0 I\left(\frac{L}{2}\right)^2}{4\pi} \int_{\tan^{-1}\frac{|y_p|-\frac{W}{2}}{\frac{L}{2}}}^{\tan^{-1}\frac{|y_p|+\frac{W}{2}}{\frac{L}{2}}} \frac{1}{(\cos\theta')^2\left(\left(\frac{L}{2}\right)^2+\left(\frac{L}{2}\tan\theta'\right)^2+\left(z_p-\frac{z_{Gap}}{2}-\Delta\right)^2\right)^{3/2}} d\theta'(-\hat{k})$$

$$\frac{\mu_0 I\left(\frac{L}{2}\right)^2}{4\pi}\int_{\tan^{-1}\frac{|y_p|-\frac{W}{2}}{\frac{L}{2}}}^{\tan^{-1}\frac{|y_p|+\frac{W}{2}}{\frac{L}{2}}}\frac{1}{(\cos\theta')^2\left(\left(\frac{L}{2}\right)^2+\left(\frac{L}{2}\tan\theta'\right)^2+\left(z_p+\frac{z_{Gap}}{2}+\Delta\right)^2\right)^{3/2}}d\theta'(-\hat{k})$$

$$+\frac{\mu_0 I\left(\frac{L}{2}\right)^2}{4\pi}\int_{\tan^{-1}\frac{|y_p|-\frac{W}{2}}{\frac{L}{2}}}^{\tan^{-1}\frac{|y_p|+\frac{W}{2}}{\frac{L}{2}}}\frac{1}{(\cos\theta')^2\left(\left(\frac{L}{2}\right)^2+\left(\frac{L}{2}\tan\theta'\right)^2+\left(z_p-\frac{z_{Gap}}{2}-\Delta\right)^2\right)^{3/2}}d\theta'(-\hat{k})$$

$$\Rightarrow\quad \vec{B}_{p,3,b,d}=$$

$$\mathbf{2}\times\frac{\mu_0 I\left(\frac{L}{2}\right)^2}{4\pi}\int_{\tan^{-1}\frac{|y_p|-\frac{W}{2}}{\frac{L}{2}}}^{\tan^{-1}\frac{|y_p|+\frac{W}{2}}{\frac{L}{2}}}\frac{1}{(\cos\theta')^2\left(\left(\frac{L}{2}\right)^2+\left(\frac{L}{2}\tan\theta'\right)^2+\left(z_p+\frac{z_{Gap}}{2}+\Delta\right)^2\right)^{3/2}}d\theta'(-\hat{k})$$

$$+2\times\frac{\mu_0 I\left(\frac{L}{2}\right)^2}{4\pi}\int_{\tan^{-1}\frac{|y_p|-\frac{W}{2}}{\frac{L}{2}}}^{\tan^{-1}\frac{|y_p|+\frac{W}{2}}{\frac{L}{2}}}\frac{1}{(\cos\theta')^2\left(\left(\frac{L}{2}\right)^2+\left(\frac{L}{2}\tan\theta'\right)^2+\left(z_p-\frac{z_{Gap}}{2}-\Delta\right)^2\right)^{3/2}}d\theta'(-\hat{k})$$

$$\Rightarrow\quad \vec{B}_{p,3}=\frac{\mu_0 I\left(\frac{W}{2}+y_p\right)^2}{4\pi}$$

Eq. (A.23)

$$\times\int_{-\tan^{-1}\frac{L}{2\left|\frac{W}{2}+y_p\right|}}^{\tan^{-1}\frac{L}{2\left|\frac{W}{2}+y_p\right|}}\frac{1}{\cos^2\theta\left(\left(\left|\frac{W}{2}+y_p\right|\tan\theta\right)^2+\left(\frac{W}{2}+y_p\right)^2+\left(z_p+\frac{z_{Gap}}{2}+\Delta\right)^2\right)^{3/2}}d\theta(\hat{k})$$

$$+\frac{\mu_0 I\left(\frac{W}{2}+y_p\right)^2}{4\pi}$$

$$\times\int_{-\tan^{-1}\frac{L}{2\left|\frac{W}{2}+y_p\right|}}^{\tan^{-1}\frac{L}{2\left|\frac{W}{2}+y_p\right|}}\frac{1}{\cos^2\theta\left(\left(\left|\frac{W}{2}+y_p\right|\tan\theta\right)^2+\left(\frac{W}{2}+y_p\right)^2+\left(z_p-\frac{z_{Gap}}{2}-\Delta\right)^2\right)^{3/2}}d\theta(\hat{k})$$

$$+\frac{\mu_0 I\left(\frac{W}{2}-y_p\right)^2}{4\pi}$$

$$\times \int_{-\tan^{-1}\frac{L}{2\left|\frac{W}{2}-y_p\right|}}^{\tan^{-1}\frac{L}{2\left|\frac{W}{2}-y_p\right|}} \frac{1}{\cos^2\theta\left(\left(\left|\frac{W}{2}-y_p\right|\tan\theta\right)^2+\left(\frac{W}{2}-y_p\right)^2+\left(z_p+\frac{z_{Gap}}{2}+\Delta\right)^2\right)^{3/2}} d\theta(-\hat{k})$$

$$+\frac{\mu_0 I\left(\frac{W}{2}-y_p\right)^2}{4\pi}$$

$$\times \int_{-\tan^{-1}\frac{L}{2\left|\frac{W}{2}-y_p\right|}}^{\tan^{-1}\frac{L}{2\left|\frac{W}{2}-y_p\right|}} \frac{1}{\cos^2\theta\left(\left(\left|\frac{W}{2}-y_p\right|\tan\theta\right)^2+\left(\frac{W}{2}-y_p\right)^2+\left(z_p-\frac{z_{Gap}}{2}-\Delta\right)^2\right)^{3/2}} d\theta(-\hat{k})$$

$$+2\times\frac{\mu_0 I\left(\frac{L}{2}\right)^2}{4\pi} \int_{\tan^{-1}\frac{|y_p|-\frac{W}{2}}{\frac{L}{2}}}^{\tan^{-1}\frac{|y_p|+\frac{W}{2}}{\frac{L}{2}}} \frac{1}{(\cos\theta')^2\left(\left(\frac{L}{2}\right)^2+\left(\frac{L}{2}\tan\theta'\right)^2+\left(z_p+\frac{z_{Gap}}{2}+\Delta\right)^2\right)^{3/2}} d\theta'(-\hat{k})$$

$$+2\times\frac{\mu_0 I\left(\frac{L}{2}\right)^2}{4\pi} \int_{\tan^{-1}\frac{|y_p|-\frac{W}{2}}{\frac{L}{2}}}^{\tan^{-1}\frac{|y_p|+\frac{W}{2}}{\frac{L}{2}}} \frac{1}{(\cos\theta')^2\left(\left(\frac{L}{2}\right)^2+\left(\frac{L}{2}\tan\theta'\right)^2+\left(z_p-\frac{z_{Gap}}{2}-\Delta\right)^2\right)^{3/2}} d\theta'(-\hat{k})$$

A5. Total Magnetic field

For each section, the equations are reduced to a function of two variables: an angle and a z or y parameter. Integrating the equation over the angle means sweeping the entire coil to find the magnetic field at each point P along the Amperian loop.

The next step is to apply Ampère's Circuital Law. Since each coil has “n” windings, we need to multiply each field value by n.

$$n\left(\int \frac{\vec{B}_{p,1}}{\mu_{iron}}.d\vec{l}_1+\int \frac{\vec{B}_{p,2}}{\mu_{iron}}.d\vec{l}_2+\int \frac{\vec{B}_{p,3}}{\mu_{iron}}.d\vec{l}_3+\int \frac{\vec{B}_{p,4}}{\mu_{iron}}.d\vec{l}_4+\int \frac{\vec{B}_{p,5}}{\mu_{iron}}.d\vec{l}_5\right)+\frac{\vec{B}_{Gap}}{\mu_0}h_{Gap}=I_{enc.}$$

$$\vec{\boldsymbol{B}}_{\boldsymbol{Gap}} = \frac{\boldsymbol{2\mu_0 nI}}{\boldsymbol{h_{Gap}}} - \frac{\mathbf{n\mu_0}}{\mathbf{h_{Gap}}}\left(\int \frac{\vec{\mathbf{B}}_{\mathbf{p,1}}}{\boldsymbol{\mu_{iron}}}.\mathbf{d\vec{l}_1} + \int \frac{\vec{\mathbf{B}}_{\mathbf{p,2}}}{\boldsymbol{\mu_{iron}}}.\mathbf{d\vec{l}_2} + \int \frac{\vec{\mathbf{B}}_{\mathbf{p,3}}}{\boldsymbol{\mu_{iron}}}.\mathbf{d\vec{l}_3} + \int \frac{\vec{\mathbf{B}}_{\mathbf{p,4}}}{\boldsymbol{\mu_{iron}}}.\mathbf{d\vec{l}_4} + \int \frac{\vec{\mathbf{B}}_{\mathbf{p,5}}}{\boldsymbol{\mu_{iron}}}.\mathbf{d\vec{l}_5}\right)$$

$$\Rightarrow \vec{B}_{Gap} = \frac{2\mu_0 nI}{h_{Gap}} - \frac{n\mu_0}{h_{Gap}}\left(\int \frac{\vec{B}_{p,1}}{\mu_{iron}}.d\vec{l}_1 + \int \frac{\vec{B}_{p,2}}{\mu_{iron}}.d\vec{l}_2 + \int \frac{\vec{B}_{p,3}}{\mu_{iron}}.d\vec{l}_3 + \int \frac{\vec{B}_{p,4}}{\mu_{iron}}.d\vec{l}_4 + \int \frac{\vec{B}_{p,5}}{\mu_{iron}}.d\vec{l}_5\right)$$

$$\Rightarrow \vec{B}_{Gap} = \frac{2\mu_0 nI}{h_{Gap}} \qquad \textbf{Eq. (A.24)}$$

$$-\frac{\boldsymbol{n\mu_0}}{\boldsymbol{h_{Gap}\mu_{iron}}} \times \left(\int_{-\frac{z_{Gap}}{2}}^{-\frac{z_{Gap}}{2}-z_{15}} \int_{-\tan^{-1}\frac{L}{W}}^{\tan^{-1}\frac{L}{W}} \frac{\frac{\mu_0 I\left(\frac{W}{2}\right)^2}{\pi}}{(\cos\theta)^2\left(\left(\frac{W}{2}\tan\theta\right)^2 + \left(\frac{W}{2}\right)^2 + \left(z_p + \frac{z_{Gap}}{2} + \Delta\right)^2\right)^{3/2}} d\theta dz_p \right.$$

$$+ \int_{-\frac{z_{Gap}}{2}}^{-\frac{z_{Gap}}{2}-z_{15}} \int_{-\tan^{-1}\frac{L}{W}}^{\tan^{-1}\frac{L}{W}} \frac{\frac{\mu_0 I\left(\frac{W}{2}\right)^2}{\pi}}{(\cos\theta)^2\left(\left(\frac{W}{2}\tan\theta\right)^2 + \left(\frac{W}{2}\right)^2 + \left(z_p - \frac{z_{Gap}}{2} - \Delta\right)^2\right)^{3/2}} d\theta dz_p$$

$$+ \int_{-\frac{z_{Gap}}{2}}^{-\frac{z_{Gap}}{2}-z_{15}} \int_{-\tan^{-1}\frac{W}{L}}^{\tan^{-1}\frac{W}{L}} \frac{\frac{\mu_0 I\left(\frac{L}{2}\right)^2}{\pi}}{(\cos\theta')^2\left(\left(\frac{L}{2}\right)^2 + \left(\frac{L}{2}\tan\theta'\right)^2 + \left(z_p + \frac{z_{Gap}}{2} + \Delta\right)^2\right)^{3/2}} d\theta' dz_p$$

$$\left. + \int_{-\frac{z_{Gap}}{2}}^{-\frac{z_{Gap}}{2}-z_{15}} \int_{-\tan^{-1}\frac{W}{L}}^{\tan^{-1}\frac{W}{L}} \frac{\frac{\mu_0 I\left(\frac{L}{2}\right)^2}{\pi}}{(\cos\theta')^2\left(\left(\frac{L}{2}\right)^2 + \left(\frac{L}{2}\tan\theta'\right)^2 + \left(z_p - \frac{z_{Gap}}{2} - \Delta\right)^2\right)^{3/2}} d\theta' dz_p \right)$$

$$+ \int_{-y_{24}}^{0} \int_{-\tan^{-1}\frac{L}{2\left|\frac{W}{2}+y_p\right|}}^{\tan^{-1}\frac{L}{2\left|\frac{W}{2}+y_p\right|}} \frac{\frac{\mu_0 I\left|\frac{W}{2}+y_p\right|\left(z_p + \frac{z_{Gap}}{2} + \Delta\right)}{2\pi}}{\cos^2\theta\left(\left(\left|\frac{W}{2}+y_p\right|\tan\theta\right)^2 + \left(\frac{W}{2}+y_p\right)^2 + \left(z_p + \frac{z_{Gap}}{2} + \Delta\right)^2\right)^{3/2}} d\theta dy_p$$

$$+ \int_{-y_{24}}^{0} \int_{-\tan^{-1}\frac{L}{2\left|\frac{W}{2}+y_p\right|}}^{\tan^{-1}\frac{L}{2\left|\frac{W}{2}+y_p\right|}} \frac{\frac{\mu_0 I\left|\frac{W}{2}+y_p\right|\left(z_p - \frac{z_{Gap}}{2} - \Delta\right)}{2\pi} 1}{\cos^2\theta\left(\left(\left|\frac{W}{2}+y_p\right|\tan\theta\right)^2 + \left(\frac{W}{2}+y_p\right)^2 + \left(z_p - \frac{z_{Gap}}{2} - \Delta\right)^2\right)^{3/2}} d\theta dy_p$$

$$-\int_{-y_{24}}^{0}\int_{-\tan^{-1}\frac{L}{2\left|\frac{W}{2}-y_p\right|}}^{\tan^{-1}\frac{L}{2\left|\frac{W}{2}-y_p\right|}}\frac{\frac{\mu_0 I\left|\frac{W}{2}-y_p\right|\left(z_p+\frac{z_{Gap}}{2}+\Delta\right)}{2\pi}}{\cos^2\theta\left(\left(\left|\frac{W}{2}-y_p\right|\tan\theta\right)^2+\left(\frac{W}{2}-y_p\right)^2+\left(z_p+\frac{z_{Gap}}{2}+\Delta\right)^2\right)^{3/2}}d\theta dy_p$$

$$-\int_{-y_{24}}^{0}\int_{-\tan^{-1}\frac{L}{2\left|\frac{W}{2}-y_p\right|}}^{\tan^{-1}\frac{L}{2\left|\frac{W}{2}-y_p\right|}}\frac{\frac{\mu_0 I\left|\frac{W}{2}-y_p\right|\left(z_p-\frac{z_{Gap}}{2}-\Delta\right)}{2\pi}}{\cos^2\theta\left(\left(\left|\frac{W}{2}-y_p\right|\tan\theta\right)^2+\left(\frac{W}{2}-y_p\right)^2+\left(z_p-\frac{z_{Gap}}{2}-\Delta\right)^2\right)^{3/2}}d\theta\, dy_p$$

$$+\int_{-\frac{z_3}{2}}^{\frac{z_3}{2}}\int_{-\tan^{-1}\frac{L}{2\left|\frac{W}{2}+y_p\right|}}^{\tan^{-1}\frac{L}{2\left|\frac{W}{2}+y_p\right|}}\frac{\frac{\mu_0 I\left(\frac{W}{2}+y_p\right)^2}{4\pi}}{\cos^2\theta\left(\left(\left|\frac{W}{2}+y_p\right|\tan\theta\right)^2+\left(\frac{W}{2}+y_p\right)^2+\left(z_p+\frac{z_{Gap}}{2}+\Delta\right)^2\right)^{3/2}}d\theta dz_p$$

$$+\int_{-\frac{z_3}{2}}^{\frac{z_3}{2}}\int_{-\tan^{-1}\frac{L}{2\left|\frac{W}{2}+y_p\right|}}^{\tan^{-1}\frac{L}{2\left|\frac{W}{2}+y_p\right|}}\frac{\frac{\mu_0 I\left(\frac{W}{2}+y_p\right)^2}{4\pi}}{\cos^2\theta\left(\left(\left|\frac{W}{2}+y_p\right|\tan\theta\right)^2+\left(\frac{W}{2}+y_p\right)^2+\left(z_p-\frac{z_{Gap}}{2}-\Delta\right)^2\right)^{3/2}}d\theta dz_p$$

$$-\int_{-\frac{z_3}{2}}^{\frac{z_3}{2}}\int_{-\tan^{-1}\frac{L}{2\left|\frac{W}{2}-y_p\right|}}^{\tan^{-1}\frac{L}{2\left|\frac{W}{2}-y_p\right|}}\frac{\frac{\mu_0 I\left(\frac{W}{2}-y_p\right)^2}{4\pi}}{\cos^2\theta\left(\left(\left|\frac{W}{2}-y_p\right|\tan\theta\right)^2+\left(\frac{W}{2}-y_p\right)^2+\left(z_p+\frac{z_{Gap}}{2}+\Delta\right)^2\right)^{3/2}}d\theta dz_p$$

$$-\int_{-\frac{z_3}{2}}^{\frac{z_3}{2}}\int_{-\tan^{-1}\frac{L}{2\left|\frac{W}{2}-y_p\right|}}^{\tan^{-1}\frac{L}{2\left|\frac{W}{2}-y_p\right|}}\frac{\frac{\mu_0 I\left(\frac{W}{2}-y_p\right)^2}{4\pi}}{\cos^2\theta\left(\left(\left|\frac{W}{2}-y_p\right|\tan\theta\right)^2+\left(\frac{W}{2}-y_p\right)^2+\left(z_p-\frac{z_{Gap}}{2}-\Delta\right)^2\right)^{3/2}}d\theta dz_p$$

$$-\int_{-\frac{z_3}{2}}^{\frac{z_3}{2}}\int_{\tan^{-1}\frac{|y_p|-\frac{W}{2}}{\frac{L}{2}}}^{\tan^{-1}\frac{|y_p|+\frac{W}{2}}{\frac{L}{2}}}\frac{\frac{\mu_0 I\left(\frac{L}{2}\right)^2}{2\pi}}{(\cos\theta')^2\left(\left(\frac{L}{2}\right)^2+\left(\frac{L}{2}\tan\theta'\right)^2+\left(z_p+\frac{z_{Gap}}{2}+\Delta\right)^2\right)^{3/2}}d\theta' dz_p$$

$$-\int_{-\frac{z_3}{2}}^{\frac{z_3}{2}}\int_{\tan^{-1}\frac{|y_p|-\frac{W}{2}}{\frac{L}{2}}}^{\tan^{-1}\frac{|y_p|+\frac{W}{2}}{\frac{L}{2}}}\frac{\frac{\mu_0 I\left(\frac{L}{2}\right)^2}{2\pi}}{(\cos\theta')^2\left(\left(\frac{L}{2}\right)^2+\left(\frac{L}{2}\tan\theta'\right)^2+\left(z_p-\frac{z_{Gap}}{2}-\Delta\right)^2\right)^{3/2}}d\theta' dz_p\Bigg)$$

Bibliography

[1] S. Kumar, "Second malignant neoplasms following radiotherapy," *International Journal of Environmental Research and Public Health,* vol. 9, no. 12, p. 4744–4759, 2012.

[2] "News of Science," *Science,* vol. 125, no. 3236, pp. 18-22, 1957.

[3] O. Mohamad, T. Tabuchi, Y. Nitta, A. Nomoto, A. Sato, G. Kasuya, H. Makishima, H. Choy, S. Yamada, T. Morishima, H. Tsuji, I. Miyashiro and T. Kamada, "Risk of subsequent primary cancers after carbon ion radiotherapy, photon radiotherapy, or surgery for localised prostate cancer: a propensity score-weighted, retrospective, cohort study," *The Lancet Oncology,* vol. 20, no. 5, pp. 674-685, 2019.

[4] R. R. Wilson, "Radiological Use of Fast Protons," *Radiology,* vol. 47, no. 5, 1946.

[5] A. C. Knopf and A. Lomax, "In vivo proton range verification: a review," *Physics in Medicine & Biology,* vol. 58, no. 15, 2013.

[6] R. . W. Todd, J. M. Nightingale and D. B. Everett , "A Proposed γ Camera," *Nature,* vol. 251, p. 132–134, 1974.

[7] F. Roellinghoff, M. H. Richard, M. Chevallier, J. Constanzo, D. Dauvergne, N. Freud, P. Henriquet, F. Le Foulher, J. M. Létang, G. Montarou, C. Ray, E. Testa, M. Testa and A. H. Walenta, "Design of a Compton camera for 3D prompt-γ imaging during ion beam therapy," *Nuclear Instruments and Methods in Physics Research Section A: Accelerators, Spectrometers, Detectors and Associated Equipment,* vol. 648, pp. S20-S23, 2011.

[8] T. Conka Nurdan, K. Nurdan, A. B. Brill and A. H. Walenta, "Design criteria for a high energy Compton Camera and possible application to targeted cancer therapy," *Journal of Instrumentation,* vol. 10, no. 7, p. C07018, 2015.

[9] J. H. Kim, Y. S. Kim, H. S. Lee, H. Seo and C. H. Kim, "Optimization of DPC dSiPM-Based DOI Compton Camera by Monte Carlo Simulation," *IEEE Transactions on Nuclear Science,* vol. 65, no. 7, pp. 1424-1431, 2018.

[10] T. E. Peterson, A. B. Brill and A. H. Walenta, "High Energy Gamma-Ray Imaging Using Cherenkov Cone Detection - A Monte Carlo Study with Application to a Compton Camera System," in *IEEE Nuclear*

Science Symposium and Medical Imaging Conference Record (NSS/MIC), 2012.

[11] G. F. Knoll, Radiation Detection and Measurement, Fourth ed., Wiley, 2010.

[12] D. Lunney, J. M. Pearson and C. Thibault, "Recent trends in the determination of nuclear masses," *Rev. Mod. Phys.,* vol. 75, no. 3, pp. 1021-1082, 08 2003.

[13] S. K. Basu and E. A. Mccutchan, "Nuclear Data Sheets for A = 90," *Nuclear Data Sheets,* vol. 165, pp. 1-329, 2020.

[14] W. Huang, G. Audi, M. Wang, F. Kondev and S. Naimi, "The AME 2020 atomic mass evaluation (I). Evaluation of input data, and adjustment procedures," *Chinese Physics. C,* vol. 45, no. 3, 2021.

[15] Laboratoire National Henri Becquerel, "NUCLÉIDE-LARA Spectrum Processing," [Online]. Available: http://www.lnhb.fr/rd-activities/spectrum-processing-software/. [Accessed 20 12 2020].

[16] . D. J. Griffiths, Introduction to Electrodynamics, 4th ed., Cambridge University Press, 2017.

[17] A. F. Bielajew, Introduction to Special Relativity, Quantum Mechanics and Nuclear Physics for Nuclear Engineers, Michigan: The University of Michigan, 2014.

[18] K. S. Krane, Introductory Nuclear Physics, 3rd ed., Wiley, 1987.

[19] X. Mougeot, "Reliability of usual assumptions in the calculation of β and ν spectra," *Phys. Rev. C 91, 055504,* 2015.

[20] W. Andrä and H. Nowak, Eds., Magnetism in Medicine: A Handbook, Second ed., Wiley-VCH Verlag GmbH & Co. KGaA, 2006.

[21] T. Zickler, "Basic design and engineering of normal-conducting, iron-dominated electromagnets," pp. 65-102, March 2011.

[22] J. Tanabe, "Iron Dominated Electromagnets: Design, Fabrication, Assembly and Measurements," 2005.

[23] The Engineering Toolbox, "Permeability".

[24] C. Grupen and B. Shwartz, Particle Detectors, 2nd ed., Cambridge University Press, 2009.

[25] "M87, Black Hole-Powered Jet of Electrons and Sub-Atomic Particles Streams From Center of Galaxy," Space Telescope Science Institute (STScI), [Online]. Available: https://hubblesite.org/contents/media/images/2000/20/968-Image.html. [Accessed 1 2 2023].

[26] G. Barr, R. Devenish, R. Walczak and T. Weidberg, Particle Physics in the LHC Era, Oxford University Press, 2016.

[27] J. Larmor, "IX. A dynamical theory of the electric and luminiferous medium.— Part III. relations with material media," *Philosophical Transactions of the Royal Society of London,* vol. 190, pp. 205-300, 1897.

[28] H. Kolanoski and N. Wermes, Particle Detectors: Fundamentals and Applications, Oxford University Press, 2020.

[29] A. H. Compton, "A Quantum Theory of the Scattering of X-rays by Light Elements," *Phys. Rev.,* vol. 21, pp. 483-502, 1923.

[30] C. M. Davisson, "Interaction of γ-radiation with matter," *Alpha, Beta and Gamma-Ray Spectroscopy,* pp. 37-78, 1968.

[31] M. Tanabashi and et al., "(Particle Data Group) Review of Particle Physics," *Phys. Rev. D,* vol. 98, no. 3, 2018.

[32] P. Cherenkov, "Visible Radiation Produced by Electrons Moving in a Medium with Velocities Exceeding that of Light," *Physical Review,* vol. 52, pp. 378-379, 15 August 1937.

[33] I. M. Frank and I. Tamm, "Coherent Visible Radiation of Fast Electrons Passing Through Matter," *Dokl. Acad. Sci. URSS,* no. 14, pp. 109-114, 1937.

[34] "The Nobel Prize in Physics 1958," Nobel Prize Outreach AB 2022.

[35] M. Pierre and E. Sheldon, Physics of Nuclei and Particles, vol. 1, Academic Press, 1969.

[36] J. V. Jelley, "Cerenkov Radiation and Its Applications," *British Journal of Applied Physics,* vol. 6, no. 227, 1955.

[37] M. J. Berger, J. S. Coursey, M. A. Zucker and J. Chang, "Stopping-Power & Range Tables for Electrons,

Protons, and Helium Ions," NIST Standard Reference Database 124, 1999.

[38] H. A. Bethe, "Zur theorie des durchgangs schneller korpuskularstrahlen durch materie," *Annalen der Physik,* vol. 397, no. 3, pp. 325-400, 1930.

[39] R. M. Sternheimer, "The Density Effect for the Ionization Loss in Various Materials," *Physical Review,* vol. 88, no. 4, pp. 851-859, 1952.

[40] R. M. Sternheimer, S. M. Seltzer and M. J. Berger, "Density effect for the ionization loss of charged particles in various substances," *Physical Review B,* vol. 26, no. 11, pp. 6067-6076, 1982.

[41] S. M. Seltzer and M. J. Berger, "Bremsstrahlung spectra from electron interactions with screened atomic nuclei and orbital electrons," *Nuclear Instruments and Methods in Physics Research Section B: Beam Interactions with Materials and Atoms,* vol. 12, no. 1, pp. 95-134, 1985.

[42] R. H. Pratt, H. K. Tseng, C. M. Lee, L. Kissel, C. MacCallum and M. Riley, "Bremsstrahlung energy spectra from electrons of kinetic energy 1 keV < T1 < 2000 keV incident on neutral atoms 2 < Z < 92," *Atomic Data and Nuclear Data Tables,* vol. 20:2, pp. 175-209, 1977.

[43] S. Kasap and P. Capper, Eds., Springer Handbook of Electronic and Photonic Materials, 2nd ed., Springer Cham, 2017.

[44] A. S. Sedra and K. C. Smith, Microelectronic Circuits, 6th ed., Oxford University Press, 2009.

[45] D. Renker and E. Lorenz, "Advances in solid state photon detectors," *Journal of Instrumentation,* vol. 4, 2009.

[46] "A technical guide to silicon photomultipliers," Hamamatsu, 2018. [Online]. Available: https://hub.hamamatsu.com/us/en/technical-notes/mppc-sipms/a-technical-guide-to-silicon-photomutlipliers-MPPC-Section-1.html. [Accessed 12 2022].

[47] S. Gundacker and A. Heering, "The silicon photomultiplier: fundamentals and applications of a modern solid-state photon detector," *Physics in Medicine & Biology,* vol. 65, 2020.

[48] T. Nagano, K. Yamamoto, K. Sato, N. Hosokawa and A. Ishida, "Improvement of Multi-Pixel Photon Counter (MPPC)," in *IEEE Nuclear Science Symposium Conference Record*, 2011.

[49] Y. Tao, A. Rajapakse and A. Erickson, "Advanced antireflection for back-illuminated silicon photomultipliers to detect faint light," *Scientific Reports,* vol. 12, 2022.

[50] S. Piatek, "Silicon Photomultiplier, Operation, Performance & Possible Applications".

[51] "What is an SiPM and how does it work?," Hamamatsu, 2016. [Online]. Available: https://hub.hamamatsu.com/us/en/technical-notes/mppc-sipms/what-is-an-SiPM-and-how-does-it-work.html. [Accessed 12 2022].

[52] R. Newman, "Visible Light from a Silicon p-n Junction," *Phys. Rev.,* vol. 100, no. 2, pp. 700-703, 1955.

[53] A. L. Lacaita, F. Zappa, S. Bigliardi and M. Manfredi, "On the bremsstrahlung origin of hot-carrier-induced photons in silicon devices," *IEEE Transactions on Electron Devices,* vol. 40, no. 3, pp. 577-582, 1993.

[54] I. Rech, A. Ingargiola, R. Spinelli, I. Labanca, S. Marangoni, M. Ghioni and S. Cova, "Optical crosstalk in single photon avalanche diode arrays: a new complete model," *Opt. Express,* vol. 16, no. 12, pp. 8381-8394, 2008.

[55] J. Hagedorn, F. Blanc and J. Fleischer, "Winding technology," in *Handbook of Coil Winding: Technologies for efficient electrical wound products and their automated production*, Springer Berlin Heidelberg, 2018, pp. 139-243.

[56] H. Wiedemann, Particle Accelerator Physics, Springer International Publishing, 2015.

[57] D. Griffiths and D. Schroeter, Introduction to Quantum Mechanics, Cambridge University Press, 2018.

[58] G. Rüdiger, R. Hollerbach and L. L. Kitchatinov, Magnetic Processes in Astrophysics: Theory, Simulations, Experiments, Wiley, 2013.

[59] K. C. Ludema and O. O. Ajayi, Friction, Wear, Lubrication: A Textbook in Tribology, second ed., CRC Press, 2019.

[60] R. Bayerlein, *Coincident Detection of Cherenkov Photons for Medical Applications,* University of Siegen, 2020.

[61] "TOFPET2 ASIC SiPM Readout System - Hardware User Guide V1.6," PETsys Electronics, 2019.

[62] "Time-of-Flight Front End Board D (TOF FEB/D_v2) - Hardware User Guide V1.8," PETsys Electronics, 2020.

[63] "TOFPET2 ASIC SIPM Readout System - Software user guide V2022.04," PETsys Electronics, 2022.

[64] "PETsys TOFPET 2C/D ASIC (Rev. 13)," PETsys Electronics, 2021.

[65] "Hamamatsu technical notes on SiPMs," Hamamatsu, [Online]. Available: https://hub.hamamatsu.com/us/en/technical-notes/mppc-sipms.html. [Accessed 12 2022].

[66] International Atomic Energy Agency, "Live Chart of Nuclides".

[67] J. L. Autran, D. Munteanu, T. S. Saoud and S. Moindjie, "Characterization of atmospheric muons at sea level using a cosmic ray telescope," *Nuclear Instruments and Methods in Physics Research Section A: Accelerators, Spectrometers, Detectors and Associated Equipment,* vol. 903, pp. 77-84, 2018.

[68] W. L. L. Lenders, "The orthocyclic method of coil winding," *Philips Technical Review Vol. 23,* pp. 365-404, 16 October 1962.

[69] H. G. de Cock, "Wire Winding," in *Handbook of Precision Engineering Vol. 5*, London, Philips Technical Library, 1972.

[70] C. Piemonte and A. Gola, "Overview on the main parameters and technology of modern Silicon Photomultipliers," *Nuclear Instruments and Methods in Physics Research Section A: Accelerators, Spectrometers, Detectors and Associated Equipment,* vol. 926, pp. 2-15, 2019.

[71] C. Kittel, Introduction to Solid State Physics, 8th ed., John Wiley & Sons, 2004.